Electrochemical Nanofabrication for More Sustainable Photovoltaics

Electrochemical Nanofabrication for More Sustainable Photovoltaics
Ph.D. Thesis, University of Amsterdam, March 2024
Yorick Bleiji

ISBN: 978-94-92323-73-6

Cover design: *Silver nanowire grids as transparent electrode. The front cover represents the front side of the electrode, which is transparent to light and hence has a black background. By looking at the back cover, the light transmitted by the silver nanowire grid is represented by the white background. The nanowire grid shade an area that is smaller than its geometric coverage, as represented by the narrower black lines at the back cover. Silver ions surrounded by water molecules represent the electrochemical growth process.*

The work described in this thesis was performed between September 2019 and February 2024 at NWO-Institute AMOLF, Science Park 104, 1098 XG Amsterdam, The Netherlands.

This work is part of the Dutch Research Council (NWO) supported through the Joint Solar Program III (680-91-011).

A digital version of this thesis is available at:
https://ir.amolf.nl, https://www.lmpv.nl/Theses/ and https://dare.uva.nl.

Printed by Ridderprint, the Netherlands.

Electrochemical Nanofabrication for More Sustainable Photovoltaics

ACADEMISCH PROEFSCHRIFT

ter verkrijging van de graad van doctor

aan de Universiteit van Amsterdam

op gezag van de Rector Magnificus

prof. dr. ir. P.P.C.C. Verbeek

ten overstaan van een door het College voor Promoties ingestelde commissie,

in het openbaar te verdedigen in de Agnietenkapel

op donderdag 6 juni 2024, te 13.00 uur

door Yorick Bleiji

geboren te Leiden

Promotiecommissie

Promotores:	prof. dr. E. Alarcón-Lladó	Universiteit van Amsterdam
	prof. dr. A. Polman	Universiteit van Amsterdam
Overige leden:	prof. dr. E.C. Garnett	Universiteit van Amsterdam
	prof. dr. P. Schall	Universiteit van Amsterdam
	prof. dr. M. Morales Masis	Universiteit Twente
	dr. A. Baldi	Vrije Universiteit Amsterdam
	dr. S. Pullen	Universiteit van Amsterdam

Faculteit der Natuurwetenschappen, Wiskunde en Informatica

Contents

1

Introduction

1.1 The climate crisis

1.1.1 The demand for energy

The global demand for energy has seen a significant and sustained increase in recent decades, driven by a combination of economical, technological and societal factors. [1–3] There are many sources and forms of energy. Energy itself is never lost, but it is rather converted from one kind into another (conservation of energy). Plants, for example, use the energy from light to convert CO_2, water, and some other nutrients into organic building blocks, allowing them to grow. Effectively, plants convert solar energy into chemical energy which is stored in organic molecules. When these plants die, the energy that was stored in the organic molecules is buried in the ground. After repeating this cycle for millions of years, the remaining plant remnants went through a process known as fossilisation, and the energy has now been stored in the form of coal, oil, and natural gas. These fossil fuels have been the predominant sources of energy for much of the industrial era and continue to play a central role in meeting the world's energy needs. [1,3,4]

Fossil fuels are not sustainable since we need to wait millions of years for new fossil fuel deposits to form. Furthermore, the extensive use of fossil fuels has led to environmental challenges, with climate change being one of the most significant and has far-reaching consequences. [6] The burning of fossil fuels releases large amounts of greenhouse gases into the atmosphere of the Earth, in particular CO_2 (see Figure 1.1). [5,7,8] In addition to the burning of fossil fuels, other sources for the large amount of CO_2 emissions are the result of certain chemical reactions used in industry [9] (in particular steel production), [10] construction [8] (in particular concrete), [11] agriculture industry, [12] and deforestation. [7] The increasing demand for energy due to the rising population, industrialisation and economic factors in combination with the primary use of fossil fuels resulted in a stunning 33% increase in the concentration of CO_2 in the atmosphere, since 1958. The increasing concentrations of greenhouse gases are causing global warming, which causes the climate to change. The consequences of climate change are diverse and far-reaching, affecting ecosystems, weather patterns, sea levels, and biodiversity. [6]

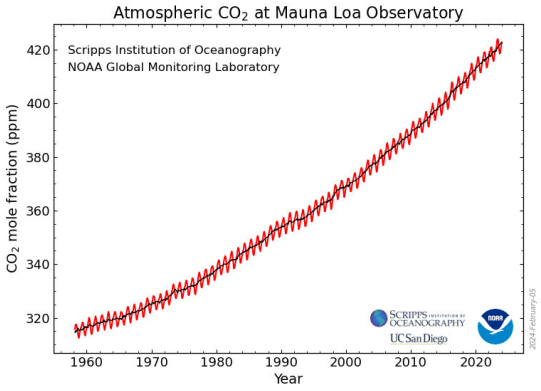

Figure 1.1: *Monthly average (red) and the seasonally corrected (black) atmospheric CO_2 concentration in parts per million (ppm) measured at the Mauna Loa Observatory by the National Oceanic and Atmospheric Administration (NOAA).*[5] *The data ranges from March 1958 to December 2023.*

The Paris Agreement, adopted on the 12^{th} of December 2015, at the 21^{st} Conference of the Parties (COP21) to the United Nations Framework Convention on Climate Change (UNFCCC), represents a collective commitment by the global community to limit global warming and reduce the impacts of climate change.[14] The primary objective is to limit the increase in global average temperature well below 2 °C above pre-industrial levels, with efforts to limit the increase in temperature up to 1.5 °C. Although the definition of the pre-industrial era is not defined by the agreement, the 1850-1900 period is used as baseline by the IPCC.[6] Figure 1.2 shows the annual global temperature anomaly of the land and ocean surface for the period 1850-2023, compared to the average temperature of 1850-1900, obtained by the National Oceanic and Atmospheric Administration (NOAA).[13] Since 1960, there has been a

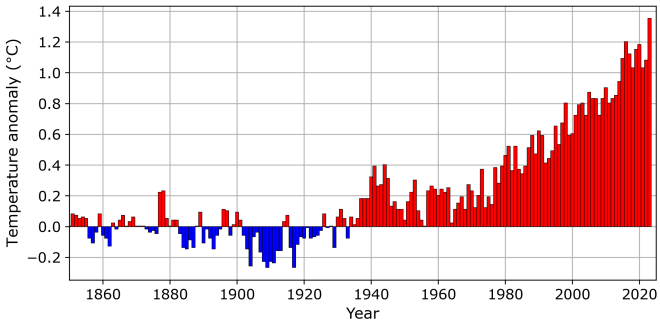

Figure 1.2: *The global land and ocean surface temperature per year compared to 1850-1900 average from 1850–2023. The years which are cooler/warmer than the average years are represented by blue/red bars, respectively. Data obtained from the National Oceanic and Atmospheric Administration (NOAA).*[13]

steady and even accelerating increase of the temperature anomaly. As of December 2023, the average global increase in temperature reached a value of +1.35 °C, [13] and it is expected that the average global temperature will increase to +2.7 °C by 2100, [15] far above the target of 2 °C. The question is therefore not whether we reach a global temperature increase of 2 °C, but when. The IPCC special report on the impacts of global warming of 1.5 °C above pre-industrial levels confirms that climate change is already affecting ecosystems, people and livelihoods around the world. [6] Furthermore, it shows that limiting global warming to 1.5 °C is possible, but would require extraordinary transitions in all aspects of society. Therefore, humanity should ask themselves the question how to reduce the emission of the green house gasses as soon as possible, and how to deal with the changing climate.

1.1.2 The transition to renewable energy sources

To address the challenges posed by the current reliance on fossil fuels, there is a growing global push toward transitioning to cleaner and more sustainable energy sources. Renewable energy technologies, such as solar (photovoltaic [16–18] or solar-thermal [19]), wind, [20] hydroelectric power, [21] and geothermal power, [22,23] offer viable alternatives that produce energy with lower carbon emissions. The shift towards renewable energy is essential not only for mitigating the impacts of climate change, but also for ensuring a more resilient and sustainable energy future for generations to come.

Central to the renewable energy transition is the electrification, a strategy that aims to replace conventional fossil fuel-powered systems with electric alternatives. [24] Electrification is driven by the recognition that electricity, when sourced from renewable sources, can serve as a versatile and clean energy carrier. Electric vehicles (EVs) replace combustion engine vehicles, [25] industries are adopting electric technologies, [26] and residential areas are increasingly relying on electricity for heating, cooling, and powering appliances. [24] The electricity produced by these renewable sources should be capable of being transmitted and stored for longer periods of time. The decentralisation of power generation requires complete transformation of the electrical power infrastructure, as the current infrastructure does not meet the requirements. [27,28] Storage of the generated electricity also faces some challenges. Unlike traditional power plants, which typically generate electricity in real-time to match the electricity demand, renewable sources like solar and wind farms face constraints. They can only produce electricity when conditions, such as sunlight intensity or wind speed, are adequate. To address this issue, short- and long-term storage solutions are crucial. Batteries, for example, store surplus electricity during peak production times and discharge it when needed, helping to balance short-term supply and demand in the electrical grid. As these batteries are great for remote low-energy-consuming devices, electrical energy storage in batteries on an industrial scale faces many challenges, such as limited energy density, resource scarcity, toxicity, and weight. [29,30] Long term electrical storage could be done by, for example, converting electricity into hydrogen [31] and other types of gasses and liquids (solar fuels), [32,33] or pumped hydroelectric energy storage. [29,34] These two aspects are still in need of further development in the case of electricity. [35,36]

This widespread electrification is seen as a powerful tool in the broader mission to decarbonise economies and mitigate the impacts of climate change. As a result of electrification and the general increase in electricity, the International Energy Agency (IEA) expects that the demand for electrical energy will almost double by 2050. [4] It is therefore of uttermost importance to generate this electricity using high-efficiency renewable sources, and renewable energy technology should be able to be installed at a rapid rate.

1.2 Photovoltaics (PV)

1.2.1 An important renewable technology

One important source of energy that will never deplete as long as humankind will exist, is solar energy. Each second, the Earth receives a tremendous amount of energy from the Sun (about 1.3 kW/m^2).[37] The total solar power that reaches the Earth is on the order of petawatts (10^{15} W), which means that the energy that the Earth receives in just one hour satisfies the world energy demand of a whole year.[38] As mentioned earlier, plants have long been harnessing solar energy for growth, and over millions of years, this solar energy has been transformed into fossil fuels. Instead of extracting and burning these finite fossil fuel resources, there is a more direct and sustainable solution: converting solar energy directly into electricity using solar cells, also known as photovoltaics (PV).

The concept of PV technology goes back almost two centuries, when in 1839 the photovoltaic effect was described for the first time by Edmund Becquerel.[40–42] Nearly a century later, the first practical solar cell was developed by Bell labs.[43] However, only in the last few decades significant breakthroughs have been made,[44] leading to high-efficiency devices (close to the detailed balance limit) that can last more than 25 years.[3] As a result, policy makers have started to acknowledge the potential of PV resulting in an exponential increase in installed capacity (see Figure 1.3). The installed capacity is expected to increase to multi-terawatts in the coming decade.[3,4,39]

One of the reasons for the rapid instalment rate is the modular nature of the technology. Unlike coal, gas, or nuclear power plants, the construction time of solar farms could be completed in several months instead of years,[45] since the individual panels can be manufactured off-site using optimised manufacturing processes. Solar panels are (relatively) light and small, which allows for easy transport around the world. Furthermore, solar cells can be used at (remote) locations where access to the power grid is not possible. Therefore, it could also contribute to the green development of some undeveloped countries, mainly on

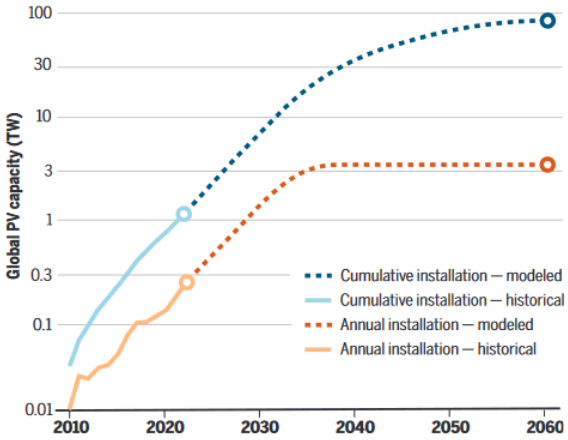

Figure 1.3: *Historic and modelled cumulative capacity (solid and dashed blue), and the historic and modelled annual installation (solid and dashed orange), respectively. Adapted from Ref. [39].*

the African continent.[46] Nowadays, solar panels have become one of the cheapest sources of energy.[4,47–49]

As the demand for solar energy continues to grow, it is expected that the installation of PV systems will increase exponentially in the coming decades.[39] Materials such as Cadmium Telluride (CdTe),[50] Copper Indium Gallium Selenide (CIGS),[51] Copper Zinc Tin Sulphide (CZTS),[52] and emerging perovskite-based solar cells[53] are gaining attention for their potential to revolutionise the industry. Perovskite materials, in particular, have attracted significant attention in recent years due to their remarkable optoelectronic properties, including high absorption coefficients and tunable bandgaps, and can be processed using low-cost solution-based techniques.[53]These thin-film technologies provide flexibility, making them suitable for easy installation on almost all types of roofs, including those of air planes.[54,55] Moreover, their lightweight nature enables rollable applications, allowing fast and temporary installations in various settings, including agricultural fields. To fully capitalise on the exponential growth and overcome the limitations of PV technologies, the development and adoption of these thin-film solar technologies will play a crucial role in the accessibility and affordability of solar energy worldwide.

Currently, silicon-based solar cells dominate the PV industry.[3] The great success of silicon in this field can be attributed to several factors, one of which is its long-standing use in the semiconductor industry for the manufacture of electronic chips.[56] Moreover, advancements in semiconductor fabrication technologies have enabled the production of extremely pure monocrystalline silicon, offering significant advantages to the photovoltaic industry.

Although silicon-based and thin-film PV technologies offer promising advantages, the available area for PV installations remains a limiting factor, particularly in densely populated or urban areas. Additionally, the balance of system costs currently represents a significant portion of the overall expense associated with solar energy systems.[57] To overcome these limitations, the efficiency of solar energy generation should be improved to extract the maximum amount of energy from the available surface area. One approach is to enhance the efficiency of solar cells by using a tandem configuration, in which multiple layers of different absorbs are stacked to capture a broader spectrum of sunlight and increase overall efficiency.[58] Silicon-perovskite tandem solar cells have emerged as a promising candidate for exceeding the detailed balance limit, which represents the theoretical maximum efficiency of a single junction solar cell.[59] Despite their promise, silicon-perovskite tandem solar cells still face challenges related to stability, scalability, and manufacturing reproducibility. Addressing and solving these challenges is an active field of research that includes research on material synthesis, device design, and encapsulation techniques.[60,61] If successfully commercialised, silicon-perovskite tandem solar cells could significantly increase the efficiency and viability of solar energy systems, unlocking new opportunities for the deployment of renewable energy in both urban and remote areas with limited available space.

1.2.2 Basic principles of solar cells

But how can the energy from the Sun be converted into usable energy in the first place? The energy carrier of light (photons) can be converted into the energy carrier of electricity (electrons) by what is known as the photovoltaic effect. This conversion from light to electricity can take place in multiple materials. The material needs to be able to absorb light, hereby generating free carriers, from which their electrical energy can be harvested.

The energy of the photons originating from the Sun span over a broad range, ranging from the ultra-violet to the far infrared, while peaking in the visible. The broad solar spectrum is the result of black-body radiation from the Sun at its surface temperature of 5772 K.[62] According

to Planck's law of black-body radiation, the black-body photon flux is given by:

$$\phi_{BB}(\lambda, T) = \frac{2\pi c}{\lambda^4} \frac{1}{\exp\left(\frac{hc}{\lambda k_B T} - 1\right)} \tag{1.1}$$

where c is the speed of light, T is the temperature, k_B and h are the Boltzmann and Planck constant, respectively. However, not all of these photons will reach the surface of the Earth. Part of the light is reflected into space by the atmosphere, whereas another part is absorbed by certain gases in the atmosphere. Moreover, the solar spectrum can differ throughout the day and year, but also depends on the location on Earth. For practical analysis purposes, reference datasets that serve as the standard for the solar spectrum have been established. The most practical one is the AM1.5G (air mass 1.5 global) spectra.[37] It describes the irradiance at noon at an average lattice under clear-sky conditions, including both diffuse and direct light. The integrated power is 1 kW/m^2, which is the total power density that we practically receive on Earth.

In semiconducting materials, the only photons from the solar spectrum that can be absorbed by the solar cell are photons that have an energy above the bandgap of the semiconductor $E_\gamma \geq E_{BG}$ (see Figure 1.4). After the absorption of a photon, the energy is therefore stored in the semiconductor by the excitation of a negatively charged electron and a positively charged hole, which are left behind in the conduction and valence bands, respectively. Each photon γ excites a highly energetic electron-hole pair and, due to rapid thermalisation, they end up with all having the same energy equal to the bandgap E_{BG} regardless of the photon energy. After the electron is thermalised to the bottom of the conduction band, it can lose its energy by recombining with the leftover hole. Recombination can be either radiative (by the emission of a photon) or nonradiative (by the emission of a phonon). The amount of time it takes for the excited electron to lose all its energy is called the lifetime. For an ideal solar cell, the only energy losses are the thermalisation of above-bandgap photons and absorption losses of below-bandgap photons. Based on these losses and in combination with thermodynamic constraints, the maximum efficiency of a single junction solar cell can be calculated, which is given by the detailed balance limit.[63,64]

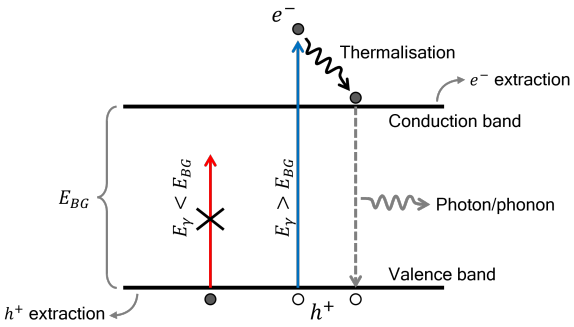

Figure 1.4: *Schematic of the working principle of a solar cell. Photons having an energy greater than the bandgap excites an electron from the valence band into the conduction band. The excess amount of energy is thermalised to the bottom of the conduction band. If the photogenerated carriers are not extracted within a their lifetime, they recombine by emitting a photon/phonon.*

To extract energy from the excited electron, the electron and hole need to be separated before they recombine. The longer the lifetime of the excited electron, the higher the chance of the separation of the electron from the hole. Separation of the electron hole pair is possible by having an internal electric field, often by using a p-n junction. A p-n junction could be created by doping the silicon with impurities. These impurities create regions with excess positive charge carriers (p-type) or negative charge carriers (n-type), by which a p-n junction is created (homo-junction). Alternatively, a p-n could be formed by contacting two dissimilar materials having a dissimilar bandgap (hetero-junction).

The maximum amount of electrical potential energy that can be extracted from the solar cell strongly depends on the alignment of the energy bands within all active layers.[65] At equilibrium, the potential energy of the electrons and holes is described by the Fermi level. However, when the solar cell is under illumination, the system is not in equilibrium due to the excitement of electron-hole pairs. In fact, it reaches a steady state as a function of the intensity of light, where the number of excited electrons is constant over time. The average energies of the excited electrons and holes can be described by the quasi-Fermi levels.[65] The difference between these two quasi-Fermi levels translates into a difference in voltage for electric charges. This is similar to the voltage of a charged battery, where the solar cell is continuously recharged by the incident light.

When contacting these two electric poles of the solar cell, a current can flow through an external load. The current density that flows when the two poles are in short circuit is referred to as the short-circuit current density J_{sc}. The J_{sc} is proportional to the amount of absorbed photons $N_\gamma(E_{ph} \geq E_{BG})$ within a certain time frame τ, multiplied by the charge of an electron q:

$$J_{SC} = \frac{qN_\gamma(E_{ph} \geq E_{BG})}{\tau} = q\int_{E_{BG}}^{\infty} \phi_{AM1.5G}(E)dE \tag{1.2}$$

where $\phi_{AM1.5G}(E)$ is the AM1.5G solar flux (amount of photons per unit area reaching the solar cell per second), as function of the energy of the photon E.

In the dark and at thermal equilibrium (i.e., the cell has the same temperature as its environment), the reverse process will occur. Namely, a (dark) recombination current density J_0 occurs via photon emission. Due to reciprocity, the rate of absorption and emission is the same and J_0 is described by:

$$J_0 = q\int_{E_{BG}}^{\infty} \phi_{BB}(E, T = 300\text{ K})dE \tag{1.3}$$

where $\phi_{BB}(E, T = 300\text{ K})$ is the black-body spectrum at 300 K as given by Equation 1.1.

The voltage difference between the two poles of the solar cell at open circuit is called V_{oc}. The $V_{oc}$is determined by the difference between the quasi-Fermi levels, which results from the photo-generated carrier density. Therefore, the V_{oc} is a function of the incident light intensity and is given by

$$V_{OC} = \frac{kT}{q}\ln\left(\frac{J_{SC}}{J_0} + 1\right) \tag{1.4}$$

The V_{oc} does therefore not only depend on the J_{sc}, but also on the recombination current J_0. At similar values of the J_{sc}, V_{oc} can be therefore be regarded as a measure of charge recombination, where the larger the voltage, the better the passivisation of the device. Furthermore, the open-circuit voltage is also influenced by the series resistance R_S of the device, which will result in ohmic losses. Therefore, it is important that the charge carriers are extracted with the least amount of electrical resistance.

Experimentally, these two solar cell parameters are extracted by performing current density-voltage (J-V) measurements. In a J-V measurement, the current is measured as the

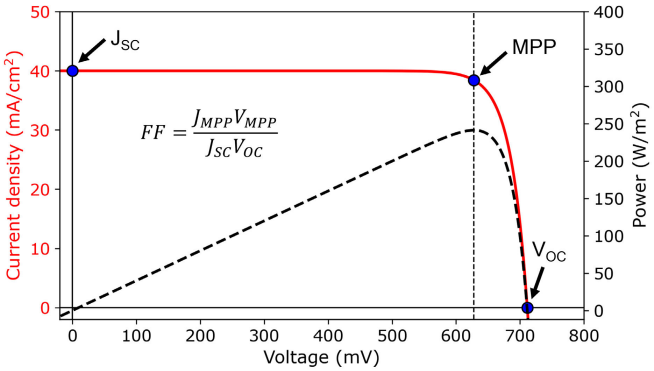

Figure 1.5: *Typical current density J - voltage V curve for a silicon based solar cell represented by the red line. The voltage-dependent power is represented by the dashed black line. The three marked points represent the short circuit current density J_{sc}, the open circuit voltage V_{oc}, and the maximum power point (MPP). The fill factor (FF) can be calculated from these three points. The values of the solar cell parameters were inspired by Ref. [66].*

potential is swept linearly from negative to positive values while the cell is illuminated with an intensity of 1 Sun using a calibrated solar simulator that mimics the AM1.5G spectrum, and the cell is kept at a temperature of 25 °C. [67] A typical J-V curve of a solar cell is shown in Figure 1.5 represented by the red curve. The J_{sc} and the V_{oc} correspond to the current density at zero voltage and the voltage at zero current density, respectively, indicated by the blue points. Another important point in the J-V curve is the maximum power point (MPP), which is the maximum power density ($P = J \times V$, dashed black line in Figure 1.5) that the cell can generate. The MPP ($P_{max} = J_{MPP} \times V_{MPP}$) is related to J_{sc} and V_{oc} via the fill factor (FF):

$$FF = \frac{J_{MPP} V_{MPP}}{J_{SC} V_{OC}} \tag{1.5}$$

In essence, the FF is a measure of the squareness of the J-V curve, where the larger the FF, the larger the power output.

The last and perhaps the most important descriptor of the solar cell performance is the efficiency, η. The efficiency is defined as the amount of power the solar cell generates normalised by the total incident power. The maximum efficiency is thus:

$$\eta = \frac{P_{MPP}}{P_{AM1.5G}} = \frac{J_{SC} V_{OC} FF}{P_{AM1.5G}} \tag{1.6}$$

where $P_{AM1.5G}$ is the incident power density of the AM1.5G spectrum and equals 1 kW/m^2.

1.2.3 Critical material usage in PV

As the development of solar cell technology advances, the demand for several materials is expected to increase significantly. [39] However, the availability of raw elements may be limited, raising concerns about potential supply constraints as the demand for solar energy continues to grow. [39,69] As shown in Figure 1.6, important PV materials such as indium, gallium, silver, cadmium, arsenic, and tellurium are limited by their abundance. [68]

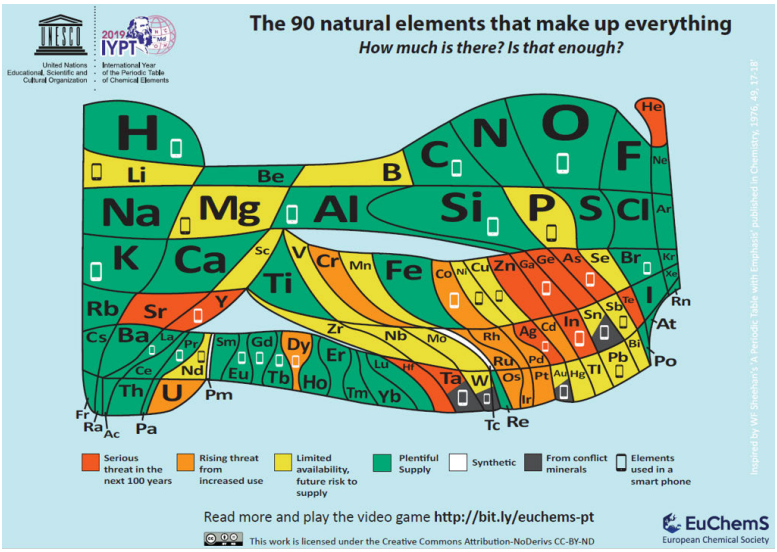

Figure 1.6: *EuChemS periodic table of elements illustrating the relative abundance of the elements (the larger the box, the more abundant) and highlights potential supply issues. Adapted from Ref. [68].*

The main component in a solar cell (and probably the most predominant in terms of quantity) is the absorbing semiconductor, such as silicon, perovskite, CdTe, or CIGS. Arsenic, along with indium and gallium, is the main element in high-efficiency III-V solar cells and is also commonly used as a dopant in silicon cells.[70] Tellurium is mainly used in CdTe-based solar cells.[50] All of these are limited in abundance (see Figure 1.6), and supply is under serious threat in the next 100 years.[68] Silicon, on the other hand, although abundant, its use is potentially limited by geopolitical arguments.[71] In 2021, more than 70% of the global silicon supply came from China,[72] which leaves the PV industry highly dependent on a single country.

Aside from the light absorber, solar cells require many other layers containing various elements to facilitate the extraction of the generated electricity from the device. These additional layers play a crucial role in transporting photogenerated carriers selectively (electrons and holes) to large metal electrodes in the form of bus bars and fingers, where the charge is collected and used to perform electrical work. A key requirement of these layers is that they must be optically inactive, meaning that any photons absorbed in these layers will not be transformed into electricity. In traditional silicon solar cells, these charge transport layers typically consist of materials such as doped (crystalline, nano-crystalline or amorphous) silicon, metal oxides, microscale metal contacts, and transparent conductive materials (TCMs). Sometimes, a combination of a few of the above are necessary to ensure high transparency, charge collection efficiency, and efficient lateral charge transport to the macroscopic metal electrodes.

Silver, a scarce material, is frequently used in its metal form as contact due to its excellent electrical conductivity, great optical properties (e.g., as a back reflector), and corrosion resistance.[73,74] Ultimately, indium could be deemed most critical due to its prevalence

in most solar cell types and in many other (opto)electronic devices (LEDs, touchscreens, etc.) such as TCM in the form of indium tin oxide (ITO). Indium is also one of the main elements of CIGS based solar cells.[51]

Therefore, efforts are made to mitigate material scarcity, including research on alternative materials with similar or superior properties, recycling initiatives to recover and reuse valuable materials from end-of-life solar panels,[3] and diversification of supply sources to reduce dependence on limited geographic regions. Additionally, advances in solar conversion efficiency and manufacturing processes aim to reduce the overall material consumption per unit of energy produced, thus relieving pressure on scarce raw resources.

In this thesis, we focus on developing new materials and methods for a more sustainable TCM production. We focus on the replacement of ITO in transparent conducting materials used in solar cells by metal nanowire networks, as will be discussed in the next section.

1.3 Transparent conductive materials (TCM)

Transparent conductive materials (TCMs) are essential in photovoltaic applications. TCM layers are needed at the front of a solar cell to reduce the sheet resistance of the emitter/base layer in most solar cells, facilitating the collection of photogenerated electrons and holes, and thereby optimising the overall efficiency of the photovoltaic device. TCMs provide efficient lateral transport of photogenerated charge to larger metal electrodes, located either on the sides of the solar cell or in the form of fingers and busbars across the cell. Fingers and busbars are micro- and mm-sized metal lines that shadow part of the solar cell surface, but are so far still essential to collect charges from solar cells. The better the TCM, the lower the density of fingers and busbars, or may even be eliminated altogether, therefore allowing for better solar cell performance and removing an additional fabrication step. Besides the high electrical performance, TCMs must maintain high optical transparency to allow sunlight to reach the absorber layer in the solar cell. Photons absorbed by the TCM is called parasitic absorption, and it is one of the losses in a solar cell.

The field of transparent conducting materials has been mainly dominated by transparent conducting oxides (TCOs), in particular indium tin oxide (ITO).[75–78] Because indium is a scarce element, its usage should be minimised or substituted by other elements whenever feasible. Furthermore, ITO faces other challenges, such as brittleness,[77,79] low infrared transmittance,[80] and poor resource efficiency.[76,77] In summary, there is a great drive to find alternatives to indium-based TCMs.

An alternative to ITO is fluorine-doped tin oxide (FTO), which has the potential to offer similar electrical conductivity and transparency properties,[81] but still contains elements with limited availability (i.e., tin) and it is hard to fabricate with low surface roughness. Carbon-based materials such as graphene[82,83] and carbon nanotubes[84,85] have gained recent attention for their excellent electrical conductivity and mechanical flexibility, but their stability and the ability to obtain low sheet resistance remains a challenge.[84] The combination of ultrathin metal films with ITO layers has also been proposed as a measure to reduce the amount of ITO with similar electrical and optical performance.[86,87]

An attractive approach is the use of nanostructured metal networks as TCMs, as they offer unique control over the optical properties that can be exploited for light management in photovoltaic devices.[88–90] Nanowire networks are the topic of this thesis, and it is explained in more detail in the following section. Exploring these alternative materials and technologies not only addresses the challenge of indium scarcity but also opens new possibilities for improving the efficiency and performance of solar cells.

1.3.1 Metal nanowire networks as TCM

This thesis aims to address the challenge of indium scarcity in solar cell manufacturing by focussing on the replacement of these indium-based TCMs with metal nanowire networks. Metal nanowire networks (MNNs) consist of interconnected metallic nanowires, typically ranging from tens to hundreds of nanometers in diameter and several micrometers in length. These networks are formed by assembling metallic nanowires into a mesh-like structure, often through techniques such as solution-based deposition, printing, or self-assembly processes. The small cross-section of the nanowires (smaller than the wavelength of visible light) results into reduced light-matter interactions and therefore in high transparency. Metal nanowires exhibit efficient electron transport along the length of the wires. The network geometry offers explicit conducting pathways with large open areas, resulting in high electrical conductivity, transparency, and mechanical flexibility.

An interesting advantage of MNNs is their inherent high design flexibility. Specifically, the ability to control nanowire size, shape, and arrangement enables tailoring the optical behaviour of the network to fulfil specific requirements, such as enhancing light absorption or minimising reflection at certain wavelengths.[88,91–93] Nanophotonic engineering applied to MNNs can transform the typically optically inactive TCM layer into an "optically smart" component within the solar cell architecture[94] For instance, the MNN can serve not only for charge transport, but also as a spectral splitter, selectively transmitting or reflecting light of different wavelengths.[95,96] Another example is the use of MNNs for light trapping, where the regular arrangement of nanowires introduces additional in-plane momentum to incident light, enhancing the optical path length within the light absorber, thereby maximising absorption.[91,97] Furthermore, MNNs often have a large haziness (defined as the ratio between diffuse and total transmitted light), which is beneficial for solar cell applications.[98,99] Their flexibility and mechanical robustness also make them ideal for flexible and lightweight solar cell applications.[100]

Nanophotonic and electrical engineering in MNNs requires high control over the dimensions, shape, and arrangement of the nanowire. For PV applications, it is also important that the fabrication method is compatible with current manufacturing processes in the solar cell industry, including high throughput and scalability. Multiple metals have been used for the fabrication of MNNs. With an electrical conductivity of $6.3 \cdot 10^7$ S/m, silver is the best electrical conductor and is therefore the most promising MNN material.[75,101] Next to its excellent electrical properties, silver offers high chemical stability,[98] and optical transparency due to the plasmonic resonance being outside the visible region.[88] Silver nanowire networks offer versatility and compatibility with a wide range of substrates and fabrication techniques, making them suitable for use in various solar cell architectures and manufacturing processes.[98]

In addition to silver, studies have also explored the use of copper because of its higher abundance and lower cost compared to silver. However, the adoption of copper nanowire networks still has some challenges. One significant disadvantage is its chemical stability, particularly in the presence of moisture and oxygen, which leads to copper oxidation and performance degradation over time. Furthermore, copper adheres poorly and can easily diffuse into silicon, which adversely and irreversibly affecting the performance and reliability of solar cells.[102] Thin nickel layers have been proposed to increase adhesion and act as a diffusion barrier. Strategies, including protective coatings, are also being explored to reduce the risk of oxidation and degradation, thereby improving the chemical stability of copper electrodes.[103]

In this thesis, we develop and investigate MNNs with PV applications in mind. However,

it is important to keep in mind that MNNs can be used in many applications beyond solar cells, including flexible electronics,[98,104] touchscreens,[105] and displays.[106]

1.3.2 Figure of Merit (FoM) for TCMs

The two main attributes in TCMs are high electrical conductivity and high optical transparency in the visible spectral range. Transparency and conductivity are coupled physical properties, and therefore it is not easy to achieve high transparency and conductivity at the same time.[98] The trade-off and optimisation of transparency and conductivity have been the focus of most TCM-related works.[107–110] To benchmark the performance across different TCMs, it is important to define a single parameter as the figure of merit (FoM).

In 1972, Fraser and Cook defined the first FoM for a TCM using the ratio between the transmittance T and sheet resistance $R_{\square}$,[111] giving equal weight to optical and electrical parameters:

$$FoM_{FC} \equiv \frac{T}{R_{\square}} \tag{1.7}$$

Transmittance (i.e., the fraction of light that is transmitted) in itself is ill defined here as it may depend on the application. For solar applications, the AM1.5G averaged transmittance is most relevant. For transparent optoelectronics, the average transmittance convoluted by the human-eye response should be used. In either case, many works use the transmittance value at 550 nm, as it corresponds to the wavelength with the highest irradiance in the solar spectrum[37] and also to the wavelength to which the eye is most sensitive. $R_{\square}$ on the other hand is a size-independent value describing the resistance of an equivalent thin film of thickness t and equal length l and width w:

$$R = \frac{l}{wt\sigma} \overset{w=l}{=} \frac{1}{t\sigma} = \frac{\rho}{t} \equiv R_{\square} \tag{1.8}$$

where $\sigma = 1/\rho$ is the electrical conductivity of the film, with ρ being the electrical resistivity. The units of the sheet resistance are Ohms per square (noted as $\Omega/\square$ or Ω/sq), where the square is dimensionless but it just indicates it is a special kind of resistance.

The definition of Fraser and Cook was simple and efficient, but its usage is rather limited. The sheet resistance can be expressed in terms of conductivity and thickness (Equation 1.8), and the transmittance is determined by the Beer-Lambert law for thin films. Therefore, the FoM by Fraser and Cook can be written as:

$$FoM_{FC} = \sigma t \exp(-\alpha t) \tag{1.9}$$

where α is the optical absorption coefficient. The maximum of the FoM ($\partial FoM_{FC}/\partial t = 0$) occurs at a film thickness that corresponds to an optical transmittance of only $T_{max} = 1/e =$ 37%, which is very low for any practical purposes.[75,112,113] Therefore, in 1976, Haacke[113] introduced a modification by introducing an exponent to the transmission, as:

$$FoM_{Haacke} \equiv \frac{T^{10}}{R_{\square}} \tag{1.10}$$

The power 10 was chosen to ensure that the maximum FoM in a given material has a transmittance greater than 90%.[75]

Later, Dressel and Grüner suggested a dimensionless FoM by considering the physical link between electrical and optical properties. These are both determined by the response of electrons to an electric field, either dynamic (light) or static (voltage). They define the FoM as

the ratio between static (or DC) and optical conductivity, which are linked to sheet resistance and the transmittance, respectively, as: [114]

$$FoM_{DG} \equiv \frac{\sigma_{DC}}{\sigma_{opt}} = \frac{Z_0}{2R_\square} \frac{1}{T^{-1/2}-1} \approx \frac{188.5}{R_\square (T^{-1/2}-1)} \tag{1.11}$$

where Z_0 is the impedance of free space, σ_{DC} and σ_{op} are the DC electrical and optical conductivity, respectively.

Both FoM$_{Haacke}$ and FoM$_{DG}$ are widely used for TCM benchmarking. [75,107,109,110,115–117] However, these two FoMs in principle only hold for thin films. In MNNs, both FoMs can be made arbitrarily large since by increasing the pitch and nanowire width proportionally, transparency (considered here as the geometrical shading) is kept constant while $R_\square$ steadily decreases. Therefore, FoM$_{Haacke}$ and FoM$_{DG}$ are not suitable for comparing TCMs based on discontinued structures, such as MNNs. There is no universal FoM for TCMs, and it is thus better to focus on a specific application. In photovoltaics, the power output of the device is the parameter that needs to be maximised. Both the transmittance and the sheet resistance of the TCM will influence the maximum power point, but one might be more important than the other, depending on the device architecture.

Recently, a more accurate FoM for TCMs in PV applications was introduced by Anand *et al.*. [112] The PV specific FoM is based on the impact of sheet resistance and transmittance on the maximum attainable power in a solar cell, normalised to that of an ideal TCM (i.e., $T = 100\%$ and $R_\square = 0.0001\Omega\square^{-1}$, set for practical reasons):

$$FoM = \frac{P_{MPP}(E_G, T(\lambda), R_\square)}{P_{MPP}(E_G, T = 100\% \forall T, R_\square = 0.0001\Omega/sq)} \tag{1.12}$$

where E_G is the bandgap of the absorber (usually Si: 1.14 eV). Therefore, this FoM has a dimensionless value that ranges from zero to unity, where a unity value corresponds to the power output of an ideal solar cell.

Compared to the detailed balance described previously, the extracted current in a realistic solar cell includes the series resistance R_s in the contact layers. The maximum power is then calculated by solving the self-consistent 1-diode implicit equation:

$$I = I_0(T)\left[\exp\left(\frac{q(V-IR_s)}{k_B T} - 1\right)\right] - I_{SC}(T) \tag{1.13}$$

where q is the elementary charge, k_B is the Boltzmann constant, and T is the ambient temperature. The series resistance R_s is linked to the TCM sheet resistance $R_\square$ and cell dimensions, where the length l_{cell} and the width w_{cell} define the area between the fingers and the busbars (see the sketch in the Figures 1.7a and b:

$$R_s = R_\square \frac{l_{cell}}{3w_{cell}} \tag{1.14}$$

In here, the factor 3 arises from the differential of the power dissipation based on the geometry of the solar cell. [118] For the calculation of the FoM, it is therefore assumed that the current needs to travel a length of l_{cell} until it reaches a metal contact. For the calculation of the series resistance, Anand *et al.* uses $l_{cell} = 5$ mm and $w_{cell} = 10$ cm as a standard. Of course, the better the TCM, the more the cell area can be expanded and the less fingers/busbars electrode area is needed. In general, these values must be adjusted to the architecture of the device of interest.

To account for the optical properties of the TCM in the calculation of I_{SC} and I_0 we must normalise the solar spectrum and black-body radiation by the TCM transmittance, respectively. Instead of just integrating the flux of the AM1.5G solar spectrum, the short-circuit current density J_{sc} generated by the solar cell depends on the transparency of the TCM. Therefore, the short-circuit current is given by:

$$I_{SC} = J_{SC}\ w_{cell} l_{cell} = q \int_0^{\lambda_G} T(\lambda)\phi_{AM1.5G}(\lambda) d\lambda\ w_{cell} l_{cell} \tag{1.15}$$

where $T(\lambda)$ is the wavelength dependence transmission spectrum of the TCM, and λ_G is the bandgap of the absorber. In a similar way, the dark current is given by:

$$I_0 = q \int_0^{\lambda_G} T(\lambda)\phi_{BB}(\lambda, T = 300\ \mathrm{K}) d\lambda\ w_{cell} l_{cell} \tag{1.16}$$

as determined by the black-body radiation photon flux $\phi_{BB}(\lambda, T = 300\ \mathrm{K})$ of the device at its temperature of 300 K (see Equation 1.1).

Figures 1.7c and d show the contour plot of the PV-specific FoM as a function of sheet resistance and transmittance for a silicon-based solar cell having 3 busbars and having either

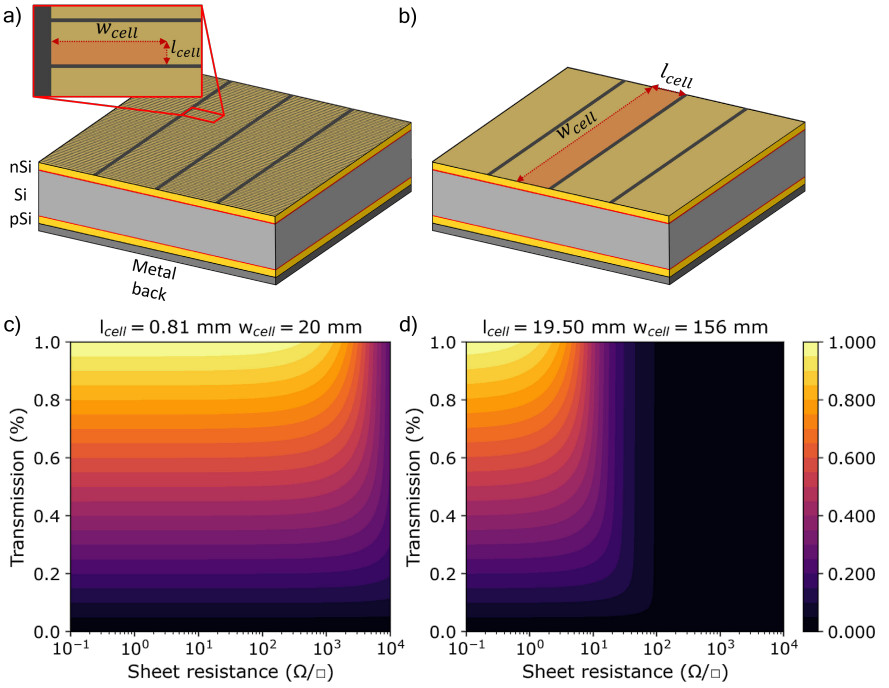

Figure 1.7: *Schematic of a silicon-based solar cell having 3 busbars a) with 95 fingers and b) without fingers. The length and width of the unit cell is marked by the red area. Contour plot of the PV-specific FoM for the corresponding geometries for a solar cell length and width of c)* $l_{cell} = 0.81$ *mm and* $w_{cell} = 20$ *mm, and d)* $l_{cell} = 19.50$ *mm and* $w_{cell} = 156$ *mm.*[119] *The colour bar is identical for a) and b).*

95 fingers (Figures 1.7a and c) or is finger-free (Figures 1.7b and d).[119] By comparing the two contour plots, one can see how the choice of geometry is important to the absolute value of the FoM, and hence, one should always specify it. Nevertheless, the absolute value of the FoM for both contour plots is directly proportional to the power output of the device. Clearly, the PV-specific FoM can not be made arbitrarily large, as the FoM ranges from zero (no power output) to unity (theoretical maximum power output). Furthermore, Figure 1.7d shows that the front metal contact can be even made finger-free as long if the sheet resistance of the TCM is below 1 Ω/□ while maintaining > 90% transparency.

On the other hand, the contour plots reveal a very important feature: for low enough sheet resistance values, the power output is only limited by optical transmittance. The point at which the sheet resistance can be considered low enough depends on the cell geometry, where the larger the distance between the electrodes, the lower the sheet resistance has to be. In the opposite case of large sheet resistance, the power output is limited by the series resistance, and hence TCM transparency has no effect on the power output. This important feature is lacking for the other types of FoM, as they can be made arbitrarily large by reducing the sheet resistance to zero, even though the actual device performance is not improved.

In this thesis, we will use the PV-specific FoM introduced by Anand *et al.*, hereby using silicon as the absorber material and the system parameters of l_{cell} = 0.5 cm and w_{cell} = 10 cm.[112]

1.4 Sustainable TCM fabrication methods: Electrodeposition

Efficiency and sustainability are therefore key considerations in the PV manufacturing processes. To address these challenges, fabrication methods that minimise material usage, reduce waste, and reduce energy consumption are essential. In the literature, several fabrication methods have been explored to achieve random and regular MNNs. Commonly used sputtering or thermal evaporation techniques for depositing silver onto a masked surface present several challenges, particularly with respect to energy consumption and material efficiency.[98,120] Sputtering and thermal evaporation of silver is energy intensive and requires significant power to eject silver atoms from a target onto a substrate.[120,121] Moreover, substantial material wastage occurs during the lift-off process, where excess silver is removed along with the mask, leading to inefficiencies in material use. Although screen printing offers a more resource-efficient alternative to sputtering, it comes with its own set of limitations. Screen printing has limited line-width capability, restricting its applicability to produce nanosized structures.[73,122]

For a more sustainable and scalable approach, solution-based growth of silver nanowires offers a promising alternative.[76,106,123] A widely spread method involves the colloidal growth of nanowires, where nanowires are synthesised in a solution and deposited on a substrate using drop casting techniques,[124,125] spray coating,[126–128] or dip coating techniques.[115,129] Although this method can result in high transparency and conductivity, the arrangement of nanowires is random, leading to low yield and high performance variations.[104,130] Also, post-annealing or other post-treatment of the metal nanowires is often necessary to reduce contact resistance at interconnections.[109,130–132] Moreover, controlling the sheet resistance and transparency independently remains a challenge, limiting the optimisation of nanowire properties for specific applications. Furthermore, spatial control is challenging, as the dropcasted nanowires result in a random network and limit their use for well-defined nanowire struc-

tures. Direct printing techniques, such as electrohydrodynamic (EHD) printing,[107,133–135] inkjet printing,[105] and aerosol printing,[136] offer precise control over nanowire placement and orientation, enabling the fabrication of transparent electrodes with tailored properties. However, scalability is a great challenge for these direct printing techniques.

On the contrary, photolithography and roll-to-roll printing with UV-curable materials allow for large-scale production of transparent electrodes with high resolution and consistency.[137] A more controlled approach can be achieved by using masks during deposition, which guide the placement of nanowires to some extent. Self-cracking techniques,[110,117] nature inspired templates,[138] bubble templates,[98] or microsphere lithography[139] have also been used to control the arrangement of the nanostructure, resulting in more uniform and ordered structures with enhanced electrical properties. Finally, nano- or micro-imprint lithography,[108,140] and direct laser writing techniques[141,142] provide additional options for patterning transparent electrodes with nanoscale precision.

A sustainable method that allows for the fabrication of well-defined silver nanowire structures is template assisted electroplating or electrodeposition.[108,143,144] Electrodeposition is a solution-based technique that can be performed at relatively low temperatures, minimising energy consumption compared to high-temperature deposition techniques. Lower operating temperatures not only reduce energy costs but also contribute to environmental sustainability by decreasing greenhouse gas emissions and energy-related environmental impacts. The industrial use of electroplating is well established, and the technique has been employed in various industries for more than 150 years.[145] The compatibility with current manufacturing processes makes it an attractive option for integrating MNNs fabrication into existing solar cell production lines.[146] Moreover, electroplating offers high throughput and scalability, allowing for the mass production of MNNs to meet industrial demands.[147]

Electroplating or electrodeposition involves depositing a layer of metal onto a substrate by performing an electrochemical reaction controlled by the current passing through an bath containing the metal ions. This method enables precise control over the deposition process, resulting in uniform layers with minimal material wastage. Combining electroplating with nanoimprint lithography is a powerful approach for the fabrication of MNNs with precise control over size, shape, and alignment.[108] Nanoimprint lithography enables the creation of nanoscale patterns on a substrate, which serves as a mask for the subsequent electroplating process.[148,149] By filling these areas selectively with a metal by electrodeposition, highly uniform and well-defined MNNs can be produced, and therefore allows for the efficient use of materials, reducing the overall amount of precious metal (e.g., silver) required for manufacturing. This combined approach offers scalability, high throughput, and potential for large-scale production of MNNs with tailored properties.

1.5 Thesis outline

This thesis focuses on the fabrication of well-defined silver nanowire grids for the use as transparent conducting material (TCM) in PV applications, by combining substrate conformal imprint lithography and electrochemical deposition. By focusing on the replacement of indium with silver nanowires in solar cell manufacturing, this thesis aims to contribute to the development of a more sustainable and resource-efficient PV technology.

In Chapter 2, we start with an overview of electrochemical theory, covering electrochemical reactions, thermodynamics, electrode kinetics, mass transport, and commonly used electrochemical techniques. We then delve into the electrochemical deposition of metals on foreign substrates, emphasising the importance of the current density distribution on the uniformity of the deposit. Furthermore, we introduce a finite element method for simulating spatial-temporal electrochemical responses in 2D electrodes, particularly focusing on cyclic voltammetry and chronoamperometry. These simulations reveal that the cyclic voltammogram for an electrode with a roughness in the order of microns is very sensitive to the tertiary current distribution as determined by the concentration profile. Finally, we model the double pulse experiments in nanoscale trenches, demonstrating that 1D diffusion simulations are sufficient because the trench depth is much smaller compared to the diffusion length.

Chapter 3 explores the electrochemical control of silver nanoparticle nucleation and growth on ITO substrates by using the double pulse technique. We find that despite identical technical specifications, variations in the crystalline texture of polycrystalline indium tin oxide (ITO) substrates affect the nucleation of silver nanoparticles. Substrates with preferential lower index surfaces exhibit significantly lower island density, a feature sensitive to nucleation pulse potential. Conversely, island density on <111> orientated ITO remains largely unaffected by the nucleation pulse potential, but is rather limited by diffusion and therefore by the concentration of silver ions. These findings underscore the necessity of detailing substrate surface properties in studies of nucleation and metal nanoparticle growth via electrochemical processes.

In Chapter 4, we combine the double pulse method with substrate conformal imprint lithography to fabricate silver nanowire grids for the application of transparent conducting materials. The presented method is based on a through-the-mask electrodeposition method, in which the mask is fabricated using substrate conformal imprint lithography (SCIL). We find that the nucleation density of the silver nanoparticles is the key parameter for the successful homogeneous void-free filling of the nanosized trenches in the mask. We investigated the electrical and optical properties of the electrodeposited silver nanowire surface up to a certain height of the nanowire, after which the resistivity is limited by the average grain size. Due to the bottom-up nature, high aspect ratio wires could be obtained, hereby decreasing the sheet resistance but maintaining their high optical transparency and carrier collection, leading to a high FoM.

In Chapter 5, we describe light-matter interactions in metal nanowire grids and their characterisation. We outline the origin behind characteristic spectral features in transmission and how these are affected by geometry and dielectric environment. We introduce the use of FDTD simulations to predict light transmission and absorption by the grids. We used the simulated data to explain our experimental observations and to validate the normalisation method to decouple light transmission of the silver nanowire grids from that of the substrate in the experiments. Furthermore, in-situ bright-field optical microscopy and reflection measurements were performed during the electrochemical filling of the trenches. The small nuclei that are formed directly after nucleation strongly absorb light, resulting in a more

darker appearance of the trenches as observed with in-situ bright field microscopy, which is confirmed by the in-situ reflectance. When the silver particles are growing larger, they start to reflect more and more light and appear as bright lines after merging into a single nanowire.

In Chapter 6, we take the fabrication of the silver nanowire grids one step further by demonstrating the presented electrochemical method on TOPCon silicon solar cells. The TOPCon solar cells are used as a platform to measure the transparency of the silver nanowire grids in the right dielectric environment via J_{sc} monitoring. SR-LBIC measurements on the patterned devices show that the transmission of the silver nanowire grids is greater than expected from their geometrical footprint. Moreover, we investigate the effect of the nanowire aspect ratio on the angle-dependent J_{sc}. We find that the J_{sc} is virtually constant up to an angle of incidence of approximately 40°, after which the current drops which is attributed to increased absorption by the silver nanowire grid.

Finally, in Chapter 7, we discuss the importance of crystallinity of silver nanowire grids. As will be discussed in detail in Chapter 4, the resistivity is dominated by electron scattering with grain boundaries for high aspect ratio wires. Therefore, it is important to have a grain size larger than the electron mean free path. Instead of nucleating the silver on the substrate by using a nucleation pulse, nanocube imprint assembly is used to predefine the location of monocrystalline silver nanocubes on ITO substrates. Subsequently, this chapter focuses on welding these silver nanocubes via electrochemical overgrowth. We took advantage of the silver nucleation overpotential on foreign materials to selectively electrodeposit silver on the nanocubes without inducing the formation of new silver nuclei on the ITO substrate. We find indirect evidence for epitaxial overgrowth, as the electrochemically-induced grain size increase in the nanocubes, as obtained from XRD, coincides with that from morphological measurements (AFM and SEM).

Overall, the thesis demonstrates a scalable technique based on substrate conformal imprint lithography and electrochemical deposition, that is energy and material efficient, for the fabrication of metal nanowire networks which could be used as transparent electrodes for photovoltaic applications.

2

Fundamentals of Electrochemistry

We start by giving a brief introduction into electrochemical theory. We describe the definition of an electrochemical reaction, discuss the importance of thermodynamics, electrode kinetics, and mass transport, and describe the most commonly used electrochemical techniques. We then focus on the electrochemical deposition of metals on foreign substrates and discuss the importance of the current density distribution on the uniformity of the deposit. In this chapter, we also describe a finite element method to simulate the electrochemical spatial-temporal response in 2D electrodes, including cyclic voltammetry and chronoamperometry. From our simulations we find that cyclic voltammogram simulations having electrodes with a roughness in the order of microns are very sensitive to the tertiary current distribution, as determined by the concentration profile. Finally, we use our finite element simulation platform to model the chronoamperometry of the growth of metal in nanosized trenches, which is the main topic of this thesis. We show that these nanosized trenches can be simply modelled by 1D diffusion, as the trench depth is much smaller compared to the diffusion length.

2

2.1 A brief introduction to electrochemical theory

Electrochemistry is the study of chemical reactions driven by charge transfer at a polarised surface (i.e., the electrode) in contact with an electrolyte as a result of electrochemical potential differences. It deals with the theory of thermodynamics, the double layer at the electrode/solution interface, and charge transfer kinetics across the interface. Unlike in common chemical reactions, electron transport in electrochemical reactions occurs through electronically conducting phases, often through the use of an external circuit. Charge transport in the electrolyte and electrode is also important, taking either place by ions in the electrolyte or by free electrons in solids (metals or doped semiconductors). It therefore requires a conductive environment consisting of (metal) electrodes and an electrolyte consisting out of mobile ions.

2.1.1 RedOx reactions

An electrochemical process consists of two half reactions, a reduction reaction, and an oxidation reaction. Hence, electrochemical processes are also known as redox reactions (reduction-oxidation). A reduction reaction involves the gain of one or more electrons n from the oxidant (Ox) to the reductant (Red),

$$\mathrm{Ox}^{m+} + ne^- \rightleftharpoons \mathrm{Red}^{(m-n)} \tag{2.1}$$

hereby changing the oxidation state from m to $m-n$. The reverse reaction in which electrons are removed is known as oxidation. Reduction and oxidation reactions are also known as cathodic and anodic reactions, respectively. In this thesis, we will mainly focus on the reduction reaction of silver ions,

$$Ag^+ + e^- \rightleftharpoons Ag(s) \tag{2.2}$$

where a silver ion is reduced to metallic silver at the electrode surface. This electrochemical half-reaction involves not only the transfer of an electron from the electrode to the ions in solution, but also the transfer of mass (i.e., Ag^+) across the double layer, which is discussed in the next section.

2.1.2 The electrical double layer

In this thesis, we focus on heterogeneous electrochemistry, meaning that charge transfer takes place at a solid electrode/solution interface. This charge transfer is mainly an electron-tunnelling (single or multiple) process between the solid and the reactant species. An effective tunnelling process implies a sharp potential drop in the solution (i.e., within a few nanometers close to the interface). According to Nernst theory, an immersed electrode in equilibrium will set up an electric potential difference with the solution. Because of the different surface potential of the electrode, the solvent and mobile ions in the electrolyte will re-distribute at the interface to screen the electric field, resulting in what is called the electric double layer (or EDL). The screening power (or screening length) of the solution is determined by the amount of active mobile ions.

According to the Gouy-Chapman-Stern theory, the EDL consists of several parts: the Stern, inner Helmoltz, outer Helmoltz and diffuse layer. When polar solvents are used, the inner Helmholtz plane consists of a dense layer of solvent molecules, and the outer Helmholtz plane is formed by solvated counterions bound to the interface. Specifically, adsorbed ions that are partially desolvated form the Stern layer. The diffuse layer is formed by loosely bound

ions that complete the charge screening. In equilibrium and in the absence of the Stern layer, the electrical potential decays exponentially with distance from the electrode surface. The characteristic length scale of the double layer screening is called the Debye screening length.

The double layer plays an important role in the electrochemical reaction as the reactant species must be sufficiently close to the surface of the electrode for the electrochemical reaction to occur. The buildup of ions in the double layer affects the transport of the reactant species through the double layer, and hence the type of solvation molecules and other ions that might be present influence the electrochemical reaction.

2.1.3 The driving force of the electrochemical reaction

The driving force behind the electrochemical reaction is the gradient in the electrochemical potential $\overline{\mu_i}$. The electrochemical potential consists of a chemical and electrical potential, as given by:

$$\overline{\mu_i} = \mu_i + z_i F \phi^{\alpha} \tag{2.3}$$

where μ_i is the chemical potential, z_i is the charge number of species i, F is the Faraday constant, and ϕ^{α} is the inner potential of phase α. All species have their own specific chemical energy. When two dissimilar materials are contacted, an electrical field is created at their interface. At equilibrium, the electrochemical potentials are equal, and hence the difference in chemical potential must result in a difference in inner potential, leading to a difference in potential at the interface. The same concept holds for the metal/solution interface and hence for the formation of the double layer. For a monovalent metal ion (M^+) in solution that is in equilibrium with the solid metal electrode, we can write

$$\Delta\mu_{M^+}/F = -\Delta\phi \tag{2.4}$$

The chemical potential μ_{M^+} is actually related to the activity of the species M^+ by

$$\mu_{M^+} = \mu^0_{M^+} + RT\ln(a_{M^+}) \tag{2.5}$$

where the activity is equal to $a_{M^+} = \gamma_{M^+} c_{M^+}$, where γ_{M^+} is the activity coefficient, and c_{M^+} is the concentration of the metal ion, R is the gas constant, and T is the temperature. We can now rewrite Equation 2.4 as:

$$\Delta\phi = \Delta\phi^0 + \frac{RT}{F}\ln(a_{M^+}) \tag{2.6}$$

where $\Delta\phi^0$ is defined as $-\Delta\mu_{M^+}/F$, and recall that the activity of the solid metal is unity. The equation above is in the form of the Nernst equation but is now written for a single interface. When combining two of these equations, for both the Red and Ox species, one obtains the usual Nernst equation, which describes therefore the change in reduction potential as a function of the concentration of the metal ion.

2.1.4 Thermodynamics: Gibbs free energy of activation

We just described how the electrical potential affects the electrochemical potential. In the same way, an applied electrical potential affects the Gibbs free energy of the system. Consider the Gibbs free energy curves of the Red and Ox species as shown in Figure 2.1a. The applied external electrical potential is able to shift the Gibbs free energy curve up and down in energy. The relation between the standard electrochemical Gibbs free energy of activation and the electrical potential for a cathodic and anodic reaction, respectively, is given by:

$$\Delta\overline{G_i}^{0\ddagger} = \Delta G_i^{0\ddagger} \pm \alpha z_i F \Delta\phi_i \tag{2.7}$$

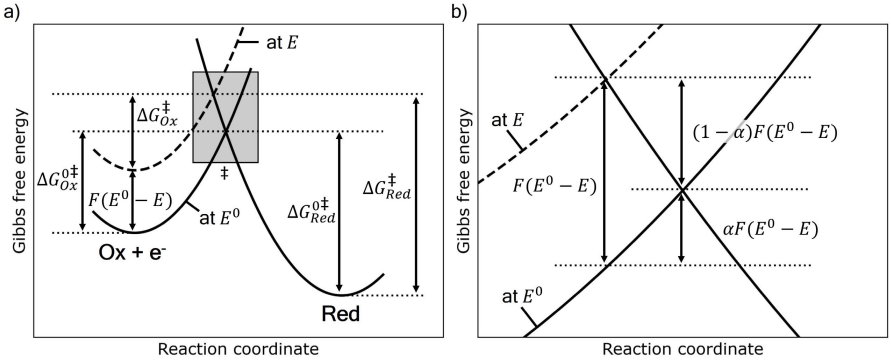

Figure 2.1: *The effect of the change in Gibbs free energy of activation by the applied potential E. Inspired by Figure 3.3.2 in Ref. [150].*

where $\Delta G_i^{0\ddagger}$ is the standard Gibbs free energy of activation of species i at the standard electrode potential E^0 (which is a measure for how much energy is required to drive the electrochemical reaction), and α is the charge transfer coefficient, ranging between zero and unity. The standard reduction potential E_0 is measured at 298.15 K (25 ° C), a pressure of 101.325 kPa (1 atm) and it is assumed that the activity of all soluble species is 1.000 M.[151] The charge transfer coefficient α describes how much of the applied potential is used to change the Gibbs free energy of activation and it is a measure of the symmetry of the redox reaction (i.e., ratio of energy being used to shift the free energy curve of the reductant/oxidant). Therefore, α is also known as the symmetry factor.

The meaning of α becomes clearer when considering the crossing of the Gibbs free energy curves in Figure 2.1b. At some reaction coordinate, the Gibbs free energy curves of the Red and Ox species in equilibrium cross. Intuitively, one would say that the energy required to drive the electrochemical reaction is the energy difference between the lowest point of the Gibbs free energy curve and the crossing between the two curves, which is equal to the Gibbs free energy of activation $\Delta G_i^{0\ddagger}$. However, when this energy is provided through an applied electrical potential, the Gibbs free energy curve of the Ox species shifts to higher values (dashed curve in Figure 2.1a). As a result, the crossing between the two free energy curves occurs at a different reaction coordinate, and more importantly, at a different energy. This effectively means that a larger potential must be applied than just the Gibbs free energy of $\Delta G_i^{0\ddagger}$, and this additional energy is proportional to the symmetry factor α. For most systems, the symmetry parameter α is close to 0.5 in which the system is said to be symmetric, as the free energy curves of the Red and Ox species are shifted by the same amount. Nevertheless, the applied electrical potential can lower the Gibbs free energy of activation and hence can drive and control the electrochemical reaction.

2.1.5 Electron kinetics: Butler-Volmer

In addition to thermodynamics, as we have just discussed, electrode kinetics is also important to understand electrochemical reaction rates. The heterogeneous rate constant is described

by the Eyring equation and is given by

$$k = k_0 \exp\left(-\frac{\Delta G^{0\ddagger}}{RT}\right) \tag{2.8}$$

where k_0 is the chemical rate constant in equilibrium. As a result of the electrochemical reaction, an electron is transferred, and hence a current can be measured. The cathodic current density is proportional to the amount of electrons transferred per reaction n, the heterogeneous reaction rate v (in mol cm^{-1} s^{-1}) and the Faraday constant F. The cathodic current density is given by

$$j_c = -nFv = -nFkc_{Ox} = -nFk_0 c_{Ox} \exp\left(-\frac{\Delta G^{0\ddagger}}{RT}\right) \tag{2.9}$$

where the heterogeneous reaction rate is expressed in terms of the rate constant k and the concentration c_{Ox} of the oxidant. Note that in this thesis we use the IUPAC convention, for which the current density of a reduction reaction (i.e., cathodic current) is considered negative. Oppositely, the current density of the oxidation reaction (i.e., anodic current) is positive. Using Equation 2.7, we obtain the following expression for the cathodic current density:

$$j_c = -nFk_0 c_{Ox} \exp\left(-\frac{\Delta \overline{G_{Ox}}^{0\ddagger}}{RT}\right) \exp\left(\frac{-\alpha nF\Delta\phi}{RT}\right) \tag{2.10}$$

where the charge number z as used in Equation 2.7, equals to the amount of electrons n involved in the reaction.

The above equation can be simplified by grouping all prefactor constants into a single value, defined as the exchange current density j_0, and using $\Delta\phi = E - E^0$, where E is the applied electrical potential. The difference between the standard reduction potential and the applied electrical potential is commonly known as the overpotential η. Therefore, the cathodic current density can be written as:

$$j_c = -j_0 \exp\left(\frac{-\alpha nF}{RT}\eta\right) \tag{2.11}$$

The total current density of an electrochemical reaction is the sum of the cathodic and anodic current densities, and is given by:

$$j = j_a + j_c = j_0 \left[\exp\left(\frac{\beta nF}{RT}\eta\right) - \exp\left(\frac{-\alpha nF}{RT}\eta\right)\right] \tag{2.12}$$

which is commonly known as the Butler-Volmer equation. Note that the expression of the anodic reaction is almost identical to that of the cathodic one, but is a positive contribution to the total current density and has a transfer coefficient $\beta = 1-\alpha$. It is also important to note that at equilibrium the total current density is equal to zero, hence the cathodic and anodic current densities are equal to each other but not necessarily non-zero. Electrochemical reactions are therefore in a dynamic equilibrium in which, for example, metal atoms on a surface can still be deposited/stripped and thus may be constantly changing the surface morphology of the metal electrode. Another important takeaway from the Butler-Volmer equation is that the current density, and hence the reaction rate, of the electrochemical reaction can be controlled by the temperature, concentration of the active species, and applied electrical potential, where the latter has the strongest effect and can be easily controlled with an external source.

2.1.6 Mass transport: Nernst-Planck equation

The previous section describes how the rate of charge transfer can be controlled by an applied potential. We described that the cathodic current density is a function of the concentration of the Ox species at the surface of the electrode. As the reaction evolves, the consumption of the Ox species leads to a decrease in the concentration at the surface. As a result, a gradient in the concentration of the Ox species has formed, resulting in the mass transport of the Ox species toward the electrode in the form of diffusion.

In general, mass transport can occur through diffusion (gradient in concentration), migration (gradient in electric field), or convection (fluid movement). The flux of the chemical species by mass transport is given by

$$\mathbf{J} = -D\nabla c + c\mathbf{v} + \frac{Dze}{k_B T} c\mathbf{E} \tag{2.13}$$

where D is the diffusion constant, e the elementary charge, $\mathbf{E}$ the electric field, $\mathbf{v}$ the velocity field of the moving fluid, and c the concentration. The equation above describes the flux at each position for a given moment in time. By using the continuity equation, one can determine how the concentration will change in time as a function of the gradient of the flux and is given by:

$$\frac{\partial c}{\partial t} = -\nabla \cdot \mathbf{J} = -\nabla \cdot \left[-D\nabla c + c\mathbf{v} + \frac{Dze}{k_B T} c\mathbf{E} \right] \tag{2.14}$$

which is also known as the Nernst-Planck equation.

For most electrochemical systems, the conductivity of the electrolyte is sufficient for the complete screening of the electric field in the bulk electrolyte, and thus the electric field is confined to the EDL. Therefore, ion migration is relevant only within the double layer. In the case where the electrolyte is not stirred (i.e., no convection $\mathbf{v} = 0$), the only remaining driving force of mass transport in the bulk is diffusion.

To calculate the concentration of Ox species as a function of time near the electrode surface and therefore the resulting current density, it is necessary to solve the partial differential equation stated in Equation 2.14. There are a few special cases in which the Nernst-Planck equation can be solved analytically. For example, when the electrochemical reaction is limited by mass transport, the concentration of the metal species near the interface can be assumed to be equal to zero (i.e., any ions that arrive at the interface will immediately react). Using this condition and assuming that the concentration linearly increases from zero to the bulk value c_{red} over a distance of δ, which is known as the Nernst diffusion length. Equation 2.14 can then be simply expressed as:

$$j = \frac{nFDc_{red}}{\delta} \tag{2.15}$$

From this equation it can be seen that the ratio D/δ has the same role as the rate constant k, except that the current is now independent of the applied potential. This means that the current density will saturate at a finite value upon a given applied potential. Yet, note that the Nernst diffusion layer is time-dependent, which can be estimated by:

$$\delta(t) = \sqrt{\pi D t} \tag{2.16}$$

This means that upon a bias is applied, the current density shall decrease over time due to mass transport limitations, and a steady state will never be reached. Charge transfer and mass transport are two independent consecutive processes. The electrochemical reaction

rate shall be limited by the slowest of the two processes. When the applied overpotential is small, the electrochemical reaction rate is typically limited by charge transfer (electron kinetics), while when the applied overpotential is very large, the electrochemical reaction rate is typically limited by mass transport. For applied overpotentials in between those limits, the electrochemical reaction rate is in a mixed control state, which is neither fully limited by charge transfer nor by mass transport.

2.1.7 Solid-state nucleation and growth

Electrocrystallization is defined as the nucleation and growth of electrodeposition. For electrocrystallization, active sites on the substrate are essential. At these active sites, ion adsorption and nucleation take place. The kinetics of electrocrystallization has been a major research topic for years. [152–156] In a simple model, the growth rate of the nuclei is assumed to be described by first-order kinetics. The number of active growth sites as a function of time t is given by:

$$N_c = N_0[1 - \exp(-k_n t)] \tag{2.17}$$

where N_0 is the maximum number of nuclei obtainable, and k_n is the nucleation rate constant. In the case where the nucleation rate constant is $k_n \gg 1$, the maximum number of active growth sides is reached instantaneously, and hence this case is known as instantaneous nucleation. For the opposite case, when the nucleation rate constant is $k_n \ll 1$, the number of active growth sides increases linearly with time and is known as progressive nucleation. The total current is determined by the sum of the currents of all the growing nuclei at the active sites. For instantaneous nucleation, the resulting current transient depends only on the growth mode of the individual nuclei (which can be 2D or 3D) [157,158]. In contrast, in progressive nucleation more nuclei are formed with time and therefore the current transient will depend on the number of active sites at a given moment in time t. Depending on the applied overpotential, the nucleation mode can switch from progressive to instantaneous. [153]

In the following, we describe the thermodynamics framework of nucleation. There exist two types of nucleation, homogeneous and heterogeneous. For homogeneous nucleation, supersaturation is required, which results in solid formation in the bulk liquid, such as precipitation of salt crystals in a supersaturated solution. For heterogeneous nucleation, the solid material grows on the surface of a substrate, as is the case in the electrodeposition of metals. Yet, the thermodynamics that describes the two types of nucleation are rather similar.

The change in Gibbs free energy of the solid nucleus contains two parts, the change in Gibbs free energy due to the increase in the surface and volume of the nuclei. For most cases, the solid state has a lower Gibbs free energy compared to the source phase (liquid, gas, or solution) as a result of the contraction in volume. Additionally, in the initial stages of solid-state formation, the creation of a new nucleus with a growing surface costs energy. The Gibbs free energy for a growing nucleus with radius r can be written as:

$$\Delta G = 4\pi r^2 \gamma + \frac{4}{3}\pi r^3 \Delta G_v \tag{2.18}$$

where ΔG_V is the reduction in chemical free energy by volume contraction, and γ is the surface energy density. The shape of the Gibbs free energy as a function of the radius of the nucleus is shown in Figure 2.2. Initially, creating a nucleus with a radius r costs energy due to the relatively large surface contribution to the Gibbs free energy. There exists a critical radius r^* after which the nucleus becomes thermodynamically stable, i.e., an increase in radius leads to a lower Gibbs free energy. Nuclei that have a radius larger than the critical

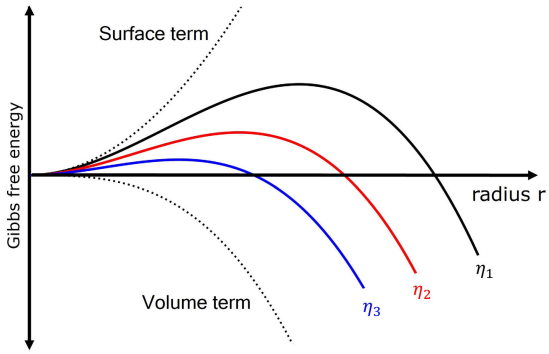

Figure 2.2: *The effect of the overpotentials ($\eta_1 < \eta_2 < \eta_3$) on the radius dependent Gibbs free energy of a spherical nucleus. Inspired by Figure 3.7 in Ref. [157].*

radius are therefore stable after the growth process has been terminated. The associated Gibbs free energy at the critical radius is called the nucleation energy barrier ΔG^*. The expression for the critical radius r^* and the nucleation energy barrier ΔG^* is very similar for both homogeneous and heterogeneous reactions. The main difference lies in the fact that, in a heterogeneous reaction, there exists more than one type of surface/interface as the nucleus grows on a substrate. In fact, the expressions for the critical radius r^* and the nucleation energy barrier ΔG^* for homogeneous and heterogeneous reactions are coupled through the wetting or contact angle defined by Young's equation. [157] The nucleation energy barrier for the heterogeneous reaction is equal to or lower than that for the homogeneous reaction. On a highly non-wetting substrate surface, the contact area between a growing nucleus and the substrate is minimal, and thus the nucleation energy barrier for homogeneous and heterogeneous nucleation is equal. On the contrary, on a highly wetting substrate surface, as is the case with epitaxial growth, the nucleation energy barrier approaches zero.

In the case of electrodeposition, we consider the reduction reaction of metal ions to metal atoms on a (foreign) electrode, which involves heterogeneous nucleation. At equilibrium ($\eta = 0$), there is no net driving force for the reduction reaction, so a cathodic overpotential ($\eta < 0$) is required to drive the metal electrodeposition. By using the Nernst equation, and considering that every transferred electron n increases the size of the nucleus by one atom, the volume Gibbs free energy ΔG_V can be written as a function of overpotential:

$$\Delta G_v(\eta) = -\frac{\eta F \rho n}{M} \tag{2.19}$$

where ρ is the mass density, and M the molar weight. The total Gibbs free energy of nucleation is now expressed in terms of overpotential by:

$$\Delta G(\eta) = 4\pi r^2 \gamma + \frac{4}{3}\pi r^3 \left(\frac{\eta F \rho n}{M}\right) \tag{2.20}$$

Figure 2.2 shows the effect of the applied (negative) overpotential on the Gibbs free energy of the nucleus. For an increase in overpotential, the strength of the volume term of the Gibbs free energy increases, effectively lowering the nucleation energy barrier ΔG^*. Therefore, a key takeaway from Equation 2.20 is that the nucleation energy barrier can be effectively lowered

by a (negative) overpotential η. Equation 2.20 also implies that a non-uniform distribution of the interface potential will result in large variations in nuclei density.

As the nucleation energy barrier is lowered by the applied overpotential, it is likely that more nuclei are formed at higher (negative) overpotentials. At these high applied overpotentials, nucleation takes place in a short time window, pushing the nucleation mode toward instantaneous nucleation. In Chapter 3 we discuss the importance of the overpotential in the nucleation of silver nanoparticles on ITO substrates and show that higher (negative) overpotentials indeed lead to instantaneous nucleation resulting in the saturation of the nuclei density.

2.1.8 Further reading

Most of the theory described in this chapter was obtained from the books:

- Electrochemical Methods: Fundamental and Applications, 2^{nd} edition, by A.J. Bard and L.R Faulkner (2000) [150]
- Electrodeposition of Nanostructed Materials, by F. Nasirpouri (2017) [157]
- Fundamentals of Electrochemical Deposition, 2^{nd} edition, by Paunovic and Schlesinger (2005) [158]
- Physical Electrochemistry: Fundamentals, Techniques, and Applications, 2^{nd} edition, by Eliaz and Gileadi (2019) [145]

2.2 Electrochemical methods

2.2.1 Electrochemical Cell

In essence, an electrochemical cell is nothing more than just some sort of container to hold the electrolyte in place and at least two submerged electrodes. The two electrodes are typically named differently depending on their polarity (cathode or anode for negative and positive potentials, respectively). We call the electrode where the half-reaction of interest takes place the working electrode (WE). The other electrode, which performs the other half-reaction necessarily to close the current loop, is called the counter electrode (CE). Typically, the area of the CE is made much larger than that of the WE, so that the electrochemical reaction is not limited by the CE and thus the reaction at the WE can be properly studied.

In addition to these two electrodes, a third electrode is used to measure the potential between the electrolyte and the WE, known as the reference electrode (RE). Measured potentials in electrochemistry are not absolute and need to be specified versus some primary reference value. An RE can only be used as a reference when the electrode has a stable and well-defined potential in the solution, and it is not affected by the passage of a (small) current (i.e., ideal non-polarisable electrode). The distance between the WE and RE should ideally be small to minimise the ohmic drop that arises from the electrical resistance of the electrolyte. If possible, an inert or supporting electrolyte is used to reduce the ohmic drop. The ions of the supporting electrolyte should not participate in the electrochemical reaction but is only used to increase the conductivity of the electrolyte.

The internationally accepted primary reference is the standard hydrogen electrode (SHE). [150] However, from a practical point of view, other reference electrodes are often used.

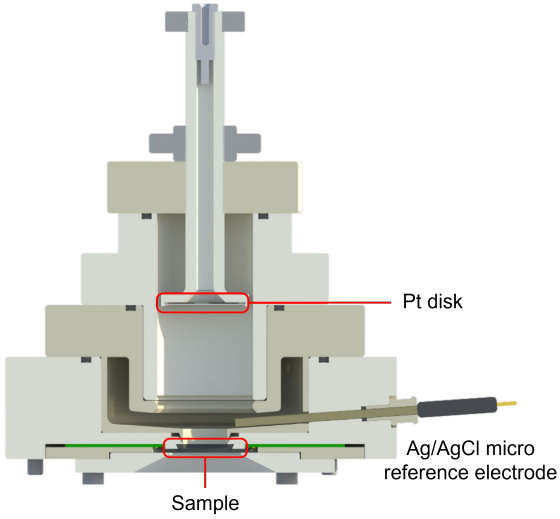

Figure 2.3: *Schematic overview of the Nano Superfilling Electrochemical Cell (NSECC) which is used for the fabrication of metal nanowire grids.*

Throughout this thesis, we use the silver-silver chloride reference electrode (Ag/AgCl), which is based on the equilibrium of:

$$AgCl(s) \rightleftharpoons Ag^{+} + Cl^{-} \tag{2.21}$$

This reference electrode has fast kinetics, and has a well known potential vs SHE, equal to +0.197 V vs SHE in a saturated KCl solution.[150,159] The use of these three electrodes in an electrochemical cell is known as the three-electrode configuration.

The electrochemical cell used in this thesis is shown in Figure 2.3, and was named the Nano Superfilling Electrochemical Cell (NSECC). The cell was designed and manufactured at AMOLF for this thesis. The cell has a total volume of 24 ml and the main material is PEEK, which is resistant to most chemicals.[160,161] The viton O-ring at the bottom of the cell determines the electrochemical active area and is equal to 0.95 cm^2. A platinum disk with an area of 3.08 cm^2 was used as CE, where the distance between the CE and the WE is adjustable, to allow the current density distribution to be tuned. A Ag/AgCl electrode (leakless miniature ET072, EDAQ) is typically used as a reference electrode. An SP-300 Biologic potentiostat is used to control and measure the potential between the WE and the RE or the current between the WE and the CE, respectively. It should be noted that accurate control of the potential is possible only through the use of the reference electrode.

2.2.2 Cyclic Voltammetry (CV)

A widely used technique to study electrochemical reactions is Cyclic Voltammetry (CV). This technique involves a linear sweep in potential applied between the WE and RE ranging from E_1 to E_2, and back to E_1. The potential is swept with a constant sweep rate dE/dt, and typically the values range from 1 to 100 mV/s. During the potential sweep, the current is measured.

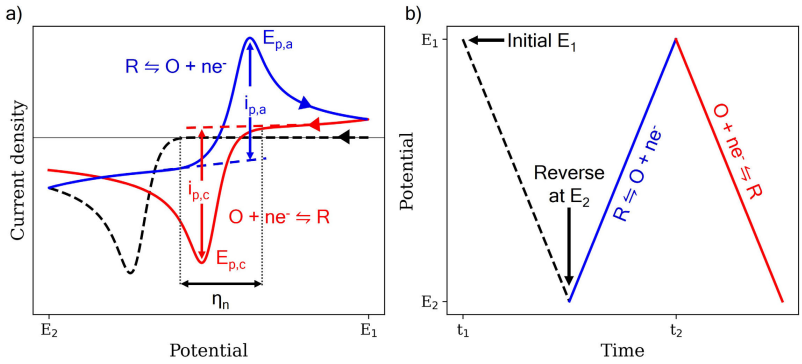

Figure 2.4: *a) A typical voltammogram for an one electron reaction. The cathodic/anodic peak current and position are indicated by $i_{p,c/a}$ and $E_{p,c/a}$, respectively. The dashed black line highlights the effect of an additional nucleation barrier. b) Corresponding time dependence applied potential. The slope of the line is determined by the scanrate.*

A typical CV for a simple one electron process is shown in Figure 2.4 by the red and blue curves, which correspond to the reduction and oxidation reactions, respectively. When the applied overpotential is sufficiently large, an electrochemical reaction is initiated, which results in an increase in current density (positive or negative), as described by the Butler-Volmer Equation 2.12. However, as time passes, the current density decreases as a result of mass transport limitations, as described in Section 2.1.6. The mass transport limited current density is determined by the rate of diffusion towards the electrode. Given the coupling between time and voltage, this effect results in a peak in current density, which is known as the cathodic/anodic peak $i_{p,c/a}$ for the reduction/oxidation reaction. The cathodic/anodic peak is a function of, among others, the scan rate and the diffusion constant, which both determine at which moment in time the electrochemical reaction becomes diffusion limited.

The CV in Figure 2.4 is typical for a one electron reversible electrochemical reaction. However, for most electrochemical deposition systems, the metal deposition takes place on a foreign substrate, and therefore, an additional energy is often required to nucleate on the foreign substrate. This additional energy is refereed to as the nucleation overpotential and is defined as:

$$\eta_{nucl} = |E_n - E^0| \tag{2.22}$$

The nucleation overpotential η_{nucl} could be estimated from the onset potential E_n of the cathodic reaction in the CV. The black dashed line in Figure 2.4 highlights the effect of an additional nucleation energy barrier in the system. Effectively, the onset potential at which the cathodic reaction starts is shifted towards more negative potentials, and the distance between the cathodic and anodic peak is increased.

For more details on cyclic voltammetry, the reader is referred to the work of Elgrishi *et al.*, where the authors describe a practical beginner's guide to Cyclic Voltammetry. [162]

2.2.3 Electrodepostion, Electrochemical Deposition, and Electroplating

The terms electrodeposition, electrochemical deposition, and electroplating are interchangeably used and are, in essence, a process in which a material is deposited on a substrate through a reduction or oxidation reaction. The term electroplating is commonly used in industry, whereas electrochemical deposition and electrodeposition are more common in academia. There is, however, often a subtle difference in how the electrochemical reaction is controlled. In academia, the electrochemical reaction is most often controlled by an external applied potential, which can be accurately controlled by the use of a potentiostat and reference electrode. In industry, for practical reasons, the electrochemical reaction is controlled by the current flowing between the WE and CE, thereby omitting the reference electrode. The potential and current controlled modes are known as chronoamperometry and chronopotentiometry, respectively. In essence, the chronoamperometry mode controls the thermodynamics of the electrochemical reaction, while the chronopotentiometry controls the deposition rate. An important difference is that, when the electrochemical reaction is controlled by the current, the potential is adjusted by the potentiostat so that the requested current is reached. This could result in unwanted (thermodynamically allowed) side reactions, such as hydrogen evolution. On the contrary, when the electrochemical reaction is controlled by the potential, the electrochemical reaction can be driven more selectively, minimising side reactions.

In this thesis, the electrodeposition is controlled by an applied potential. We are mainly interested in the deposition of silver on a foreign substrate, and, as discussed in more detail in Chapter 3, a significant nucleation overpotential must be overcome for nucleation to occur. This overpotential can be several hundredths of mV. If the potential is kept at such high overpotentials, the electrodeposition of silver will quickly be limited by mass transport, resulting in dendritic growth.[163–165] To prevent dendritic growth, one should limit the duration of the large applied potential required for nucleation. As such, applying a double potential pulse allows for controlling the nucleation and growth independently from each other, known as the double pulse technique.[166,167] A typical potential scheme for the double

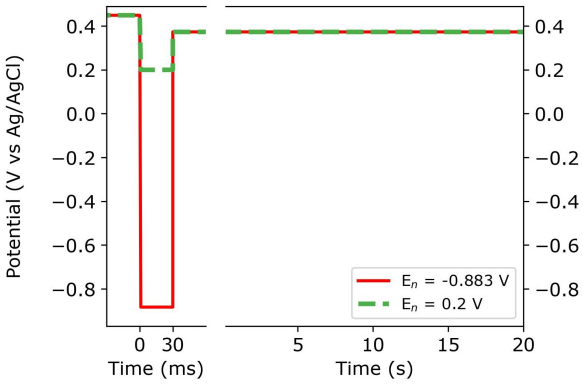

Figure 2.5: *Schematic potential scheme for the nucleation and growth pulse as used in the double pulse technique for a low (dashed green) and high (solid red) nucleation pulse overpotential*

pulse technique is shown in Figure 2.5, where the duration of the nucleation pulse is on the order of 10 to 100 ms, and the duration of the growth pulse depends on the required thickness of the deposit.

2.2.4 The importance of the current density distribution

The distribution of the current density determines the uniformity of the thickness and morphology of the deposit. The current density distribution is strongly affected by the composition of the bath, which determines the solution resistance and the electron kinetics. Furthermore, it also depends on the temperature, the geometry of the substrate, and the applied current/potential. Edge effects can present challenges, [145,168] at which the current density could be completely different compared to locations closer to the centre of the electrode, hence the position of the CE plays an important role in the uniformity of the deposit.

The current, or deposition rate, is ruled by the potential drop at the (working) electrode interface. If the electrolyte is too resistive, the resistance between the WE and CE/RE effectively decreases the potential drop at the double layer, and hence results in lower deposition rates than expected for the given bias. The resistance between the electrodes can be modelled by two resistors in series: the solution resistance R_S (determined by the ion concentration) and the Faradaic resistance R_F (resistance at the double layer). In a typical electrochemical cell, the relevant scale of the solution resistance is in the order of millimeters to centimeters, while the Faradaic resistance is only relevant in the first few nanometers from the electrode surface. If $R_S \gg R_F$, the process is said to occur under conditions of primary current distribution. A broad primary current distribution usually leads to a non-uniform thickness of electrodeposit. as the points closer to the CE/RE experience a larger potential drop over the double layer compared to points further away, resulting in a runaway situation by means of a positive feedback mechanism. On the contrary, if $R_F \gg R_S$, the process is under conditions of secondary current distribution. The limiting resistance now takes place across the double layer, and regardless of the electrode geometry, the thickness of the deposit will be uniform. Therefore, it is important to minimise the solution resistance R_S by adding a supporting electrolyte.

The measure of producing a uniform thickness of the deposits is known as the throwing power. The throwing power can be divided into macro and micro throwing power. The macro throwing power determines the uniformity of the deposit for millimeter to centimeter rough electrodes, and is mainly influenced by the primary and secondary current distribution. The micro throwing power controls the smoothness and brightness of the deposit, which is in the order of nanometers to micrometers. The micro throwing power is influenced by the tertiary current distribution, which is affected by mass transport. In the case of mass transport limited deposition, protruding parts of the electrode shall receive a higher flux of ions compared to valleys and hence shall grow faster, which results in a positive feedback mechanism, making the deposits rougher if the thickness is increased. The tertiary current distribution can be improved by increasing the metal ion concentration or by stirring the electrolyte, which is most commonly done in industrial operations. However, (organic) additives can be added to the electrolyte, which influences the mass transport properties. [169,170] A leveller, for example, adsorbs strongly on the protruding parts of the electrodes and therefore reduces the deposition rate at protruding part, resulting in a smoother deposit. [171] Complexing agents are used to create a buffered solution, [172,173] where the metal ion of interest is bound to a complexing agent, which could be released as soon as another ion was consumed in the plating process, thus keeping the concentration rather constant near the surface of the

electrode. The additives might be incorporated into the deposit and might therefore also change the mechanical properties of the deposit.[174–176] For example, stress reducers are used to reduce the internal stress in the deposit material, caused by lattice mismatch. There are different types of additives available, each with their unique properties.[177,178]

2.3 Numerical modelling of electrochemical processes

As described in Section 2.2.4, a uniform (tertiary) current density distribution is of uttermost importance for the uniformity of the deposited layer. Unfortunately, most electrodes have a rather complex geometry, which makes it hard to calculate the tertiary current distribution analytically.[157] Instead, the tertiary current density distribution can be modelled by, for example, using a finite element method.[179] In this section, we present a Python-based finite element model to simulate electrochemical phenomena at 3D interfaces developed in this thesis.

2.3.1 Discretisation of the fundamental equations

To calculate the potential-dependent current density at an electrode, we need to solve the two main governing equations described in Section 2.1.8: Nernst-Planck equation (Equation 2.14), which describes the time-dependent mass transport; and Butler-Volmer equation (Equation 2.12), which describes the concentration- and potential-dependent reaction rate. In other words, solving the Nernst-Planck equation gives the concentration at the electrode at a given time t, which is needed to calculate the reaction rate. This, in turn, modifies the reactant concentration at the surface.

The Nernst-Planck equation can only be solved analytically for some specific set of boundary conditions (e.g., the concentration is kept at a constant value at the surface). However, for a more complex set of boundary conditions, the Nernst-Planck equation must be numerically solved. To do so, we divide time and space into discrete points spaced by Δt and Δx. For simplicity, we focus on the finite element model for a 1D system, but it can be easily generalised to 2D and 3D. We also assume that diffusion is the most important mode of mass transport. In this case, the Nernst-Planck equation is simplified to:

$$\mathbf{J} = -D\nabla c \tag{2.23}$$

which is known as Fick's first law of diffusion. The Nernst-Planck equation is therefore written as:

$$\frac{\partial c}{\partial t} = -\nabla \cdot \mathbf{J} = -D\nabla^2 c \tag{2.24}$$

which is known as Fick's second law of diffusion. There are three different schemes to discretise the derivative: backward-, central- or forward-difference.[180] We use the forward-difference to calculate the concentration for the next time step using the current time step as input. The time derivative of the concentration can then be written as:

$$\frac{\partial c}{\partial t} = \partial_t c = \frac{c_j^{l+1} - c_j^l}{\Delta t} \tag{2.25}$$

where the superscript l denotes the concentration at a given time step, and the subscript j denotes the concentration at a given position in space. To discretise the second order

derivative in Fick's second law, we use the central-difference scheme since it is more accurate:

$$\begin{aligned}\nabla^2 c = \partial_x^2 c &= \frac{(\partial_x c)_{j+1/2} - (\partial_x c)_{j-1/2}}{\Delta x} \\ &= \frac{1}{(\Delta x)^2}\left(c_{j+1}^l - c_j^l - (c_j^l - c_{j-1}^l)\right) \\ &= \frac{1}{(\Delta x)^2}\left(c_{j+1}^l - 2c_j^l + c_{j-1}^l\right)\end{aligned} \tag{2.26}$$

The equation above shows that the concentration at the position j and at time stamp l depends on the concentration of the adjacent positions. When we now combine Equation 2.25 and Equation 2.26, we obtain the following expression for the concentration at time step $l+1$ and position j:

$$c_j^{l+1} = \frac{D\Delta t}{(\Delta x)^2}\left(c_{j+1}^l - 2c_j^l + c_{j-1}^l\right) + c_j^l \tag{2.27}$$

The pre-factor $D\Delta t/(\Delta x)^2$ can be regarded as the stability factor, and must be < 0.5 to prevent the simulation from diverging. Therefore, the maximum Δt for a given Δx is:

$$\Delta t < \frac{(\Delta x)^2}{2D} \tag{2.28}$$

Solving Equation 2.27 requires a set of boundary conditions. In a 3D system the boundary conditions are:

1.	$t = 0, \forall x, y, z \in V$	:	$c(x, y, z, 0) = c_0$	the initial concentration at any point in the simulation space is equal to c_0
2.	$t > 0, \forall i \in \partial V$	:	$\nabla c(i, t) = 0$	no ions are allowed to leave the simulation space
3.	$t > 0, \forall x, y, x \in El$	:	$c(x, y, z, t) = 0$	the concentration is always equal to zero inside the electrode
4.	$t > 0, \forall i \in \partial El$	:	$\nabla c(i, t) = -\frac{1}{D}\mathbf{J}_{Ox} \cdot \hat{n}$	the concentration gradient at the electrode surface is determined by the flux of the oxidant

where V is the simulation volume, El is volume of the electrode, and ∂V and ∂El are the surface of the simulation volume and the electrode, respectively.

Equation 2.27 states how the concentration at position j can be found for the next timestamp. However, this cannot be used to find the concentration at the surface of the electrode since the adjacent grid point to the electrode lies outside the simulation volume. To solve for the concentration at the surface of the electrode, the Bulter-Volmer equation is used. The Butler-Volmer equation states that the flux of oxidised species $\mathbf{J}_{Ox}$ normal to the surface of the electrode ∂El is equal to:

$$\mathrm{J}_{Ox}^l \cdot \hat{n} = k_a c_{Red,0}^l - k_c c_{Ox,0}^l \tag{2.29}$$

where k_a and k_c are the anodic and cathodic reaction rate, respectively, which are both dependent on the applied overpotential. Therefore, Equation 2.29 describes how many ions are being removed from the electrolyte at time l over a period of Δt. $c_{Red,0}^l$ and $c_{Ox,0}^l$ are the concentrations of the reductant and oxidant at the surface of the electrode, respectively. Yet again, we do not know the concentration of the Red and Ox species at the surface at the timestamp l. Fortunately, we can derive the concentration of the oxidant and reductant at the surface by using Fick's first law of diffusion (Equation 2.23), written as:

$$c_{Ox,0} = c_{Ox,1} + \frac{\Delta x}{D}\mathbf{J}_{Ox} \tag{2.30}$$

Considering that the flux of the oxidant species is equal but opposite to the flux of the reductant species $\mathbf{J}_{Ox} = -\mathbf{J}_{Red}$, we conclude that:

$$c_{Red,0} = c_{Red,1} - \frac{\Delta x}{D}\mathbf{J}_{Ox} \tag{2.31}$$

By combining Equations 2.29, 2.30, and 2.31, we find an expression for the flux of the oxidant species consumed by the electrochemical reaction:

$$\mathbf{J}_{Ox} \cdot \hat{n} = \frac{k_a c_{Red,1} - k_c c_{Ox,1}}{1 + \frac{\Delta x}{D}(k_a + k_c)} \tag{2.32}$$

By using Fick's first law of diffusion (See Equation 2.23), we can now calculate the new value of the concentration of the oxidant $c_{Ox,0}^{l+1}$ at the surface at time $l+1$.

Finally, the current density at a given element on the surface can be calculated by:

$$j = \frac{i}{A} = \hat{n} \cdot \mathbf{J}_{Ox} nF = -nF\left(\frac{k_a c_{Red,1} - k_c c_{Ox,1}}{1 + \frac{\Delta x}{D}(k_a + k_c)}\right) \tag{2.33}$$

2.3.2 Numerical simulation of cyclic voltammograms

In this section we use the previously discussed discretised equations to simulate the current transient as a function of constant changing overpotential, e.g., a cyclic voltammogram (CV). Figure 2.6 shows a 1D simulated CV for a single electron electrochemical reaction with fast kinetic, along with the corresponding concentration profiles at different characteristic moments in the CV, indicated by letters. We used the electrochemical parameters of the silver reduction reaction (Equation 2.2). Namely, we use the standard reduction potential of silver (E^0_{Ag} = 0.6 V vs Ag/AgCl [181]) corrected by the Nernst equation for c_{Ox} = 100 mM, the diffusion constant of silver ions ($D = 1.6 \cdot 10^{-5}$ cm/s) [182], and the rate constant k_0 was set sufficiently large ($> 10^{-3}$ cm/s) to ensure that the reaction is diffusion limited. For simplicity, we consider that the reduced species are able to diffuse away from the electrode. Although this is not true in the case of electrodeposition, it applies to any ion-to-ion reaction, and it is therefore of great value for understanding the typical shape of a CV. In reality, electrodeposition is based on a slightly different mechanism. [183,184]

The CV is initiated at point A, at which point c_{Ox} and c_{Red} are constant in space and have their initial values (Figure 2.6a). With time, the potential is decreased and eventually the reduction reaction is allowed (onset potential), and a cathodic current starts to flow. Under diffusion-limited conditions, point B describes the potential at which $c_{Ox} = c_{Red}$ (see Figure 2.6b) and it coincides with the reduction potential (dashed vertical line). Note that this only holds for a (symmetric) diffusion-limited electrochemical reaction.

Point C is the moment at which the maximum current density is reached, when the concentration gradient is the largest (see Figure 2.6c). The potential is reversed at point D and at this moment the reaction rate is completely dominated by diffusion, since c_{Ox} is zero (see Figure 2.6d). As the potential is reversed back to the initial value, we observe an equivalent situation for the newly generated oxidised species. At point E, the two concentrations are again equal, but their gradients are flipped with respect to point B. The concentration gradient of the reductant species is the largest at the maximum anodic current density at point F. Once back to the initial potential, the concentrations at the surface recover their initial value, yet the concentration profile is not constant. This results in a non-zero current density and implies that the reaction is not fully reversible. The reason lies in the fact that part of the reduced

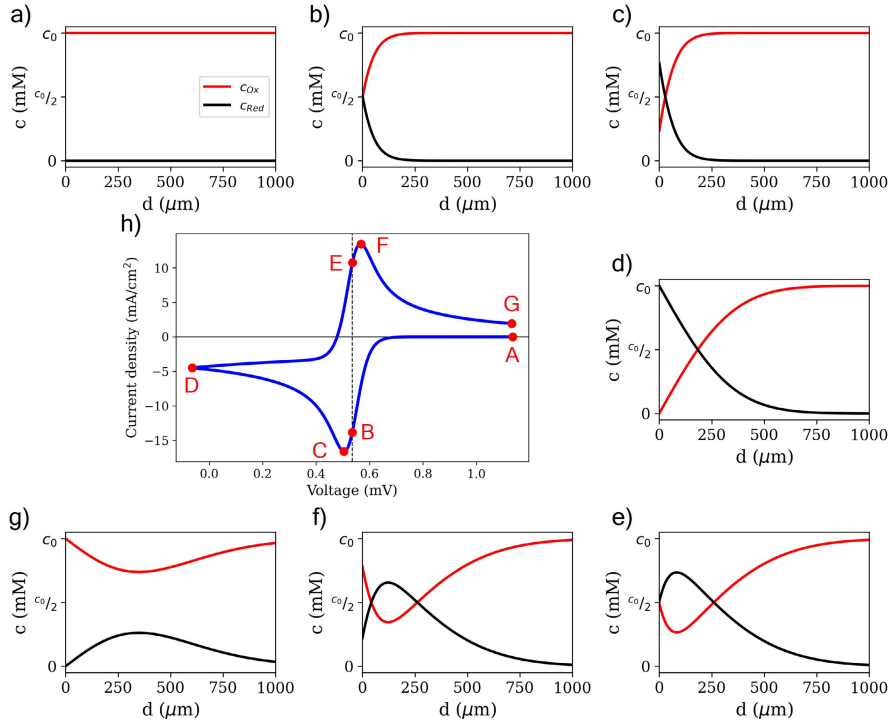

Figure 2.6: *(a-g) Concentration profiles of the oxidant c_{Ox} (red) and reductant c_{Red} (black) as a function of the distance d from the electrode. The initial concentration of the oxidant species is equal to c_0 = 100 mM. h) Simulated cyclic voltammogram with a scanrate of 25 mV/s using the parameters k_0 = 0.01 cm/s, α = 0.5, and D = $1.6 \cdot 10^{-5}$ cm^2/s. The vertical black dashed line represents the reduction potential. The concentration profiles in (a-g) correspond to the red dots in (h) labelled by (A-G). The figure was inspired by the work of Elgrishi* et al.*.*[162]

species diffused away from the surface during the cathodic voltage sweep and do not reach the electrode ever again to be oxidised back.

Now we look at the effect of two key electrochemical parameters on the CV shape. Figure 2.7a shows the effect of the electrochemical rate constant k_0 and the diffusion constant D. As mentioned before, the electrochemical reaction is under diffusion limitations if the electrochemical rate constant is sufficiently large (red curve). If the diffusion constant is reduced by a factor 5 (slow diffusion, dashed green curve), the overall current density decreases while the potential at which the cathodic and anodic peaks occur remains the same. Given that the reaction is diffusion-limited, the reaction rate and hence the current density are fully determined by the diffusion flux, which depends on the diffusion constant.

Next, instead of decreasing the diffusion constant, we play with the electrode kinetics. Decreasing the reaction rate constant by two orders of magnitude ($k_0 = 10^{-4}$ cm/s) results in the reaction no longer being under diffusion-limited conditions, but rather under kinetic limitations. As a result, the cathodic and anodic peaks are further distanced in potential (blue curve). The potential at which the concentration is half of its initial value does not occur at

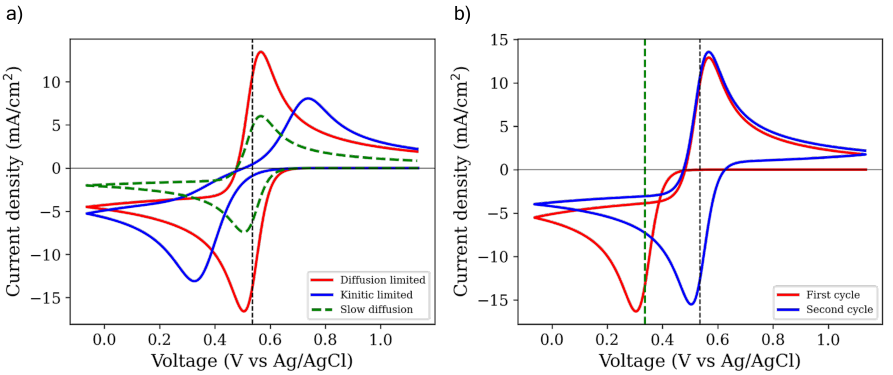

Figure 2.7: *Simulated cyclic voltammograms in 1D a) under diffusion limitations, having a large (red) and a small diffusion constant (dashed green), and under kinetic limitations (blue). b) Effect of the nucleation overpotential on the cathodic peak location during the first cycle (red). The second cycle (blue) does not have a nucleation overpotential. The nucleation potential E_{nucl} is represented by the dashed green line, and the reduction potential is represented by the vertical dashed black line. A scanrate of 25 mV/s was used in all simulated CVs.*

the reduction potential, but rather at more negative/positive values for the forward/backward scan, respectively.

Given our focus in this thesis on the electrodeposition of silver onto a foreign substrate, it is important to understand the effect of the nucleation energy barrier on the shape of the CV, which is shown in Figure 2.7b. To mimic the nucleation barrier, the standard reduction potential is judiciously made more negative by an amount of E_{nucl}, such that the electrochemical reaction takes place at lower potentials. The nucleation overpotential is present only when no deposit/reductant species are present. We assume that some reduced species are left on the electrode surface after the first CV cycle, and thus the reduction potential is gradually decreased to its original value before the anodic reaction is initiated. For the second cycle (shown in blue), no nucleation barrier is present. Experimentally, we observe a very similar behaviour for silver electrodeposition, shown in Figures 3.1 and 3.10 that will be discussed in more detail in Chapter 3.

2.3.3 Effects of electrode topography on the local electrochemical current density

In the previous section, we considered an ideally uniform electrode surface, which is not always the case. In this section, we discuss the effect of the electrode surface roughness by using 2D diffusion simulations. Figure 2.8a shows the cross-section profile of the electrode considered, which has been randomly generated with a protrusion and two depressions in the micrometer regime. The surface of the electrode has been colour coded as a function of the activity of the surface pixel, where darker red represents higher activity. The activity is defined as the total amount of charge Q transferred per unit area A over the whole duration of the simulation.

The activity profile clearly shows that the current is higher at the tip of the protrusions. A more quantitative representation of the total charge (or surface activity) at each position of

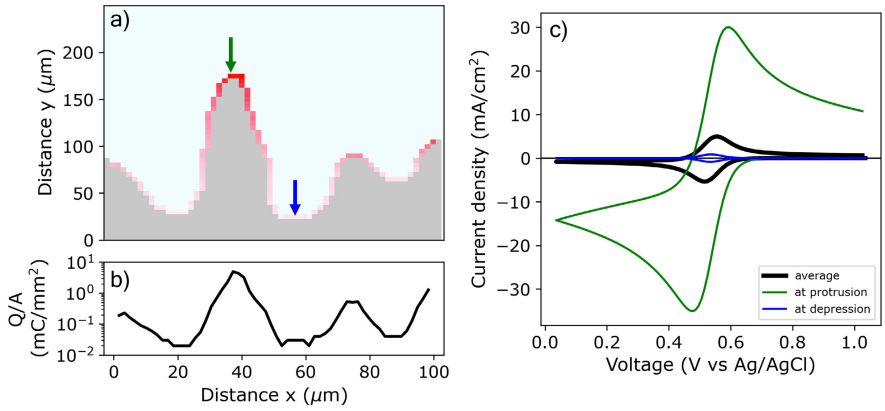

Figure 2.8: *Two dimensional CV simulations using a custom shaped electrode. a) Shape of the electrode including the activity at the surface. The electrode and electrolyte are represented by grey and light blue areas, respectively. The activity at the surface is represented by red pixels, where the brightness of the colour is a function of the activity. b) Logarithm of the electrochemical activity along the electrode surface given in the transferred charge Q per unit area A. c) Resulting CVs of the 2D simulation. The integrated current density is represented by the thick black line. The current densities corresponding to the pixel at the protrusion and depression are represented by the green and blue curves, respectively. The pixels corresponding to the curves are marked by the arrows in b).*

the profile is shown in Figure 2.8b in semilog-scale. The charge density at the protruding sites is almost three orders of magnitude larger compared to that at the depressions.

The corresponding simulated CV at each pixel of the surface is shown in Figure 2.8c. The current density integrated over the whole surface, i.e., the current that one would measure, is represented by the thick black line. We used the same electrochemical parameters as for the 1D simulation of the red curve in Figure 2.4a. We find that the shape of the 2D simulated CV is similar to the 1D simulated one, thus not revealing much information about the electrode roughness. The CVs at the protrusion and depression are represented by the green and blue lines, respectively. As expected, the current density at the protruding side is almost two orders of magnitude larger compared to the current density at the depression. The reason for the much higher current density at the protrusion is that this surface has much greater accessibility to ions compared to the surface in the depression. In practice, the protruding sites will therefore be more active and, in the case of metal deposition, the deposit will grow much faster in those regions, leading to even rougher deposits. The tertiary current density distribution is therefore key to obtain smooth deposits. Therefore, the use of additives is essential to obtain smooth deposits.

In addition to CV simulations, where the potential is swept with a constant scanrate, we also simulate the current density when applying a double potential pulse to an electrode with an insulating mask, similar to what will be used in the coming chapters for the fabrication of the nanowire grid. The insulating mask contains nanosized trenches reaching to the substrate, which have a depth of 1 μm and a width of 100 nm. In particular, we are interested in assessing

diffusion limitations through the mask openings during the nucleation and growth pulses.

Considering that silver ions diffuse over a distance of $\sqrt{Dt} \approx 13$ μm within the time span of 100 ms, the diffusion through 1 μm-deep trenches should not pose a significant restriction. Consequently, the insulating mask primarily reduces the active surface area of the electrode. Therefore, simulating the current density transient with 1D simulations suffices, and adjusting the current density for the electrochemical active area becomes straightforward. Figure 2.9 shows the current density transient for an 1D simulated system (black curve). Experimental data corresponding to the filling of nano-sized trenches with silver (as will be discussed in Chapter 4), is included for comparison (red curve). In general, we find a good agreement between the experimental and the numerical data. A slight difference in the current density between the experimental and numerical data is observed just after the potential switch. This difference is likely caused by the kinetic limitations of the reaction. In the simulations, the kinetics are infinitely fast and the rate is purely defined by the applied potential, while in reality the kinetics are not infinitely fast and hence limit the current density. Furthermore, the effects of the additives are not implemented in the simulation, and for longer time scales ($t > 5$ s), the simulated concentration profile is expected to differ from the experimental concentration profile. Note also that the experimental current density is obtained by normalising the measured current by the submerged electrode area. However, the actual current density as perceived by the bottom of the trench is much larger than reported.

The insets of Figure 2.9 show the concentration profiles during the nucleation pulse and near the end of the growth pulse, as indicated by the black arrows. During the nucleation pulse, the applied nucleation overpotential is large enough to drive the reaction under pure diffusion limitations, as the concentration at the surface almost instantly drops to zero. As discussed previously, diffusion-limited growth of silver leads to dendrite growth, and therefore the duration of the nucleation pulse should be limited. During the growth pulse, the concentration at the surface of the electrode is not zero, and hence the growth is kinetically

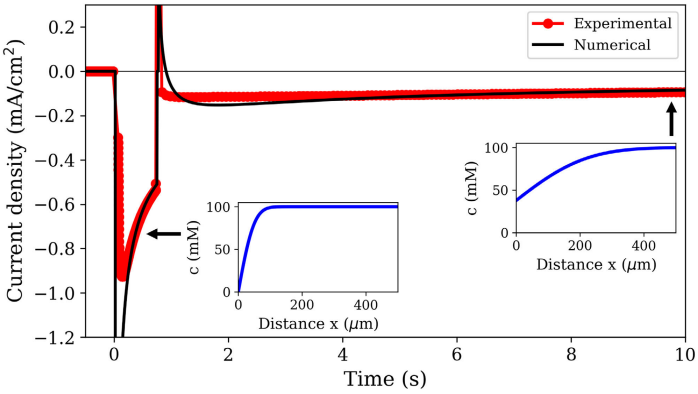

Figure 2.9: *Experimentally obtained current transient (red) overlapped with the numerically obtained current transient (black) for an experiment using the double pulse technique. The insets shows the concentration profile of the silver ion as function of distance from the electrode, during the nucleation and growth pulse, as represented by the arrows. The used parameters for the 1D simulation:* $D = 1.6 \cdot 10^{-5}$ *cm*^{2}*/s,* $k0 = 0.01$ *cm/s,* $c_0 = 2$ *mM,* $E^0 = 0.6$ *V vs Ag/AgCl,* $\eta_n = 400$ *mV,* $\eta_g = 15$ *mV,* $E_{nucl} = 120$ *mV.*

controlled. Interestingly, both the experimental and the numerical simulations show a small positive current density just after switching from the nucleation to the growth pulse. This is the result of a sudden change in the rate constant in combination with the depletion of silver ions at the surface, which results in a net oxidation reaction. However, as the concentration of silver ions increases at the surface, at a certain concentration the reaction again becomes in favour of silver reduction, as the growth potential is below the reduction potential.

The developed Python simulation package for the simulations of the cyclic voltammograms and the chronoamperometry is available on GitHub and can be found in Ref. [185].

3

Influence of the Crystallographic Texture of ITO on the Electrodeposition of Silver Nanoparticles

The electrochemical control over nucleation and growth of metal nanoparticles on foreign substrates is an active field of research, where the surface properties of the substrate play a key role in nucleation dynamics. Polycrystalline indium tin oxide (ITO) films are highly desired substrates for many optoelectronic applications, for which the only parameter that is often specified is the sheet resistance. As a result, growth on ITO is highly irreproducible. In this chapter, we show that ITO substrates with the same technical specifications (i.e., sheet resistance, light transmittance and roughness) and supplier may still have a different crystalline texture, which we find it has a strong impact on the nucleation and growth of silver nanoparticles during electrodeposition. We find that the preferential presence of lower index surfaces leads to a few orders of magnitude lower island density, which is strongly dependent on the nucleation pulse potential. By contrast, the island density on ITO with preferential <111> orientation is barely affected by the nucleation pulse potential. This work highlights the importance of reporting the surface properties of polycrystalline substrates when presenting nucleation studies and metal nanoparticle electrochemical growth.

3.1 Introduction

Nanometer-scale metal particles exhibit chemical and physical properties which differ significantly from macroscopic metal phases, including strong interaction with visible light due to their localised surface plasmon resonances. This strong optical response creates bright colours that can be fine-tuned by the nanoparticle size and composition. In particular, silver nanoparticles (NPs) have received extensive attention since it can support a strong surface plasmon polariton modes resulting in high quality factors, which can be tuned all across the visible and NIR regime.[88,186] This strong and tuneable interaction of visible light with silver NPs has found applications in sensing,[187] surface enhanced Raman spectroscopy (SERS),[188,189] smart windows,[190–193] dynamic colour displays,[194] plasmonic colour filters,[195] photo(electro)catalysis[196,197] and more.[198] For many of these applications, it is essential to reliably and precisely control the size and density of silver NPs on conducting transparent supports, such as indium tin oxide (ITO).

Electrochemical deposition is an attractive growth method owing to its inherent low cost, minimal raw material usage, low temperatures and high throughput. Electrochemical deposition of silver on ITO naturally leads to scattered, low density irregular island growth owing to the low surface energy and high nucleation barrier of ITO, which poses a challenge for smooth continuous deposits. Several works have shown that cyanide compounds and other organic additives in the electrolyte solution can lead to high density island formation, which can be controlled by a nucleation pulse step.[166,167,199,200] However, the high toxicity and environmental impact of such electrolytes demands the search for more sustainable alternatives, such as thiosulfate baths,[201] non-toxic organic additives,[202] or even plant extracts.[203] While the nucleation kinetics and growth dynamics of silver on ITO are well studied for cyanide-based electrolytes,[166,167] nucleation studies with non-toxic and sustainable electrolytes are scarce.[189,190,194,204,205]

In all these works, attention is given to the nucleation pulse parameters (i.e., pulse potential and time) on island density and size, while the influence of the surface properties of the ITO substrate are highly omitted. The uncertainty in the physico-chemical properties of commercial ITO (e.g., chemical composition, roughness or crystalline orientation) is typically reduced down to reporting the sheet resistance and average optical transmission. There is no straightforward connection between these characteristics and the ITO surface properties, despite it is well known that the substrate surface plays a key role in the nucleation and growth dynamics.

In this chapter we elucidate the impact of crystallographic texture of ITO substrates with the same nominal specifications (i.e., roughness, sheet resistance and supplier) on silver nucleation dynamics in a silver sulphate based aqueous solution. We find that the nucleation density as a function of nucleation pulse potential can differ by several orders of magnitude depending on the surface properties (i.e., the preferred ITO crystal orientation, grain size, and grain misorientation angle). In particular we find that the ITO from batch 2 having small randomly oriented grains, leads to a high nuclei density and diffusion coupled growth that is barely affected by the nucleation pulse potential. By contrast, ITO from batch 1 having larger grains with strong preference for low Miller index surfaces, leads to island densities that can be tuned by the nucleation pulse potential. This work highlights the importance of reporting the surface properties of ITO substrates for improved reproducibility of metal NPs growth.

3.2 Results and discussion

Figure 3.1 shows the first cycle of the cyclic voltammogram (CV) for silver deposition in aqueous electrolyte on two nominally equal sheets of ITO (see Experimental Section). The CV is initiated at open circuit potential (OCP, 0.49 and 0.47 V vs Ag/AgCl for batch 1 and 2, respectively) and scanned with a scan rate of 25 mV/s toward the cathodic direction, as indicated by the arrows. During the first cycle, silver is deposited onto the clean ITO surface upon overcoming the onset potential for silver nucleation, as indicated by the sharp increase in cathodic current (marked by the red and green dashed vertical lines). At more negative potentials, the cathodic current rapidly increases after nucleation and reaches a maximum, a characteristic of diffusion-limited growth. [162]

The onset potential for silver nucleation (0.32 and 0.27 V vs Ag/AgCl for batch 1 and batch 2, respectively) is found to be more negative than the experimentally determined Nernst equilibrium potential of silver E_{Ag/Ag^+} (0.39 V vs Ag/AgCl). The difference between the onset potential and the Nernst equilibrium potential is known as the nucleation overpotential η_{nucl}, [206] which is typical in deposition onto foreign non-wetting substrates. The fact that the nucleation potential is the lowest for batch 1 is in agreement with its preferential crystallographic orientation, since the ITO from batch 1 has a greater amount of higher surface energy planes in comparison to the ITO from batch 2 ($\gamma(400) > \gamma(222)$). [207,208] Nucleation on higher energy surfaces is expected to be thermodynamically more favourable, and hence occurs at reduced nucleation overpotentials. The ratio between the (222) and (400) peak intensity in batch 2 (see Figure 3.6) indicates that these substrates have significantly less (400)-oriented surface area compared to batch 1. One might thus expect that the reductive current due to nucleation on the (400)-oriented surface in batch 2 is negligible, and most of the current is due to nucleation on the (222)-oriented surface, which takes place at a larger overpotential.

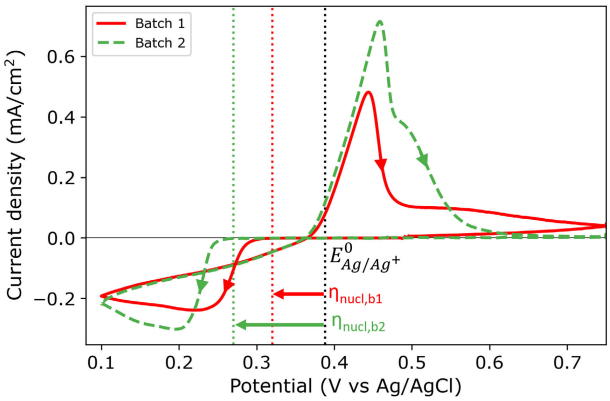

Figure 3.1: *First cycle of the cyclic voltammogram (25 mV/s) for the silver sulphate electrolyte containing saccharin on ITO batch 1 (red solid) and batch 2 (green dashed). The arrows indicate the direction of the scan. The nucleation onset potential is indicated with red and green dotted lines for batches 1 and 2, respectively. The black dotted line indicates the experimentally found Nernst equilibrium potential* E^0_{Ag/Ag^+}.

During the reverse scan in the cyclic voltammogram, the current transient crosses the forward scan (i.e., crossover) in both cases. This is an indication of nucleation and growth, where growing nuclei result into a larger surface area and hence an increase in current, and deposition onto the already formed nuclei does not require an overpotential. [153] The total amount of transferred charge and hence the amount of deposited silver is virtually the same for both batches (2.61 and 2.59 mC/cm^2 for batch 1 and 2, respectively). In both batches, the current flips from cathodic to anodic at 0.37 V vs. Ag/AgCl and defines the onset of silver dissolution. Integrating over the anodic peak current, we find that more silver is being stripped from batch 2 compared to batch 1 (2.07 and 2.54 mC/cm^2 for batch 1 and 2, respectively). During the second cycle of the CV (see Figure 3.10 in the Supplementary Information), the nucleation overpotential of silver deposition on batch 1 is close to zero due to incomplete stripping (79%). Silver nuclei are still present on the surface of batch 1 at the start of the second cycle, and therefore nucleation and growth can occur at near-zero nucleation overpotential. However, the stripping of silver was more complete in batch 2 (98%). Therefore, almost no silver nuclei are present on the surface at the end of the first cycle, hence the large nucleation overpotential in the second cycle.

In the following, we study the effect of the nucleation pulse potential in the double-pulse method [167,202] on the nucleation and growth of silver NPs on the two types of ITO substrates. In order to qualitatively compare the nucleation kinetics in both types of ITO, we convert all applied voltages to the overpotential relative to the nucleation overpotential η_{nucl} of the respective batch. As such, the nucleation pulse overpotential η_n is defined as:

$$\eta_n = |\eta_{n,IR} - \eta_{nucl}| \tag{3.1}$$

where

$$\eta_{n,IR} = E_n - E^0_{Ag/Ag^+} - IR_s \tag{3.2}$$

where E_n is the applied nucleation pulse potential, E^0_{Ag/Ag^+} is the Nernst equilibrium potential, I is the current during the nucleation pulse, and R_s is the solution resistance. Since the nucleation overpotential η_{nucl} is defined as the difference between the onset potential and the Nernst equilibrium potential, equation 3.1 can be simplified to:

$$\eta_{n,IR} = |E_n - IR_s - E_{nucl}| \tag{3.3}$$

Note that the exact value of the Nernst equilibrium potential is therefore not relevant for the value of the nucleation pulse overpotential, since the term drops out from the equation.

Figure 3.2 shows representative SEM images of the silver islands on ITO obtained at nucleation pulse overpotentials of 0.2 V (a,d), 0.5 V (b,e) and 0.9 V (c,f), for the two different batches of ITO substrates (top and bottom rows). In line with electrochemical theory for kinetically controlled nucleation, [154,166,209] we observe that the island density increases with increasing nucleation pulse overpotential regardless of substrate, owing to the increased electrodeposition kinetics as the potential is increased. At the same time, we observe that the size of the islands decreases with increasing density (see Figure 3.12), likely as a result of higher ion competition between nuclei as the number of nuclei increases. In fact, since we kept the growth pulse constant for all samples, the mean island radius is fully determined by the island density (see Figure 3.13a in the Supplementary Information).

Despite the qualitative agreement between the trends for both substrates and the fact that electrochemical parameters were carefully kept constant throughout the study, the island density is quantitatively not reproduced for the two ITO batches with the same nominal specifications (roughness, sheet resistance and supplier, see Experimental section

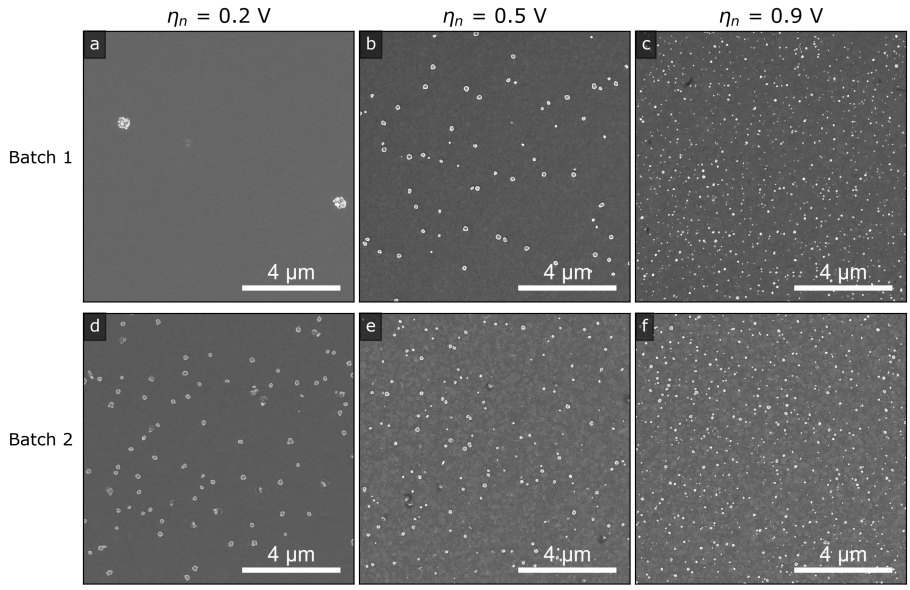

Figure 3.2: *Representative SEM images of the silver islands on ITO from (a-c) batch 1 and (d-f) batch 2 using a nucleation pulse overpotential of (a,d) 0.2 V, (b,e) 0.5 V and (c,f) 0.9 V.*

and Supplementary Information). This is most evident by comparing the images in figures 3.2a and 3.2d, both deposited at a low nucleation pulse overpotential. Such inconsistencies between growths on presumably equivalent substrates make the reproducibility of published works difficult and may hamper the overall understanding of silver nucleation (and any other metal) on ITO.

For a more quantitative assessment, Figure 3.3 shows the island density as a function of the nucleation pulse overpotential, as extracted from the SEM images. The samples corresponding to batch 1 and batch 2 are shown in red circles and green squares, respectively. From the semi-logarithmic representation, one can see that for $\eta_n < 0.8$ V the island density exponentially increases with increasing nucleation pulse overpotential for both substrates. However, the rate of increase is much more pronounced for batch 1 compared to batch 2, which leads to a difference of 2 to 3 orders of magnitude between particle densities for the same (low) nucleation pulse overpotential.

Previous studies have empirically shown [154,210–214] that an exponential relationship exists between island density and overpotential following:

$$N_p(\eta_n) = A \exp\left(-\frac{1}{B}\,\eta_n\right) \tag{3.4}$$

Here, A and B are voltage independent empirical parameters, where the pre-exponential factor A is thought to be related to the surface density of available sites at OCP, and the exponential component B is an activation term related to the electron kinetics. Equation 3.4 is valid for the assumption of instantaneous nucleation or progressive nucleation where the nucleation pulse duration is sufficient long enough to nucleate on all active sites. Fitting our data to the equation above, we find the inverse slope B is 259 ± 20 and 645 ± 84 mV/dec, and

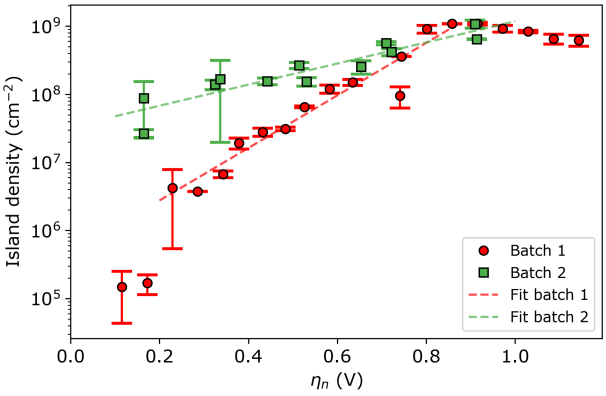

Figure 3.3: *Island density versus nucleation pulse overpotential for batch 1 (red circles) and batch 2 (green squares). The red and green dashed lines are the fits to the data points of batch 1 and 2, respectively. The inverse slope B is* 250 ± 23 *and* 625 ± 84 *mV/dec, and the pre-exponential factor A is* $4.7 \cdot 10^5 \pm 2.2 \cdot 10^5$ *and* $3.4 \cdot 10^7 \pm 9.5 \cdot 10^6$ *cm*$^{-2}$ *for batch 1 and 2, respectively. Note that a logarithmic scale is used for the vertical axis.*

the pre-exponential factor A is $4.7 \cdot 10^5 \pm 1.8 \cdot 10^5$ and $3.3 \cdot 10^7 \pm 9.0 \cdot 10^6$ cm^{-2} for batch 1 and 2, respectively. It is important to note that the two data points at the lowest nucleation pulse overpotentials were left out of the fitting procedure because the duration of the nucleation pulse was not long enough to complete nucleation at such low nucleation pulse overpotentials. In other words, the island density was still not saturated within the duration of the nucleation pulse (incomplete progressive nucleation). We therefore find that batch 1 has a greater tunability by nucleation pulse overpotential than batch 2.

At nucleation pulse overpotentials larger than 0.8 V, the island density saturates in the order of 10^9 cm^{-2}, in both types of substrates. Considering the classical nucleation and growth models, a saturated island density with increasing nucleation pulse overpotential indicates that nucleation is limited by mass transport, a condition that depends on the properties of the electrolyte and the electrochemical cell.[152–155] Under such circumstances, the island density saturates once the diffusion zones of the islands overlap, preventing the formation of new nuclei and resulting in a constant mean island radius with increasing nucleation pulse potential (see Figure 3.13b). In addition to the limitations by mass transport, spurious hydrogen evolution at high cathodic potentials may poison the ITO surface, thereby reducing the number of active sites for silver nucleation. This effect explains the small decrease in island density at large nucleation pulse overpotentials.

We verify the mass transport limited island density through a spatial correlation analysis using the nearest-neighbour distance (nnd). In the case where nucleation and growth of the islands is not limited by mass transport, the nnd distribution obeys complete spatial randomness (CSR).[155] In other words, in a random point pattern the probability of finding n points (i.e., islands) within a certain distance from an arbitrary island is Poisson distributed, and has a well-defined probability density function (pdf) $p(r)$:[155,215]

$$p(r) = 2\pi\rho r \exp(-\pi\rho r^2) \tag{3.5}$$

where r is the distance from the central point, and ρ is the number of points per unit area

(i.e., island density).

Figure 3.4 shows three representative *nnd* distributions for three different island densities from low (a) to high (c). The solid red line indicates the Poisson distribution given by Equation 3.5. Due to the finite size of the islands, the histogram is distorted at short *nnd*, as indicated by the black line that represents the mean diameter of the common island. To verify the results from the first *nnd* distribution analysis, we also analysed the second *nnd* (i.e., next nearest neighbours) distribution where these short *nnd* are less important due to the r^3 dependency of the pdf function (see section 3.5.6 in the Supplementary Information). From the histograms it seems that the *nnd* distribution obeys CSR in all cases. However, the high island density distributions lack close neighbouring particles. This effect is more visible in the cumulative distribution function (cdf) of the highest and lowest particle density, shown in Figures 3.4d and 3.4e. While the cdf of the lowest density *nnd* distribution (black curve in Figure 3.4d) falls within the confidence interval of the Poisson cdf (shaded grey area), the cdf of the highest density *nnd* distribution (black curve in Figure 3.4e) clearly falls outside the Poisson confidence interval.

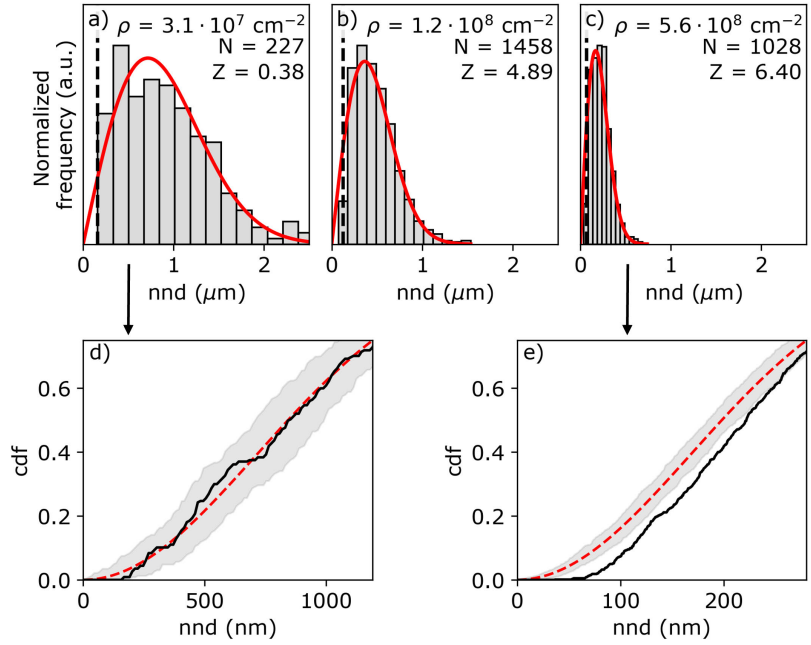

Figure 3.4: *Histograms of the (a-c) nnd obtained from SEM images for the island densities of a)* $3.1 \cdot 10^7$ *cm*$^{-2}$ *(batch 1,* $\eta_n = 0.46$ *V), b)* $1.2 \cdot 10^8$ *cm*$^{-2}$ *(batch 1,* $\eta_n = 0.55$ *V), and c)* $5.6 \cdot 10^8$ *cm*$^{-2}$ *(batch 2,* $\eta_n = 0.67$ *V). The histograms are normalised and compared with the Poisson distribution (solid red line). The black dashed line in (a-c) indicates the mean diameter of the islands. The island density* ρ*, number of islands N, and the Z value are listed in each histogram. d) and e) are the cumulative distribution functions of a) and c), respectively. The shaded area indicates the 95% confidence interval.*

To confirm whether the island patterns obey CSR or not, we perform a Z-test, where the Z-value is defined as:

$$Z = \frac{\langle nnd \rangle - \langle nnd \rangle_{CSR}}{\sqrt{\sigma^2_{CSR}/N}} \tag{3.6}$$

where $\langle nnd \rangle$ is the mean value of the nnd distribution, N is the number of points in the distribution, and $\langle nnd \rangle_{CSR}$ and σ^2_{CSR} are the mean nnd value and variance of the CSR probability density function. Distributions having a Z-value within ± 1.96 are considered to be CSR with 95% confidence (two tailed test with $p > 0.05$). Contrarily, if $Z < -1.96$ the distribution is considered to be clustered, while if $Z > 1.96$ the distribution is considered to have a globally ordered structure. [155] A more detailed derivation of the first and second order of the pdf, and the definition of the mean and variance of the distribution can be found in Section 3.5.6 of the Supplementary Information.

The resulting Z-values for the examples shown in Figures 3.4a-c are 0.38, 4.89 and 6.4, respectively, which undoubtedly shows that only the spatial distribution of islands having the lowest density is completely random. The analysis of the Z-test of the first and second nnd is performed for all samples, where the first-nnd Z-values are shown in Figure 3.5 as a function of the island density for the two types of substrate (red circles for batch 1 and green squares for batch 2). Second-nnd Z-values are shown in the Supplementary Information in Figure 3.15. The Z-values for both the first and second nnd distributions indicate CSR at low island densities and up to approximately 10^8 cm^{-2}. For higher island densities, the Z-value rapidly increases, meaning that the island distribution is becoming globally more ordered. This ordered structure is caused by the transition from uncoupled 3D to diffusion-coupled 1D deposition due to the overlap of diffusion zones around the growing islands. [209,213,215,216] In the regime of coupled growth, no new islands can nucleate within the diffusion zone, hence forcing an exclusion zone between the islands and leading to a globally more ordered pattern. It is important to note here that almost all of the batch 2 samples fall in the diffusion coupled regime, which is in contrast to the batch 1 samples. This partly explains why the inverse slope of the island density versus nucleation pulse overpotential is much different from any other values found in the literature. Silver nucleation on batch 2 ITO is under mixed kinetic/diffusion control, leading to an unreasonably large apparent inverse slope B (i.e. an apparent small electrode kinetics).

Interestingly, a similar conclusion can be drawn from the total transferred charge during growth as a function of the island density (see Figure 3.14 in the Supplementary Information). Again, the two regimes can be discerned. At low island densities (i.e., below 10^8 cm^{-2}), the amount of transferred charge increases with island density. This behaviour agrees well with the uncoupled growth regime. On the contrary, at high island densities, the amount of transferred charge saturates. This suggests that at these densities the silver deposition is limited by mass transport instead of by electrode kinetics, which agrees well with the diffusion-coupled growth. In summary, both the nnd and the transferred charge analysis confirm that island density saturation at large nucleation pulse overpotentials arises from mass-transport limitations rather than the surface properties of the ITO substrate, therefore invalidating Equation 3.4 to assess nucleation kinetics in batch 2. In fact, we suspect that batch 2 samples have high electrode kinetics, where very small nucleation pulse overpotentials (< 100 mV) can lead to very high particle densities.

We have shown that two batches of ITO sheets, even though they are from the same supplier having the same nominal specifications, display a large discrepancy in the silver island density for nucleation pulse overpotentials η_n smaller than 0.8 V. Batch 1 samples, which show a preference for (400) crystal orientation having large grain sizes, display the

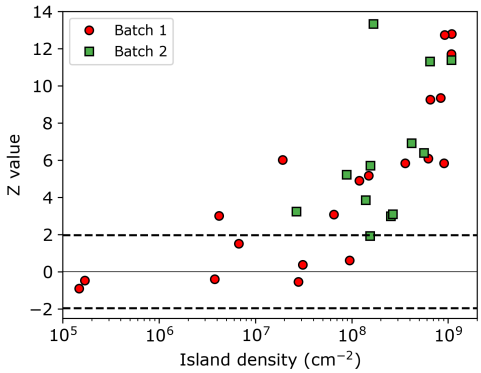

Figure 3.5: *Z-value obtained from individual nnd distributions as function of the island density. Samples from batches 1 and 2 are indicated by red circles and green squares, respectively. Horizontal black dashed lines indicate the region for which the distribution of islands exhibit CSR.*

lowest nucleation overpotential and a kinetically-controlled island density that increases exponentially with nucleation pulse overpotential. Contrarily, batch 2 samples with a slight (222) preferential crystal orientation and having smaller grains show a high nucleation overpotential. However, the fast electrode kinetics lead to such high nucleation densities that nucleation is diffusion limited for almost all nucleation pulse overpotentials as small as 100 mV. As previously mentioned, the lower surface energy in high index surfaces imposes a thermodynamic barrier for growth. Yet, this thermodynamic barrier may be compensated for by high electrode kinetics. In fact, it has been reported that {222}-terminated surfaces of ITO typically show metal sites with incomplete coordination, and are therefore expected to be highly reactive.[217] As a result, a very high number of nuclei can be formed once the thermodynamic barrier is overcome even with nucleation pulse overpotentials of few tenths of mV. This concept could be extended to similar systems in which the electrochemical reaction is limited by the electron kinetics. Therefore, we expect that the texture of the ITO substrates also influences the growth of different materials. Despite the thermodynamic preference for nucleating on the high surface energy facets and on the grain boundaries, from SEM and AFM images we were not able to unequivocally identify if the islands are located on specific facets and/or grain boundaries.

3.3 Conclusion

In this chapter, we elucidate the influence of ITO surface orientation on the growth of silver NPs through a careful and quantitative study on nanoparticle nucleation and growth on two batches of ITO substrates. We use seemingly equal ITO substrates (in terms of sheet resistance, surface roughness, and optical transparency) that have a clear different surface texture. We find that in the kinetic regime, silver nucleation dynamics are slower for ITO films with preferential (400) orientation, leading to several orders of magnitude lower silver island densities compared to those found in substrates having a slight preference for the (222) orientation. We elucidate that the empirical exponential relationship between island density

and nucleation pulse overpotential is not enough to draw conclusions on electrode kinetics, where additional validation of the growth process is essential. We argue that the enhanced electron transfer rates at {222}-terminated surfaces during the nucleation and growth pulses may be responsible for the larger island density.

Beyond careful control of electrochemical parameters, here we show that neglecting the macroscopic surface characteristics of ITO (and any other polycrystalline substrate) can lead to major ambiguity in nucleation and growth dynamics of metal nanoparticles. Controlling metal particle density and size is crucial in many applications. We show here that XRD characterisation prior to deposition is a simple additional measure to tailor metal nanoparticle electrochemical growth on ITO.

3.4 Methods

3.4.1 ITO substrates

Two sheets of ITO coated glass (KinTec, nominal sheet resistance 10-15 Ω/□, 150x150 mm^2) were cut into 25x25 mm^2 pieces and used as working electrodes (exposed area 0.95 cm^2). Pieces taken from the first sheet of ITO shall be referred to as batch 1, and similarly ITO pieces taken from the second sheet are referred to as batch 2. The average root mean square (rms) surface roughness of two batches are 2.0 ± 0.1 and 3.4 ± 0.2 nm, respectively, as measured with AFM. Despite the relatively large range for the specified nominal sheet resistance, we measured $R_{\square} = 15.8 \pm 0.2$ Ω/□ and $R_{\square} = 14.8 \pm 0.5$ Ω/□ for batch 1 and 2, respectively.

XRD and electron back-scattered diffraction (EBSD) analysis (Figure 3.6a and section 3.5.1 in the Supplementary Information) reveal that the ITO pieces from batch 1 have a strong preference for the (400) orientation, while the ITO pieces from batch 2 have near random oriented grains with a slight preference for the (222) orientation. All ITO pieces within the

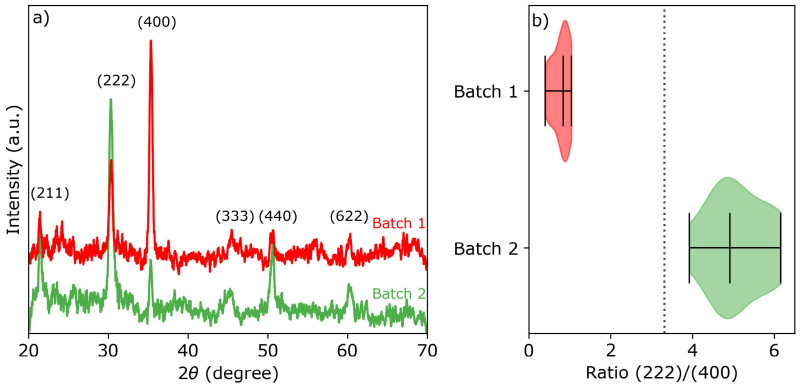

Figure 3.6: *a) 2θ scans of representative batch 1 (red) and batch 2 (green) samples with the corresponding crystallographic orientations. b) Violin plot of the peak intensity ratio distribution between the (222) and (400) peaks for samples from each batch. The distribution medians and limits are marked by the bars. The vertical dotted line represents the value of the theoretical ratio I_{222}/I_{400} for powder diffraction of In_2O_3.*

same batch show similar XRD patterns, represented by the intensity ratio I_{222}/I_{400} of the (222) and (400) peaks in Figure 3.6b. The theoretical peak intensity ratio I_{222}/I_{400} is represented by a vertical black dashed line. The theoretical peak intensity ratio was simulated for the In_2O_3 crystal structure (bixbyite, space group 206, $Ia\bar{3}$, a=10.117 nm) using CaRIne Crystallography version 3.1.

The ITO substrates were cleaned by brushing with soap and ethanol to remove any residual glue that was used for cutting the samples. After, the ITO substrates were sonicated for 10 min in ultra pure water, 10 min in acetone and 5 min in isopropanol (IPA). The ITO substrates were treated with ozone for 15 min (UV/Ozone ProCleaner BioForce Nanosciences) to remove any organics and to activate the surface just before the start of the experiment,[218] resulting in a more hydrophilic surface.

3.4.2 Electrochemical cell and electrolyte

A custom build PEEK cell of 24 mL volume was used, using a standard three-electrode configuration (see Figure 2.3 in Chapter 2). A Pt disc (exposed area 3.08 cm^2) was used as the counter electrode, and an Ag/AgCl electrode (leakless miniature ET072, EDAQ) was used as the reference electrode. The miniature reference electrode was calibrated against a saturated Ag/AgCl reference electrode (XR300, Hach) just before the start of each experiment. All experiments were performed using a SP-300 Bio-Logic potentiostat.

An aqueous (Millipore Milli-Q® , ρ > 18.2 MΩ·cm) electrolyte containing 1 mM Ag_2SO_4 (99.999%, Sigma-Aldrich), 1 mM saccharin (≥ 99%, Sigma-Aldrich), 100 mM Na_2SO_4 ≥ 99.0%, anhydrous, granular, Sigma-Aldrich), 38 mM H_2SO_4 (96% solution in water, ACROS Organics) (pH of 1.7) was used for the electrodeposition of silver. The solution resistance R_s was determined by electrochemical impedance spectroscopy and was found to be $25 \pm 5\ \Omega$. The solution resistance value was used for the IR correction of the applied potential. A double pulse method was used to perform the silver deposition.[167,202] A nucleation pulse E_n was applied for 30 ms followed by a growth pulse E_g = +0.373 V vs Ag/AgCl for 20 s, which was taken from Kung *et al.*.[202] The nucleation potential E_n was varied between +0.2 and −0.883 V vs Ag/AgCl. Figure 2.5 in Chapter 2 shows a schematic of the used potential scheme, where the lowest and highest potentials are indicated by a dashed green and solid red line, respectively. All experiments were performed at room temperature (18-21 °C) without stirring. For each experiment a fresh ITO sample was used which was cleaned as described above. Directly after deposition, the samples were rinsed in ultra pure water and IPA to remove any precipitation and were dried using a flow of nitrogen gas.

3.4.3 Characterisation

Morphological and structural characterisation of the deposited silver nanoparticles was performed using a FEI Verios 460 scanning electron microscope (SEM), operated at 5 kV and 100 pA, using a working distance of 4 mm. Topographical maps were obtained with atomic force microscopy (AFM), using a Bruker Dimension Icon and a ScanAsyst-Air probe (Bruker, nominal tip radius 2 nm). Details on SEM image processing can be found in section 3.5.3 of the Supplementary Information.

X-ray diffraction (XRD) was performed on most ITO substrates using a Bruker D2 Phase diffractometer. The Cu K_α irradiation was operated at 30 kV and 10 mA. The substrates were scanned between 2θ = 25° and 70°, with 0.016° increment using a dwell time of 0.1 s.

Electron back scatter diffraction (EBSD) patterns were collected in a FEI Verios 460 SEM, operated at 10 kV and 800 pA using a working distance of 8.2 mm, using an Amsterdam Scientific Instruments Timepix detector. The EBSD maps were obtained using a sample tilt of 70° relative to the electron beam, an exposure time of 10 ms, and a step size of 20 nm. The collection and analysis was done using the software OIM Analysis of EDAX.

Author Contributions

Y.B. and M.D. synthesised the silver particles, I.S. and H.S. performed the EBSD measurements, I.S performed the EBSD analysis and Y.B. performed all the data analysis. Y.B. and E.A.L. wrote the manuscript. E.A.L. supervised the project.

3.5 Supplementary Information

3.5.1 Obtaining crystallographic orientation by EBSD

Electron back scatter diffraction (EBSD) is a SEM-based technique in which the diffraction patterns (Kikuchi patterns) of the back-scattered electrons are detected. The diffraction pattern is a result of the interaction of inelastically scattered electrons with the crystal structure of the sample, and hence provide information about the type of crystal structure, lattice constant, and orientation. EBSD maps were obtained

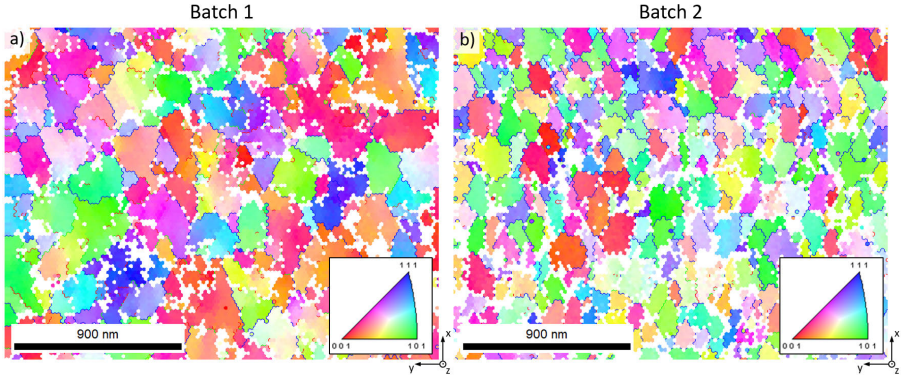

Figure 3.7: *IPF EBSD maps of a) ITO batch 1 and b) ITO batch 2, showing different crystallographic orientation perpendicular to the ITO surface. The area of both scans is 4.17 μm^2.*

by transforming the Kikuchi lines into points (Hough space), which are fitted using the simplified crystal structure of In_2O_3 (a face-centered cubic 2 × 2 × 2 supercell, space group 225, $Fm\bar{3}m$) using a lattice constant of $a = \frac{1}{2} \cdot 10.12$ Å = 5.05 Å.[207] When using the actual crystal structure of In_2O_3 (bixbyite, space group 206, $Ia\bar{3}$) in the fitting procedure, it resulted into pseudo-symmetrical solutions which could not be distinguished. Based on this data the software cannot distinguish the (101) and (110) directions in the crystal, because their difference is too subtle. However, the distinction between the (200) and (444) directions can be made, and their ratio is not affected by fitting the data with the simplified crystal structure.

Figure 3.7 shows the crystallographic orientation along the z-axis in inverse pole figure (IPF) maps for batch 1 and batch 2. Confidence interval (CI) standardisation clean up was used with a CI of 0.1. After two rounds of refitting only the data with CI > 0.1 was kept and used for the determination of grains and grain boundaries. Grains were determined based upon 5° tolerance with a minimal size of 2 pixels. The colours in the map represent the crystallographic orientation perpendicular to the surface.

To get a better insight into the distribution of crystallographic orientations, we represent every pixel from the EBSD map in Figure 3.7 by a dot in the IPF, as shown in Figure 3.8a. In line with the XRD spectra shown in figure 3.6, we find that the surface of batch 1 has a strong preference for the <100> orientation, while the distribution of orientations for batch 2 seems to be more random.

Next to the orientation of the grains, we can also extract the size of the grains from the EBSD maps. We observe a clear difference in the size of the grains between ITO from batch 1 and 2. The average grain size is found to be 0.022 μm^2, and 0.072 μm^2 for batch 1 and 2, respectively. Consequently, the total length of the grain boundaries is larger for batch 2. It is interesting to consider the misorientation of the grains since in general a higher misorientation angle leads to higher grain boundary energies.[219] However, this relation only holds up to a certain misorientation angle, since for larger misorientation angles coincidence take place which results into a maximum of grain boundary energy. Regarding electrochemical nucleation, it would be thermodynamically more favourable to nucleate on the grain boundaries with a higher misorientation angle. We therefore look to the grain boundary length density for small (5-10°), medium (10-20°) and large (> 20°) misorientation angles, which is shown in Figure 3.8b. Next to the larger grain boundary length density, batch 2 also has a larger misorientation between the grains. These observations are in line with the observed fast kinetics of batch 2.

To correlate the morphology of the surface with the EBSD maps, we show in Figure 3.9 the overlap between the EBSD map of Figure 3.7a with the corresponding SEM image. It is clear that the morphology of the ITO already reveals the location of the grains. Furthermore, it was found that grains in the <100> and <111> direction could be recognised by the subgrains which are vertically, or horizontally orientated rods, respectively. The morphology of the SEM image can therefore already provide some information about the grain size.

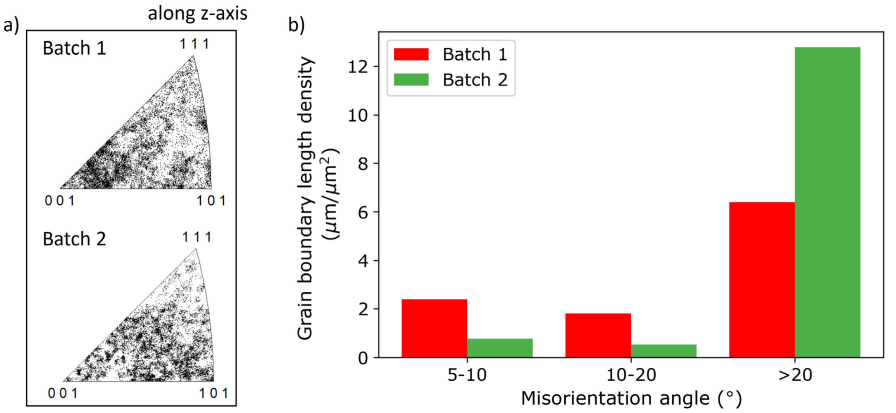

Figure 3.8: *a) IPF showing the distribution of orientations for ITO batch 1 and 2 samples along the z-axis. b) Grain boundary length density for small (5-10°), medium (10-20°) and large (> 20 °) misorientation angles. The grain boundary length density is defined as the grain boundary length divided by the area of the scan.*

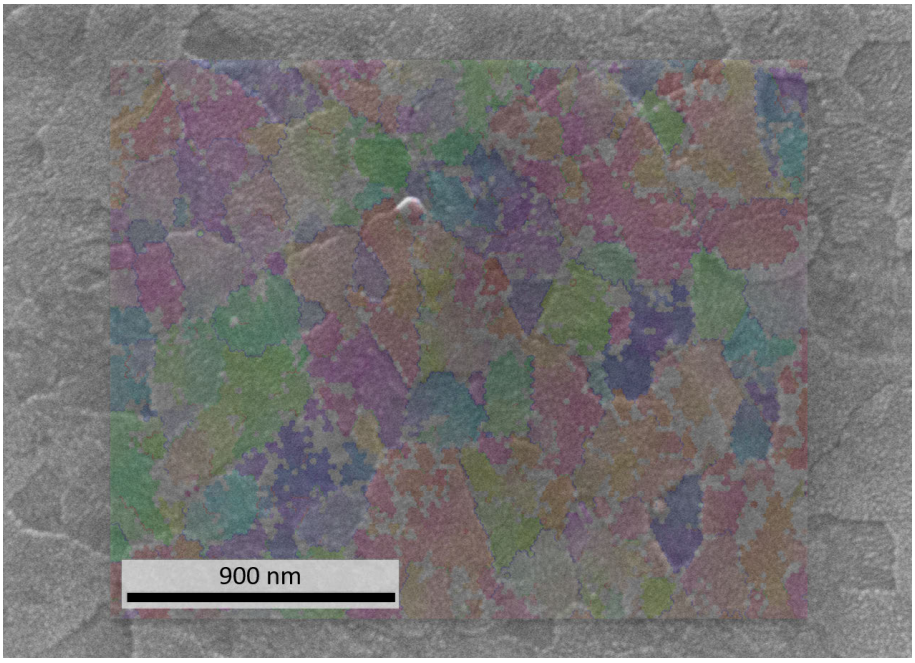

Figure 3.9: *Overlay of the EBSD map of ITO batch 1 as seen in Figure 3.7a with the corresponding SEM image.*

3.5.2 Cyclic voltammograms

Figure 3.10 shows the first and second cycle of the cyclic voltammogram of batch 1 (red) and batch 2 (green). Due to the incomplete stripping of the deposited silver, the large nucleation overpotential is significantly decreased in the second cycle of the cyclic voltammogram for both batches. This is because the silver is now also able to nucleate on the already existing silver nuclei which were formed during the first cycle. This effect is more pronounced for batch 1 than batch 2.

The experimental Nernst equilibrium potential E^0_{Ag/Ag^+} was determined by extracting the halfway potential from the second cycle of the saccharine electrolyte. Since for batch 2 most of the silver was stripped, the onset potential of the second cycle is still significant and hence the cathodic peak is shifted to more negative potentials. Therefore, for batch 2 the halfway potential of the blank electrolyte was used instead (which is very similar to the found value for batch 1). The corresponding free silver ion concentration was found to be 0.26 mM.

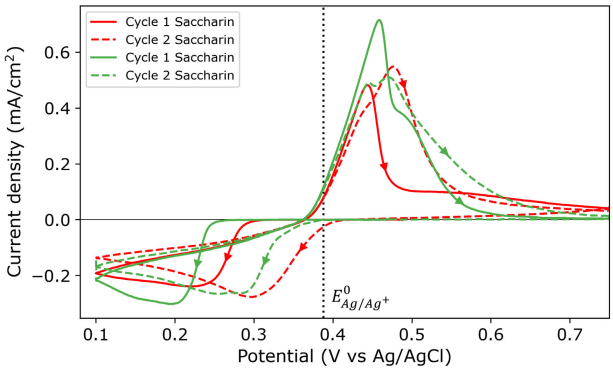

Figure 3.10: *Cyclic voltammogram for batch 1 (red) and batch 2 (green). The first cycles are represented by a solid line, while the second cycles are represented by a dashed line. The dotted black line indicates the experimentally found Nernst equilibrium potential.*

3.5.3 SEM data treatment

The obtained SEM images were analysed using a Python script, which is based on a watershed image recognition method. From these images, the particle density and size distribution were extracted. The SEM images were analysed using the OpenCV package in Python (https://opencv.org/). A threshold of the raw SEM image was obtained using the *adaptiveThreshold* function. The image was then split into a sure foreground image and a sure background image. The difference between these images was used in a watershed method to determine the contour of the edges. The final contours and therefore the area of the particles were obtained by using the function *connectedComponentsWithStats*. One example of an analysed SEM image

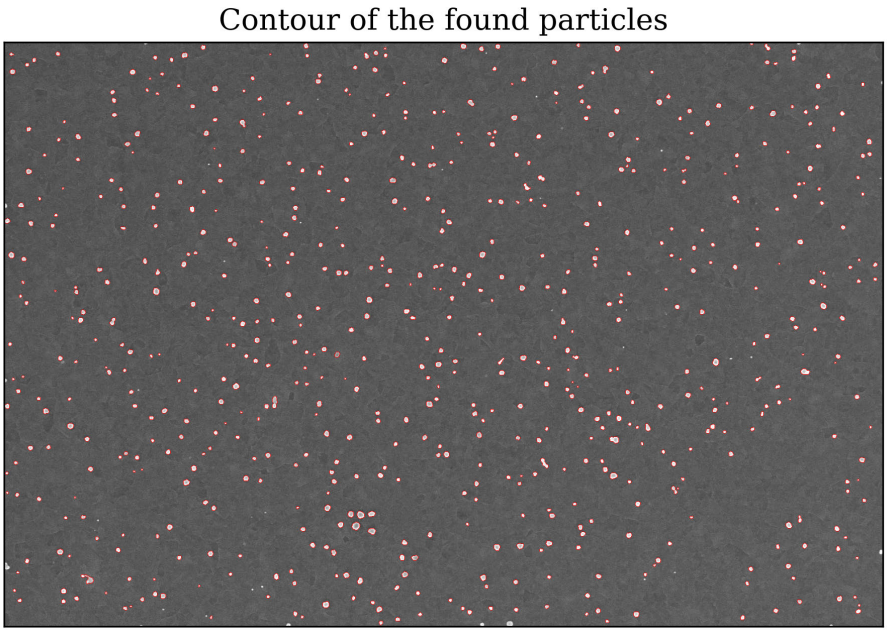

Figure 3.11: *Analysed SEM image from a sample corresponding to batch 1 grown at a nucleation pulse overpotential of 0.74 V. The detected particles are highlighted by the red contour.*

is shown in Figure 3.11. The contour of the found particles is shown in red. Particles which were lying on the outline of the image were discarded from the analyses.

3.5.4 Particle size distribution

Figure 3.12 shows the size distribution of the selected samples shown in the SEM images in Figure 3.2. The size distributions move to smaller radii as the nucleation pulse overpotential increases. Although it seems that the distribution becomes more narrow, the relative standard deviation (RSD = SD/r_{mean}) is constant and might even slightly increase (especially for batch 1). For each SEM image such a distribution is obtained.

Per sample (applied nucleation pulse overpotential), multiple size distributions were obtained. These distributions were merged such that there is only one size distribution per nucleation pulse overpotential. From the final size distribution per nucleation pulse overpotential, one can obtain the mean island radius r_{mean}. Figure 3.13a shows the mean island radius as a function of the corresponding island density for both batch 1 (red) and batch 2 (green). From this figure, it is clear that the mean island radius is determined by the island density, irrespective of the used nucleation pulse overpotential.

The mean island radius as a function of the nucleation pulse overpotential is

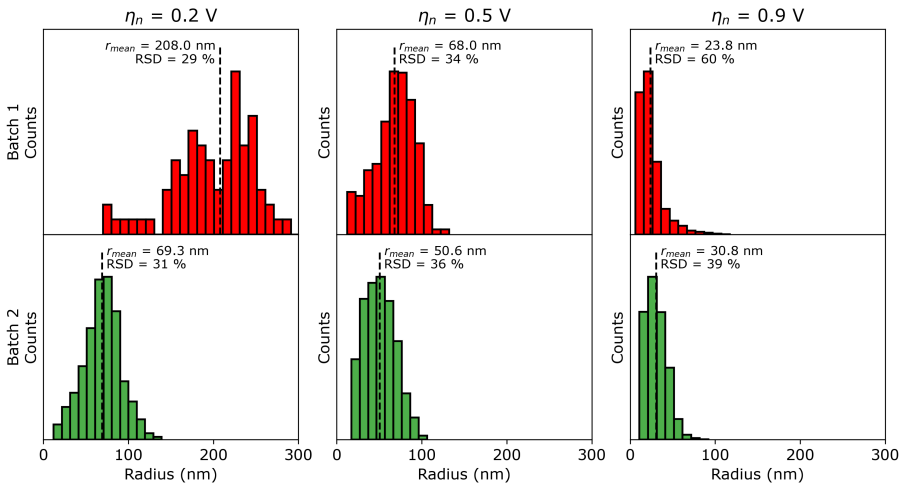

Figure 3.12: *Island size distribution for the selected samples as shown in figure 3.2. The first row shows the size distribution for batch 1 (red), and the bottom row for batch 2 (green). The mean of the distribution is indicated by the dashed black line and the value is reported next to it together with the relative standard deviation (RSD).*

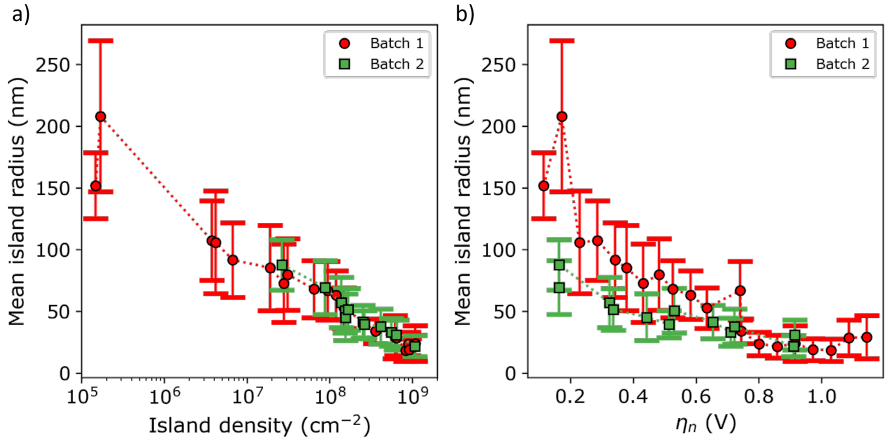

Figure 3.13: *Mean island radius as function of the a) island density, and b) of the nucleation pulse overpotential for batch 1 (red) and batch 2 (green). The error bars are the standard deviation of the mean values.*

shown in Figure 3.13b. The mean island radius of batch 1 decreases with increasing nucleation pulse overpotential up to a value of 0.8 V, after which it stays constant. A similar trend for batch 2 is observed, although it is not clear whether batch 2 also reaches a constant value due to the lack of data points.

3.5.5 Transferred charge calculation

The total transferred charge can be calculated in two ways. The first and simplest method is by integrating the current to obtain the total amount of transferred charge Q:

$$Q = \int i(t)dt \tag{3.7}$$

The second method is by combining the obtained island density with the mean radius of the particles as seen in Figure 3.13a. From these parameters, one can calculate an effective volume by assuming that the islands are spherical.

$$V_{est} = \frac{4}{3}\pi\langle r\rangle^3 N = \frac{4}{3}\pi\langle r\rangle^3 \rho A\,, \tag{3.8}$$

where $\langle r\rangle$ is the mean radius of the islands, and N is the total amount of islands which can be obtained by multiplying the island density ρ with the total exposed area A (0.95 cm^2). The total amount of deposited volume can then be converted into a expected transferred charge by using the constant of Faraday F, the molar mass M_{Ag} and density ρ_{Ag} of silver. The total expected transferred charge can then be calculated by:

$$Q_{exp} = \frac{V_{est} F \rho_{Ag}}{M_{Ag}}. \tag{3.9}$$

Figure 3.14a shows the amount of transferred charge (deposited silver) and Figure 3.14b shows the amount of expected transferred charge as a function of the island density, where samples from batch 1/2 are shown as circles/squares. Here, the shade of red/green of each data point indicates the nucleation pulse overpotential that was used for that sample.

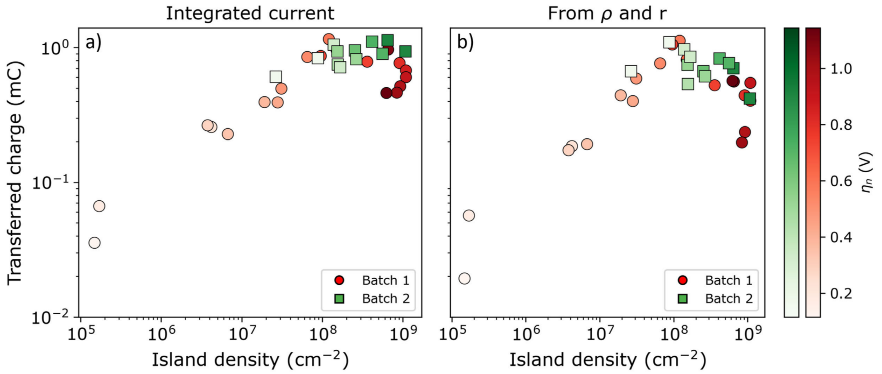

Figure 3.14: *a) Total transferred charge, obtained from integrating the current, as function of island density, and b) the total equivalent transferred charge, obtained from the island density and mean radius, as function of island density. The colour bar indicates the used nucleation pulse overpotential for batch 1 (red) and batch 2 (green) samples.*

In batch 1 samples, which exhibit a large spread in the island density for this nucleation potential range, two growth regimes can be discerned. At low island densities (i.e., below 10^8 cm^{-2}), the amount of transferred charge increases with island density. This behaviour agrees well with an uncoupled growth regime, where each silver island grows independently with an unrestricted supply of Ag^+ ions. By contrast, once the island density increases beyond 10^8 cm^{-2}, ion diffusion becomes restricted by neighbouring islands, which leads to the diffusion-coupled growth regime. Given the consistently larger density of silver islands in batch 2 samples, the silver island growth is always in the diffusion-coupled regime in agreement with the behaviour observed in batch 1 samples with similar island density.

3.5.6 Nearest Neighbour distance analyses

In the nearest neighbour distance (nnd) analyses, the distances between each island and its nearest neighbour is compared to the expected values for a spatially random point pattern to determine if the sample obeys complete spatial randomness (CSR). For a random point pattern, the nnd distribution should follow a Poisson distribution.

The SEM images were treated as described in Section 3.5.3, from which the centroid of each island was extracted for all individual SEM images. The nnd was calculated by finding the minimum distance between the centroid of a given island and the centroid of all the other islands present in that image. In order to get a decent number of points for the histogram, the nnd of multiple SEM images per sample were combined to a single nnd histogram. The bin size of the histograms is not relevant for the calculation of the Z-score (see eq 3.6), since only the mean value of the nnd distribution is used. Hence, the number of bins was chosen to be 14 for the histograms shown in Figure 3.4a) to c).

The probability density function (pdf) for a random pattern (Poisson distribution) is derived in the work of Guo *et al.*,[155] and is summarised below:

The probability of finding n particles in an area $A = \pi r^2$ is given by:

$$f(n) = \frac{(\rho A)^n}{n!} \exp(-\rho A) = \frac{(\rho \pi r^2)^n}{n!} \exp(-\rho \pi r^2) \tag{3.10}$$

where ρ is the island density (assumed to be zero-volume particles).

To derive the pdf for the first order, one needs to consider the probability of finding no particles within an area of radius r from an arbitrary particle. This probability of finding zero particles within a radius r is given by (n=0):

$$f(0) = \exp(-\rho \pi r^2) \tag{3.11}$$

Therefore, the probability of finding at least one particle between a radius r and $r + dr$ is then given by:

$$P(r) = 1 - f(0) = 1 - \exp(-\rho \pi r^2) \tag{3.12}$$

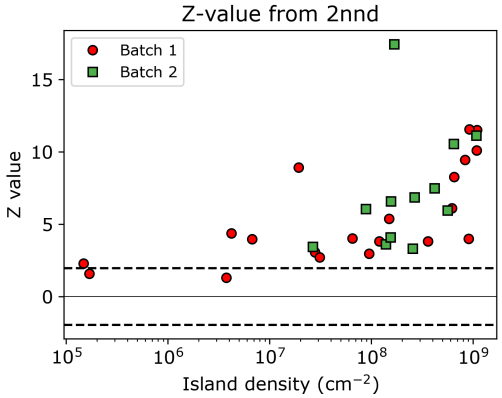

Figure 3.15: *Z-value obtained from individual second nnd distributions as function of the island density. Samples from batch 1 and 2 are indicated by red circles and green squares, respectively. The black horizontal dashed lines indicates the region for which the distribution of islands exhibit CSR.*

At last the pdf $p(r)$ can be found by differentiating the equation above, and is given by:

$$dP(r) = p(r)dr = 2\pi\rho r \ \exp(-\rho\pi r^2)dr \tag{3.13}$$

To to derive the pdf for the second and higher orders, one needs now to consider the probability of finding at least two particles inside a radius r, which is given by:

$$P(r) = 1 - f(0) - f(1) = 1 - \exp(-\rho\pi r^2) - \rho\pi r^2 \ \exp(-\rho\pi r^2) \tag{3.14}$$

and hence,

$$\begin{aligned} dP(r) &= p(r)dr \\ &= 2\pi\rho r \ \exp(-\rho\pi r^2)dr + 2\rho^2\pi^2 r^3 \ \exp(-\rho\pi r^2)dr - 2\pi\rho r \ \exp(-\rho\pi r^2)dr \\ &= 2\rho^2\pi^2 r^3 \exp(-\rho\pi r^2)dr \end{aligned} \tag{3.15}$$

Once the pdf is known, the mean nnd and variance can be obtained by:

$$\begin{aligned} \langle r_{CSR}\rangle &= \int_0^\infty p(r) r dr \\ \sigma^2_{CSR} &= \langle r^2_{CSR}\rangle - \langle r_{CSR}\rangle^2 \end{aligned} \tag{3.16}$$

The Z-value is defined in the main manuscript. The Z-values as function of island density for the first nnd are shown in the main manuscript in Figure 3.5. The Z-values as function of the island density for the second nnd is shown in Figure 3.15. The trend of both graphs are similar, indicating that sample with a higher particle density do in general not obey CSR.

4

High Aspect Ratio Silver Nanogrids by Bottom-Up Electrochemical Growth as Transparent Electrode

In this chapter, we combine the double pulse method with substrate conformal imprint lithography to fabricate silver nanowire grids for the application of transparent conducting materials. We report a scalable selective area electrochemical method for the fabrication of interconnected metal nanonetworks. The presented method is based on a through-the-mask electrodeposition method, in which the mask is made using substrate conformal imprint lithography (SCIL). We find that the nucleation density of the silver nanoparticles is the key parameter for the successful homogeneous void-free filling of the template. We independently control the density of the silver nuclei and their growth by using the double pulse technique. The silver nanowire grids show high transmission (95.9%) and low sheet resistance (as low as 3.7 Ω/□), resulting into a superior Figure of Merit (FoM). Due to the bottom-up nature of this technique, arbitrarily high aspect ratio nanowires can be achieved and therefore decreasing the sheet resistance without affecting transmittance and carrier collection. The presented method can be generalised to the large-area nanofabrication of any well-defined nanostructure design of any metal transparent conducting material for multiple applications.

4.1 Introduction

Transparent conducting materials (TCMs) are critical components in numerous optoelectronic devices, such as displays,[220] smart windows,[221] touchscreens,[222] (organic) light emitting diodes (LEDs),[223] and solar cells.[78,89,224–226] As technology advances, high-quality TCMs are nowadays required to reduce power consumption in efficient optoelectronic devices. In solar cells, high-quality TCMs are essential to minimise power losses, particularly in those cells with the top layer having a short carrier diffusion length, such as amorphous silicon, silicon heterojunction (SHJ), perovskite, CIGS, or organic cells.[89,226–228] In most commercial applications, metal oxides, and in particular indium tin oxide (ITO), have been most widely used due to their high transmittance, good conductivity, and CMOS compatible fabrication.[78,226] However, indium is a rare element which should be replaced,[229] and after decades of optimisation, ITO has reached its fundamental limits for transparency and sheet resistance, where the two are linked by the ITO thickness.[230,231]

In recent years, metal nanowire (NW) networks have received strong attention due to their excellent conductivity and mechanical flexibility, which broadens the range of TCM applications to flexible optoelectronics.[232]

A wide variety of NW network geometries have been proposed in the context of solar cell applications, which can be designed to increase device performance by making use of nanophotonic effects such as (plasmonic) light trapping,[89,90,233] or spectral splitting for tandem devices.[91,234] Metal NW networks can be fabricated using solution-based processes that enable high-throughput large-scale manufacturing.[108] Random networks have been demonstrated by colloidal synthesis of NWs followed by drop casting.[94,235–237] As-deposited networks often result in poor electrical uniformity throughout the electrode, which is improved by subsequent thermal annealing.[94,235–237] Similar to ITO, colloidal-based NW networks suffer from a trade-off between transparency and resistance. Increasing the NW radius or density is used to reduce sheet resistance but reduces transparency at the same time.

On the other hand, increasing the aspect ratio of the NW cross-section offers the possibility to break this transparency-resistance trade-off. A reliable approach to fabricate arbitrary NW cross-sections is the use of lithography. Initial work demonstrated the high potential of periodic silver NW networks by using e-beam evaporation and lift-off. While post-annealing is not necessary for a low junction resistance, this method still suffers from complex and expensive fabrication and is limited to small NW heights (i.e., low aspect ratio of the NW cross-section) to avoid lift-off issues.[89,231,238,239]

On the contrary, template-assisted electrodeposition combines solution-based processing with well-defined bottom-up patterning without the need for lift-off. In template-assisted electrodeposition, tailored made trenches in an insulating mask are conformally filled from the bottom up. Metal microwire grids have been demonstrated by this method, where the original template mask can be even reused multiple times by carefully peeling off the metal grid.[140,240] However, as the trenches are scaled down to the nanoscale, achieving uniform, void-free filling over a large

area without a seed layer remains a challenge.[241]

In this work, we demonstrate the fabrication of highly performing TCMs by combining substrate conformal imprint lithography (SCIL) with electrodeposition as a scalable and sustainable method for the large-scale fabrication of sub-100-nm metal nanostructures. It has been shown that SCIL can be used for imprinting both rigid and flexible substrates up to an area of a 200 mm wafer with sub-10-nm resolution.[148] First, SCIL is used to make an insulating template consisting of a grid of deep nano-trenches (80 nm in width and up to 300 nm in depth). Subsequently, these nanotrenches are selectively filled with silver by electrodeposition. Using this method, we obtain NW grids with tailored aspect ratio wires (height to width ratio up to ~ 3.5). We show that the high aspect ratio silver NW grids have a superior Figure of Merit, where we improve the sheet resistance without affecting transmittance and carrier collection. This template-assisted electrodeposition method is therefore a more sustainable method, enabling wafer-scale manufacturing of highly performing TCMs.

4.2 Results and Discussion

The fabrication of the high aspect ratio silver NW grids is schematically shown in Figures 4.1a-c. First, a PMMA/sol-gel mask on an ITO substrate was made using Substrate Conformal Imprint Lithography (SCIL). Note that ITO was used here as a proof of concept, but any other conductive substrate can be used, including doped silicon (see Chapter 6). Alternatively, subsequent peel-off and transfer of the nanowires to another substrate may be considered.[240,242] To pattern the mask, the sol-gel layer is imprinted with a PDMS stamp with the desired grid geometry and is then transferred to PMMA using a reactive ion etch (RIE) until the substrate is exposed. The PMMA/sol-gel stack determines the final depth of the trench, which in this work is typically around 300-350 nm (aspect ratio ~4). Here, we used two different stamps with square grids of 80 nm-wide nanowires and a pitch Λ of either 2 μm or 4 μm. Both stamps have an imprint area of 2.0×2.0 cm^2. After imprinting, the nanosized trenches are filled with silver using electrochemical deposition using a commercial silver plating solution (see Experimental Section). The growth area is restricted to an area of 0.95 cm^2 by the O-ring used in the electrochemical cell.

To achieve high-quality, homogeneous, and void-free NW grids, we use the double potential pulse technique to independently control the nucleation density and the grain growth rate.[166] More details on the nucleation mechanism of silver on ITO substrates can be found in Chapter 3. For a complete filling, the nucleation density must be sufficiently large ($> 2 \cdot 10^9$ cm^{-2}) such that the coalescence thickness is smaller than the depth of the trench, as schematically represented in Figure 4.1d. On non-wetting substrates, a high nucleation density is achieved by applying a high overpotential ($E_n = -0.96$ V) over a short period of time. Once the grids are filled with small silver nuclei, a small overpotential ($E_g = -0.06$ V) is applied to slowly and uniformly grow the nuclei until they coalesce into a connected grid. The height of the grid is then determined by the duration of the growth pulse.

An SEM image of a typical electrochemically-grown silver NW grid is shown in Figure 4.1e. The grid is highly uniform over large areas (see Section 4.5.2 of the Supplementary Information). The inset of Figure 4.1e shows that the edges of the individual wires are straight and well defined, suggesting a highly conformal filling (for more evidence of conformal filling, see Section 4.5.3 of the Supplementary Information). We note that in some cases small voids can be found at the bottom of the grid owing to the limited density of silver nuclei. More interestingly, from the close-up SEM image, one can also see that the intersections of the individual wires consist of a continuous deposit. This suggests that no additional resistance is expected at the junctions.

The SEM width as a function of height is shown in Figure 4.2a. We find a clear linear increase in width as a function of height, consistent with the trapezoidal trench profile. By extrapolating the width to zero height, we find that the base width of the trapezoid is 80 ± 3 nm and 78 ± 3 nm for the 2 μm and 4 μm samples,

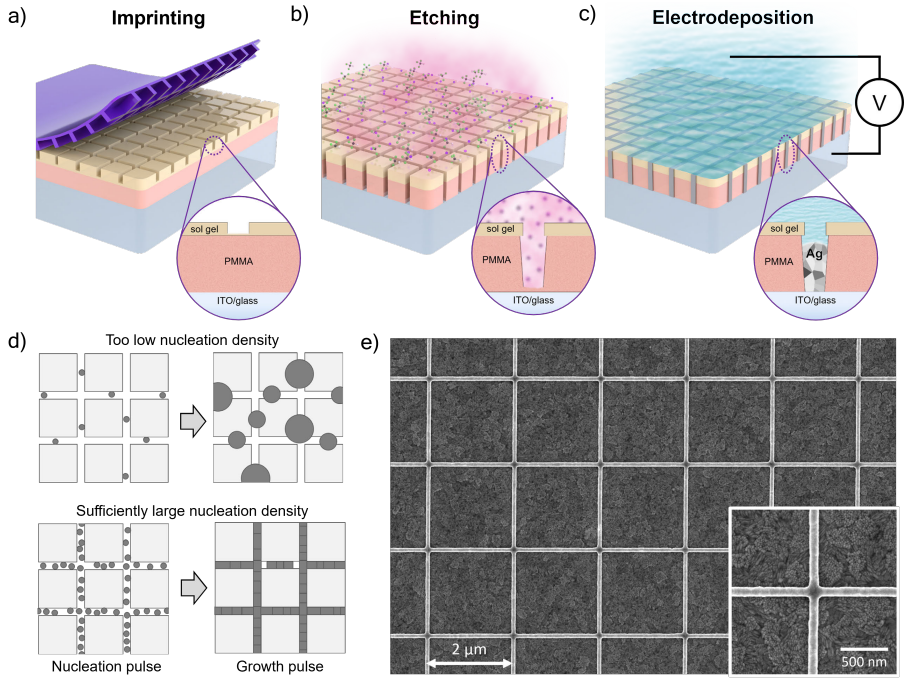

Figure 4.1: *a) Schematic representation of the SCIL imprinting procedure. b) Schematic representation of the RIE of the mask to etch the residual layer of the sol-gel and transfer the pattern to the PMMA layer. c) Schematic representation of the electrochemical filling of the trenches. d) Schematic representation of the influence of the nucleation density. The top and bottom rows show the effect of a too low and sufficiently large nucleation density, respectively. e) SEM image of a typical template-assisted electrodeposited silver NW grid having a pitch of 2 µm. The inset shows the crossing of two NWs in more detail.*

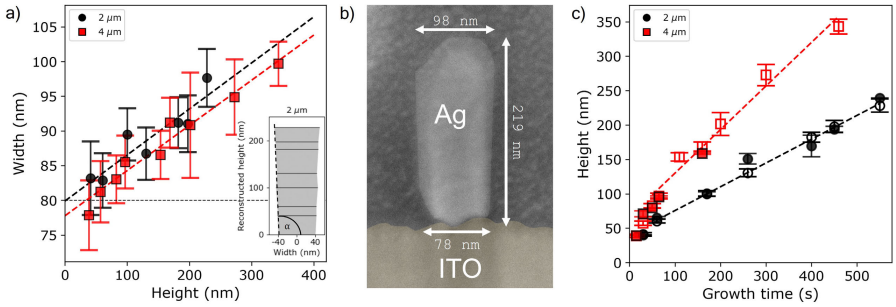

Figure 4.2: *a) Width of the wires as seen from the top (SEM) vs. the grid height obtained from the transferred charge for a pitch of 2 μm (black circles) and 4 μm (red squares). The inset shows the reconstructed height profile for the 2 μm pitch, including the definition of the inner angle α. The error bar corresponds to the standard deviation of the Gaussian fit to the width distribution obtained from the SEM images. b) Cross-sectional SEM image of a silver NW grid having a pitch of 2 μm, height of 219 nm, top width of 98 nm and base width of 78 nm. The inner angle α between the ITO substrate and silver NW is 92.6°. c) Height of the silver NW grids vs. the growth time for a pitch of 2 μm (black circles) and 4 μm (red squares). The height obtained from AFM and the transferred charge are represented by closed and open markers, respectively. The error on the height obtained from the transferred charge method is propagated from the error on the width, and the error on the height obtained from AFM is the standard deviation of the Gaussian fit the to height distribution.*

respectively, which agrees well with the nominal width of the stamp of 80 nm. The reconstructed silver NW grid height profile from the width-vs-height measurements is shown in the inset of Figure 4.2a. The inner angle α of the reconstructed height profile is calculated to be 93.8 ± 1.4° and 93.7 ± 0.8° for the 2 μm and 4 μm samples, respectively.

The cross-sectional SEM image of a NW is shown in Figure 4.2b. Due to the non-perfect anisotropic plasma etch of the PMMA layer, the trench has a slight trapezoidal profile (i.e., narrow at the bottom, wide at the top, and a characteristic inner angle $\alpha > 90°$) that is followed by silver filling. The inner angle α extracted from the cross-sectional SEM image is found to be $\alpha_{SEM} = 92.6°$, which is highly consistent with that calculated from the reconstructed height. As such, the width extracted from SEM images by using an edge detection algorithm always results in a value slightly larger than the nominal width from the stamp (80 nm), and this value increases as the grid grows taller.

To assess the growth rate and the effect of the geometry of the grid, we plot the grid height as a function of the growth time as shown in Figure 4.2c. The height of the electrochemically deposited silver NW grids was determined using two methods. The first method calculates the height based on the total charge transferred during the electrochemical deposition. Here, we assume a Faradaic efficiency of 100% for the silver deposition and homogeneous growth across all the electrochemical active areas, as such it serves as an upper limit for the height (for more details see Section

4.5.4 of the Supplementary Information). The second method is by using atomic force microscopy (AFM), for which the PMMA/sol-gel mask was removed. Mask removal is unfortunately not easy for tall NWs (> 200 nm). For samples where lift-off was unsuccessful, the height is only estimated from the integrated electrical charge during electrochemical deposition.

Figure 4.2c shows that both the height from AFM and that from the charge agree well with each other (validating the near 100% Faradaic efficiency and homogeneous deposition) and scales linearly with growth time. At the early stages of growth (growth time < 50 s), the height increases rapidly with time, indicative of the still 3D diffusion-limited growth of individual nuclei. Under this condition, homogeneous growth does not hold and there might be a higher discrepancy between the height values obtained from the two methods.

Once coalescence is reached (growth time >50 s), the growth rate (given by height vs. time slope) stabilises to a constant value, which is highly dependent on the geometry of the grid. Note that under the same growth conditions, the growth rate for the 4 μm pitch samples (0.64 nm/s) is almost twice as large compared to that of the 2 μm samples (0.35 nm/s). The increased growth rate in the sparser grid is explained by the reduced ion competition between neighbouring grid lines. In either case, we can tune the aspect ratio of the tailored NW grid from ~0.5 up to ~3.5, within a maximum growth duration of 500 s. Knowing the trench geometry, the highly reproducible and homogeneous growth enables in-situ monitoring the grid height by using the total transferred charge.

Now, we focus on the functional performance of the NW grids as TCMs. First, we investigate the electronic characteristics. We focus on the resistivity ρ, as it is important not only for the electronic performance of the electrodeposited grids, but also for assessing material quality. We obtain the resistivity from the sheet resistance of the silver NW grid $R_{\square}^{Ag}$ by using $\rho = R_{\square}^{Ag} \times h_{eff}$, where $h_{eff} = hw/\Lambda$ is the effective thickness of an equivalent silver film. Here, h is the height of the NW obtained from the charge measurement, w is the average width of the NW, and Λ is the pitch of the grid. $R_{\square}^{Ag}$ is in turn obtained by measuring the sheet resistance of the ITO substrate and ITO+silver NW grids using the van der Pauw configuration just before and after the electrochemical filling of the trenches, respectively (see the Experimental Section for more details). The two contributions (ITO and silver grid) are decoupled by assuming two parallel resistors. For more information on the measurement and sheet resistance calculation, see Section 4.5.1 of the Supplementary Information.

Figure 4.3 shows the normalised resistivity as a function of the silver NW grid height. We find that the resistivity of all samples follows the same monotonic increase with decreasing height, irrespective of pitch, which is consistent with the fact that electrons in smaller NWs will suffer from increased surface scattering. As a check, we consider the model for the resistivity that includes both inelastic scattering with the surface and scattering at grain boundaries described by the models of Fuchs and Sondheimer[243,244] and Mayadas and Shatzkes,[245] respectively. The combined

model results into:[246,247]

$$\frac{\rho}{\rho_{Ag}} = \left[1 - \frac{3}{2}\alpha + 3\alpha^2[1 - \alpha\ln(1+1/\alpha)]\right]^{-1} + \frac{3}{8}C(1-p)\frac{w+h}{h}\frac{\lambda}{w} \tag{4.1}$$

where ρ_{Ag} is the bulk resistivity of silver (1.59 $\mu\Omega$·cm), $\alpha = \frac{\lambda}{d}\frac{R}{1-R}$ is a scattering factor, d is the average grain diameter, λ is the electron mean free path (52-58 nm for Ag)[108,248,249], R is the electron reflectivity coefficient (e.g., fraction of electrons that are scattered by grain boundaries between 0 and 1) and C is a geometric constant which is 1.2 for nanowires with a rectangular cross-section.[247,250] The parameter p is the fraction of electrons that are specularly scattered at the NW surface.

To determine the average grain diameter d, we use the position and full width half maximum (FWHM) of the Ag(111) X-ray diffraction (XRD) peak in combination with the Scherrer equation (see Section 4.5.5 of the Supplementary Information).[108,202,251] Due to the overlap of the Ag(111) peak with that of the ITO, we have grown additional samples on thinner ITO substrates ($R_{\square}$ =100 $\Omega/\square$). The silver NW grids grown on thin ITO substrates are represented by the green triangles in Figure 4.3 and show comparable resistivity values for the given grid height.

From the XRD analysis, we obtain an average grain diameter d of 32 ± 2 nm, which is much smaller than expected from the nucleation density (i.e., average distance between nuclei is ~130 nm for a nucleation density of $\approx 7 \cdot 10^9$ cm^{-2}). This result suggests that re-nucleation takes place during growth, resulting in a smaller average grain diameter. Kung *et al.* found a similar average grain diameter, using the same electrolyte for the electrodeposition of silver NWs.[202]

Using the average grain diameter from XRD and the average NW width, Equation 4.1 is fitted to the resistivity data in Figure 4.3 (represented by the blue dashed line)

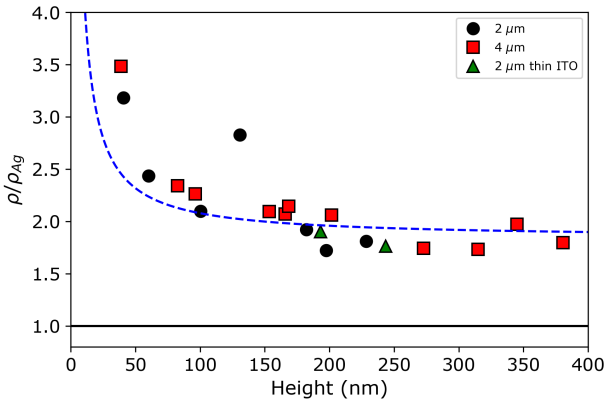

Figure 4.3: *Normalised resistivity vs. the height of the silver NW grids as obtained from the transferred charge for a pitch of 2 µm (black circles: thick ITO, green triangles: thin ITO) and 4 µm (red squares). The dashed blue line represents the best fit to the electron scattering model using the parameters $\lambda = 58$ nm, $w = 94$ nm, $R = 0.20$, $p = 0$ and $d = 32$ nm.*

with fit parameters being $R = 0.20$ and $p = 0$. The latter indicates that electron surface scattering is completely diffuse, which is typical for rough surfaces.[252] As the surface scattering contribution is most relevant in shallow silver NW grids, where the surface is roughest, it is not surprising that the fit leads to $p = 0$.

From our data and the model, we see that surface scattering is responsible for the strong increase in resistivity for silver NWs with an aspect ratio ≤ 1.5, and it stabilises to a constant value of $\rho/\rho_{Ag} \approx 1.7 - 1.8$ for NW aspect ratios ≥ 2.3. This result highlights not only the high quality of our deposits (resistivity less than 2 times that of bulk silver), but also the need for high aspect ratio NWs.

Now we turn our attention to the optical properties of the silver NW grids. The transmission of the silver NW grids is obtained by normalising the experimentally obtained transmission spectra of the silver NW/ITO/glass by the experimentally obtained ITO reference spectra of each corresponding sample (for more details see the Experimental Section). The normalised transmission spectra for three different grid heights of the 2 μm series are shown in Figure 4.4a. Despite the strong diffracting nature of the sample, no diffraction signatures are observed in the transmission spectra for all heights. This is most likely due to the fact that we use a focused non-coherent, non-polarised light source. In general, it is found that the transmission is quite flat over a broad spectral range of 500-1200 nm, which uniformly decreases for increasing grid height. The dip in the normalised transmission spectra around 400 nm may be attributed to the increasing contribution of the surface plasmon resonance (SPR) of individual silver NWs (for more details see Section 5.3 in Chapter 5). The overall trend of decreasing transmission with increasing height is also reflected in the average transmission obtained by taking the AM1.5G spectrum weighted average of the individual transmission spectra over the spectral range of 350-1200 nm (see Figure 5.7 in Chapter 5). The decreased average transmission

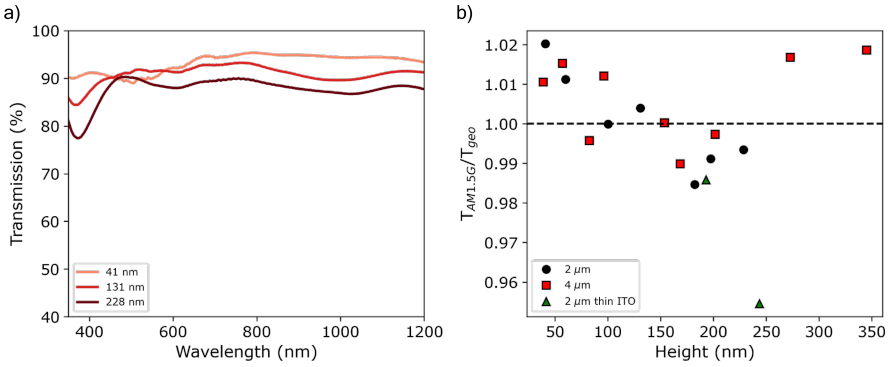

Figure 4.4: *a) Normalised transmission spectra for a pitch of 2 µm for three different heights (41, 131, and 228 nm). b) The ratio of the AM1.5G weighted transmittance spectra $T_{AM1.5G}$ by its geometric shading T_{geo} for a pitch of 2 µm (black circles: thick ITO, green triangles: thin ITO) and 4 µm (red squares).*

in taller grids is mainly the result of the increased shading of the grid due to the trapezoid shape of the wires (i.e., taller wires are wider). Figure 4.4b shows that the average transmission is indeed very similar to that expected from geometric shading, where $T_{geo} = (\Lambda - w)^2/\Lambda^2$, with w and Λ being the width and pitch of the grid, respectively.

Finally, we compile both the optical and electronic characteristics in the typical transmittance vs. sheet resistance plot as shown in Figure 4.5. Here, we also include the used ITO substrate and several other silver NW networks from the literature for reference. In all the previous works with colloidal-based NW networks, there is a clear trade-off between transparency and sheet resistance. Namely, resistivity is reduced at the expense of transparency by introducing either wider or more NWs. Similarly, the thickness is the main tuning knob for adjusting sheet resistance in ITO, which has a direct impact on its transparency.

On the contrary, our approach reduces the sheet resistance through anisotropic addition of material only in the vertical direction, keeping the optical footprint (almost) untouched. As such, the transmittance of the grids and the carrier collection are not significantly affected by decreasing the sheet resistance. While the average transmittance is tuned by the grid filling fraction ($\propto w/\Lambda$), the sheet resistance is

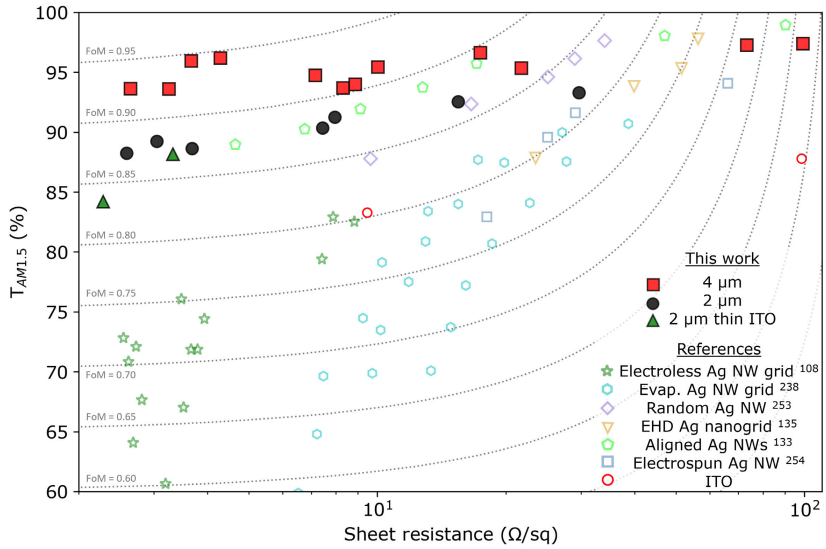

Figure 4.5: *Performance characterisation of the silver NW grids including similar systems found in literature (electroless silver nanogrids,[108] evaporated silver nanogrids,[238] random silver NWs,[253] EHD printed silver nanogrids,[135] aligned silver NWs,[133] electrospun silver NWs[254]). The data from this work is represented by red squares, black circles, and green triangles for the 2 µm, 4 µm and 2 µm on thin ITO, respectively. Different values of the FoM are represented by the dashed gray lines.*

independently controlled by the NW aspect ratio (h/w). As such, by tweaking the aspect ratio in the 4 μm pitch grid between $\sim 0.5-3.5$, we cover about 2 orders of magnitude in sheet resistance with less than 3% absolute change in transmittance.

Comparing the performance of various TCMs is not straightforward. Often, only the sheet resistance and transparency (either at 550 nm or weighted by the AM1.5G spectrum) are specified. Two commonly used Figures of Merit (FoM) for TCMs are the Haacke FoM[113] and the Dressel-Grüner (DG) FoM.[114] The Haacke FoM considers the ratio of transparency (raised to the power of 10) by the sheet resistance. On the other hand, the DG FoM accounts for the electron response to electric fields, either dynamic (light) or static (voltage). While the sheet resistance is determined by electrical DC conductivity, the transmittance is determined by optical conductivity. Both the Haacke and DG FoMs hold only for thin films.[255] In grid-like networks, their value can be made arbitrarily large as the sheet resistance decreases by increasing the pitch and width proportionally. In this case, transparency is maintained while the sheet resistance is reduced. A more relevant FoM for comparing all kinds of TCMs is defined by Anand *et al.*, developed explicitly for assessing TCM performance in photovoltaic applications.[112] The FoM is based on the impact of sheet resistance and transmittance on the maximum attainable power according to the detailed balance limit:

$$FoM_{PV} = \frac{P_{MPP}(E_G, T(\lambda), R_{\square})}{P_{MPP}(E_G, T = 100\% \forall T, R_{\square} = 0.0001\Omega/sq)} \tag{4.2}$$

where the bandgap E_G of the absorber is taken to be the bandgap of Si (1.14 eV). The maximum power point P_{MPP} can be calculated by solving the single-diode implicit Shockley equation, where the short circuit current I_{SC} is calculated by considering the transmission spectra of the TCM weighted by the AM1.5G solar spectrum, and the series resistance of the device is determined by the sheet resistance of the TCM. More details about the calculation of the FoM can be found in Section 1.3.2 in Chapter 1.

FoM isolines are shown in Figure 4.5 as given by Equation 4.2. At low sheet resistance values, the output power of the device is limited by the total amount of absorbed photon. Therefore, for a specific solar cell configuration, improving transparency is more important than decreasing the sheet resistance at those low values ($< 10\ \Omega/\square$). Interestingly, most literature values exhibit a decrease in the exact FoM as the sheet resistance decreases, due to a significant decrease in transmission. On the contrary, our approach decreases the sheet resistance without compromising transmittance and carrier collection by maintaining a constant distance from the exciton generated in the active layer to the silver NW grid.

Table 4.1 summaries the performance of the best electrochemically grown silver NW grid (w = 99 nm, L = 4 μm, h = 345 nm), and that for similar other silver NW TCMs, as well as for 80 nm thick ITO, which is used as industrial standard.[224,226,238,256] From the table, one can clearly see how the electrochemically-grown silver NW grid largely outperforms all other nano-scale approaches. This result was obtained for the most sparse grid with the largest aspect ratio. We expect that even more sparse grids (i.e., larger pitch) and even higher aspect ratios will lead

	$R_{\square}$ ($\Omega/\square$)	$T_{AM1.5G}$ (%)	FoM Haacke ($m\Omega^{-1}$)	FoM DG	FoM_{PV}
This work	**3.7**	**95.9**	**179.9**	**2447**	**0.944**
Aligned Ag nanowires [133]	17.1	95.7	37.8	500	0.888
Cu micro grids [140]	0.03	86.6	7816.5	83321	0.866
Randomly dispersed silver NWs [253]	16.6	92.4	27.3	281	0.861
Evaporated Ag nanowire grids [238]	17.2	87.7	15.7	162	0.819
Electrospun Ag random nanowires [254]	29.0	91.6	14.4	146	0.810
Electroless filled Ag nanowire grids [108]	7.9	82.9	19.5	244	0.805
ITO (used in this work)	9.5	83.2	17.0	208	0.804
Electrohydrodynamic printed Ag nanogrids [135]	23.5	87.8	11.7	120	0.799
ITO (industrial standard) [238]	58.2	87.7	4.6	48	0.683

Table 4.1: *Comparison of different silver NW based TCMs reported in literature.*

to even higher FoM. However, at some point, potential mechanical and electronic stability issues of the grids must be considered.

It should be noted that Chen *et al.* demonstrated electrochemically grown Cu micro grids (L = 320 μm) using very large pitch distances that exhibit a very high Haacke and DS FoM. [140] However, as discussed earlier, the FoM of Haacke and DS can be made arbitrarily large by increasing the pitch. When looking at the PV specific FoM introduced by Anand *et al.*, despite the extremely low sheet resistance of the Cu micro grid, the power output of the solar cell is still worse than that expected by our nanowire grids. Furthermore, it is important to keep in mind that in solar cells the pitch distance will be limited to the diffusion length of the minority carrier of the underlying layer. Especially amorphous silicon, perovskite, CIGS or organic solar cells suffer from short diffusion lengths, [89,226–228] limiting the pitch only to tens of microns.

An additional potential advantage of silver NW grids with pitch distances of the order of the wavelength of light (up to a few microns) is that the grid adds in-plane momentum to the incident light that can help trap the light in thin-film solar cells. Smart geometric designing of the NW grid can thus have dual optical-electric functionality in thin-film solar cells.

4.3 Conclusion

In this work, we have demonstrated the large-area (0.95 cm^2) fabrication of highly performing transparent silver nanowire electrodes by using a combination of substrate conformal lithography and electrochemical filling. This lift-off free and bottom-up nature of this method has allowed us to grow grids with high aspect

ratio NWs, resulting in highly transparent (95.9%) and low sheet resistance (3.7 Ω/□) TCMs.

We show that by increasing the height of the silver NW, the grid resistance decreases while the NW grid footprint remains constant, without affecting carrier collection. We demonstrate that the FoM of our silver NW grids is precisely controlled by adjusting the grid height through the deposition time, resulting in a large PV specific FoM.

While in this work we have mostly focused on the silver NW grid transparency, the design can be taken a step further by incorporating smart optical functionalities, such as tailored diffraction and other forms of light steering. The presented method is highly scalable, and it takes advantage of the fact that nanoimprint lithography has been demonstrated in an industrial roll-to-roll process, and electroplating is a well-established industrial technology.

This approach can be generalised to the large-area nanofabrication of a wide range of metals and nanostructure designs, with the potential to be used for multiple applications. The main limitation of the method is the need for a conductive substrate, such as ITO, to enable the electrochemical deposition. Although grid transfer onto other substrates may be possible, we show that the grids are equally uniform and with the same material quality when grown on substrates of higher resistance (i.e., 100 Ω/□ ITO). Consequently, we infer that uniform silver NW grids can be grown directly on the emitter layer of a solar cell, as is shown in Chapter 6.

4.4 Methods

4.4.1 Preparation of the mask

Substrate Conformal Imprint Lithography (SCIL) was used for the fabrication of the mask. ITO substrates (KinTec, 10 Ω/□ and 100 Ω/□, 25x25 mm^2) were cleaned by brushing with soap and sonicated for 10 min in ultra-pure water, 10 min in acetone, and 5 min in isopropanol. The ITO substrates were cleaned for 1 min using an oxygen plasma (Oxford Plasmalab 80+, 50 W, 5 mTorr) to activate the surface. The PMMA (MW=950 A8 1:1 anisole, Kayaku Advanced Materials, Inc.) spacer was spin coated on the ITO substrate at 2000 RPM for 45s and was baked at 150 °C for 2 min. The surface of PMMA was activated using a 30 s oxygen plasma etch (Oxford Plasmalab 80+, 50 W, 5 mTorr). The sol-gel (T1100, SCIL Nanoimprint Solutions) was spin-coated on the PMMA layer at 2000 RPM for 10 s. The PDMS stamp was pushed into the sol-gel layer and removed after 6 min of curing at room temperature. The residual layer of the sol-gel at the bottom of the imprint was removed using a reactive ion etch using HF_3/Ar (Oxford Plasmalab 80+, 67 W, 15 mTorr) for 2 min and 30 s, and the PMMA was etched using O_2 plasma (Oxford Plasmalab 80+, 200 W, 5 mTorr) for 228 s. The final depths of the trenches are between 300 and 350 nm.

4.4.2 Electrochemical superfilling of the trenches with silver

A custom build PEEK cell of 24 mL volume was used, using a standard three-electrode configuration (see Figure 2.3 in Chapter 2). A Pt disc (exposed area 3.08 cm^2) was used as the counter electrode, and an Ag/AgCl electrode (leakless miniature ET072, EDAQ) was used as reference electrode. Before the start of each experiment, the miniature reference electrode was calibrated against a saturated Ag/AgCl reference electrode (XR300, Hach). All experiments were performed using an SP-300 Bio-Logic potentiostat.

A commercial silver plating solution (Clean Earth Solutions™, 45.220) was used for the electrochemical superfilling of the nanotrenches. The double pulse method was used to control the nucleation density and the growth rate of the wires independently. A nucleation pulse of $E_n = -0.96$ V vs Ag/AgCl was applied for $t_n = 750$ ms, followed by a growth pulse of $E_g = -0.06$ V vs. Ag/AgCl, with varying growth time t_g from 14 to 550 s.

4.4.3 Sheet resistance measurements

The sheet resistance $R_\square$ of the samples was obtained directly before and directly after the electrochemical deposition of silver, using the van der Pauw method. Four gold pins located at the bottom of the electrochemical cell were used to perform a 4 point probe resistance measurement using a SP-300 Bio-Logic potentiostat. A cloverleaf type of configuration was used, where 4 scratches were made on the ITO substrate to make sure that the current runs through the center region of the sample. For a more detailed description and calculation of the sheet resistance see section 4.5.1 of the Supplementary Information.

4.4.4 Mask removal

The PMMA/sol-gel mask was removed by submerging the samples (vertically orientated) in 40 °C acetone for >15 min, while stirring the solution with a magnetic stir bar.

4.4.5 Transmission measurements

The transmission spectra of the samples were obtained using a Perkin Elmer UV/VIS/NIR Lambda 750 integrating sphere. The transmission spectra of bare ITO/glass were obtained at an area of the sample where no mask and silver NWs were present, while the transmission spectra of the silver NW/ITO/glass were obtained in the center of the sample. The transmission spectra of purely the silver NW grids were obtained by normalising the silver NW+ITO/glass spectra by the ITO/glass reference spectra. The average transmission was obtained by taking a weighted average using the AM1.5G spectrum $\phi_{AM1.5G}(\lambda)$ given by:

$$T_{AM1.5G} = \frac{\int_{350nm}^{1200nm} T(\lambda)\phi_{AM1.5G}(\lambda)d\lambda}{\int_{350nm}^{1200nm} \phi_{AM1.5G}(\lambda)d\lambda} \tag{4.3}$$

The AM1.5G weighted averaged was taken over the spectral range of 350-1200 nm to exclude the strong absorption of the ITO/glass substrate.

4.4.6 Morphological characterisation

Morphological and structural characterisation of silver NW grids was performed using a FEI Verios 460 scanning electron microscope (SEM), operated at 5 kV and 100 pA, using a working distance of 4 mm. An edge detection Python algorithm was used to extract the width from the SEM images. First, a threshold was used to convert the SEM images into a binary image. Next, the width in pixels of the nanowires was extracted line by line for both the vertical and horizontal directions, and transformed into the width in nanometers by using the pixel size. The average width was obtained by extracting the expected value from a Gaussian fit to the combined width distribution of the horizontal and vertical nanowires. The error on the width is taken to be the standard deviation of the Gaussian fit.

Topographical maps were obtained with atomic force microscopy (AFM), using a Bruker Dimension Icon and a ScanAsyst-Air probe (Bruker, nominal tip radius 2 nm). The height of the wires was extracted by fitting a Gaussian distribution to the masked area corresponding to the wires on the AFM images.

4.4.7 X-ray diffraction

X-ray diffraction (XRD) was performed on silver NW grids on thin ITO substrates (100 Ω/□) using a Bruker D2 Phase diffractometer. The Cu K_α irradiation was operated at 30 kV and 10 mA. The substrates were scanned between 2θ = 36° and 40°, with 0.008° increment using a dwell time of 0.1 s. More than 40 scans were obtained to increase the signal-to-noise ratio. The XRD scans were corrected by subtracting the background and removing the $K_{\alpha 2}$ peak.

4.5 Supplementary Information

4.5.1 Obtaining resistivity by the decoupling the sheet resistance

The sheet resistance $R_\square^{Ag}$ of the samples was obtained directly before and directly after the electrochemical deposition of silver, using the van der Pauw method. Four gold pins located at the bottom of the electrochemical cell, as shown in Figure 4.6a, were used to perform a 4-point probe resistance measurement using a SP-300 Bio-Logic potentiostat. A clover-leaf type of configuration was used, where four scratches were made on the ITO substrate to make sure that the current runs through the center region of the sample. A representative sample after the filling of the trenches including the 4 scratches into the ITO substrate is shown in Figure 4.6b. The sheet resistance was calculated using the van der Pauw formula:

$$e^{-\pi R_{hor}/R_\square} + e^{-\pi R_{ver}/R_\square} = 1 \tag{4.4}$$

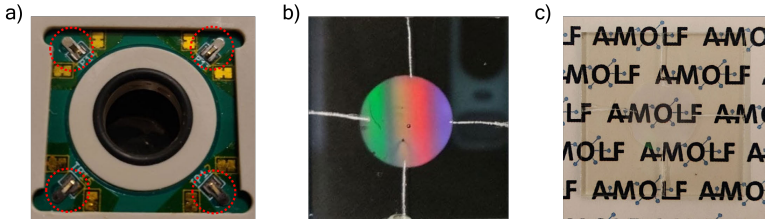

Figure 4.6: *a) Bottom of the electrochemical cell showing the O-ring (D=11 mm) and the 4 gold pins (highlighted by the dashed red circle) used for the van der Pauw measurements. Photograph taken under b) a slight angle and c) normal incidence of a representative sample after the filling of the trenches including the scratches in the ITO.*

By assuming that the ITO substrate and the silver NW grids are two parallel resistors, the sheet resistance of the bare silver NW grids could be calculated by:

$$R_{\square}^{Ag} = \left(\frac{1}{R_{\square}^{ITO+Ag}} - \frac{1}{R_{\square}^{ITO}} \right)^{-1} \tag{4.5}$$

The resistivity ρ of the wires was extracted from the sheet resistance using an effective height as if the grids were a film:

$$R_{\square} = \frac{\rho}{h_{eff}} \tag{4.6}$$

where $h_{eff} = hw/\Lambda$, where h is the height of the silver NW grids, w the average width of the trapezoidal shaped cross section, and Λ is the pitch.

Another method to extract the resistivity is by using Kirchoff's rules, where the total sheet resistance is the sum of the individual wires in the horizontal direction (resistors in series), normalised by the wires in the vertical directions (resistors in parallel).[238] The sheet resistance $R_{\square}$ for a NxN network is then given by:

$$R_{\square} = \frac{N}{N+1} R_{wire} = \frac{N}{N+1} \frac{\rho\Lambda}{wh} \tag{4.7}$$

For large N, this expression is identical to the effective height method.

4.5.2 Large area deposition

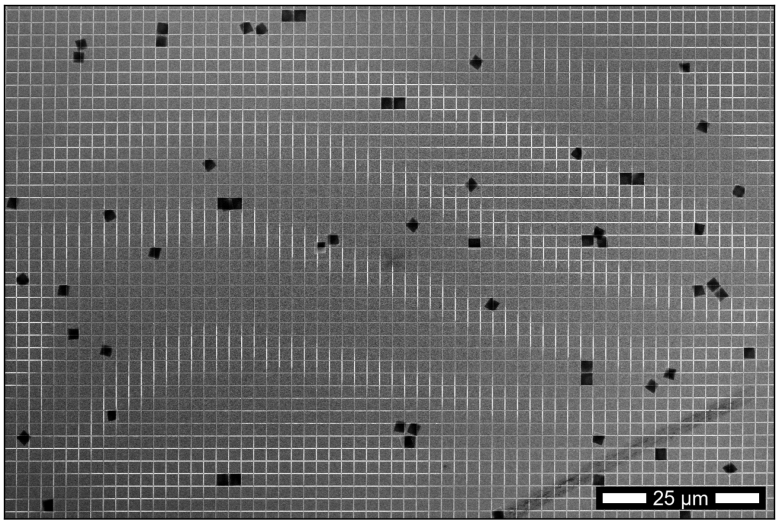

Figure 4.7: *Large area SEM image of a sample having a pitch of 2 µm and a height of 219 nm. The black spots on the sample are sol-gel slabs, which were redeposited during the removal of the template. The wrinkles in the contrast are Moire patterns due to the overlap of the grid with the pixels of the SEM detector.*

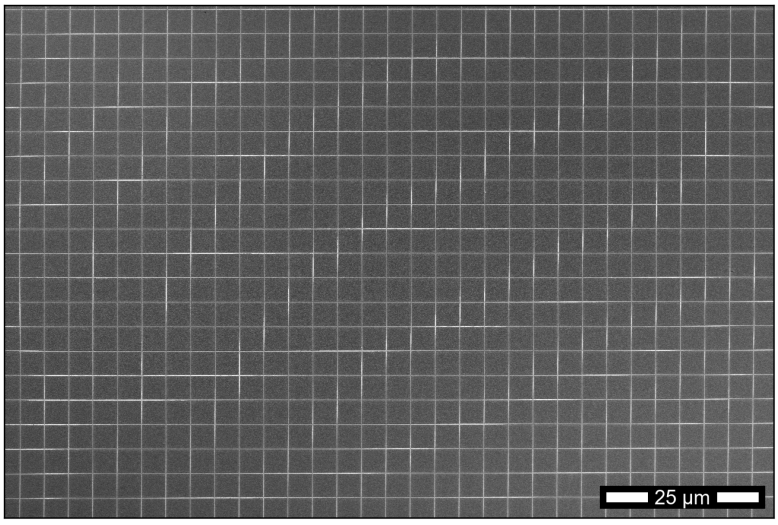

Figure 4.8: *Large area SEM image of a sample having a pitch of 4 µm and a height of 82 nm. In this area on the sample, all the PMMA/sol-gel slabs have been successfully removed. The wrinkles in contrast are Moire patterns due to the overlap of the grid with the pixels of the SEM detector.*

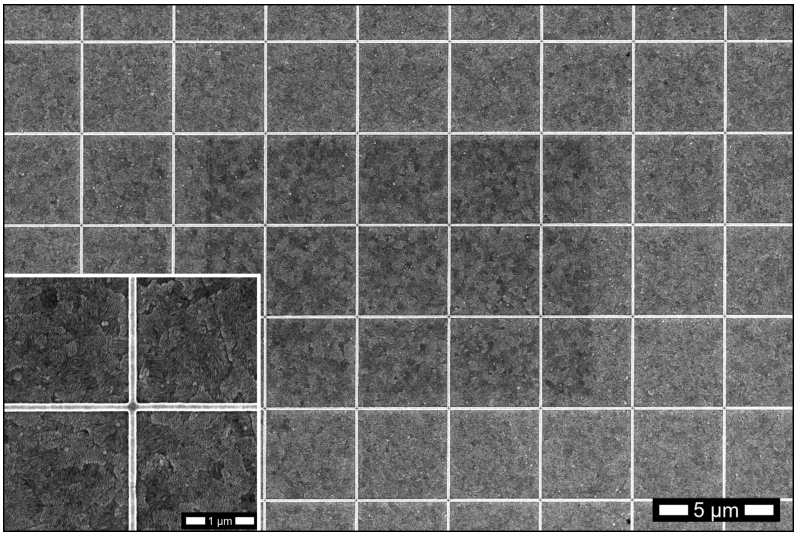

Figure 4.9: *SEM image of a typical template-assisted electrodeposited silver NW grid having a pitch of 4 µm. The inset shows the crossing of two NWs in more detail.*

4.5.3 Conformal growth

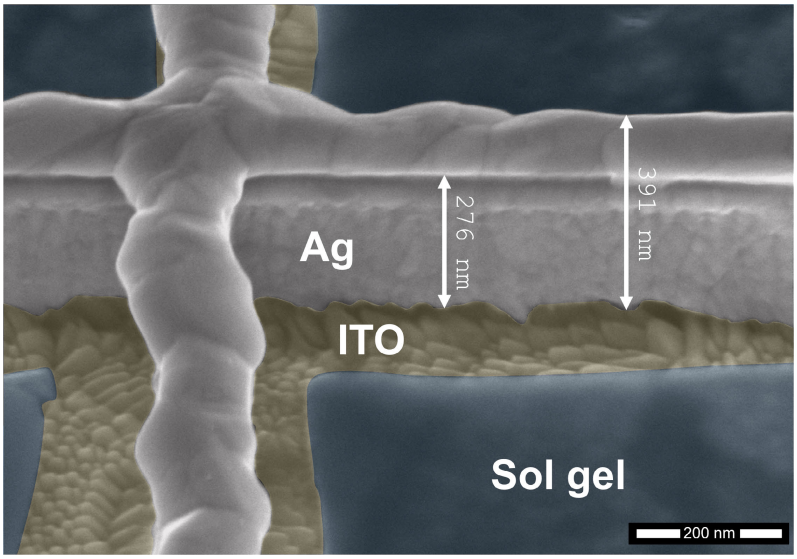

Figure 4.10: *False-coloured cross sectional SEM image of a sample with pitch 4 µm, taking with an image tilt of 45°. The silver, ITO and sol-gel are represented in gray, yellow and blue, respectively.*

Figure 4.10 shows a false-coloured SEM image of an overgrown sample with pitch 4 μm. In this false-coloured image, silver, ITO, and sol-gel are represented in grey, yellow, and blue, respectively. From this tilted SEM image, the conformal growth is clearly demonstrated. The horizontal wire shows three distinct regions. The first is a smooth wall whose smoothness is defined by the smoothness of the PMMA. On top of that, a darker region is observed, which is an indent in the silver NW. This indent is caused by the sol-gel layer, which has a slightly smaller trench width than the PMMA layer. Above the indent, the silver NW start to grow out of the trench, which results in a dome-like shaped deposit (unrestricted growth).

The reason behind this particular shape of the wire is represented in Figure 4.11. The non-isotropic reactive oxygen ion etch results in a slight undercut, meaning that the sol-gel layer is slightly extending further into the trench than the PMMA layer. The electrochemical filling of the trenches is a conformal process, so the deposit follows the shape of the template. After filling, the template is removed by dissolving the PMMA layer in acetone. However, due to the shape of the template, the sol-gel layer is trapped in the silver NW and therefore it is hard to remove the sol-gel. After the sample was taken out the acetone, the sol-gel layer collapses and redeposits onto the ITO substrate. The suggested indent in the silver NW is confirmed by the cross-sectional false-coloured SEM image shown in Figure 4.11d

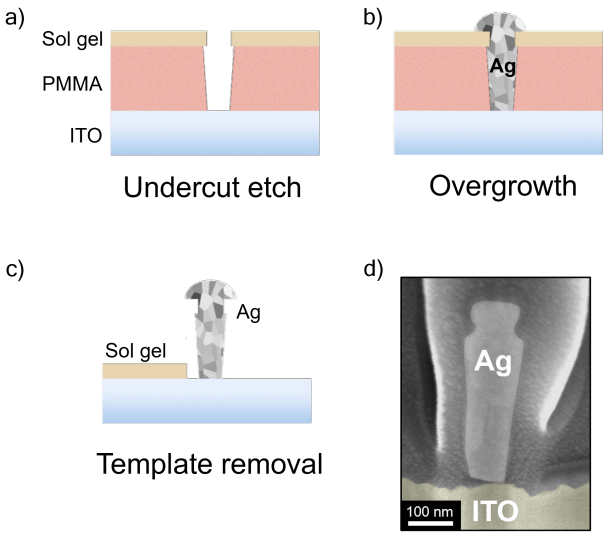

Figure 4.11: *Schematic illustrating the conformal growth. a) The non-isotropic reactive ion etch results into an undercut type of etch. b) The electrodepostion of silver is conformal until overgrowth. c) The template has been removed by dissolving the PMMA in acetone. Due to the encapsulation of the sol-gel by silver NW, the sol-gel layer could not by fully removed and falls down to the substrate. d) False-coloured cross section SEM image of a sample that was overgrown confirming the suggested cross-sectional shape.*

4.5.4 Extracting the grid height using the total transferred charge method

The total deposited charge Q is obtained by integrating the current over the deposition time, hereby assuming a Faradaic efficiency of 100%. Using the total footprint area of the silver NW grids A_{grids} (homogeneous filling), the Faraday constant F, the amount of electrons involved $n = 1$, molar weight MW_{Ag} and density of silver ρ_{Ag}, the height from the transferred charge can be calculated by:

$$h_Q = \frac{Q}{nFA_{grids}} \frac{MW_{Ag}}{\rho_{Ag}} \ , \tag{4.8}$$

where

$$A_{grids} = \frac{2\Lambda w_{ave} - w_{ave}^2}{\Lambda^2} A_{EC} \ , \tag{4.9}$$

where $A_{EC} = 0.95$ cm^2 is the electrochemical active area, w_{ave} and Λ are the *average* width and pitch of the silver NW grid, respectively. Since the cross sectional of the silver NW is not a perfect rectangle, the average width of the silver NW was used to obtain the total footprint area of the silver NW grids A_{grids}. The average width is obtained by taking the average of the width as seen from the top by SEM and the width at the bottom of the trench (found by extrapolating to zero time in Figure 4.2a). We therefore implicitly assume a trapezoidal shape of the wires in the calculation of the height using the total transferred charge.

4.5.5 Average Grain Diameter

The average grain diameter was obtained by XRD using thin ITO samples (100 Ω/□). The XRD scans were corrected by subtracting the background and removing the $K_{\alpha,2}$ peak. The average grain diameter was determined by the Scherrer equation:[108,202,251]

$$L = \frac{K\lambda}{\beta \cos(\theta)} \tag{4.10}$$

where L is the average grain diameter, $K = 0.9$ is the Scherrer constant, λ is the wavelength of the X-ray ($\lambda = 0.154$ nm for Cu K_α), β is the FHHM peak in radians, and θ is the Bragg angle (half of the 2θ peak position). The FHHM β of Ag(111) ($2\theta = 38.4°$) was corrected for the instrument broadening by using a Corundum reference sample using the peak at $2\theta = 37.8°$.

Author Contributions

D.L. and S.W.T. fabricated the master and stamp. Y.B., S.W.T. and A.C. fabricated the mask by using SCIL. Y.B. performed the electrodeposition of silver, optical, and electrical measurements. Y.B. performed all the data analysis. Y.B. and E.A.L. wrote the manuscript. E.A.L. supervised the project.

5

Optical Properties of Silver Nanowire Grids

In this chapter, we describe light-matter interactions in metal nanowire grids and their characterisation. We outline the origin behind characteristic spectral features in transmission and how these are affected by geometry and dielectric environment. We introduce the use of FDTD simulations to predict light transmission and absorption by the grids. We use the simulated data to explain our experimental observations and to validate the normalisation method to decouple light transmission of the silver NW grids from that of the substrate in the experiments.

The second part of this chapter discusses the use of in-situ bright field microscopy to monitor the nucleation and growth of the grid formation in-situ. We show that upon nucleation, the silver nanoparticles strongly absorb light, resulting in a sudden decrease in reflectance. As the nanoparticles grow larger and eventually coalesce, more light is scattered, which makes the grid pattern appear bright in the microscopy images.

5.1 Introduction

When light is incident on a metal, free electrons inside the metal respond to the oscillating electric field (E-field) of the electromagnetic wave.[257] The quantum of the collective oscillation of free electrons is called a plasmon. The characteristic plasma frequency is given by the density of free electrons. In metals, the characteristic plasma frequency is in the visible-UV, while in highly doped semiconductors it is in the far infrared.

Now consider a finite-sized metal object with diameter D. The metal object is fully reflective in the case where the wavelength is much smaller than its size ($\lambda << D$). On the contrary, the metal object is completely transparent when the wavelength is much larger than its size ($\lambda >> D$). In between these two cases, where the wavelength of the incident light is in the same order as that of the (nano)particle, a strong resonance can occur which is known as the localised plasmon resonance.

The extinction of light in these metallic nanoparticles is well described by Mie theory, which is an analytical solution to Maxwell's equations describing the scattering of light of a plane wave incident on a spherical homogeneous nanoparticle.[258,259] Figure 5.1a shows the absorption and scattering efficiency (ratio between the absorption/scattering cross-section σ and its corresponding geometrical cross-section σ_{geo}) of a silver nanoparticle for different diameters. Mie theory predicts that small nanoparticles strongly absorb light in an area that is much larger than its geometrical cross section, whereas large nanoparticles are strong light scatters. This optical phenomenon has many applications,[260–263] and is for example the reason behind the colours of stained glass.[264]

In the case of a NW, the excitation of localised plasmons is strongly dependent on the polarisation of the incident light, as the resonance can only occur when the electric-field (E-field) is polarised perpendicular to the main NW axis. The FDTD-simulated absorption and scattering efficiency for an infinity long silver NW

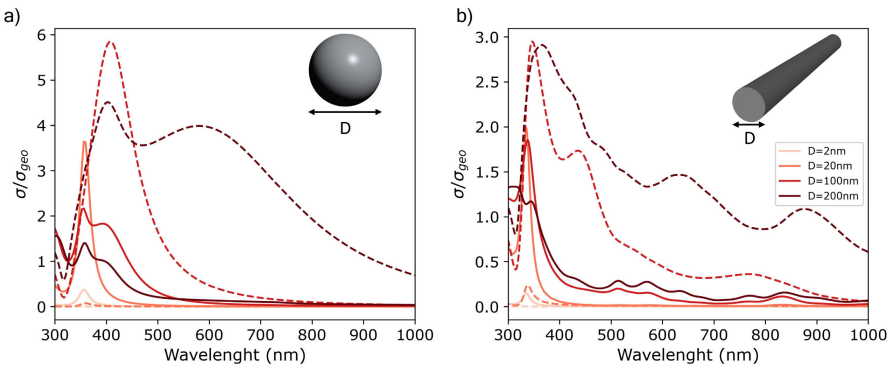

Figure 5.1: *Absorption (solid) and scattering (dashed) cross-section σ normalised by its geometrical cross-section σ_{geo} for a silver a) sphere and b) infinitely long wire in air for different diameters D. The E-field is polarised perpendicular to the infinity long NW.*

is shown in Figure 5.1b, having the E-field perpendicular to the NW. The plasmon response is similar to that described by Mie theory of a spherical particle, where NWs with a small diameter strongly absorb light and NWs with a large diameter strongly scatter light. Because the confinement in the NW is only in one dimension, the absorption/scattering efficiency of the NW is smaller compared to that of the spherical nanoparticle. In addition to the geometry of the NW, the frequency of the localised plasmon resonance is also affected by the dielectric environment of the NW.[265,266] The effect of the substrate on the plasmonic response in NW structures are described in a later section.

5.2 Finite-Difference Time-Domain (FDTD) simulations of silver nanowire grids

Finite-Difference Time-Domain (FDTD) is a 3D electromagnetic field numerical solver to model light-matter interactions.[267] FDTD belongs to grid-based differential numerical modelling methods (finite difference method), in which the time-dependent Maxwell's equations (in partial differential form) are discredited using central-difference approximations to the space and time partial derivatives. The time-domain offers covering a wide frequency range in a single simulation. The finite-difference equations are solved by first finding the electric-field (E-field) vector components in a simulation volume at a given time, after which the magnetic-field (H-field) vector components in the same spatial volume are solved at the next timestamp. This process is repeated until a certain amount of the input power has been dissipated, such that the transient or steady-state solution has fully evolved, as determined by the auto-shutoff level. The result of the FDTD simulation contains the steady-state vector field profiles for both the electric and magnetic components at all grid points in the simulation volume. The Poynting vector describing the power flow in the simulation can be calculated from the electric and magnetic field components.

5.2.1 FDTD setup

In this thesis, FDTD simulations were performed using Lumerical by Ansys.[268] Periodic boundary conditions were used to simulate an infinite network that has a span equal to the pitch of the silver NW grid. The optical constants for Si, Ag and glass were obtained from Palik,[269] the optical constant of ITO was obtained from König.[270] The refractive index of the background was set to unity. A broad band (280-1200 nm) plane wave of type bloch/periodic is used at normal incidence, while the type BFAST is used for non-normal incidence.

A typical layout of a 2D FDTD simulation of transmission through the silver NW/ITO/glass stack is shown in Figure 5.2. In this example, the E-field is polarised perpendicular to the NW (TE-polarised) as represented by the blue arrow. For these simulations, the power monitor that records the transmission of the full NW/glass/ITO stack was placed 1.22 μm below the ITO/glass interface and 100

nm above the end of the simulation box. On the x-boundaries (perpendicular to the propagation of light), perfectly matched layer (PML) boundary conditions with a steep angle profile were used to prevent any unwanted backscattering at the edge of the simulation box (represented by the orange box on top and on the bottom). On the y-boundaries, anti-symmetrical boundary conditions were used to split the simulation volume in half. A custom non-uniform mesh using the conformal variant 1 mesh refinement was used with a maximum mesh step of 10 nm. A finer mesh surrounds the silver NW having a mesh step of 0.5 nm (as indicated by the orange box around the silver NW). In the FDTD simulation, the semi-infinite glass does not include any absorption, as the k-values were set to zero. All simulated FDTD transmission spectra are corrected for the absorption of 1.0 mm thick BK7 glass.

5.2.2 Light transmission in silver NW grids

At normal incidence, the 2D nanowire grid may be regarded as the sum of two orthogonal 1D arrays of infinitely-long nanowires, as long as the two grids do not interact. Given that 3D simulations needed for a 2D grid are time and resource intensive, we investigate the validity of the two-1D grid approach, which requires two 2D FDTD simulations.

The two 2D simulations have the E-field polarised along (TM-polarised) and perpendicular (TE-polarised) to the NW. The combined transmission is based on the sum of the absorption by the two orthogonal arrays, corrected for the overlap (i.e. at the crossings) and by the additional reflectance by the substrate (i.e. note that substrate reflectance is accounted for twice). The combined transmission from 2D

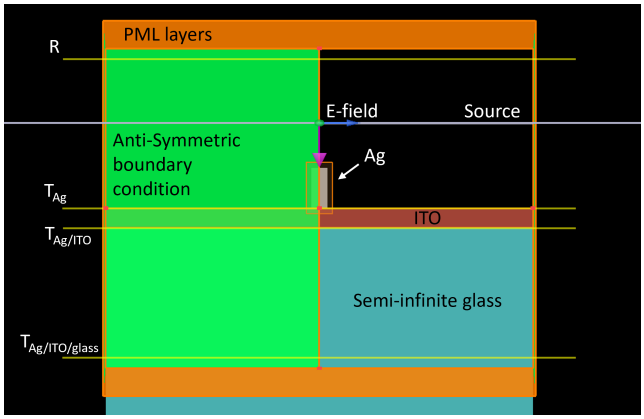

Figure 5.2: *Screenshot of the graphical user interface of the Lumerical software showing the setup for the FDTD simulation of a silver NW grid on ITO/glass having height of 201 nm, a width of 102 nm, and a pitch of 4 µm. The polarisation of the plane wave source is perpendicular to the silver NW (TE-polarised), as represented by the blue arrow.*

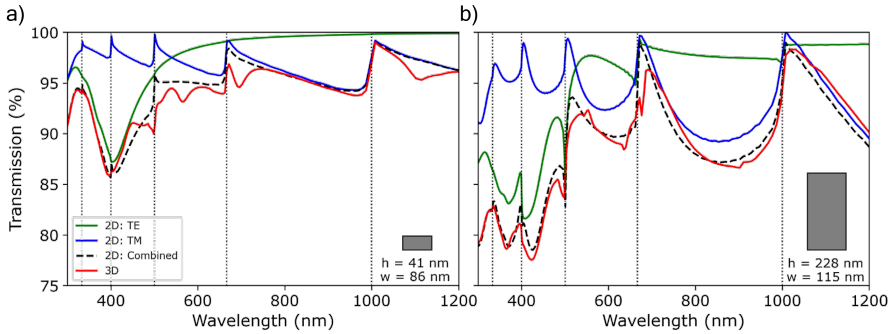

Figure 5.3: *Simulated transmission spectra with FDTD of an a) short and b) tall silver NW grid surrounded by air. The geometry of an individual silver NW is shown in the inset. The 2D simulations having TE and TM-polarisation's, are represented by the solid green and blue line, respectively. The approximated 3D spectrum is represented by the dashed black line. The spectrum obtained from the 3D simulation is represented by the red line. The horizontal dotted black lines represent the Rayleigh-Wood anomalies of the 1D grating.*

simulations at normal incidence is given by:

$$T_{tot} = 1 - \left(1 - \frac{w}{2\Lambda}\right)(2 - T_{\perp} - T_{//}) + \left(1 - \frac{w}{\Lambda}\right)\left(1 - T^{sub}\right) \tag{5.1}$$

where w is the NW width, Λ the pitch, T^{sub} is the transmission at the substrate/air interface, and $T_{\perp}/T_{//}$ is parallel/perpendicularly-polarised transmission of the silver NW grids including the substrate, respectively. Note that this approach can only be used for normal incidence.

Figures 5.3a and b compare the transmission spectra of two silver NW grids in air with different NW height obtained from either a 3D simulation (red line, 3 hour computation time for the tallest silver NW) or by adding the spectra of two cross-polarised 2D simulations (black dashed line, computation time about 5 min for the tallest silver NW). The two spectra are in very good agreement, where most spectral features in the 3D simulation are captured by the combined 2D one.

Looking closer at the two 2D simulations, we can also disentangle the contributions from each sub-grid. When the E-field is polarised perpendicular to the NW axis for a small NW height (green curve, labelled as TE in Figure 5.3a), a pronounced plasmonic resonance emerges at a wavelength of approximately 400 nm. The plasmon resonance is strongly dependent on the NW width. In contrast, the spectrum of the the TM-polarised transmittance (i.e. polarisation parallel to the NW long axis) does not reveal the strong plasmon resonance, as the "width" of the NW is now regarded as infinite. Instead, we observe the appearance of lattice modes or Rayleigh-Wood anomalies (RA). An RA is the interference between diffracted waves by the individual NWs in an array, the frequency of which is tuned by the grid periodicity Λ.[271,272] In momentum space, incident photons on a 2D grid gain additional momentum $|G_x| = |G_y| = 2\pi/\Lambda$. The RA occurs when the following

condition is satisfied:

$$\frac{2\pi}{\lambda_0}\sqrt{\epsilon_d} = |\mathbf{k}_0 \sin(\theta) + i\mathbf{G}_x + j\mathbf{G}_y| \tag{5.2}$$

where λ_0 is the wavelength in vacuum, $\mathbf{k}_0 \sin(\theta)$ is the in-plane momentum of the indecent wave having a length $|\mathbf{k}_0| = 2\pi/\lambda$, and ϵ_d is the relative permittivity of the dielectric surrounding, which can be expressed in terms of the refractive index for weak absorbing materials as $\epsilon_d = n^2$. Strong light scattering occurs at the wavelengths at which the RA occurs.

As shown in Equation 5.2, the wavenumber at which these anomalies occur depends on the refractive index of the surrounding medium, the momentum of the incident plane wave, and on the periodicity Λ of the grid. For the 1D silver NW grating surrounded by air, Equation 5.2 can be simplified to:

$$\lambda_i = \frac{\Lambda}{i} \tag{5.3}$$

The RA wavelengths are represented by the dotted black lines in Figure 5.3. The lines match perfectly with the sharp changes in transmittance of the TM-polarised spectrum, therefore confirming their RA nature. The strength of the RA is strongly dictated by the height of the NW grid. As the height of the silver NW is increased (see Figure 5.3b), the light-matter interaction increases, resulting in a more pronounced RA, overshadowing the plasmon resonance even in the TE-polarised spectrum.

The RA nature of the spectral features becomes more obvious when we look at the dispersion plot shown in Figures 5.4a-c, which show the transmittance of a 1D silver NW grating (having a width, height, and pitch of 86 nm, 41 nm, and 2 μm), as a function of the angle of incidence. The modes dispersion with angle is clearly visible, which follow the expected ones for RAs as represented by the red and black dashed lines. Similarly to Figure 5.3, the plasmon resonance is visible for all angles of incidence in the TE-polarised spectra, while it is absent for the TM-polarised dispersion. As a result of the plasmon resonance, the power of the indecent wave is stored for a longer period of time in the simulation volume for the TE-polarised simulations. For some particular angle of incidence, the simulations did not fully converge, as more than 10^{-5} times the initial power was still present in the system. This resulted in simulation artefacts that are clearly visible at an angle of incidence of 32°, where a clear black spot is visible around a wavelength of 1050 nm.

In the 1D grating, the RAs occur at an integer times the wavevector of the lattice (Equation 5.2). Combining the two orthogonal directions only accounts for the RA in the orthogonal directions $(\pm i, 0)$, with $i = 1, 2, 3, ...$, as highlighted by the red and black dashed lines in the combined dispersion plot in Figure 5.4c. However, the actual 2D grating also contains superimposed modes rising from the periodicity in the y-direction, such as $(i, j) = (1,1), (1,2), ...$ Combining the 2D TE and TM polarised transmission spectra using Equation 5.1 does not account for these superimposed modes. Therefore, the small differences around the wavelengths of about 500, 580, 680, and 1100 nm between the 3D and the combined 2D spectra (Figure 5.3) can therefore be attributed to these superimposed higher-order modes of RAs.

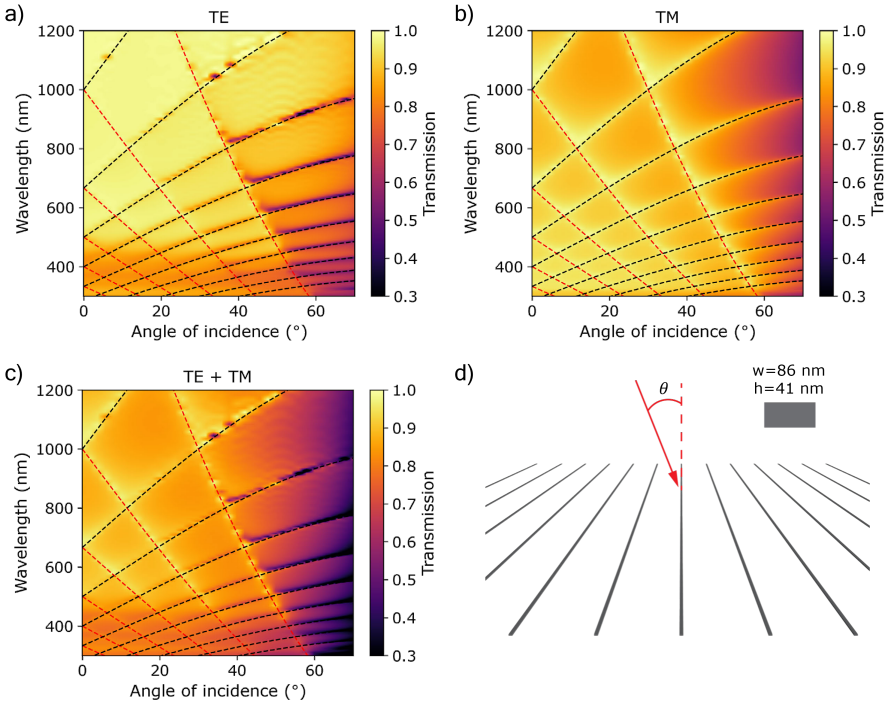

Figure 5.4: *Transmission through a 1D silver grating suspended in air as a function of the angle of incidence for the a) TE/perpendicular, b) TM/parallel, and c) combined polarisation. The grating has a height, width and pitch of 41 nm, 86 nm, and 2 µm, respectively. The* $(i,0)$ *modes and* $(-i,0)$ *modes are represented by the red and black dashed lines, respectively. d) Schematic of the 1D silver grating highlighting the used geometry and the angle of incidence.*

5.3 Substrate effects on transmittance

To further investigate the physical phenomena of the measured transmission spectra of silver NW grids on ITO/glass substrates, as discussed in Chapter 4, 2D finite-difference time domain (FDTD) simulations were performed. In these 2D FDTD simulations, the silver NWs have a width and height as extracted from SEM and AFM measurements and are either placed on 180 nm thick ITO with a semi-infinite glass substrate or surrounded by air. Figure 5.5 shows the experimental (red) and simulated (black) transmission spectra, for a pitch of 2 and 4 μm for a silver NW grid having a low and high aspect ratio (height over width). The spectra overlap quite well in the spectral range of 280 to 750 nm. However, for longer wavelengths, the measured spectrum shows a consistent lower transmission, which is explained by the difference in the optical constants between the experimentally used ITO and the theoretical values used in the FDTD simulations. The broad bands around 390, 460 and 620 nm in the simulated spectra correspond to thin film interference. These overlap well with those in the experimental spectra, validating the ITO thickness of

180 nm used in the FDTD simulations. The sharp spectral modulations appearing in the simulated spectra are attributed to the RA anomalies. Compared to the spectra of the grid in air from the previous section, the RAs are now less pronounced and have additional peaks due to the presence of substrate. These sharp features are not observed experimentally, which is likely due to the fact that a focused non-coherent, non-polarised light is used, resulting in a broadening of the features.

Figure 5.6 shows the simulated (solid black) and experimental (solid red) *normalised* transmission for the same silver NW grids as shown in Figure 5.5. Here, the transmission is normalised by the corresponding ITO/glass transmission spectra (i.e. without the grid). To validate this normalisation method, the transmission spectrum of the bare silver NW grid in air (dashed blue) is also included. Qualitatively, the normalised spectra and those calculated in air are in very good agreement. Looking closer, one can note several differences in the plasmon resonance region (i.e. around 400 nm) and also in the RAs. Remarkably, the plasmon resonance around 400 nm is not clearly prominent in any of the normalised spectra from the grids on ITO/glass, in contrast to what is observed in the spectra of the grids in air. This is due to the presence of the ITO substrate, which modifies the electric field along the edges of the silver NW, thereby blue shifting and damping the plasmon resonance. Yet, increasing silver NW height enhances the plasmon resonance excitation, given by the increased absorption in the blue spectral range. On the other hand, the Rayleigh-

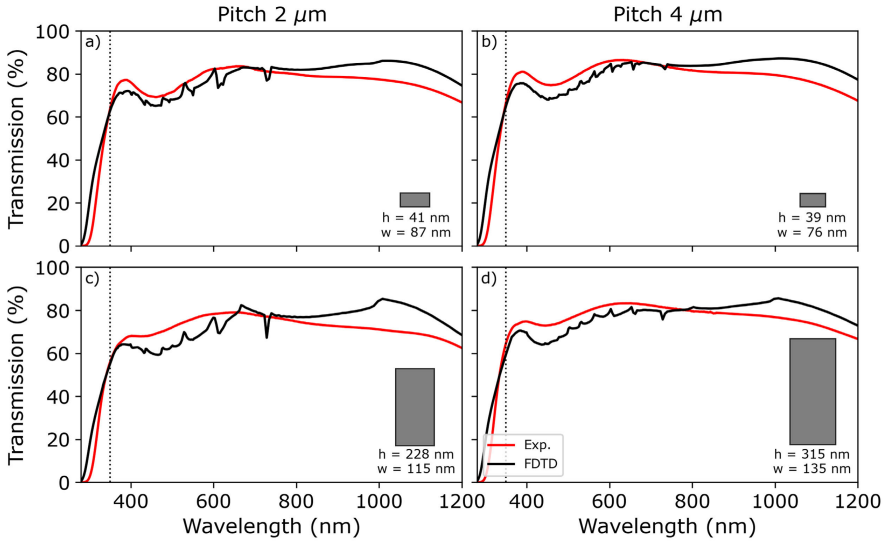

Figure 5.5: *Simulated transmission spectra (black) of infinite silver NW 1D grating, having a pitch of (a,c) 2 μm and (b,d) 4 μm, and having a geometry as specified by the inset, overlapped with the experimentally obtained transmission spectra (red) of silver NW/ITO/glass. The AM1.5G weighted average was taking in the spectral range of 350-1200 nm as indicated by the dashed vertical line.*

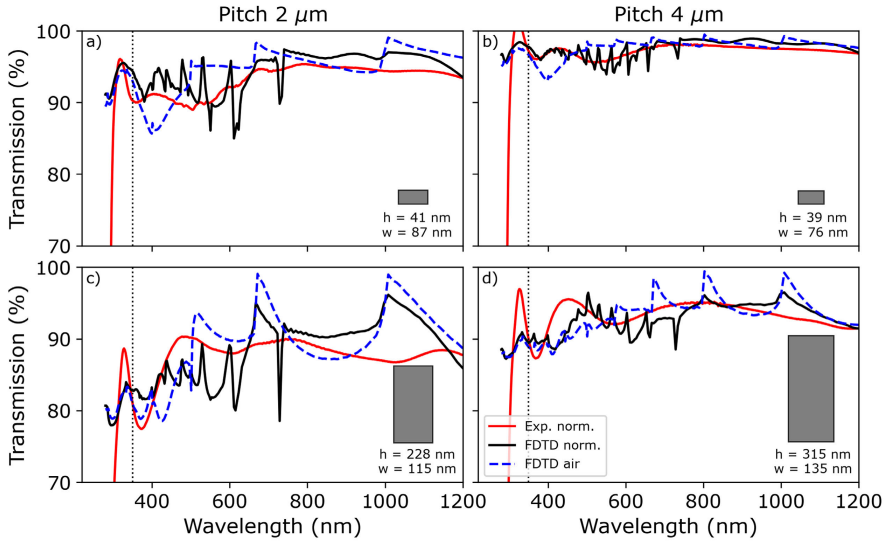

Figure 5.6: *Normalised experimental (red) and simulated (black) transmission spectra overlapped with the simulated transmission spectra of the same silver NW grating surrounded by air (dashed blue), having a pitch of (a,c) 2 μm and (b,d) 4 μm, and having a geometry as specified by the inset.*

Wood anomalies are more pronounced and there are more peaks in the presence of the ITO/glass substrate. The latter is due to the fact that two sets of modes are now available (i.e. in air and in ITO/glass), each of which has different spectral positions, as given by Equations 5.2.

In the world of TCMs, we are mostly interested in the spectral-average of the transparency. Figure 5.7 shows the AM1.5G weighted average of the raw and normalised simulated transmission of grids on ITO/glass and in air, represented by open red and black squares, respectively. Here, we plot the data for all samples having a pitch of 2 μm and 4 μm. The average simulated transmission for the grids in air (black squares) and the normalised one for the grids on ITO/glass (red squared) overlap almost perfectly, hereby validating this normalisation method to deconvolute the grids' optical characteristics from the substrate. The average normalised transmission in the experiment (red circles) is very close to that obtained from simulations, only with slightly lower values. The difference may be due to the different optical constants used for ITO in the simulation, as explained earlier. The same reasoning can be used for the difference between the simulated and experimentally obtained average transmission of the full silver NW/ITO/glass stack (in blue). Remarkably, the average of the experimental normalised transmission is very similar to the transmission expected from its geometric shading (based on the width and pitch of the silver NW grating), which was discussed in Chapter 4.

So far, we have demonstrated that the presence of ITO has very little effect on

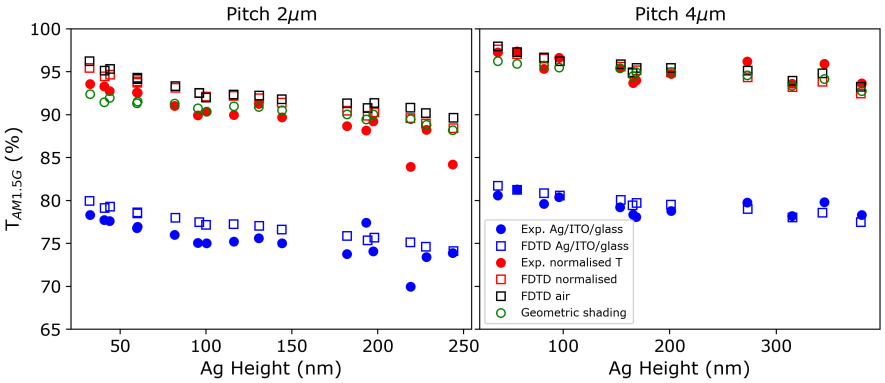

Figure 5.7: *AM1.5G weighted average transmission as function of the silver NW grating height, for gratings having a pitch of 2 µm (left) and 4 µm (right). Experimental and simulated data is represented by closed circles and open squares, respectively. The average transmission of the normalised spectra and total transmission of the silver NW/ITO/glass stack are represented by red and blue, respectively. The simulated transmission of the silver NW grating in air is represented by open black squares. The transmission expected from geometric shading is represented by the open green circles.*

the AM1.5G weighted average transmission of the grids. In reality, these grids will be fabricated on a substrate with a much higher refractive index compared to ITO, such as silicon. In Chapter 6, we actually show that the silver NW grids can be grown electrochemically directly on TOPCon solar cells that have a highly doped n-Si surface. Silicon is not only a high index material, but also highly absorbent.

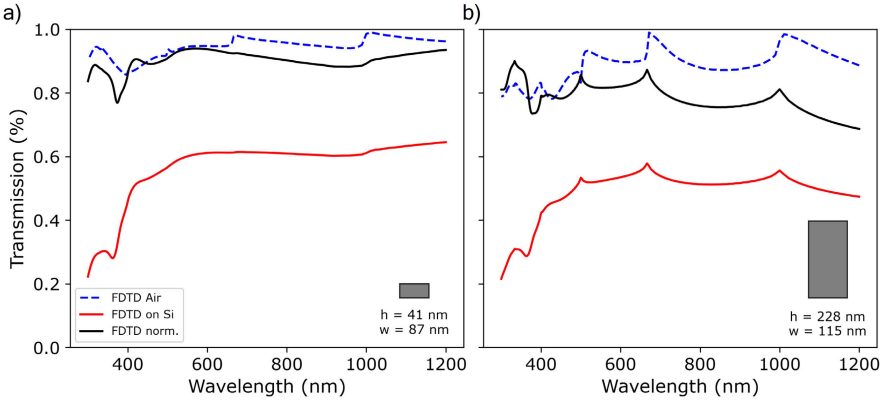

Figure 5.8: *Simulated transmission spectra of a 1D silver NW grating having pitch of 2 µm on Si (solid red), normalised for Si absorption (solid black), and free standing in air (dashed blue). The geometry is specified by the inset.*

Therefore, we have also simulated the effect of a silicon substrate on the grids optical performance by placing a power monitor 1 nm below the Ag/Si interface to avoid accounting for the absorption in Si.

In Figure 5.8, we compare the transmitted spectrum of the same grid as shown in Figure 5.5a,c suspended in air (dashed blue line) and on a Si substrate (solid red line), and normalised by the transmittance of the Si reference (solid black line). As the refractive index of the Si substrate is much greater than that of ITO, the transmission spectra of the silver NW grids on the Si substrate is much lower due to the increased reflectance. Similar to the case of ITO/glass substrates, the transmission spectrum of purely the silver NW grating can well be approximated by normalising by the transmission spectrum of bare Si. Therefore, we conclude that light transmission through the grid is only marginally affected by the presence of the higher-index dielectric substrate, once the substrate transmittance has been taken into account (i.e., normalised spectrum).

5.4 Experimental in-situ optical properties of silver NW grids

5.4.1 NSECC microscope

A custom-made microscope was built for the in-situ microscopy and spectroscopy of the electrochemical filling of the trenches, which is called the Nano Superfilling Electrochemical Cell (NSECC). A schematic overview of the used microscope is shown in Figure 5.9. The sample is illuminated with white light (Ocean Optics, DH-2000), where an objective (Nikon, CFI L Plan EPI CR) with a magnification of 100x and an NA of 0.85 was used to focus the white light on the sample and collect the reflected light. Because the sample is illuminated through the back side, only

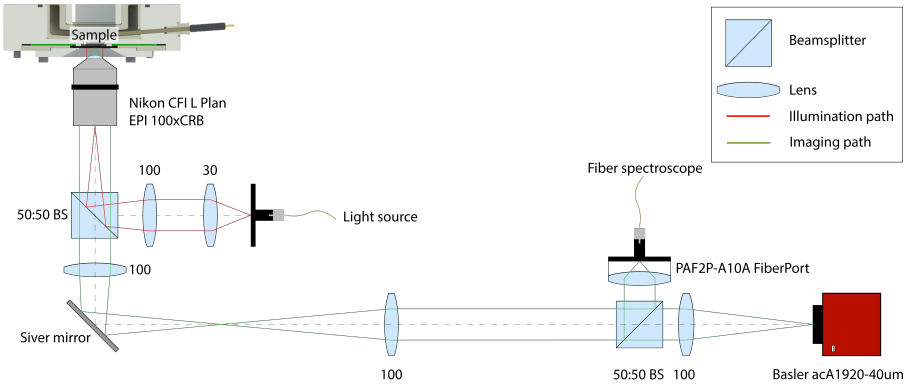

Figure 5.9: *Schematic representation of the Nano Superfilling Electrochemical Cell (NSECC) microscope. The focal length is given in mm. For a more detailed illustration of the electrochemical cell, see Figure 2.3 in Chapter 2.*

transparent substrates can be used in the NSECC microscope. The incident light first passes through the glass and ITO layers before being back-scattered by the silver nanoparticles. A 50-50 beam splitter was used to send the reflected light either to the camera or to the spectrometer. Reflection spectra were measured using a spectrometer (Ocean Optics, Maya 2000 PRO). Custom software was used to control and read out the data from the spectrometer (ENS monitor, developed by Sjoerd Wouda, 2018). A CMOS camera (Basler acA1920-40um, Sony IMX249 CMOS sensor) was used to record the bright-field microscopy videos with 40 fps. Pylon viewer (Basler, version 6.2.0) was used to control and read out the data from the camera.

5.4.2 In-situ bright-field microscopy

In electrochemistry, the time-dependent current density carries spatially-averaged information of the deposition, nucleation density and growth dynamics (see Chapter 2). A representative example of the first 12 seconds for the nucleation and growth of a silver NW grid on an ITO substrate is shown in Figure 5.10 (note that the total growth time is 50 s).

At the start of the nucleation pulse, the current density starts around -1.4 mA/cm^2 and rapidly drops to -0.8 mA/cm^2, due to the rapid depletion of silver ions close to the substrate surface. After 750 ms, the applied potential is reduced to the growth pulse potential, at which point the current density stabilises. This indicates that the electrochemical growth is not fully dominated by diffusion, but is expected to occur in the mixed kinetic-diffusion controlled regime.[145] Interestingly, no signs of silver nanoparticle merging into NW grids are discernible in the current transient.

To shed light on the nucleation and growth of silver NW grids, both in-situ bright-field microscopy and spectroscopy were used. During the deposition, a bright-field microscopy video was recorded at 40 fps. Some frames extracted from the video are

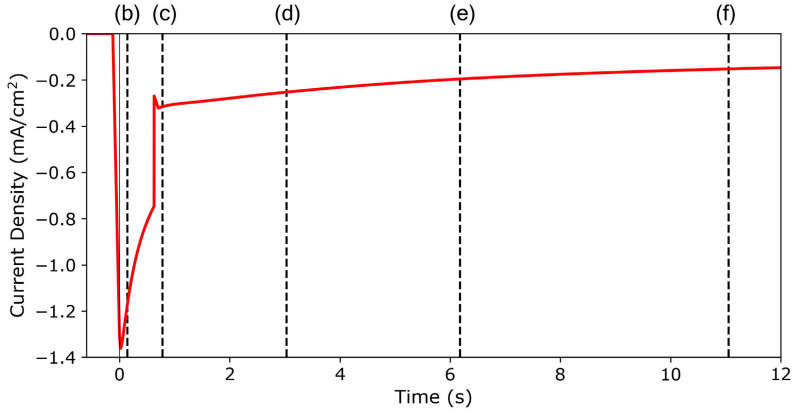

Figure 5.10: *Current density as function of time. The corresponding position of the extracted frames as shown in Figure 5.11b-f are represented by a vertical dashed black line.*

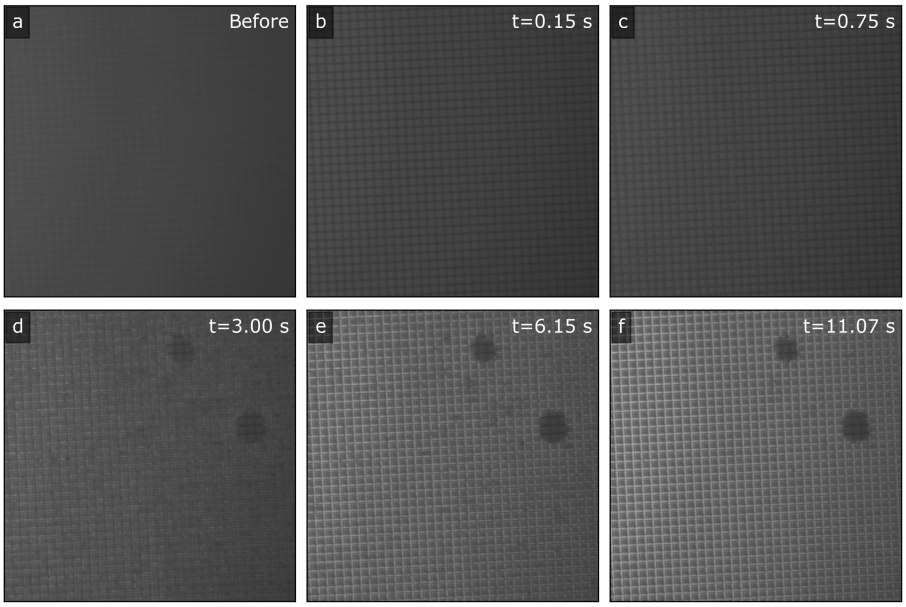

Figure 5.11: *Bright-field microscopy images recorded at different times during the nucleation and growth of the silver nanoparticles. The image of the sample without before the experiment is shown in a). The images shown in b-c) and d-f) were recorded during the nucleation and growth pulse, respectively.*

shown in Figure 5.11, the moment in time are indicated by the vertical dashed black lines in Figure 5.10. The image of the sample before the start of the experiment, in which only the PMMA mask is present, is shown in a). In this image, the PMMA appears somewhat darker than the trenches in the mask. The width of the trenches is smaller than the diffraction limit, so we do not have access to information within the trench. Instead, the used pitches of 2 and 4 μm are larger than the diffraction limit, so individual wires can be distinguished from their neighbours.

Upon nucleation, there is a sudden change in optical appearance in a time span of about 2 frames ($\approx$ 50 ms). As shown in Figures 5.11b-c, the trenches now appear darker compared to the PMMA mask. This is the result of the expected large absorption cross section of silver nanoparticles smaller than 25 nm. Because the small nanoparticles mainly absorb light instead of scattering, the amount of light that is reflected back to the camera decreases. After a few seconds of growth, the silver nanoparticles start to become bigger and therefore start to scatter more light. This is also evident in the images shown in Figures 5.11d-f, as the silver NW grids start to become much brighter than the PMMA background. We expect that interparticle merging takes place between 3 and 6 seconds after the start. Within this time span, there is no sudden change visible in the current density but we see the clear transition to bright lines in the images. While the microscopy images only show a small fraction of the total area of the sample, the current transient averages

the information of all growing nuclei. If the growth is non-homogeneous across the surface, nanoparticle merging may occur at different moments in time, and therefore the current density change due to the transition from 3D to 2D or even 1D growth is extended over a larger time span, and hence no sudden change in current density is observed.

Interestingly, two defects appear as the growth evolves in the images in Figures 5.11d-f, which are not observed in the early frames. These defects are unlikely to be related to imprint imperfections, because they appear dark during the nucleation pulse. In other words, silver nucleation is expected in these trenches. However, these particles seem to be not able to grow larger because they remain dark. During the nucleation pulse, a high overpotential pulse is applied, which is large enough to drive the hydrogen evolution reaction. [181] Therefore, the surface could be locally poisoned by hydrogen bubbles that block the diffusion of silver ions into the trenches and therefore prevent the growth of the silver nanoparticles.

5.4.3 In-situ spectroscopy

Microscopy images provide great visual feedback, but contain rather limited information.Therefore, reflection spectra were also obtained during nucleation and growth. The reflectance spectrum of the sample prior to the start of the experiment was taken as a reference. The relative changes in reflection during nucleation and growth of the silver nanoparticles in the nanotrenches are shown in Figure 5.12. During the nucleation pulse and the first seconds of growth (30 seconds), the spectrum rapidly changes, after which it remains rather constant. To highlight the initial changes, the time axis is shown in logarithmic scale. The end of the nucleation pulse and therefore the start of the growth pulse, is indicated by the white dashed line.

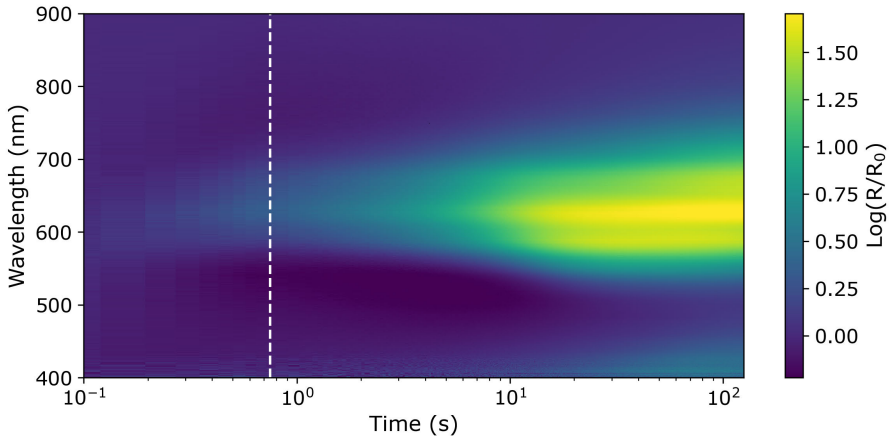

Figure 5.12: *Relative spectral changes over time during the nucleation an growth pulse. The vertical white dashed line represents the duration of the nucleation pulse.*

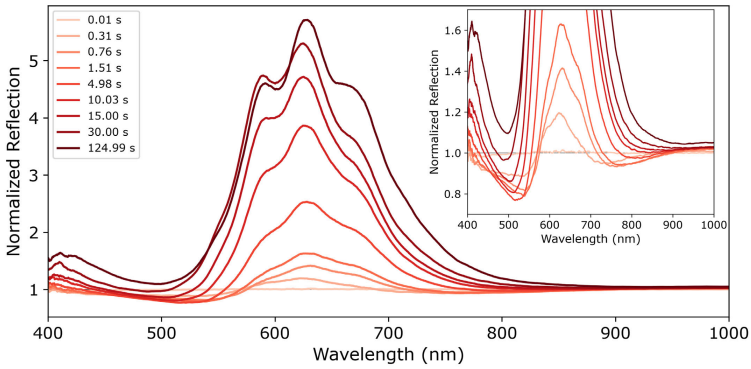

Figure 5.13: *Reflection spectra at specific moments during the growth of the silver NW wires. The inset shows a zoomed in view which highlights the drop in reflection within the first 1.5 s of the growth.*

In general, we observe that the reflection increases over time as a result of the increasing scattering of the silver nanoparticles and, at a later moment, the silver NW grids. In particular, reflectance increases in the 550-700 nm range. These spectral features become clearer in Figure 5.13, which shows the normalised reflection spectra at a few timestamps. The inset shows an enlarged view of the spectra. In this inset, one can clearly discern a reduced reflectance for the shorter wavelengths up to 550 nm in the first few seconds, next to an enhanced reflectance around 650 nm. We associate the decrease in reflection at short wavelengths with strong absorption in small silver nanoparticles at the initial stages of nucleation. The enhanced reflectance in the 550-750 nm shows a primary peak with two side bands,

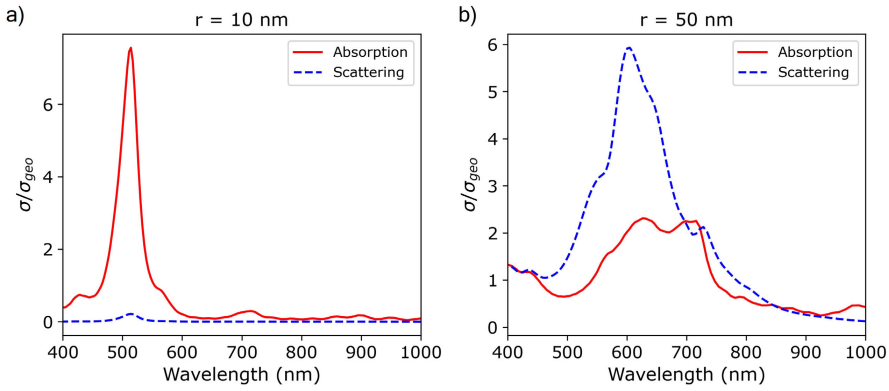

Figure 5.14: *FDTD simulations of the absorption and scattering cross section of a silver nanoparticle with a radius of a) 10 nm and b) 50 nm on ITO surrounded by water.*

the position of which red shifts within the first seconds of the experiment. Afterwards, the main reflection peak remains at the same wavelength.

We explain the main features in the time-dependent spectra by the Mie scattering of the silver nanoparticles.[258,259] Right after the nucleation of silver, small (10 nm) silver nanoparticles have a very large absorption cross section at 500 nm (Figure 5.14a), which matches well with the observed decrease in reflection around 500 nm in the in-situ reflection data. Note that for these small particles, almost no scattering is present. As the particles become larger, scattering increases and at some point it becomes more dominant than the absorption. Figure 5.14b shows the scattering and absorption cross section for a silver nanoparticle of 50 nm. The scattering cross section is now larger than the absorption cross section, showing a clear band around 600 nm, in line with the measured relative reflection spectra.

In the experiment, we expect a certain size distribution of the nanoparticles, which broadens with time. As a result, we expect a convolution of spectral features from all sizes, resulting in broad reflection peaks as obtained experimentally. More detailed analysis of the in-situ spectra may be able to reveal additional information on the size and shape of the particles, which is now difficult because of the particle polydispersity.

5.5 Conclusion

In the first part of this chapter, the transmission spectra of the silver NW grids on ITO/glass substrates were investigated by using 2D and 3D FDTD simulations. For normal incidence, the 3D FDTD simulations can be well approximated by two 2D simulations by two types of polarisation of the E-field (parallel and perpendicular to the NW). The simulations show a strong plasmon resonance around 400 nm when the E-field is polarised perpendicular to the silver NW. Furthermore, the silver NW grids show Rayleigh-Wood anomalies for both the parallel and perpendicular polarisation of the E-field, which become more pronounced for taller NWs. Although the plasmon resonance was also observed experimentally, the Rayleigh-Wood anomalies were not observed experimentally, while they are clearly present in the simulations. We address these differences to the used light source in the experiments, which is a focused, non-polarised, non-coherent source. Overall, we have shown that the used normalisation method is valid to obtain the AM1.5G weighted average transmission of the pure silver NW grids, as the average transmission of the silver NW grid in air is nearly identical to the average of the simulated normalised transmission.

Furthermore, as one of the goals is to replace the ITO by the silver NW grids, we investigate the optical properties of the silver NW grids on silicon substrates. We find that light transmission through the grid is only marginally affected by the presence of the higher-index dielectric substrate, once the substrate transmittance has been taken into account (i.e., normalised spectrum).

In the second part of this chapter, we have developed an optical microscope for in-situ microscopy and spectroscopy of the electrochemical growth of the silver NW grids. We used this microscope to investigate the nucleation and growth of

silver NW grids on ITO/glass substrates. Using in-situ bright-field microscopy and spectroscopy, we observed a sudden change in appearance of the trenches upon nucleation and subsequent growth of silver nanoparticles, which is caused by the strong plasmonic absorption by the silver nanoparticles. As the nanoparticles grow larger, the amount of reflected light is increased and hence the trenches appear brighter in the bright-field optical microscope images. Moreover, spectroscopic analysis allowed us to probe the in-situ reflection spectrum of the silver NW grids during nucleation and growth. We observed significant changes in reflection, verifying the hypothesis of absorption and scattering by the growing silver nanoparticles. The observed red shift in the reflection peak and the emergence of side peaks reveal information about the size distribution and shape evolution of the growing silver nuclei.

6

Electroplated Silver Nanowire Array as Transparent Electrode Without Seed Layer on TOPCon Solar Cells

This Chapter focuses on the investigation of silver NW grids integrated into an actual solar cell device. To do so, we first demonstrate the successful fabrication of silver NW grids grown directly on Si-based solar cells by electrochemical deposition without using a seed layer. We use tunnel oxide passivated contact (TOPCon) silicon cells as a platform to measure the transparency of the silver NW grids in the right dielectric environment via J_{sc} monitoring. SR-LBIC measurements on the patterned devices show that the transmission of the silver NW grids is greater than expected from their geometrical footprint. Interestingly, we find that the EQE at 1064 nm is increased by the addition of the silver NW grids, as a result of the increased optical path length leading to a higher absorption by the TOPCon solar cell. Furthermore, we investigated the effect of the aspect ratio of the nanowire on the angle-dependent J_{sc}. We find that the J_{sc} is virtually constant up to an angle of incidence of about 40°, after which the current drops. From FDTD simulations, we find that the silver NW grids absorb quite strongly at large angles of incidence due to the increased interaction cross-section.

6.1 Introduction

As the photovoltaic market heads toward multi-terawatt production capacity, the question of sustainable solar cell fabrication becomes more important.[39] In particular, energy usage during the fabrication process and resource availability have become increasingly important topics.[39,69,273,274] The supply of raw materials is limited, either for geopolitical or abundance reasons. For example, silicon is very abundant, however, there are only a few places in the world where the quality of the silicon is sufficient to be used in the photovoltaic industry.[71] Other elements, such as indium, are limited by their abundance.[68] Therefore, we must develop new strategies to reduce or even replace these elements in the design of solar cells. Thin film-based solar cells offer several advantages in terms of resource efficiency and energy consumption.[54,55] Several thin film solar cells based on materials from earth-abundant elements, such as CZTS[275] and zinc phosphide (Zn_3P_2),[276] are being intensively studied. Yet, these proposed solutions require a transparent conductive material (TCM), where the most commonly used TCM is indium tin oxide (ITO).

In addition to the photovoltaic industry, ITO is used in a variety of optoelectronic applications, such as displays,[277] touchscreens,[278] OLEDs,[279] etc. It is estimated that in 2020, nearly half of the refined indium went to ITO targets.[280] Replacing ITO is therefore important to secure the indium supply in the coming decades. Many alternatives have been proposed, such as indium-free transparent conducting oxides (Al-doped zinc oxide,[281] F-doped tin oxide[282]), carbon nanotubes,[85] graphene,[82] and metal micro- and nanowires.[75,76,98,104,238] An exciting alternative are silver nanowire (NW) networks, in particular due to their excellent conductivity and mechanical flexibility. In combination with solution-based fabrication, silver NW networks can be fabricated in a resource- and energy-efficient manner.[98,108]

In Chapter 4, we have shown that silver NW grids can be fabricated using template assisted electrodeposition on ITO substrates, resulting in high transparency and conductivity by increasing the NW aspect ratio. So far, these networks have been fabricated and characterised (sheet resistance and transparency) on sacrificial transparent substrates, i.e. ITO/glass.[98] While it has been shown that silver NW grids can be later transferred onto other surfaces.[242,283] the question is whether these results can be extended to device integration. Particularly challenging are the optical properties, which are difficult to disentangle from the substrate and may be quite different when on top of high-index dielectric layers. Another question is the effect of the 3D NW structure on transparency, as the structure is illuminated under an off-normal angle of incidence. Most solar cells are installed in a fixed position, resulting in a variable angle of incidence of sunlight up to 60°.[284] Therefore, it is important to understand the angle-dependent light-matter interactions of the silver NW grid.

In this work, we demonstrate the direct bottom-up fabrication and characterisation of silver NW grids on a solar cell device. We use tunnel oxide passivated contact (TOPCon) solar cells as a platform to study the growth and optical transparency of silver NW grids under realistic conditions. Due to the long minority carrier diffusion length of the emitter (up to a few cm),[285] a TCM is not required for the performance

of the solar cell. Thus, the TOPCon solar cell is used as an optical detector. We demonstrate that the direct fabrication of high aspect ratio silver NW grids on a silicon-based solar cell is possible by using selective area light-induced plating. We used spectrally resolved light-beam induced current (SR-LBIC) to locally measure the transparency of the grids, and angle-dependent short-circuit current density (J_{sc}) measurements to reveal the effects of the aspect ratio on transparency for large angles of incidence.

6.2 Results and Discussion

6.2.1 Light-induced bottom-up growth of silver nanowire grids

Selective area electrodeposition of silver directly on TOPCon solar cells was achieved by filling nanosized trenches in an insulating mask, combined with light-induced plating (see Figure 6.1). The fabrication of the silver NW grid involves mainly two steps:

i Mask fabrication: the mask was fabricated by imprinting a thin sol-gel layer on a PMMA spacer layer at the emitter side of the solar cell using substrate conformal soft-imprint lithography (SCIL). SCIL is a scalable nanofabrication method that creates high-fidelity nanostructures over up to 6" wafers and can create nanoscale features with characteristic dimensions as small as 6 nm.[286] After imprinting, a reactive ion etch is used to create a grid consisting of trenches approximately 600 nm deep in the PMMA/SiO_2 mask. The final step consists of a hydrogen fluoride (HF) vapour etch to remove the plasma-induced silicon oxide from the surface of the TOPCon cell, which is a critical step for the electrochemical growth of silver.

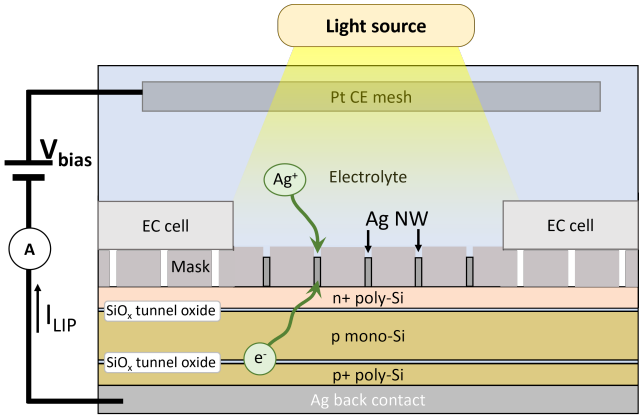

Figure 6.1: *Schematic diagram of the light induced plating (LIP) process including the schematic of the device architecture of the TOPCon solar cell and the mask.*

ii Electrochemical growth of silver: the trenches were filled with silver using potential-controlled light-induced plating (LIP). As discussed in detail in Chapter 3, we make use of a potential pulse sequence to independently tune the nucleation and growth conditions. However, the electrochemical reduction of silver cannot take place on the front side of the TOPCon solar cell because the diode configuration of the solar cell prevents the flow of current. Upon illumination, a backflow of photo-generated electrons enables the electrodeposition of silver in the mask openings. Potential control is essential to regulate the kinetics during the growth pulse.

Figure 6.2a shows an SEM image of the silver NW grids fabricated on TOPCon solar cells. The width of the wires is determined by the shape of the mask. The sample shown in Figure 6.2 exhibits an average wire width of 199.7 ± 7.9 nm, which is much wider than the 80 nm wire width of the stamp. This is due to the slight nonisotropic etching of the mask, resulting in a trapezoidally-shaped trench and thus a height-dependent wire width (see Chapter 4 for more details). The height of the silver NW grid is fully controlled by the deposition time. Figure 6.2b shows a 52° tilted SEM image that illustrates the high aspect ratio of the nanowire network. To quantify the height distribution, Figure 6.2c shows an atomic force microscopy (AFM) image of the corresponding sample shown in Figures 6.2a-b. The average height of the silver NW grid was obtained by fitting a Gaussian to the height distribution extracted from the AFM scan, and is found to be 425 ± 45 nm, which is about 3 times larger than the width (i.e. AR~3).

It can be seen that there is a wide height distribution across the wires, which may limit the electrical performance of the grid. Although most of the trenches are filled with silver, some spots display a lower height compared to the average, which we call defects. An example of the height profile of a defect is shown in Figure 6.2d through the line profile extracted from the AFM image in Figure 6.2c, indicated by the white line between the blue triangles. In contrast to our previous work, light-induced electrodeposition is used to enable a current flow through the TOPCon cell into the electrolyte. Although the overpotential and light intensity conditions have been optimised for the best growth rate, we cannot dismiss spatial inhomogeneities in the illumination or in the charge collection by the top emitter layer. In future work, the homogeneity of the height of the NW grid may be improved by using additives in the electrolyte.[171]

6.2.2 Ag grids performance assessment

In this work, we specifically focus on the optical characteristics of the grids in a realistic dielectric environment, where the TOPCon solar cell underneath acts as a photodetector. To determine the local transmission of the silver NW grids, spectrally resolved light-beam induced current (SR-LBIC) microscopy was used to obtain external quantum efficiency (EQE) maps. In this technique, the sample is illuminated using monochromatic light with a spot size ranging between 100 and 220 μm. To extract the transmission of the silver NW grids, an area containing silver NW

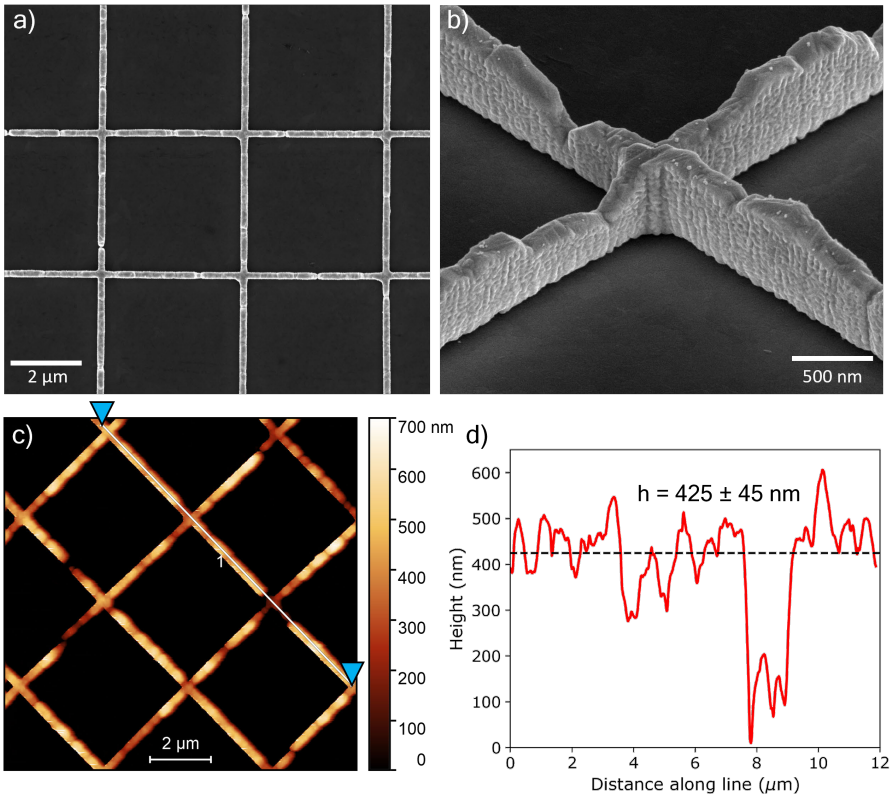

Figure 6.2: *a) SEM image of the fabricated silver NW grids using SCIL and the LIP process with a width of 199.7 ± 7.9 nm. b) Side view SEM image taken under an angle of 52° for a sample with an aspect ratio of 3.0. c) AFM surface topography of an silver NW grid with an aspect ratio of 3.0. d) Line profile taken along the segment as indicated in the AFM between the two blue triangles as shown in c).*

grids is compared with an area without silver NW grids (bare Si surface). Therefore, part of the silver NW grids were removed using a PEEK tip to create a clear boundary between areas with and without silver NW grids. Figure 6.3a shows a photograph of a sample in which a part of the silver NW grid was removed. The area containing the silver NW grid is easily recognised because of the whitish backscattering of light. The black background is the bare Si surface, and the gray areas on the top and bottom are the silver contact pad used to make an electrical connection to the front side of the sample.

Figures 6.3b-f show the EQE maps for the shortest NW grid (h = 159 nm) obtained by SR-LBIC using multiple excitation wavelengths, where the areas with and without silver NW grids are easily recognisable. The EQE map obtained at an excitation wavelength of 405 nm is shown in Figure 6.6 in the Supplementary Information.

Apart from the defect in the center, the EQE obtained in the area contained silver NW grids is homogeneous. This indicates that the transparency, and hence the width of the silver NW grid, is quite homogeneous across the sample. The interference fringes visible in the EQE map for an excitation wavelength of 1064 nm is expected to be a result of small thickness variations of the double-sided polished Si wafer, since at these wavelengths the Si solar cell becomes semi-transparent. The average value of the EQE of the silver NW grids and the bare Si area was obtained by extracting the expected value from a Gaussian fit to the corresponding histogram (see Figure 6.7 in the Supplementary Information) from the encircled areas in Figure 6.3. We find that for all wavelengths, except for 1064 nm, the EQE value is slightly lower in the area containing the silver NW grids compared to the bare Si area (see Figure 6.8a in the Supplementary Information). In a similar way, reflection maps at different excitation wavelengths were obtained. We find that the addition of silver NW grids to the TOPCon solar cell reduces the average reflection of the cell, as shown in Figure 6.8b in the Supplementary Information.

To investigate the effect of the height of the silver NW grid on the EQE, we also obtained EQE maps for the tallest silver NW grid having a height of $h = 456$ nm (see Section 6.5.2 in the Supplementary Information). Again, the areas with and without silver NW grids are easily recognisable, and interference fringes are observed for an excitation wavelength of 1064 nm. We find that for the tallest grid height, the EQE values within the silver NW grid area are lower compared to the bare Si area for all excitation wavelengths.

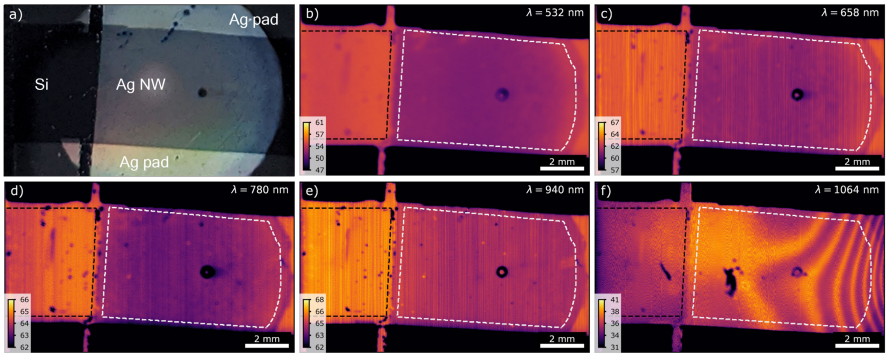

Figure 6.3: *a) The appearance of the silver NW grids on TOPCon ($h = 159$ nm, AR = 1.6). The white areas on the top and bottom are the silver contact pads used to make contact with the TOPCon cell and the silver NW grids. b-f) EQE maps of the corresponding sample. The silver NW grid and bare Si surface areas used for the analysis are encircled by dashed white and black lines, respectively. The excitation wavelength is noted in the top right corner. The colour bar in the inset specifies the range of EQE values in percentage.*

The transparency of the silver NW grid T_{grid} can be estimated by taking the ratio between the EQE of the silver NW grid and the EQE of the bare Si EQE:

$$\frac{EQE_{grid}}{EQE_{Si}} = \frac{IQE_{grid}}{IQE_{Si}} \frac{A_{grid}}{A_{Si}} = \frac{A_{grid}}{A_{Si}} = \frac{T_{grid} A_{Si}}{A_{Si}} = T_{grid} \tag{6.1}$$

where A_{grid} and A_{Si} are the amount of absorbed photons in the area containing the silver NW grid and the bare Si, respectively. We assume that the internal quantum efficiency (IQE) is spatially homogeneous throughout the device, and therefore the reduction in photocurrent is a direct result of the reduced amount of absorbed photons. Therefore, we assume that the reduction in absorbed photons is purely the result of the transmission of the silver NW grids, and hence $A_{grid} = T_{grid} A_{Si}$.

Figure 6.4 shows the transparency of the silver NW grid as extracted from the EQE maps. The AM1.5G average transmission of the shortest (h = 159 nm, AR= 1.55) and tallest (h = 456 nm, AR= 3.22) silver NW grid are found to be 96.9 ± 5.3% and 94.3 ± 5.2%, respectively. For both heights, the AM1.5G average transmission is larger than that given by the corresponding geometric shading (as indicated by the dashed horizontal lines).

To explain such differences, we refer to the fact that the optical cross section of nanostructures can be quite different from their geometric cross section.[88,287] For wavelengths much larger than the NW width, the extinction cross section is smaller than the geometric cross section. However, for wavelengths approaching the width of the silver NW, the silver NW begins to strongly extinct light due to the excitation of the local plasmon resonance.[88] The plasmon resonance of our silver NW grid occurs around 400 nm (as discussed in detail in Chapter 5), at which point the grid

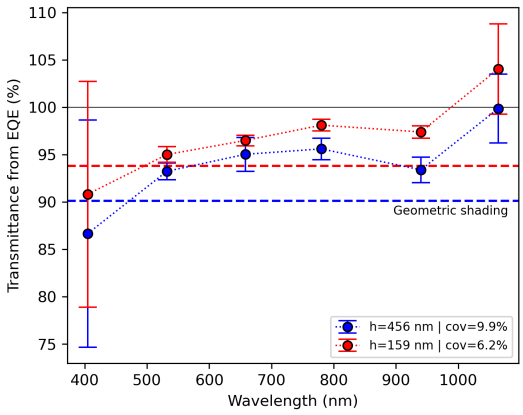

Figure 6.4: *Transmission spectrum of the silver NW grid extracted from the EQE maps for two the shortest (h = 159 nm, red circles) and tallest (h = 456 nm, blue circles) grid height. The dashed horizontal lines represent the transmission expected by geometric shading (red: shortest, blue: tallest), based on the average width. The AM1.5G weighted average transmission is* 96.9 ± 5.3% *and* 94.3 ± 5.2% *for the shortest and tallest silver NW grid, respectively.*

absorbs light strongly, resulting in a lower transparency at 405 nm than expected by geometric shading. The absorption at 405 nm is also consistent with the observed decrease in reflection.

Interestingly, for an excitation wavelength of 1064 nm, we find that the EQE of the shortest silver NW grid even exceeds that of the reference. A line profile from the EQE map (thereby excluding the area containing interference) clearly shows the jump in EQE from crossing over the bare surface to the silver NW grid area (for more details see Section 6.5.1 in the Supplementary Information). In fact, the assumption that the amount of absorbed photons being only affected by the transmission of the silver NW grids does not hold at a wavelength of 1064 nm since the Si becomes semi-transparent. At this wavelength, the silver NW grid with a pitch of 4 μm are strong scattering objects, thereby increasing the optical path length in the TOPCon underneath and thus resulting in a larger amount of absorbed photons. Furthermore, the reflection at 1064 nm for the area containing silver NW grids is lower compared to the bare Si area. Combing this with the increase of photocurrent, we conclude that more photons have been absorbed by the Si absorber. Although the transparency value for the shortest silver NW grids at 1064 nm may not be valid, the photocurrent is increased as a result of the addition of the silver NW grid and is therefore beneficial for the power output of the solar cell.

To address the effect of the high aspect ratio on the transparency of the silver NW grids, angle-dependent short-circuit current density (J_{sc}) measurements were performed. The angle-dependent J_{sc} is shown in Figure 6.5a. The current was measured at 3 different spots to average out the spatial homogeneity effects of the deposited silver NW grids. A flat reference cell without silver NW grids is also shown as a reference (black squares connected by a solid line). In all samples, including the flat reference, the J_{sc} decreases with increasing angle of incidence, mainly due to the reduced power per unit area impinging on the solar cell, which follows as a

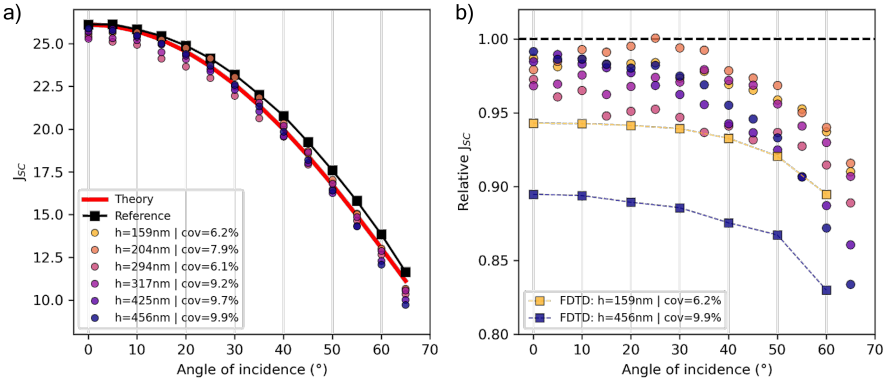

Figure 6.5: *a) J_{sc} as function of angle of incidence and b) normalised by the J_{sc} at normal incidence for silver NW grids having different aspect ratios. The experimental data is represented by the circles, and the FDTD simulation is represented by the squares connected by a dotted line.*

cosine function (for more details see section 6.5.3 of the Supplementary Information). When comparing the flat reference sample with samples containing different heights of silver NW grids, we observed a lower value of J_{sc} at all angles, as expected from the SR-LBIC data.

By normalising the measured current by that of the reference cell, we uncover the angle-dependent silver NW grid transparency. The relative J_{sc} as a function of the angle of incidence is shown in Figure 6.5b. We find that at normal incidence the reduction of J_{sc} falls within less 5% for all grid heights, while the silver coverage ranges between 6 and 10%, consistent with the SR-LBIC results. This corroborates that the transparency of the silver NW grids is more transparent than expected from its geometrical cross section. On the other hand, we find that the relative J_{sc} is fairly angle independent for all samples up to approximately an angle of incidence of 40° after which the relative J_{sc} decreases. This indicates that the transparency for even the grid with the highest aspect ratio is very robust up to angles of incidence of about 40°.

To understand the reason behind this angle dependence, FDTD simulations have been performed for the shortest (h = 159 nm) and tallest (h = 459 nm) silver NW grids on Si at multiple angles of incidence. The simulated photocurrent normalised to that of a reference without the grid is shown in Figure 6.5b as squares. We find that the angle-dependent relative J_{sc} behaviour is qualitatively very well described by the FDTD simulations. The decrease in relative J_{sc} at large angles of incidence can be attributed to an increase in absorption by the silver NW grids at those angles (see Figure 6.16 in the Supplementary Information). On the other hand, we attribute the absolute difference between the FDTD simulated and the experimentally obtained relative J_{sc} to incomplete grid coverage within the illuminated 5x5 mm^2 area. Therefore, the FDTD simulations serve as a lower limit for the relative J_{sc}. The operating angle of incidence of most solar cells is as high as 60°, and therefore the effect of parasitic absorption could be kept to a minimum.

Finally, we comment on the conductivity of the silver NW grids. The one-sun full I-V curves of the patterned solar cell devices are shown in Figure 6.17a in the Supplementary Information. Based on the results obtained in Chapter 4, one would expect the sheet resistance of the silver NW grids to be < 10 Ω/□, where the taller the silver NW grids the lower the resistance. Despite the high conductivity of the emitter in the TOPCon cell, we consistently observed an improved FF when the NW grids are present compared to the reference. This means that the sheet resistance of the front extraction layer is effectively decreased by the addition of the silver NW grids. Unfortunately, the grid height inhomogeneity hampers to draw quantitative conclusions on the effect of the grid height on the FF.

From the dark I-V curves (see Figures 6.17b-c in Supplementary Information), we find the dark current density J_0 to be greater than 1 $\mu A/cm^2$, and ideality factor n to be greater than 3. The extremely large dark current density and the shape of the n-V curve suggest that the recombination is dominated by the edges of the sample.[288,289] This is not surprising, given that the diffusion length of the TOPCon cell is on the order of the size of the samples, and therefore the carriers are rapidly distributed evenly throughout the sample. Because the edges are unprotected, they

are very sensitive to sample handling, leading to many defects and even shunting of the device.[290] This effectively means that the V_{oc}, and to a lesser extent the FF, will be dominated by recombination at the edges of the sample. Since there is a large spread in sample-to-sample variation, no useful information can be extracted from the V_{oc}.

6.3 Conclusion

We have demonstrated the electrochemical fabrication of silver NW based transparent electrodes on top of TOPCon solar cells which serve as platform to measure the transparency of the silver NW grids in the right dielectric environment via J_{sc} monitoring. We find that the t ransparency of the silver NW grids is greater than its geometric filling fraction. Moreover, we find that the EQE at 1064 nm is improved by the addition of the silver NW grids to the TOPCon solar cells, which is the result of the increased optical path length by the diffraction of the silver NW grid. We show that the high aspect ratio silver NW grids perform well up to an angle of 40°, after which parasitic absorption inside the silver NW grids starts to increase. Since for most solar cells the operating angle of incidence does not exceed 60° for direct sunlight, the parasitic absorption can be minimised.

6.4 Methods

6.4.1 Fabrication of the TOPCon solar cells

The TOPCon silicon cells were fabricated on double-side polished float-zone c-Si wafers (1 Ωcm, 300 μm, 100-oriented, 4 inch). On both sides of the wafer, tunnel oxide passivated contacts were formed. The thin oxide layers were grown thermally in a tube furnace at 600 °C. 100 nm a-Si was deposited on both sides using LPCVD, doped by ion implantation, and crystallised after at 900 °C. The front and back sides were doped with phosphorus (P) and boron-monofluroide (BF), respectively, to form an n- and p- contact layer at the front and back, respectively. A 1 μm silver back contact was made on the back side by sputtering. The layer structure of the TOPCon cell is shown schematically in Figure 6.1. More information about the manufacturing process can be found elsewhere.[291]

6.4.2 Preparation of the mask

The TOPCon solar cells were cut into 17x17 mm pieces, after which they were submerged in acetone and isopropanol (IPA), and dried with a nitrogen gun. The native silicon oxide was removed by HF vapour etching (300 s, 125 mbar, N2: 1200 sccm, EtOH: 350 sccm, HF: 300 sccm). The electrochemical mask was fabricated using substrate conformal imprint lithography (SCIL). A PMMA (MW=950 A8, Kayaku Advanced Materials, Inc.) spacer layer was used which determines the depth of the trenches, and was spin coated at 2700 RPM for 45 s on the poly n-Si front surface,

and was baked at 150 °C. A sol-gel (T1100, SCIL Nanoimprint Solutions) layer was spin coated on the PMMA spacer layer at 2000 RPM for 10s. Directly after, the PDMS stamp was pushed into the sol-gel hereby transferring the grid pattern (pitch = 4 μm, linewidth = 80 nm) from the PDMS stamp into the sol-gel layer, and is removed after 6 min of curing at room temperature. The residual layer at the bottom of the imprinted trenches was removed using a CHF_3/Ar reactive ion (Oxford Plasmalab 80+, 67 W, 15 mTorr) etch for 2 min and 30 s, and the PMMA was etched using an O_2 plasma (Oxford Plasmalab 80+, 200 W, 5 mTorr) until the poly n-Si front surface is exposed. As a result of the O_2 plasma etch, a small SiO_x layer is formed which is removed using another HF vapour etch just before the electrochemical filling with silver. The final depth of the mask was around 660 nm.

6.4.3 Electrodeposition of silver

The trenches were filled with silver by electrodeposition using a commercial silver plating solution (Clean Earth Solutions™, 45.220). Light induced plating (LIP) is used in combination with the double potential pulse method to independently control the nucleation and growth of the wires.[166] Since the plating occurs on the poly n-Si front surface, a background illumination is required to open up an electrical pathway by generating a backflow current through the p-n junction. The LIP process is shown schematically in Figure 6.1. A nucleation pulse of E_n = -2.6 V vs. Ag/AgCl was applied for t_n = 750 ms, after which a growth pulse of E_g = -0.04 V vs. Ag/AgCl is applied for a varying growth time t_g from 150 to 300 s. During both the nucleation and growth pulses, a white background illumination of 30 mW/cm^2 was used (Sciencetech, A4 Solar LightLine). Due to the high overpotential of the nucleation pulse, the current is limited by the generation of electron-hole pairs, whereas during the growth pulse the applied potential is the limiting factor. Details of the electrochemical cell and double pulse technique can be found in Chapters 2 and 3, respectively. After electroplating, the PMMA/sol-gel mask was removed by submerging the samples (vertically orientated) in acetone (40 °C) for >15 min, while stirring the solution with a magnetic stir bar.

6.4.4 Device characterisation

Morphological and structural characterisation of the silver NW grids was performed using a FEI Verios 460 scanning electron microscope (SEM) using a working distance of 4 mm, operated at 5 kV and 100 pA. An edge detection Python algorithm was used to extract the width from the SEM images, by obtaining the expected value from a Gaussian fit to all individual lines in the SEM image for both the horizontal and vertical direction.

Topographic maps were obtained with atomic force microscopy (AFM), using a Bruker Dimension Icon and a ScanAsyst-Air probe (Bruker, nominal tip radius 2 nm). The height of the wires was extracted by fitting a Gaussian distribution to the masked area corresponding to the wires on the AFM images.

6.4.5 EQE mapping

EQE maps were obtained using spectrally resolved light-beam induced current (SR-LBIC) measurements using the commercially available LOANA solar cell analysis system by pv-tools GmbH.[292] Laser light was used from six diode-lasers operation at 405 nm, 532 nm, 670 nm, 780 nm, 940 nm, and 1064 nm, all coupled to the sample using an optical fiber. The spot size of the laser spot ranges between 100 μm (for 670 nm) and 220 μm (for 405 nm), without using bias-light. The variation in the laser intensity was corrected using a monitor detector. The samples were scanned in the x-y direction which being illuminated by the monochromatic laser light under short-circuit conditions. The samples were kept at a temperature of 25°C using a temperature controlled stage. The measured short-circuit current at an excitation wavelength λ was scaled by the single-point EQE_{λ}^{ref} reference spectrum obtained in an area containing the silver NW grids see Figures 6.8a and 6.12a in the Supplementary Information). Reflection maps were obtained using the same LOANA system, where a Si solar cell was placed ≈ 1 mm above the surface of the sample, having a small hole in the center for the laser light to pass. The sample moves in x-y to map the whole area, and reflected light in a cone of about 170° is detected. The single-point reference reflection spectrum obtained in an area containing the silver NW grids, and the average reflectance values extracted from the SR-LBIC measurements are shown in Figures 6.8b and 6.12b in the Supplementary Information.

6.4.6 Angle dependence J_{SC} measurements

A custom made holder was designed and fabricated at AMOLF (see Figure 6.18 in the Supplementary Information). The sample is contacted from the top and bottom using a 4 point probe configuration, where a source and measuring unit (Keithley, 2450 SourceMeter) was used for measuring the I-V curves. One-sun I-V curves were measured using a solar simulator (Sciencetech, A4 Solar LightLine), where the angle of incidence was varied from 0° to 65° with steps of 5°. A mask was used to limit the illuminated area to 5x5 mm^2. The intensity of the solar simulator at normal incidence was calibrated by a reference cell (VLSI Standards, ORIEL 91150V) at a lamp to sample distance of 18 cm.

6.4.7 FDTD simulations

To simulate the transmission spectra, Maxwell's equations were solved numerically, using the FDTD 3D Electromagnetic Simulator by Ansys Lumerical.[268] Periodic boundary conditions were used to simulate an infinite network that has a span equal to the pitch of the silver NW grid. The optical constants for Si and Ag were obtained from Palik[269] and approximated by fitting curves to the datasets.[268] The refractive index of the background was set to unity. A broad band (300-1200 nm) plane wave of type BFAST is used. The power monitors that records the reflection and transmission of the silver NW grid, is placed 300 nm above the source and is

placed 1 nm below the Ag/Si interface, respectively, to limit the absorption by the Si. On the z-boundaries (perpendicular to the propagation of light), perfectly matched layer (PML) boundary conditions were used to prevent any unwanted backscattering at the edge of the simulation box. Periodic boundary conditions were used for the in-plane boundaries, that were over-written by the BFAST plane wave source under off-normal incidence conditions. A custom non-uniform mesh using the conformal variant 1 mesh refinement was used with a maximum mesh step of 10 nm.

Author Contributions

R.M. and O.H. fabricated the TOPCon solar cells. R.M. performed the SR-LBIC measurements. Y.B. fabricated the mask using SCIL, performed the light induced plating, I-V curve measurements, and the angle dependence J_{sc} measurements. Y.B. performed all the data analysis. Y.B. and E.A.L. performed the FDTD simulations and wrote the manuscript. B.B. and E.A.L. supervised the project.

6.5 Supplementary Information

6.5.1 EQE analysis of the shortest silver NW grid

EQE map at 405 nm (shortest grid height)

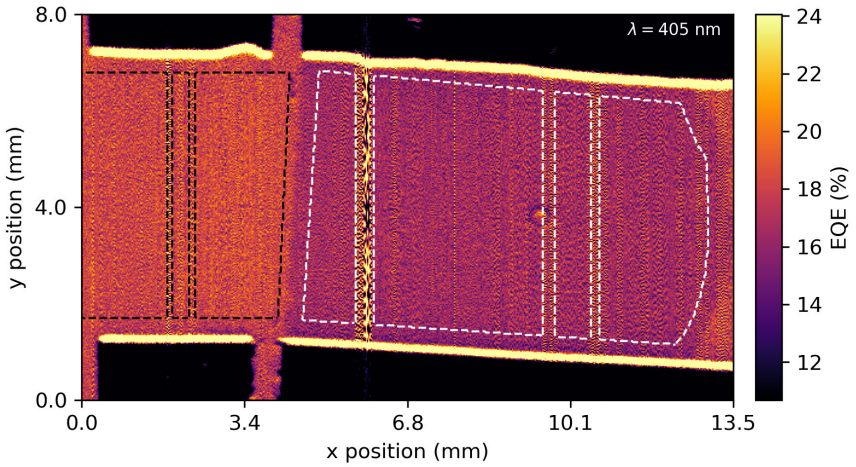

Figure 6.6: *EQE map obtained at an excitation wavelength of 405 nm for the shortest grid height ($h = 159$ nm), as shown in Figure 6.3. The vertical stripes are measurement artefacts and are excluded from the histogram analysis, as indicated by the encircled area.*

EQE map data treatment (shortest grid height)

The values corresponding to the encircled areas in the maps shown in Figures 6.3 and 6.6 are represented by a histogram shown in Figure 6.7. Since the EQE map obtained at an excitation wavelength of 405 nm contains some vertical measurement artefacts, these areas were excluded in the histograms. The data included in the histograms are represented by the white and black encircled area in the maps for the area containing the silver NW grids and the bare Si, respectively. The average value of the EQE was found by fitting a Gaussian to the histograms. The average EQE is the expected value extracted from the Gaussian fit, and the error on the average EQE value is taken to be the standard deviation extracted from the Gaussian fit.

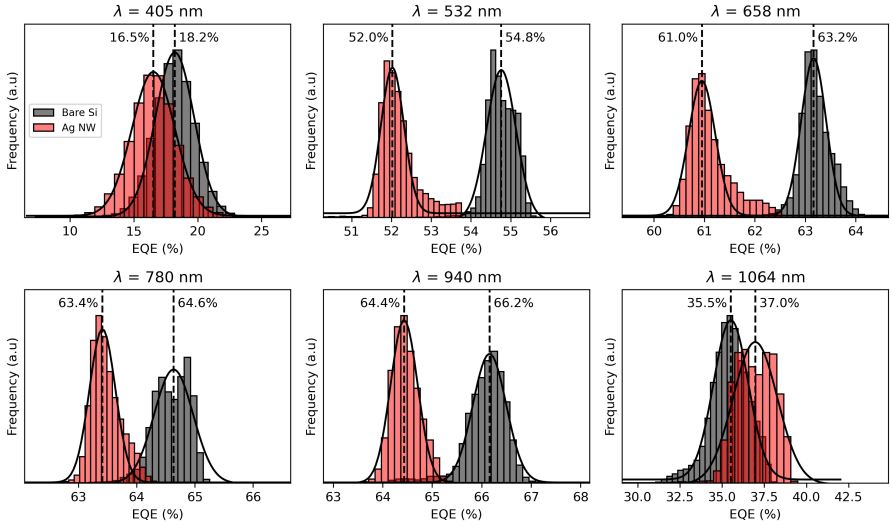

Figure 6.7: *Histograms of the EQE maps, as shown in Figures 6.3 and 6.6, for different excitation wavelengths as specified by the title of the subplots. The histograms corresponding to the area containing the silver NW grid and the area of the bare Si are represented by the red and black bars, respectively. The expected value from the Gaussian fit is represented by the black dashed line and its value is noted next to it.*

Single point EQE and reflection spectrum

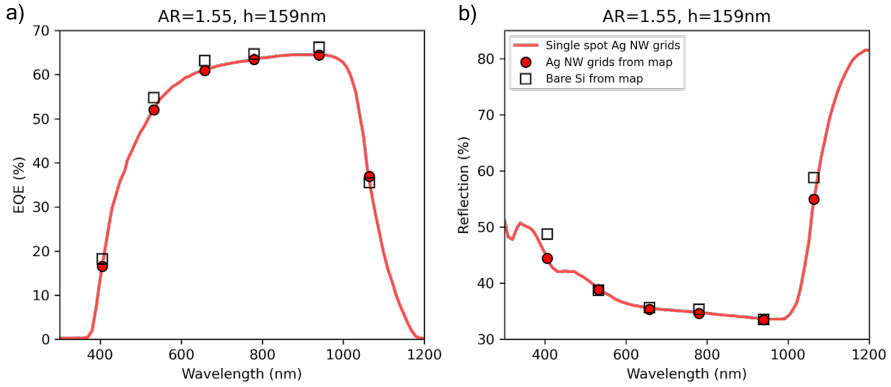

Figure 6.8: *Single-point a) EQE and b) reflection spectrum of the sample shown in the maps in Figure 3 obtained at a spot located withing the area containing silver NW grids. The average a) EQE and b) reflection values extracted from the EQE maps for the area containing the silver NW grids and the bare Si are represented by the red circles and black open squares, respectively.*

EQE analysis for 1064 nm

To further analyse the EQE maps obtained at an excitation wavelength of 1064 nm, a line profile across the interface between the bare Si and silver NW grid area in the EQE map was extracted from the map. Figure 6.9a shows the average line profile extracted from the marked area as shown on the EQE map in Figure 6.9b. Compared to the map in Figure 6.3f, the map was rotated with an angle of 3.7° so that the interface between the bare Si and the silver NW grid is vertically orientated. A box was drawn with equal widths on both sides of the interface from which the average vertical values of the EQE were obtained. At each horizontal value, the average vertical value was obtained by extracting the expected value from a Gaussian fit to the vertical line data. The mean value of the EQE in the bare Si and silver NW grid was found to be $36.7 \pm 0.8\%$ and $38.1 \pm 0.3\%$, respectively, as indicated in Figure 6.9b. The ratio between the EQE extracted from the silver NW grid by the bare Si is found to be $103.9 \pm 2.3\%$, which agrees well with the value reported in Figure 6.4. Again, it suggests that the addition of silver NW grids to the TOPCon solar cell improves the EQE at 1064 nm.

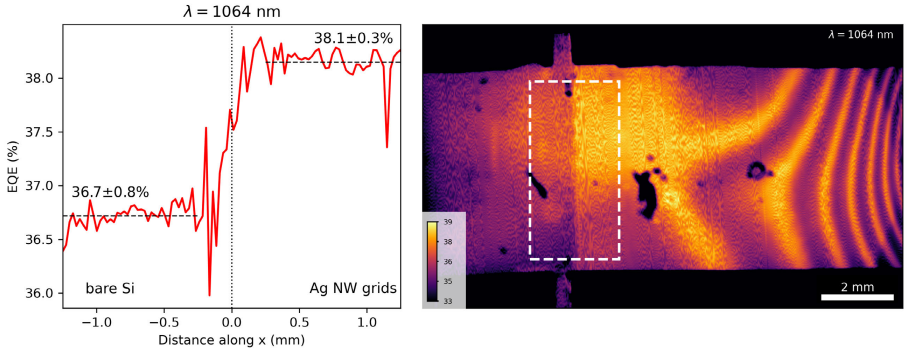

Figure 6.9: *a) Average line profile of the EQE across the interface between the bare Si and silver NW grid area, extracted from the EQE map shown in b) for an excitation wavelength of 1064 nm. The colour bar in the inset shows the values of the EQE in percentage.*

6.5.2 EQE analysis of silver NW grid with h=456 nm

Similar to the shortest grid height, the areas with and without silver NW grids for the tallest grid height are also easily recognisable in the EQE maps shown in Figure 6.10. However, the area containing the silver NW grids is not homogeneous, which means that the width or height of the grid is not homogeneous across the sample. This is confirmed by SEM, which shows disconnected lines in areas that have a higher EQE value. In the analysis of the EQE data, only the white encircled area was used, hereby excluding the area that contains fabrication defects.

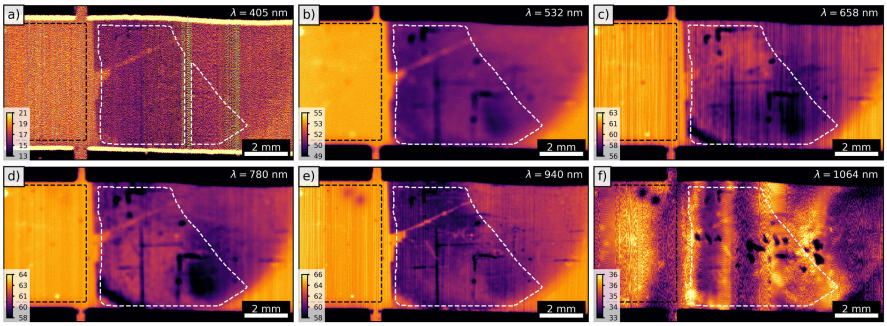

Figure 6.10: *EQE maps of a the tallest silver NW grid (h = 456 nm, AR = 3.2). The silver NW grid and bare Si surface areas used for the analysis are encircled by dashed white and black lines, respectively. The excitation wavelength is noted in the top right corner. The colour bar in the inset specifies the range of EQE values in percentage.*

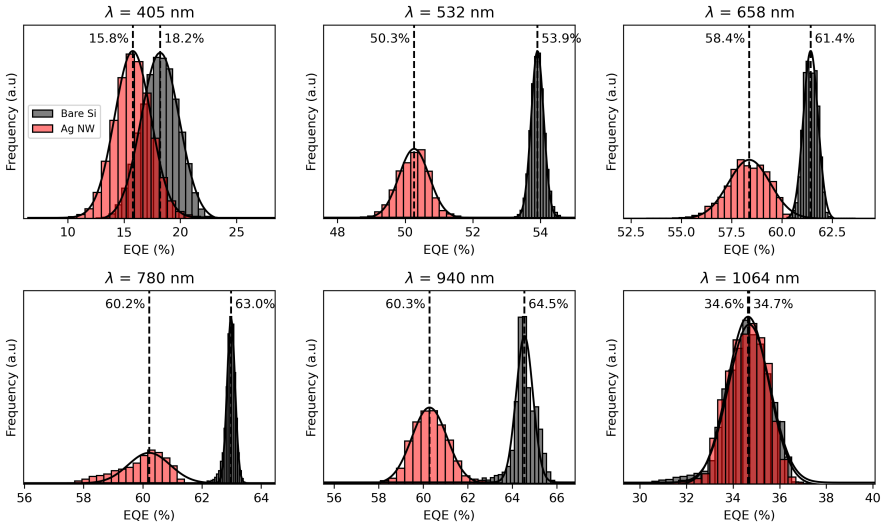

Figure 6.11: *Histograms of the EQE maps, as shown in Figure 6.10, for different excitation wavelengths, as specified in the title of the subplots. The histograms corresponding to the area containing the silver NW grid and the area of the bare Si are represented by the red and black bars, respectively. The expected value from the Gaussian fit is represented by the black dashed line, and its value is noted next to it.*

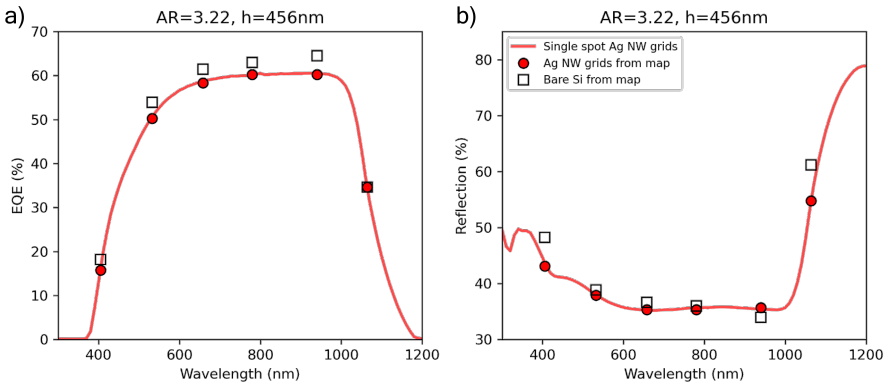

Figure 6.12: *Single-point a) EQE and b) reflection spectrum of the tallest silver NW grid (h = 456 nm) obtained at a spot located withing the area containing the silver NW grids. The average a) EQE and b) reflection values extracted from the EQE maps for the area containing the silver NW grids and the bare Si are represented by the red circles and black open squares, respectively.*

6

6.5.3 Angle dependence J_{sc}

The shape of the angle dependence J_{sc} curve shown in Figure 6.5a can be explained by the angle-dependent reflection and the decrease in intensity with increasing angle of incidence. The decrease in intensity is a result of the mask, which limits the illuminated area $A = L \times L$. Since the spot size of the solar simulator is much larger than the area of the mask, with constant output power P_0, the amount of photons falling within the area of the mask decreases with increasing angle of incidence. The intensity $I_0 = P_0 / A$ is calibrated to be 1.0 sun under normal incidence. However,

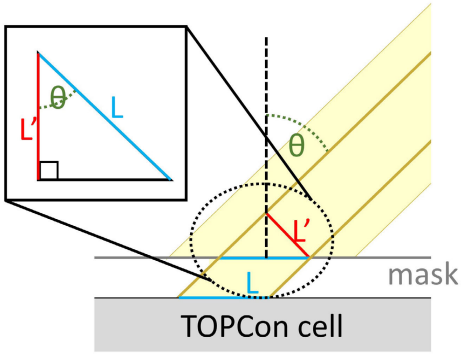

Figure 6.13: *Effect of the mask on the transmitted intensity. The area $A = L \times L$ is defined by the size of the mask. The area $A = L \times L'$ normal to the light beam.*

with an increasing angle of incidence, the power P transmitted through the mask decreases as the area A' normal to the light beam decreases (see Figure 6.13). The angle of rotation of the light source was chosen so that it is perpendicular to one of the edges of the mask, as shown in Figure 6.14. Therefore, only one of the two lengths is affected by the angle of incidence, which we call L'. The relationship between the area $A' = L \times L'$ normal to the light beam and the angle of incidence is given by:

$$A' = L \times L' = A\cos(\theta) \tag{6.2}$$

and hence the power that is transmitted through the mask is given by:

$$P = I_0 A' = I_0 A\cos(\theta) \tag{6.3}$$

where I_0 is the intensity at normal incidence. Therefore, the intensity as a function of the angle of incidence falling onto the solar cell is given by:

$$I(\theta) = \frac{P}{A} = I_0\cos(\theta). \tag{6.4}$$

The second effect that causes the J_{sc} to decrease with increasing angle of incidence is due to angle-dependent reflection. The final expression for the expected angle dependence J_{sc} normalised by its value at normal incidence is given by:

$$\frac{J_{SC}}{J_{SC,0}} = [1 - R(\theta)]\cos(\theta) \tag{6.5}$$

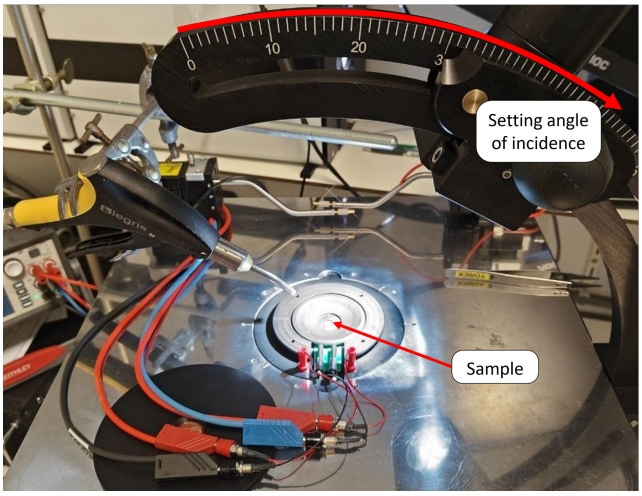

Figure 6.14: *Photograph of the used setup for the angle dependence measurements. The angle of incidence can be manually be adjusted. The sample was contacted with two pins from the top, and two pins from the bottom. A mask of 5x5 mm^2 was used to limit the illuminated area.*

where $R(\theta)$ is the angle-dependent reflection and could be calculated using the Fresnel reflection coefficient. The total (non-polarised) reflection is taken to be the average of the reflection for TE- and TM-polarised light. The normalised J_{sc} as a function of the angle of incidence is shown in Figure 6.15, and the overall shape is quite well explained by Equation 6.5. However, minor differences are present when comparing Equation 6.5 with the flat reference. These minor differences are expected to be the result of some power fluctuations of the solar simulator and due to unwanted reflection from the setup. Therefore, the relative J_{sc} shown in Figure 6.5b was normalised by the flat reference sample instead of by Equation 6.5.

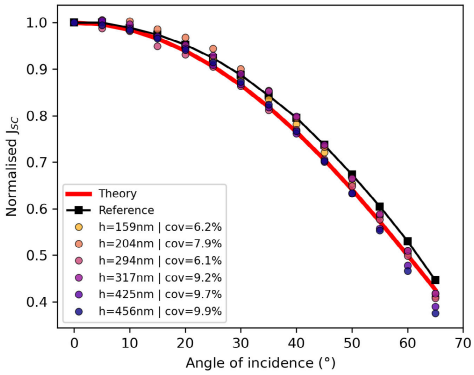

Figure 6.15: *Normalised J_{sc} as function of the angle of incidence. The theoretical curve for a flat TOPCon solar cell is represented by the red solid line. The flat TOPCon reference cell is represented by the black squares connected with a solid line, while the TOPCon cells including silver NW grids are represented by circles connected with a dashed line.*

6.5.4 FDTD simulations: angle-dependent absorption

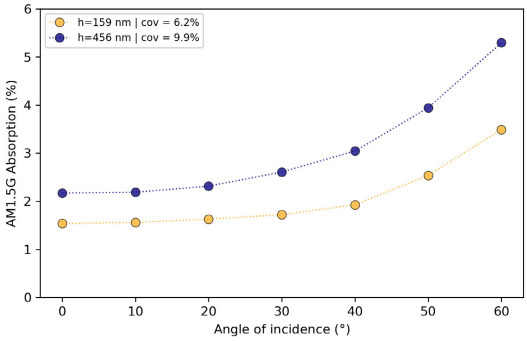

Figure 6.16: *AM1.5G weighted average absorption (1-T-R) as function of angle of incidence for the shortest ($h = 159$ nm) and tallest ($h = 459$ nm) silver NW grid. The absorption by the silver NW grids start to strongly absorb for angles of incidence greater than 40°.*

6.5.5 I-V Characteristics

One-sun and dark I-V curves were obtained for all samples. The I-V curve of the flat reference cell and two representative samples are shown in Figure 6.17a-b. To obtain the current density J, the one-sun I-V curves were normalised by their area of illumination (5x5mm^2), while the dark I-V curves were normalised by the total sample area. From the log(J) vs V plot, the dark current density J_0 and the ideality factor can be extracted. The current density in the dark is given by:

$$J = J_0 \exp\left(\frac{qV}{nk_bT}\right) \tag{6.6}$$

where q is the elementary charge, k_b the Boltzmann constant, T the temperature, and n the ideality factor. The dark current J_0 is extracted by taking the intercept with the y-axis by fitting a line to the log(J) vs. V between 400 and 650 mV. The dark current J_0 found for the reference TOPCon cell and samples having a silver NW grid height of 159 and 294 nm are $2.2 \cdot 10^{10}$, $3.7 \cdot 10^{9}$ and $8.1 \cdot 10^{9}$ fA/cm^2, respectively. The slope of this line provides information on the ideality factor n. Instead of calculating the ideality factor n for a specific voltage range, the ideality factor was calculated by taking the derivative of the log(J)-V plot, and is shown in Figure 6.17.

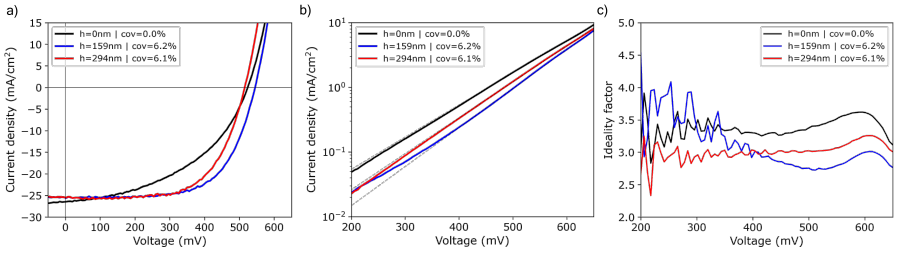

Figure 6.17: *a) One-sun J-V curves for selected samples showing the increase in FF and decrease of J_{sc} due to the silver NW grids (blue and red curve). b) Dark-current response of the selected samples, showing a large recombination current. c) Ideality factor as function of voltage extracted from the dark-current response.*

6.5.6 Illustration of the used sample holder

The sample holder used for the measurement of the angle dependence J_{sc} and the I-V characteristics is shown in Figure 6.18. The sample was contacted from the bottom and the front using 4 probes, two pins to contact the front side, and two pins to contact the rear side. The gold pins were sputter coated with silver to prevent direct contact of the Si with gold. The sample is placed between two plates that are attached to each other using four magnets. A cone-like shape was removed from the top plate to allow the sample to be illuminated up to an angle of incidence of 65°. A stainless steel mask (5x5 mm) was used to selectively illuminate the area that contains the silver NW grids.

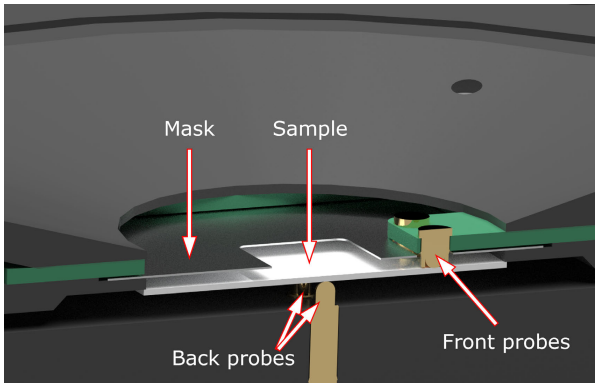

Figure 6.18: *Cross cut of the sample holder used for the measurements of the angle dependence J_{sc} and the I-V characteristics. The mask and sample are indicated by the arrows.*

7

Electrochemical Welding of Assembled Silver Nanocubes by Nanocube Imprint Lithography

This chapter investigates the use of monocrystalline silver nanocubes as seeds for the electrochemical growth of silver nanowire grids with potentially higher crystalline quality and thus better electrical performance. Nanocube imprint lithography developed by our collaborator is used to assemble colloidally-grown monocrystalline nanoparticles with a size of 40 nm into a grid-like pattern on ITO substrates. Subsequently, our investigation focuses on welding these silver nanocubes via electrochemical overgrowth. We take advantage of the silver nucleation overpotential on foreign materials to selectively electrodeposit silver on the nanocubes without inducing the formation of new silver nuclei on the ITO substrate. We find indirect evidence for epitaxial overgrowth, as the electrochemically-induced grain size increase in the nanocubes, as obtained from XRD, coincides with that from morphological measurements (AFM and SEM). Our findings also underscore the critical importance of ligand removal for the successful overgrowth and welding, also supporting the electrochemical nature of the process.

7.1 Introduction

As structures become smaller than the wavelength of light, the light-matter interaction can be controlled by their geometry (shape and size), material composition, and the dielectric environment.[92,93,293] In particular, metal plasmonic nanoparticles exhibit strong resonances.[88] By controlling the arrangement of these metal nanoparticles on a substrate, the way in which light is scattered and absorbed can be tuned for specific applications.[91] These include surface-enhanced spectroscopy,[294] catalysis,[295] sensing,[93] photovoltaics,[90–92] photothermal therapy,[296] and transparent conductive materials (TCMs).[75,98] Traditionally, a resist layer is patterned using top-down techniques such as electron-beam lithography (EBL), combined with metal evaporation followed by lift-off or selective etching.[297] Although EBL provides excellent spatial control, it is expensive, containing multiple complex steps, and is time-consuming.[298] Metal evaporation requires high temperature (energy intensive) and often often leads often to poor quality, thus limiting the electrical and optical response of the nanostructures. Furthermore, evaporation is resource-inefficient, which is particularly problematic for large-scale applications of critical raw materials such as silver and gold. These drawbacks hinder the employment of EBL-based patterning combined with the evaporation technique in large-scale high-throughput applications.

To overcome these limitations, alternative methods for metal nanostructure fabrication have been explored. Instead of evaporation, electroplating can be used for the fabrication of metal nanostructures.[108,143,144] Electroplating, or electrodeposition, is a widely used technique in industry, involving the reduction of a metal ion into solid metal onto a conductive substrate to form the desired pattern or structure by selectively filling the template. The electrochemical reaction can be simply controlled by an external applied voltage or current, can be performed at low temperatures, uses low-cost plating baths, and is resource efficient, as the metal is deposited only on the conductive part of the substrate, and not on top of the insulating template. The chemical engineering of the plating bath is highly developed, and numerous commercial plating baths are available that offer different material properties of the deposit.[299]

Alternatively, nanoimprint lithography can be used to create templates that contain nanoscale features, allowing for precise control over the deposition process during electrodeposition.[148,300,301] Nanoimprint lithography offers a versatile and efficient method for fabricating precise patterns over large areas with high resolution and throughput and has gained attention in various fields.[302,303] It is based on a polydimethylsiloxane (PDMS) stamp replicated from a master made once with EBL providing excellent spatial resolution (< 10 nm), which can be reused multiple times to create new stamps. The PDMS stamp is used to pattern a resist, and upon curing of the resist, the PDMS stamps have transferred the nanopattern defined by EBL, resulting in a copy of the master. The stamp can be used many times, thus significantly reducing the cost associated with EBL. Therefore, techniques that enable precise control over the electrodeposition process, such as the use of templates fabricated by nanoimprint lithography, are of significant interest in

nanofabrication and device manufacturing.

Aside from the multiple advantages of electrodeposition, such as an increased resource efficiency compared to conventional deposition methods, this method presents challenges in achieving uniform films with large crystal sizes. The crystal size of the nuclei is a critical parameter that influences the conductivity in metals,[246,247] as was discussed in detail in Chapter 4. In the case of metal nanowires, the resistivity is given by the inelastic electron scattering at the nanowire surface and by electron scattering at grain boundaries, as described by the combined model of Fuchs and Sondheimer[243,244] and Mayadas and Shatzkes[245] (see Equation 4.1). Based on this model, increasing the average grain diameter d to values much larger than the electron mean free path λ ($d >> \lambda$), electron scattering at grain boundaries is minimised, and thus resistivity decreased.

An exciting approach to increase the crystal size in films and nanopatterns is the welding of monocrystalline metal nanocubes that have been pre-aligned with a desired pattern. These monocrystalline nanocubes are typically obtained by solution-based colloidal synthesis, which typically results in crystals of the highest quality, which makes them ideal for obtaining optimal performance.[304] Nanocube imprint lithography is a highly promising low-cost technique for the assembly of these monocrystalline crystals into large-scale arrangements.[305–307] Similar to nanoimprint lithography, a patterned PDMS stamp is used to imprint a layer of metal nanocubes capped with polyvinylpyrrolidone (PVP). The PVP ligands are essential for the successful assembly of metal nanocubes, as they are used as lubricants and mitigate the van der Waals forces between the substrate and the nanocubes.[306] However, due to the use of these PVP ligands, the nanocubes are electrically separated from each other and subsequent removal of the ligands and welding of the nanocubes are needed.

In this work, we explore the use of electrodeposition for the overgrowth and welding of colloidally-grown monocrystalline nanocubes arranged in nanogrid patterns. The nanocubes offer a highly homogeneous initial grain size distribution. We compare the overgrowth of the nanocubes with that of silver nanoparticles that have been made via template-assisted electrocrystallization. SEM and AFM demonstrate that overgrowth is possible in both cases, although we find that complete removal of PVP ligands from the silver nanocubes is essential for enabling electrochemical overgrowth. From detailed XRD analysis we infer the average coherent crystal size (i.e., crystal grain size), and we find that the grain size increases in proportion the morphology upon electrodeposition. This is an indication of epitaxial overgrowth and is therefore highly promising for high-quality metal nanogrid fabrication. While we do not have direct evidence of coherent welding, the presented work is a first step toward low-cost fabrication of large-area and high-quality nanostructured metal films for applications such as high-performance TCMs.

7.2 Results and Discussion

Individual silver nanoparticles positioned in a grid pattern were fabricated on ITO substrates by using two distinct methods: template-assisted electrocrystallization and nanocube imprint lithography. These silver nanoparticles serve as seeds for the subsequent unconstrained silver overgrowth, with the ultimate goal of nanoparticle-nanoparticle welding and the formation of a continuously connected silver nanowire network.

In the case of template-assisted electrocrystallization for the creation of silver nanoparticles on a grid-like pattern, a PMMA mask featuring a grid pattern with a pitch of 2 μm and a width of 80 nm was fabricated using substrate conformal imprint lithography (SCIL). A low density of silver nanoparticles was then selectively deposited within these trenches by using the double pulse method. As discussed in detail in Chapter 3, the nucleation pulse potential plays a crucial role in determining the nucleation density, while the growth pulse primarily influences the radius of the nuclei without creating new nuclei on the ITO substrate. By using a nucleation pulse potential of -0.655 V vs. Ag/AgCl, a nucleation density of approximately 4 particles per line ($\approx 4 \cdot 10^8$ particles per cm^2) is achieved. The short duration of the growth pulse resulted in a particle size of 96±61 nm, which is much smaller than the 280 nm needed for coalescence (based on isotropic growth) and therefore results in incomplete trench filling. After removal of the mask, the sample consists of spaced nanoparticles arranged in a grid-like pattern, as shown in Figure 7.1a.

Later, these isolated silver nanoparticles were further grown by applying a slight overpotential, although smaller than the nucleation overpotential of ITO, thereby preventing the formation of new silver nuclei on the ITO substrate. Figure 7.1b shows the silver nanoparticles after the overgrowth step. For a growth duration of 30 s, the average particle size increased from 96±61 nm to 159±78 nm (see Figure 7.7 in the Supplementary Information). The SEM images reveal that no new silver nuclei were formed on the ITO substrate, and only pre-existing silver nanoparticles were increased in size. With the absence of the PMMA mask, the growth of silver nanoparticles is unconstrained, resulting in an increase in the width of the "wires." This can be clearly seen in the zoomed-in SEM images shown in the insets of Figure 7.1. While the particles in the inset of Figure 7.1a have a width as defined by the width of the trench, the overgrown particles in the inset of Figure 7.1b exhibit a more round morphology, indicative of the unrestricted growth of silver without geometric constraints. Note that the SEM images before and after the overgrowth were captured at different locations on the sample.

During the unconstrained growth of the silver nanoparticles, reflectance spectra were obtained (see Figure 7.8 in the Supplementary Information). The reflectance spectrum obtained just before the experiment was used as a reference, with all subsequent spectra normalised accordingly. In general, an increase in reflection across a wide spectral range from 450 to 1000 nm is observed as the silver nanoparticles grow in size. Approximately 10 seconds into the growth process, a broad band emerges in the spectral range of 500-900 nm. The increase in reflection in this range is expected to be the result of increased scattering by the growing silver nanoparticles.

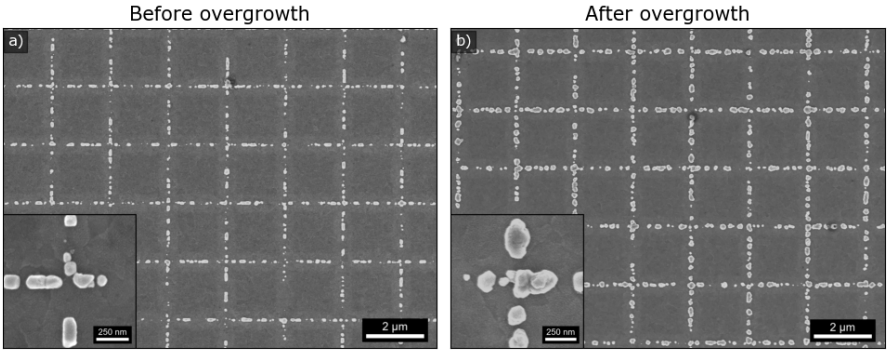

Figure 7.1: *SEM image of silver nanoparticles fabricated using template-assisted electrocrystallization for a) as deposited and b) after electrochemical overgrowth with silver. The SEM images were taken at two different spots of the sample. Silver nuclei were deposited using the silver sulphate-based electrolyte using a growth time of 90 s, while the overgrown silver was deposited using the commercial electrolyte using a growth time of 30 s. The inset shows a zoom-in of the nanoparticles.*

The determination of an average size for the growing silver nanoparticles proved challenging because of the broad distribution of nanoparticle sizes. Moreover, the morphology of the particles undergoes a transformation during growth, transitioning from rod-shaped structures to more spherical-shaped structures.

In contrast to the electrochemically grown seeds, highly monodisperse 40 nm large monocrystalline silver nanocubes were also used. The nanocubes were assembled in a grid-like pattern using nanocube imprint lithography. The nanocube-assembled grids contain nine areas with different pitches and widths (see Section 7.4.2 for more details). During the synthesis and patterning stages of the nanocubes, PVP capping ligands were used to prevent the formation of larger silver clusters.[305–307] Furthermore, these PVP ligands act as a lubricant, and reduce the van der Waals forces that are in play between the silver nanocubes and the ITO substrate,[306] and therefore the ligands are essential for nanocube assembly to be successful. However, these ligands are likely to hinder the electrical contact with the ITO substrate and also with the solution, which is crucial for the electrodeposition. Consequently, the ligands were removed prior to electrochemical welding of the nanocubes.

Figure 7.2a shows a close-up view of a ligand-free nanocube assembled grid, having a width of approximately two nanocubes (80 nm). The SEM image reveals the presence of several defects within the imprinted grid, such as nanocube vacancies and misalignment, which means that their crystal facets fail to align with neighbouring nanocubes. These defects are expected to compromise the conductivity of the grids, thereby reducing the performance of the Ag NW grid as a TCM.

To assess the structural changes resulting from the welding process, we performed an SEM analysis before and after overgrowth with silver at identical locations

on the sample. Figures 7.2a-b show two SEM images obtained before and after overgrowth of the nanocube-assembled grid, respectively, after successful removal of the ligands. No new nuclei were formed because it is thermodynamically more favourable to deposit silver on the already existing silver nanocubes rather than on the ITO substrate. Almost all individual nanocubes have increased in size from an average size of 42±3 nm to 54±17 nm (see Figure 7.9 in the Supplementary Information). This is in contrast to the lack of overgrowth when the ligands are not fully removed (see Figure 7.10 in the Supplementary Information). Instead, here we observe the emergence of new silver nuclei and the deposition of a black layer on top of the nanocubes. Therefore, removal of the ligands is of utmost importance for successful overgrowth and welding.

In the overgrown sample, we observe that the increase in size is not uniform across all particles, where some particles experience significantly larger growth than others. Larger nanocubes tend to adopt a more spherical shape, while smaller ones retain their cubic morphology. Despite the overgrowth, the nanocubes in this area do not seem to have merged into a single wire, since clear boundaries are still visible between the nanocubes. However, we note that in some other areas of the same sample (see Figures 7.3a and b), the interfaces between the silver nanocubes appear faded, indicating potential merging into a single nanowire. The side-view image also hints at merging, although individual nanocubes remain still visible.

Consistent with the observations in Figure 7.2b on the electrodeposited seeds, larger nanocubes adopt a more spherical shape, with varying amounts of growth between the individual nanocubes. Tilted SEM imaging further reveals height discrepancies, as some nanocubes appear taller than others. Despite suggestive indications of welding, confirming complete merging would require other methods. Unfortunately, verification attempts using transmission electron microscopy (TEM) were inconclusive, as the transfer of nanocubes to a TEM grid resulted in scattered

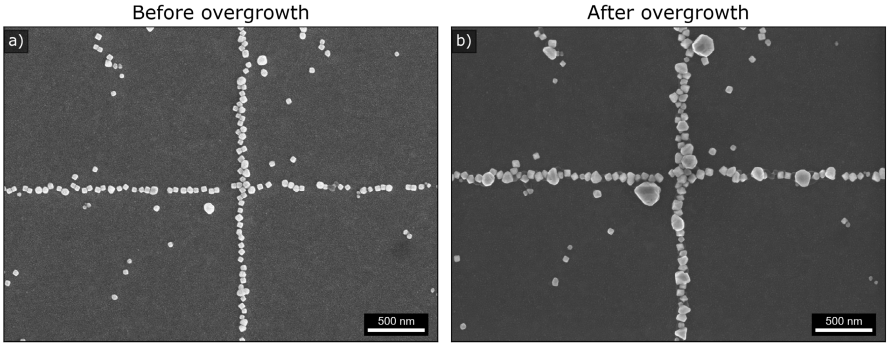

Figure 7.2: *SEM image of silver nanocubes assembled by nanocube imprint lithography for a sample a) after the removal of the PVP ligands, and b) after overgrowth. Both SEM images were obtained at the same spot of the sample. Silver was overgrown for 60 s using the silver sulphate-based electrolyte.*

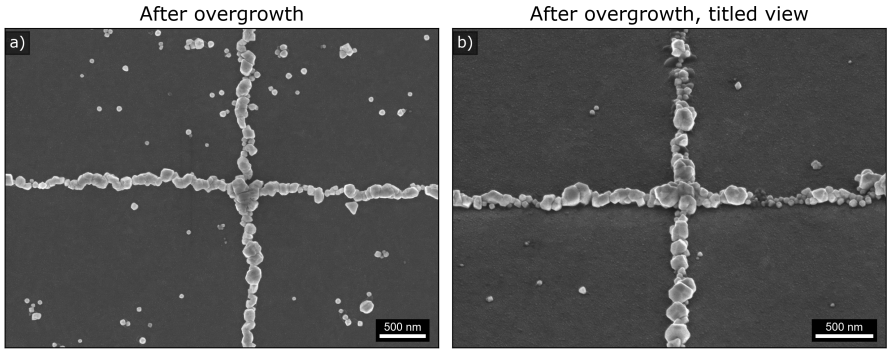

Figure 7.3: *A a) top-view and b) titled-view SEM image of overgrown silver nanocubes obtained at a spot which was not affected by the electron beam prior to the welding. The silver nanocubes were overgrown for 60 s using the silver sulphate-based electrolyte.*

particles whose origins could not be definitively identified.

The main difference between Figures 7.2 and 7.3 is the fact that the area in Figure 7.2a was imaged by SEM before overgrowth, indicating that the welding process is affected by the exposure of the electron beam of the seeds, likely due to local carbon deposition. We have obtained SEM images across multiple grid areas on the sample, each with different pitches and widths. Interestingly, we see that a black layer is present in all post-welding SEM images from areas that were previously imaged by SEM. We attribute this black layer to electron-beam-induced carbon deposition during SEM imaging prior to overgrowth. The carbon deposit passivates the nanocubes surface, thereby hindering the welding process. These findings highlight the importance of thorough removal of ligands and any other organics for effective nanocube welding.

We now further investigate the effects of overgrowth on the nanocubes. To determine the height distribution of silver nanocubes, Atomic Force Microscopy (AFM) images were obtained before and after overgrowth. Figures 7.4a and b show an AFM image of the silver nanocubes assembled by nanocube imprint lithography, before and after overgrowth, respectively. Before overgrowth, AFM gives an average nanocube height of 38±3 nm, consistent with the nominal height of 40 nm. After overgrowth, the average height increases to 58±4 nm, corresponding to a growth rate of approximately 21 nm/min. Notably, height after overgrowth closely resembles the width measured by SEM, suggesting that the nanocubes maintain their aspect ratio. Furthermore, the roughness (Sq) of the cubes increased from 10±2 nm during assembly to 23±5 nm after overgrowth. The increase in roughness indicates spatial heterogeneous silver overgrowth, with some particles experiencing faster growth, leading to a rougher surface. In applications such as transparent electrodes composed of silver nanowires, surface roughness is a critical parameter influencing performance, as the surface roughness increases the surface area of the wire, leading to more electron scattering with the surface.[243,244] Therefore, the observed variations

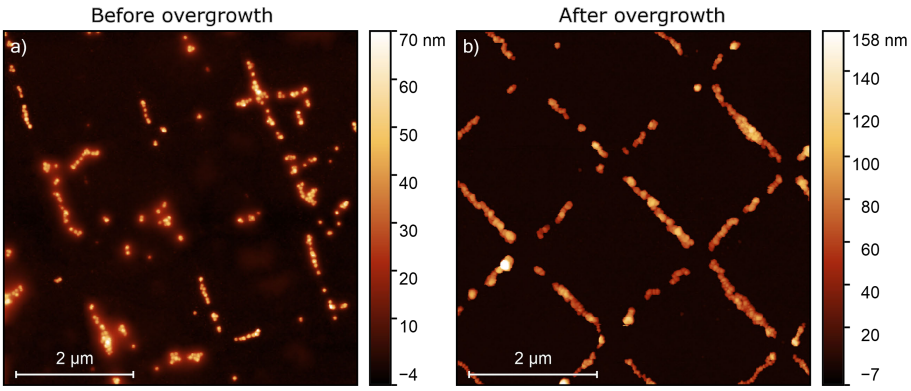

Figure 7.4: *AFM surface topography map of a) assembled nanocubes by nanocube imprint lithography, and b) after welding. The average height of the nanocubes before and after overgrowth are 37.6±3.5nm and 58.4±4.2 nm, respectively. The roughness (Sq) of the nanocubes before and after overgrowth are 10.3±1.9 nm and 23.2±5.3 nm, respectively. The silver was overgrown for 60 s using the silver sulphate-based electrolyte.*

in surface roughness underscore the importance of optimising the plating baths to achieve the desired deposit characteristics. Additives, such as levelers, can be introduced to promote smoother deposits. However, these additives may also impact crystallinity, and thus resistivity via grain boundary scattering.

To investigate crystallinity, X-ray diffraction (XRD) measurements were performed on the samples as-assembled and after overgrowth with silver. Figure 7.5 shows a representative XRD 2θ scan of the as-assembled nanocubes (black) next to that of the with silver overgrown nanocubes (red) using the silver sulphate-based

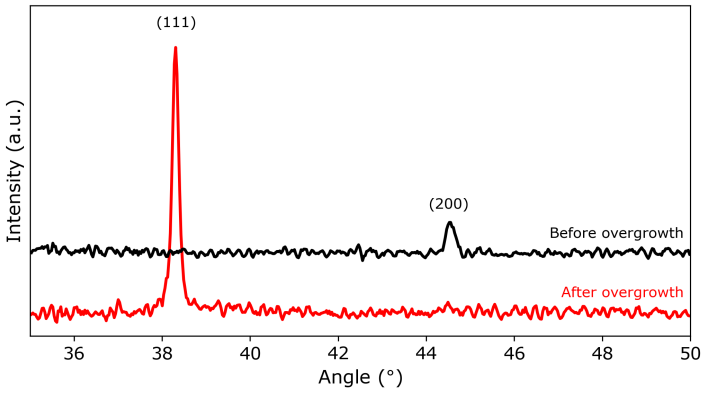

Figure 7.5: *XRD 2θ scans of silver nanocubes as assembled (black) and after welding (red), with the corresponding crystallographic orientations of silver.*

electrolyte. In the as-assembled case, we observe a single peak corresponding to (200) silver. This is in agreement with the nanocubes sitting flat on the ITO substrate with their (100) facets. The peak width reflects the average grain diameter, which can be extracted by using the Scherrer equation (see Section 7.5.5 in the Supplementary Information). From the peak width analysis, we obtain an average grain size of 40.9±1.2 nm for the assembled nanocubes, again closely matching the height given by AFM and the nominal cube size of 40 nm, as expected in monocrystalline nanocubes.

Interestingly, after overgrowth, the (200) silver peak is barely visible, while the (111) silver peak dominates the diffractogram, suggesting a crystal orientation rearrangement from the (100) to the (111) orientation. This rearrangement is in line with the associated surface energies of the facets, where the (111) surface exhibits the lowest energy.[308] From the peak width analysis, we find an average grain size of 55.1±0.8 nm, matching the AFM height and the average size observed from the SEM image shown in Figure 7.2. The same increase in grain size as in the cube height/width suggests that the overgrowth is, in fact, epitaxial.

7.3 Conclusion and Outlook

In this work, the fabrication of patterned individual silver nanoparticles on ITO substrates through template-assisted electrocrystallization and nanocube imprint lithography was investigated. These nanoparticles serve as seeds for the formation of silver nanowires by welding them together using electrochemical overgrowth of silver, with the aim of having a larger average grain size to decrease the resistivity of the silver nanowire network. In the case of template-assisted electrocrystallization, silver was selectively deposited in the trenches using the double-pulse technique, where the used nucleation pulse resulted in a nucleation density which is too low to fill the trenches, therefore resulting in disconnected silver nanoparticles. After removal of the PMMA mask, these silver nanoparticles were increased in size by overgrowth using the growth pulse only. Individual particles were successfully increased in size from 96±61 nm to 159±78 nm, while no new nuclei were formed on the bare ITO surface.

In the case of nanocubes assembled using nanocube imprint lithography, we show that removal of the ligands is crucial for successful welding. The SEM and AFM measurements reveal that the overgrown nanocubes maintain their aspect ratio, with some adopting a more spherical shape. They increased in size from 42±3 nm to 54±17 nm, which corresponds remarkably well with the average grain size obtained from XRD measurements, which was found to have increased from 40.9±1.2 nm and 55.1±0.8 nm. The closely obtained values suggest epitaxial overgrowth of silver. XRD analysis also indicates a crystal orientation shift from the (100) to the (111) orientation of silver. The AFM analysis reveals an increase in the roughness of the overgrown nanocubes, highlighting the importance of plating bath composition to achieve desired deposit characteristics. These findings underscore the importance of plating bath composition on deposit properties and highlight the necessity of

finding the balance between surface smoothness and crystallinity when optimising plating baths for specific applications.

Despite these advances, numerous defects are present within the assembled nanowires, which limits the electrical conductivity of the nanowires. Addressing these challenges is crucial to realise the full potential of silver nanowire devices in optoelectronic devices. Therefore, our study underscores the need for further optimisation of the nanocube assembly process.

7.4 Methods

7.4.1 Template-assisted electrocrystallisation of silver nanoparticles

Substrate Conformal Imprint Lithography (SCIL) was used for the fabrication of the mask. ITO substrates (KinTec, 10 Ω/sq, 25x25 mm^2) were cleaned by brushing with soap and ethanol, and were sonicated for 10 min in ultra-pure water, 10 min in acetone and 10 min in isopropanol. The ITO substrates were cleaned for 10 s using an oxygen plasma (Oxford Plasmalab 80+, 50 W, 5 mTorr) to activate the surface. The PMMA (MW=950 A8 1:1 anisole, Kayaku Advanced Materials, Inc.) spacer was spin coated on the ITO substrate at 1600 RPM for 45s and was baked at 150 °C for 2 min. The surface of the PMMA was activated using a 30 s oxygen plasma etch (Oxford Plasmalab 80+, 50 W, 5 mTorr). The sol-gel (T1100, SCIL Nanoimprint Solutions) was spin coated on the PMMA layer at 2000 RPM for 10s. A PDMS stamp having a grid pattern with a pitch of 4 μm with a width of 80 nm was pushed into the sol-gel layer and removed after 6 min of curing at room temperature. The residual layer of the sol-gel at the bottom of the imprint was removed using a reactive ion etch using an CHF_3/Ar (Oxford Plasmalab 80+, 67 W, 15 mTorr) etch for 2 min and 30 s, and the PMMA was etched using O_2 plasma (Oxford Plasmalab 80+, 200 W, 5 mTorr) for 30 s. The final depth of the trenches is around 200 nm.

A custom-built PEEK cell with a volume of 24 mL was used for the electrochemical nucleation of the silver nanoparticles, using a standard three-electrode configuration (see Figure 2.3 in Chapter 2). A Pt disc (exposed area 3.08 cm^2) was used as counter electrode, and an Ag/AgCl electrode (leakless miniature ET072, EDAQ) was used as the reference electrode. Before starting each experiment, the miniature reference electrode was calibrated against a saturated Ag/AgCl reference electrode (XR300, Hach). All experiments were performed using an SP-300 Bio-Logic potentiostat.

An aqueous (Millipore Milli-Q®, $\rho > 18.2$ MΩ·cm) electrolyte containing 1 mM Ag_2SO_4 (99.999%, Sigma-Aldrich), 1 mM saccharin (≥ 99%, Sigma-Aldrich), 100 mM Na_2SO_4 (≥ 99.0%, anhydrous, granular, Sigma-Aldrich), 38 mM H_2SO_4 (96% solution in water, ACROS Organics) (pH of 1.7) was used for the electrodeposition of silver. The double pulse method was used to control the nucleation density and the growth rate of the wires independently.[166,167] A nucleation pulse of $E_n = -0.655$ V vs Ag/AgCl was applied for $t_n = 30$ ms, which was followed by a growth pulse of

E_g = 0.373 V vs. Ag/AgCl for t_g = 90 ms. After electrodeposition, the PMMA/sol-gel mask was removed by submerging the samples (vertically orientated) in 40 °C acetone for >15 min, while stirring the solution with a magnetic stir bar.

7.4.2 Nanocube imprint lithography

Silver nanocubes with a size of 40 nm were synthesised (following the procedure of Zhang *et al.*) [309] and were assembled into grids using a commercial nanoimprint lithography (NIL) setup. The nanocube assembly process is shown schematically in Figure 7.6. First, pressurised air is used to inflate the nanopatterned PDMS stamp, thereby creating a convex bottom surface and conformal contact as the stamp is pressed onto the substrate. Creating this conformal contact minimises the misalignment between the substrate and the stamp, thereby improving reproducibility. The PDMS stamp contains 9 areas that each have a dimension of 500x500 μm. These areas contain trenches in a grid pattern with pitches ranging from 1 to 4 μm and widths between 90 and 210 nm (from 2 to 5 nanocubes) and a trench depth of 50 nm (1 nanocube).

In phase 1, silver nanocubes are deposited onto a flat PDMS membrane and then transferred to an ITO substrate using contact printing. Prior to the transfer of silver nanocubes to the ITO substrate, a thin layer of around 30 nm polyvinylpyrrolidone (PVP) was spin coated on the ITO substrate, which is essential for the proper mobility of the nanocubes during the NIL step. PVP acts as a capping ligand, a spacer layer (mitigating van der Waals (VDW) forces at play between the substrate and the nanocubes) and as a lubricant. [306] A droplet of 0.01 wt% Triton X-45 in ethanol was deposited on the PDMS stamp before pressing against the substrate at a steady speed. The solution was used to wet the nanocubes and dissolve the PVP layer, thus enabling the movement of the cubes.

In phase 2, nanocubes are imprinted by the PDMS stamp and pushes the nanocubes away from the nanopatterned area if an excessive amount of PVP is introduced in between them and the substrate, whereas they will be blocked in their starting position if not enough PVP is present on the substrate. The magnitude of

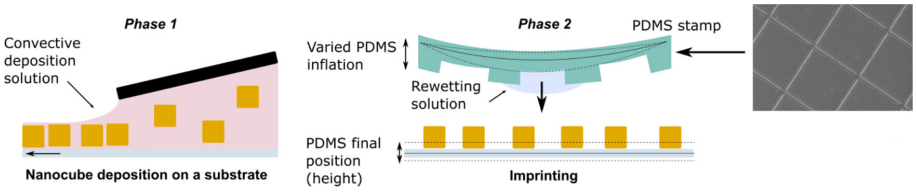

Figure 7.6: *Schematic representation of the nanocube assembly using a commercial NIL setup. In phase 1, the nanocubes are deposited on a flat PDMS membrane and transferred to the ITO substrate by contract printing. In phase 2, the nanocubes are imprinted by pressing the inflated nanopatterned PDMS stamp onto the substrate. The final PDMS position (height) and PDMS inflation are tuned to control the force exerted on the substrate. Reused with permission from reference [306].*

the normal force applied to the substrate was controlled by setting the inflating pressure and PDMS stamp final position. The substrate was then heated to 55 °C for 20 min, while maintaining the PDMS position and pressure, to ensure complete solvent drying before retracting the stamp.

7.4.3 Electrochemical welding

Prior to electrochemical overgrowth of the silver NCs, the PVP ligands were removed by performing the following procedure: The samples were rinsed subsequently in demi-water, acetone, IPA, and demi-water for 1 min per step. The ligands were removed by placing the samples (ITO surface facing up) in a 100 mM $NaBH_4$ (granular, 99.99% trace metals, Sigma-Aldrich) solution for 30 min. Subsequently, the samples were dried using a gentle flow of nitrogen gas. Too much flow of nitrogen gas can cause displacement of the silver NCs, because the ligands, which have been removed, bind them strongly to the substrate.

The same electrochemical cell, as shown in Figure 2.3 in Chapter 2 and described in Section 7.4.1, was used for the electrochemical overgrowth of the silver nanocubes. Two electrolytes were used for the overgrowth of the silver NCs: A commercial silver plating solution (Clean Earth Solutions™, 45.220), and a silver sulphate-based electrolyte, as described in Section 7.4.1. For the commercial electrolyte, a potential of $E = -0.059$ V vs Ag/AgCl and a growth time of $t_g = 30$ s were used, while for the silver sulphate-based electrolyte a potential of $E = 0.33$ V vs Ag/AgCl and a growth time of $t_g = 60$ s were used for the welding of the silver NCs.

7.4.4 In-situ reflection spectrum

In-situ reflection spectra were obtained using the NSECC microscope (see Chapter 5 and Figure 5.9 for more details). Reflection spectra were collected before, during, and after overgrowth of the silver NCs, using an integration time of 100 ms. All spectra were corrected by subtracting the background spectrum. The reflection spectrum before the overgrowth of the silver NCs was used to normalise all other spectra and was therefore used as a reference.

7.4.5 Morphological and structural characterisation

Morphological and structural characterisation of the silver NCs was performed using a FEI Verios 460 scanning electron microscope (SEM) with a working distance of 4 mm, operated at 5 kV and 100 pA. The size distribution was obtained using a watershed image recognition method, using the OpenCV package in Python (https://opencv.org/). For more details, see Section 3.5.3 in Chapter 3.

Topographical maps were obtained with atomic force microscopy (AFM), using a Bruker Dimension Icon and a ScanAsyst-Air probe (Bruker, nominal tip radius 2 nm). The height of the overgrown cubes were extracted by fitting a Gaussian distribution to the masked area corresponding to the wires in the AFM images. The roughness of the samples was obtained by extracting the RMS roughness (Sq) from

the masked area containing silver nanocubes only, using the software Gwyddion (version 2.53).[310]

X-ray diffraction (XRD) was performed using a Bruker D2 Phase diffractometer. The Cu K_α irradiation was operated at 30 kV and 10 mA. The samples were scanned between 2θ = 35° and 80°, with 0.0303° increment using a dwell time of 0.1 s. For the extraction of the average grain size using the Scherrer equation, a scan range of 2θ = 36°-40°, and 2θ = 43.5°-46.5° was used for the (111) and (200) peaks of silver, respectively, using an increment of 0.0101°.

Author Contributions

A.C. and L.F. performed the silver nanocube assembly. Y.B. performed the electrochemical welding. Y.B. performed the SEM, AFM and XRD measurements, and all the data analysis. Y.B. wrote the manuscript. L.F. wrote the experimental section about nanocube assembly. A.C. made Figure 7.6. B.S. and E.A.L. supervised the project.

7.5 Supplementary Information

7.5.1 Size distribution of overgrown nanoparticles by template-assisted electrocrystallization

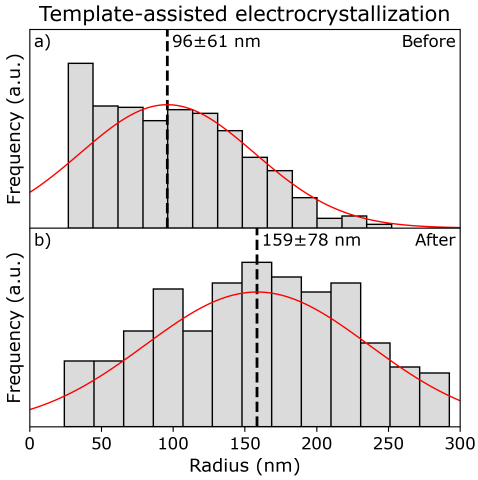

Figure 7.7: *Size distribution before and after overgrowth of the silver nanoparticles fabricated using template-assisted electrocrystallization, as shown in the SEM images in Figure 7.1. The expected value from the Gaussian fit is represented by the vertical dashed line. The error on the expected value is the standard deviation extracted from the Gaussian fit.*

7.5.2 In-situ spectroscopy

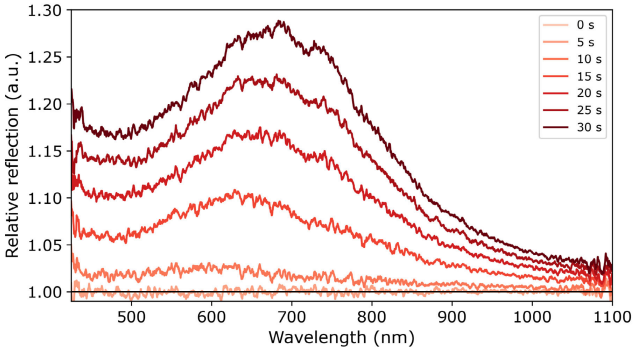

Figure 7.8: *Normalised reflection spectra obtained at different timestamps during the unconstrained growth of the silver nanoparticles. The spectra were normalised to the reflection spectrum right obtained before the start of the experiment.*

7.5.3 Size distribution of overgrown nanocubes by nanocube assembly

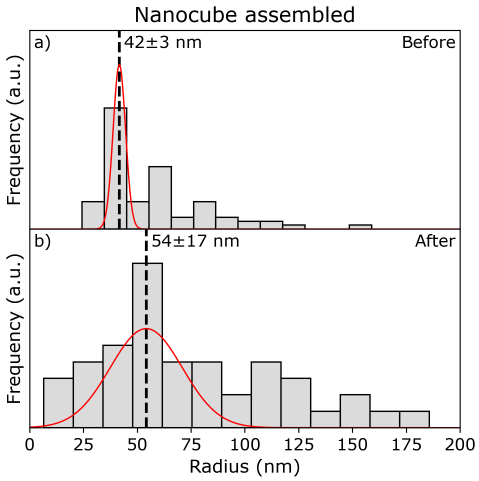

Figure 7.9: *Size distribution before and after overgrowth of the silver nanocubes assembled using nanocube imprint lithography, as shown in the SEM images in Figure 7.2. The expected value from the Gaussian fit is represented by the vertical dashed line. The error on the expected value is the standard deviation extracted from the Gaussian fit.*

7.5.4 Unsuccessful ligand removal

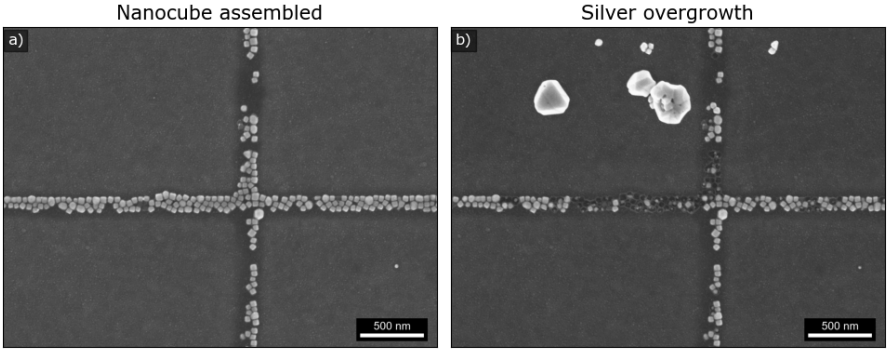

Figure 7.10: *SEM image of silver nanocubes assembled by nanocube assembly for a sample a) after the ligand removal, and b) after electrochemical overgrowth with silver. Both SEM images were obtained at the same spot of the sample. The silver was overgrown for 120 s using the silver sulphate-based electrolyte.*

7.5.5 Average Grain Diameter

The average grain diameter was obtained from the XRD scans. The XRD scans were corrected by subtracting the background and removing the $K_{\alpha,2}$ peak. The average grain diameter was determined by the Scherrer equation:[108,202,251]

$$L = \frac{K\lambda}{\beta \cos(\theta} \tag{7.1}$$

where L is the average grain diameter, $K = 0.9$ is the Scherrer constant, λ is the wavelength of the X-ray ($\lambda = 0.154$ nm for Cu K_α), β is the FHHM peak in radians, and θ is the Bragg angle (half of the 2θ peak position). The FHHM β of Ag(111) ($2\theta = 38.3°$) and Ag(100) ($2\theta = 44.5°$) were corrected for instrument broadening by using a Corundum reference sample using the peak at $2\theta = 37.8°$and $2\theta = 44.4°$, respectively.

Summary

In recent decades, there has been a significant surge in global energy demand, presenting challenges in sustainability and the environment. Renewable energy technologies, such as solar, wind, hydroelectric, and geothermal power, provide sustainable alternatives to fossil fuels with lower carbon emissions. Photovoltaic (PV) technology, which directly converts solar energy into electricity, has seen recent advances that offer higher efficiency and versatility. With the expected exponential increase in installed PV capacity in the coming decade, challenges such as material scarcity and efficiency become increasingly important.

This thesis focuses on replacing indium tin oxide (ITO) with metal nanowire networks (MNNs) as transparent conducting materials (TCMs) for PV applications. MNNs have gained attention due to their excellent electrical conductivity, mechanical flexibility, and potential for tailored optical properties. One crucial aspect in TCMs is striking a balance between electrical conductivity and optical transparency, measured by the Figure of Merit (FoM). The design flexibility of MNNs allows for precise control over optical behaviour, making them highly suitable for light management in PV devices.

In this thesis, we propose the combination of electrodeposition with nanoimprint lithography, as it offers a sustainable and scalable approach for producing well-defined MNNs with precise control over size, shape, and alignment. As demonstrated, this method enables efficient material usage, reducing the overall amount of silver required for manufacturing while maintaining high performance. The development of such materials and methods contributes to a more sustainable solar energy infrastructure, aligning with global efforts towards a cleaner, renewable energy future.

In Chapter 2 we gave a brief introduction to electrochemical theory, describing the definition of an electrochemical reaction, discussed the importance of thermodynamics, electrode kinetics, and mass transport, and described the most commonly used electrochemical techniques. We then focus on the electrochemical deposition of metals on foreign substrates and discussed the importance of the current density distribution on the uniformity of the deposit. We also described a finite element method to simulate the spatial-temporal electrochemical response in 2D electrodes, including cyclic voltammetry and chronoamperometry. From our simulations, we found that cyclic voltammogram simulations of electrodes with a roughness in the order of microns are very sensitive to the tertiary current distribution determined by the concentration profile at the morphological features. Finally, we used our finite element simulation platform to model the chronoamperometry of the growth of metal in nanosized trenches, which is the main topic of this thesis. We showed that these nano-sized trenches can be simply modelled by 1D diffusion as the trench depth is much smaller compared to

the diffusion length.

In Chapter 3 we dived into the electrochemical nucleation of silver on foreign substrates, in particular ITO, using the double pulse technique. We have showed that ITO substrates with the same technical specifications (i.e., sheet resistance, light transmittance, and roughness) and supplier may still have a different crystalline texture, which we found it has a strong impact on the nucleation and growth of silver nanoparticles during electrodeposition. We found that the preferential presence of lower index surfaces leads to a few orders of magnitude lower island density, which strongly depends on the nucleation pulse potential. On the contrary, the island density on ITO with preferential <111> orientation is barely affected by the nucleation pulse potential. This chapter highlighted the importance of reporting the surface properties of polycrystalline substrates when presenting nucleation studies and metal nanoparticle electrochemical growth.

Next, in Chapter 4, we have combined the double pulse method with substrate conformal imprint lithography (SCIL) to fabricate silver nanowire (NW) grids on ITO substrates for the use as TCM for PV applications. The presented method is based on a through-the-mask electrodeposition method, where the mask is made using SCIL. We found that the nucleation density of the silver nanoparticles is the key parameter for the successful homogeneous void-free filling of the template. By using the obtained knowledge from Chapter 3, we independently controlled the density of the silver nuclei and their growth by using the double pulse technique. The silver NW grids show high optical transmission (95.9%) and low sheet resistance (as low as 3.7 Ω/sq), resulting in a superior Figure of Merit (FoM). Due to the bottom-up nature of this technique, arbitrarily high aspect ratio nanowires can be achieved and therefore decrease the sheet resistance without affecting transmittance and carrier collection.

Until now we had only discussed the average transmission of the silver NW grids. However, their nanophotonic nature in combination with the periodic spacing opens up new possibilities for light management by NW-based TCMs. Therefore, in Chapter 5 we have described the light-matter interactions of these silver NW grids. We have discussed the origin behind the characteristic spectral features in transmission and how are these affected by geometry and dielectric environment. We used FDTD simulations to predict light transmission and absorption by the grids, and we showed that the FDTD simulated data explained our experimental observations. Furthermore, the FDTD simulations validated the normalisation method used in Chapter 4 to decouple light transmission of the silver NW grids from that of the substrate in the experiments.

The second part of Chapter 5 described the use of in-situ bright field microscopy to monitor the nucleation and growth of the grid formation. We found that the silver nanoparticles strongly absorb light upon nucleation, resulting in a sudden decrease in reflectance, which is observed both in bright-field microscopy and in spectroscopy. As the nanoparticles grow larger and eventually coalesce, more light is

scattered, which makes the grid pattern appear bright in the microscopy images.

Up until this point, we showed that the silver NW grids are highly transparent and conducting making them suitable for the usage of TCM in PV applications. In Chapter 6 we went one step further by integrating the silver NW grids into an actual solar cell device. We demonstrated the successful fabrication of silver NW grids directly grown on Si-based solar cells by electrochemical deposition without using a seed layer. We have used tunnel oxide passivated contact (TOPCon) solar cells as platform to measure the transparency of the silver NW grids in the right dielectric environment via short-circuit current density (J_{sc}) monitoring, and we showed that the transmission of the silver NW grids is greater than expected from their geometrical footprint. Moreover, we investigated the effect of nanowire aspect ratio on the angle-dependent J_{sc}. We found that the J_{sc} is virtually constant up to an angle of incidence of about 40°, after which the current drops. This decrease in current density at larger angles of incidence was attributed to the increase in absorption by the silver NW grids. Overall, this chapter showed the successful integration of the silver NW grids into real Si-based solar cells, and even improving the performance of the solar cell in the near-infrared spectral regime.

Finally, in Chapter 7, we investigated the use of monocrystalline silver nanocubes as seeds for the electrochemical growth of silver nanowire grids with potentially higher crystalline quality and thus better electrical performance. Nanocube imprint lithography developed by our collaborator was used to assemble colloidally-grown monocrystalline nanoparticles with a size of 40 nm into a grid-like pattern on ITO substrates. Subsequently, we focused on the welding of these silver nanocubes via electrochemical overgrowth. We took advantage from our knowledge obtained in Chapter 3, and used the large nucleation overpotential of silver on ITO substrate to selectively electrodeposit silver on the nanocubes without inducing the formation of new silver nuclei on the ITO substrate. We showed indirect evidence for epitaxial overgrowth, as the electrochemically-induced grain size increase in the nanocubes, as obtained from XRD, coincides with that from morphological measurements (AFM and SEM). Our findings also underscore the critical importance of ligand removal for the successful overgrowth and welding.

In general, in this thesis we have reported a scalable selective area electrochemical method for fabricating interconnected metal nanostructures for transparent conducting materials. Utilising the bottom-up approach of this technique allows for achieving arbitrarily high aspect ratio nanowires, thus reducing sheet resistance without compromising transmittance and carrier collection. This feature proves advantageous for integrating silver nanowire grids into TOPCon solar cells. As such, this thesis contributes to a more sustainable solar energy infrastructure, opening up new paths towards a cleaner, and more renewable energy future.

Samenvatting

In de afgelopen decennia heeft een aanzienlijke stijging van de mondiale vraag naar energie plaatsgevonden, wat uitdagingen met zich meebrengt op het gebied van duurzaamheid en het milieu. Het gebruik van hernieuwbare energietechnologieën, zoals zon, wind, waterkracht en aardwarmte, biedt een duurzamer alternatief met een lagere koolstofemissie vergeleken met fossiele brandstoffen. De recente ontwikkelingen in de fotovoltaïsche (PV) technologie, waarbij zonlicht direct in elektriciteit wordt omgezet, hebben geleid tot een hoger rendement en meer veelzijdigheid in verschillende toepassingen. Doordat de geïnstalleerde PV-capaciteit verwacht wordt exponentieel te stijgen in de komende decennia, worden uitdagingen zoals schaarste van materialen en rendement steeds belangrijker.

Dit proefschrift heeft als doel het vervangen van indium tin oxide (ITO) met netwerken van metalen nanodraden, die gebruikt kunnen worden als een transparant geleid materiaal (TGM) voor PV-toepassingen. Er wordt veel onderzoek gedaan naar deze metalen nanodraden-netwerken (MNN) vanwege de excellente elektrische geleiding, mechanische flexibiliteit, en de mogelijkheid om de optische eigenschappen op maat aan te passen. Een belangrijk aspect in deze TGM's is het vinden van een balans tussen de elektrische geleidbaarheid en de optische transparantie, wat wordt uitgedrukt door de Figure of Merit (FoM). De flexibiliteit in het ontwerp maakt het mogelijk om de optische eigenschappen nauwkeurig te controleren en naar wens aan te passen, waardoor ze enorm geschikt zijn voor lichtmanagement in PV-systemen.

In dit proefschrift bestuderen wij een combinatie van elektrodepositie met nano-imprint lithografie, wat een duurzame en schaalbare aanpak biedt voor de productie van nauwkeurig gedefinieerde MNN's met precieze controle over de grootte, vorm, en uitlijning. Dit proefschrift toont aan dat deze methode materialen op een efficiënte manier gebruikt. Deze techniek kan de totale hoeveelheid consumptie van zilver verminderen die vereist is voor de productie van deze TGM's, terwijl de uitstekende werking behouden blijft. De ontwikkeling van deze materialen en methodes draagt bij aan een duurzamere zonne-energie infrastructuur, wat in lijn is met de wereldwijde inspanningen naar een toekomst met schonere en duurzamere energie.

In Hoofdstuk 2 werd een korte introductie van de elektrochemische theorie gegeven, waarbij de definitie van een elektrochemische reactie werd beschreven. Het belang van thermodynamica, de kinetiek van de elektrode en massatransport zijn ook aan bod gekomen, evenals de meest gebruikte elektrochemische technieken. Vervolgens bespraken we de elektrochemische depositie van metalen op externe substraten en het belang van de verdeling van de stroomdichtheid voor de uniformiteit van de depositie. Wij hebben ook een eindige-elementenmethode beschreven om de ruimtelijk-temporele elektrochemische respons van 2D-elektroden te simuleren, inclusief cyclische voltammetrie en chronoamperometrie.

Deze simulaties hebben aangetoond dat de cyclische voltammogram zeer gevoelig is voor de tertiaire stroomverdeling van elektroden met een ruwheid in de orde van micrometers, waarbij de tertiaire stroomverdeling wordt bepaald door het concentratieprofiel van de metaal ionen rondom de oneffenheden van het oppervlak. Ten slotte hebben we dit eindige-elementenmethode platform gebruikt voor het simuleren van de chronoamperometrie tijdens de groei van zilver in geulen met een breedte van enkele tientallen nanometers, wat het hoofdonderwerp van dit proefschrift is. We hebben aangetoond dat deze nanogeulen eenvoudig kunnen worden gemodelleerd door 1D diffusie, voornamelijk omdat de diepte veel kleiner is in vergelijking tot de diffusie lengte.

In Hoofdstuk 3 hebben wij ons verdiept in de elektrochemische nucleatie van zilver op vreemde substraten, in het bijzonder ITO, met behulp van de dubbel-puls methode. We hebben aangetoond dat ITO-substraten met dezelfde technische specificaties (d.w.z. vierkantsweerstand, lichttransmissie en ruwheid) en leverancier nog steeds een verschillende kristallijne textuur kunnen hebben. In dit onderzoek concludeerde we dat de kristallijne textuur een sterke invloed heeft op de nucleatie en groei van zilveren nanodeeltjes tijdens elektrodepositie. We hebben vastgesteld dat de kiemdichtheid van nanodeeltjes op oppervlakken met een voorkeur voor een lagere kristal index (i.e. <100>) varieert over enkele orders van grootte, afhankelijk van de aangebrachte nucleatiespanning. Echter, de kiemdichtheid van nanodeeltjes op ITO met oppervlakken met een voorkeur voor de <111> kristal oriëntatie wordt nauwelijks beïnvloed door de nucleatiespanning. Dit hoofdstuk benadrukt het belang van het rapporteren van de oppervlakte-eigenschappen van polykristallijne substraten bij het rapporteren van studies naar de elektrochemische nucleatie en groei van metalen nanodeeltjes.

Vervolgens, in Hoofdstuk 4, hebben we de dubbel-puls methode gecombineerd met substraat-conforme imprint lithografie (SCIL) om roosters van zilveren nanodraden op ITO-substraten te fabriceren om te gebruiken als TGM's in PV-toepassingen. De gepresenteerde methode is gebaseerd op elektrodepositie door een masker, gefabriceerd met SCIL, dat de locatie van het zilver bepaalt. We hebben ontdekt dat de kiemdichtheid van de zilveren nanodeeltjes de belangrijkste parameter is voor het succesvol homogeen opvullen van het masker zonder resterende gaten. Dankzij de kennis die wij in Hoofdstuk 3 hebben opgedaan, kunnen we onafhankelijk de kiemdichtheid van de zilveren nanodeeltjes en hun groei controleren met behulp van de dubbel-puls methode. De zilveren nanodraadroosters vertonen zowel een hoge optische transparantie (95.9%) als een lage vierkantsweerstand (zo laag als 3.7 Ω/sq), wat resulteert in een superieure FoM. Vanwege het selectief opbouwende karakter van deze techniek kunnen nanodraden met een willekeurige hoge lengte-breedte verhouding worden bereikt, waardoor de vierkantsweerstand kan worden verlaagd zonder de transmissie en het extraheren van de lading dragers te beïnvloeden.

We hebben tot nu toe alleen het gemiddelde van het transmissie-spectrum

van de zilveren nanodraadroosters besproken. Deze op nanodraden gebaseerde TGM's bieden echter nieuwe mogelijkheden voor het controleren van het licht door hun nanofotonische aard in combinatie met de periodiciteit van de roosters. We hebben daarom in Hoofdstuk 5 de licht-materie interacties van deze zilveren nanodraadroosters beschreven. Hier bespraken we de oorzaak van de karakteristieke kenmerken in het transmissie-spectrum en hoe deze kunnen worden beïnvloed door de geometrie en de diëlektrische omgeving. We gebruikten numerieke simulaties om de transmissie en absorptie van licht door de roosters te berekenen, en verklaarden de experimentele waarnemingen. Bovendien hebben de simulaties de normalisatiemethode van Hoofstuk 4 bevestigd, waarbij we de lichttransmissie door de zilveren nanodraadroosters ontkoppelen van die van het onderliggende substraat.

In het tweede deel van Hoofdstuk 5 werd het gebruik van in-situ microscopie beschreven om de nucleatie en groei van de zilveren nanodraadroosters te bestuderen. We hebben vastgesteld dat de zilveren nanodeeltjes licht sterk absorberen direct na nucleatie, wat resulteert in een plotselinge afname van de reflectie. Dit fenomeen werd waargenomen met behulp van microscopie en spectroscopie. Naarmate de nanodeeltjes groter worden en uiteindelijk een geheel vormen wordt er meer licht verstrooid, waardoor het roosterpatroon erg helder oplicht in de microscopiebeelden.

Onze resultaten tot dusver tonen aan dat de netwerken van zilveren nanodraden zeer transparant en geleidend zijn, waardoor ze geschikt zijn voor het gebruik van TGM's in PV-toepassingen. In Hoofdstuk 6 gingen we nog een stap verder door de zilveren nanodraadroosters te integreren in een zonnecel. We hebben de succesvolle productie van zilveren nanodraadroosters gedemonstreerd die rechtstreeks op een silicium gebaseerde zonnecel zijn gegroeid door middel van elektrochemische depositie zonder gebruik te maken van een initiële metaallaag. Om de transmissie van de zilveren nanodraadroosters in de juiste diëlektrische omgeving te meten via de kortsluitstroom (J_{sc}) hebben we tunnel-oxide passivated-contact (TOPCon) zonnecellen gebruikt als platform. Hiermee hebben we aangetoond dat de transmissie van de zilveren nanodraadroosters groter is dan verwacht op basis van hun geometrische voetafdruk. Bovendien hebben we het effect van de lengte-breedte verhouding van deze nanodraden op de hoek-afhankelijke kortsluitstroom onderzocht. We hebben vastgesteld dat de kortsluitstroom vrijwel constant is tot een invalshoek van ongeveer 40°, waarna de stroomdichtheid sterk afneemt. Deze afname van de stroomdichtheid wordt verklaard door de toename van absorptie in de zilveren nanodraadroosters. Over het algemeen heeft dit hoofdstuk de succesvolle integratie van de zilveren nanodraadroosters in op silicium gebaseerde zonnecellen laten zien, waarbij zelfs het rendement van de zonnecel verbeterd wordt in het nabij-infrarood.

Ten slotte hebben we in Hoofdstuk 7 het gebruik van monokristallijne zilveren nanokubussen onderzocht als kiemen voor de elektrochemische groei van de zilveren nanodraadroosters, die potentieel een hogere kristallijne kwaliteit hebben en dus betere elektrische prestaties. Een nanokubus-imprintlithografietechniek

die door onze partners was ontwikkeld, werd gebruikt om colloïdaal gegroeide monokristallijne zilveren nanokubussen met een grootte van 40 nm samen te rangschikken tot een rooster-achtig patroon op ITO-substraten. Vervolgens hebben we ons gericht op het samengroeien van deze zilveren nanokubussen door middel van elektrochemische overgroei. De kennis die we in Hoofstuk 3 hebben opgedaan, is gebruikt om zilver selectief te groeien op de nanokubussen, zonder het creëren van nieuwe zilverkiemen op het ITO-substraat. We hebben indirect bewijs gevonden voor epitaxiale overgroei, aangezien de toename van de grootte van het kristaldomein zoals verkregen uit Röntgendiffractie overeenkomt met de toename van de grootte verkregen uit morfologische metingen (atomaire krachtmicroscopie, scanning electronemicroscopie). Daarnaast benadrukken onze bevindingen het cruciale belang van het verwijderen van de liganden voor de succesvolle overgroei en samenvoeging van de nanokubussen tot één geheel.

In dit proefschrift rapporteren we een schaalbare elektrochemische oppervlakteselectieve methode voor het maken van onderling verbonden metalen nanostructuren voor het gebruik als transparante geleidende materialen. Het selectief opbouwende karakter van deze techniek maakt het mogelijk om nanodraden met een willekeurige hoge lengte-breedte verhouding te fabriceren. Daardoor kan de vierkantsweerstand worden verlaagd zonder de transmissie en het extraheren van de lading dragers te beïnvloeden. Deze eigenschap blijkt van groot belang voor het integreren van de zilveren nanodraadroosters in TOPCon-zonnecellen. Als zodanig draagt dit proefschrift bij aan een duurzamere zonne-energie infrastructuur, waardoor nieuwe mogelijkheden worden gecreëerd voor een toekomst met schonere en hernieuwbare energie.

Bibliography

[1] Energy Institute: 72nd Statistical Review of World Energy, 2023, ISSN 2976-7857/ISBN 978-1-78725-379-7, (2023).

[2] T. Trzepieciński, T. Batu, F. Kibrete, and H. G. Lemu, *Application of Composite Materials for Energy Generation Devices,* Journal of Composites Science **7**, 55 (2023).

[3] N. Ullah, A. Ahmad, R. Sarfaraz, S. Khalid, I. Ali, M. Younas, and M. Rezakazemi, *Challenges and Solutions in Solar Photovoltaic Technology Life Cycle ,* ChemBioEng Reviews **10**, 541–584 (2023).

[4] IEA World Energy Outlook 2023, IEA, Paris https://www.iea.org/reports/world-energy-outlook-2023, (2023).

[5] NOAA GML CCGG Group, *NOAA Global Monitoring Laboratory Carbon Cycle and Greenhouse Gases Group Continuous Insitu Measurements of CO_2 at Global Background Sites, 1973-Present,* (2019).

[6] M. Allen, O. Dube, W. Solecki, F. Aragón-Durand, W. Cramer, S. Humphreys, J. K. N. M. Y. M. R. P. M. W. M. Kainuma, and K. Zickfeld, in *2018: Framing and Context. In: Global Warming of 1.5°C. An IPCC Special Report on the impacts of global warming of 1.5°C above pre-industrial levels and related global greenhouse gas emission pathways, in the context of strengthening the global response to the threat of climate change, sustainable development, and efforts to eradicate poverty [Masson-Delmotte, V., P. Zhai, H.-O. Pörtner, D. Roberts, J. Skea, P.R. Shukla, A. Pirani, W. Moufouma-Okia, C. Péan, R. Pidcock, S. Connors, J.B.R. Matthews, Y. Chen, X. Zhou M.I. Gomis, E. Lonnoy, T. Maycock, M. Tignor, and T. Waterfield (eds.)]* (Cambridge University Press, UK and New York, NY, USA, 2022) p. 49–92.

[7] C. Le Quéré, M. R. Raupach, J. G. Canadell, G. Marland, L. Bopp, P. Ciais, T. J. Conway, S. C. Doney, R. A. Feely, P. Foster, P. Friedlingstein, K. Gurney, R. A. Houghton, J. I. House, C. Huntingford, P. E. Levy, M. R. Lomas, J. Majkut, N. Metzl, J. P. Ometto, G. P. Peters, I. C. Prentice, J. T. Randerson, S. W. Running, J. L. Sarmiento, U. Schuster, S. Sitch, T. Takahashi, N. Viovy, G. R. van der Werf, and F. I. Woodward, *Trends in the sources and sinks of carbon dioxide ,* Nature Geoscience **2**, 831–836 (2009).

[8] W. F. Lamb, T. Wiedmann, J. Pongratz, R. Andrew, M. Crippa, J. G. J. Olivier, D. Wiedenhofer, G. Mattioli, A. A. Khourdajie, J. House, S. Pachauri, M. Figueroa, Y. Saheb, R. Slade, K. Hubacek, L. Sun, S. K. Ribeiro, S. Khennas, S. de la Rue du Can, L. Chapungu, S. J. Davis, I. Bashmakov, H. Dai, S. Dhakal, X. Tan, Y. Geng, B. Gu, and J. Minx, *A review of trends and drivers of greenhouse gas emissions by sector from 1990 to 2018 ,* Environmental Research Letters **16**, 073005 (2021).

[9] A. Otto, T. Grube, S. Schiebahn, and D. Stolten, *Closing the loop: captured*

CO2 as a feedstock in the chemical industry , Energy & Environmental Science **8**, 3283–3297 (2015).

[10] P. W. Griffin, G. P. Hammond, and J. B. Norman, *Industrial energy use and carbon emissions reduction in the chemicals sector: A UK perspective* , Applied Energy **227**, 587–602 (2018).

[11] A. Arrigoni, D. K. Panesar, M. Duhamel, T. Opher, S. Saxe, I. D. Posen, and H. L. MacLean, *Life cycle greenhouse gas emissions of concrete containing supplementary cementitious materials: cut-off vs. substitution* , Journal of Cleaner Production **263**, 121465 (2020).

[12] F. N. Tubiello, M. Salvatore, S. Rossi, A. Ferrara, N. Fitton, and P. Smith, *The FAOSTAT database of greenhouse gas emissions from agriculture,* Environmental Research Letters **8**, 015009 (2013).

[13] NOAA National Centers for Environmental information, Climate at a Glance: Global Time Series, published January 2024, retrieved on February 8, 2024 from https://www.ncei.noaa.gov/access/monitoring/climate-at-a-glance/global/time-series/globe/land_ocean/12/12/1850-2023, .

[14] United Nations / Framework Convention on Climate Change, "Adoption of the paris agreement, 21st conference of the parties," Report of the Conference of the Parties to the United Nations Framework Convention on Climate Change (21st Session,Paris), (2015).

[15] D. R. Rounce, R. Hock, F. Maussion, R. Hugonnet, W. Kochtitzky, M. Huss, E. Berthier, D. Brinkerhoff, L. Compagno, L. Copland, D. Farinotti, B. Menounos, and R. W. McNabb, *Global glacier change in the 21st century: Every increase in temperature matters* , Science **379**, 78 (2023).

[16] A. Polman, M. Knight, E. C. Garnett, B. Ehrler, and W. C. Sinke, *Photovoltaic materials: Present efficiencies and future challenges,* Science **352**, aad4424 (2016).

[17] N. Lago, *Advances in Photovoltaic Materials and Devices* , Crystals **13**, 925 (2023).

[18] J. Gong, C. Li, and M. R. Wasielewski, *Advances in solar energy conversion* , Chemical Society Reviews **48**, 1862–1864 (2019).

[19] H. M. Ali, T. Rehman, M. Arıcı, Z. Said, B. Duraković, H. I. Mohammed, R. Kumar, M. K. Rathod, O. Buyukdagli, and M. Teggar, *Advances in thermal energy storage: Fundamentals and applications* , Progress in Energy and Combustion Science **100**, 101109 (2024).

[20] X. Peng, Z. Liu, and D. Jiang, *A review of multiphase energy conversion in wind power generation* , Renewable and Sustainable Energy Reviews **147**, 111172 (2021).

[21] O. Paish, *Small hydro power: technology and current status* , Renewable and Sustainable Energy Reviews **6**, 537–556 (2002).

[22] T. Sharmin, N. R. Khan, M. S. Akram, and M. M. Ehsan, *A State-of-the-Art Review on Geothermal Energy Extraction, Utilization, and Improvement Strategies: Conventional, Hybridized, and Enhanced Geothermal Systems* , International Journal of Thermofluids **18**, 100323 (2023).

[23] F. Jamil, I. Shafiq, A. Sarwer, M. Ahmad, P. Akhter, A. Inayat, S. Shafique, Y.-K. Park, and M. Hussain, *A critical review on the effective utilization of geothermal energy,* Energy & Environment **35**, 438–457 (2023).

[24] R. Gold, *Status Report on Electrification Policy: Where to Next? ,* Current Sustainable/Renewable Energy Reports **8**, 114–122 (2021).

[25] W. Zhang, X. Fang, and C. Sun, *The alternative path for fossil oil: Electric vehicles or hydrogen fuel cell vehicles? ,* Journal of Environmental Management **341**, 118019 (2023).

[26] M. Wei, C. A. McMillan, and S. de la Rue du Can, *Electrification of Industry: Potential, Challenges and Outlook ,* Current Sustainable/Renewable Energy Reports **6**, 140–148 (2019).

[27] T. Kataray, B. Nitesh, B. Yarram, S. Sinha, E. Cuce, S. Shaik, P. Vigneshwaran, and A. Roy, *Integration of smart grid with renewable energy sources: Opportunities and challenges – A comprehensive review ,* Sustainable Energy Technologies and Assessments **58**, 103363 (2023).

[28] T. Ahmad, H. Zhang, and B. Yan, *A review on renewable energy and electricity requirement forecasting models for smart grid and buildings ,* Sustainable Cities and Society **55**, 102052 (2020).

[29] I. Dinçer and C. Zamfirescu, *Sustainable Energy Systems and Applications* (Springer US, 2012).

[30] T. Chen, Y. Jin, H. Lv, A. Yang, M. Liu, B. Chen, Y. Xie, and Q. Chen, *Applications of Lithium-Ion Batteries in Grid-Scale Energy Storage Systems ,* Transactions of Tianjin University **26**, 208–217 (2020).

[31] M. Hirscher, V. A. Yartys, M. Baricco, J. Bellosta von Colbe, D. Blanchard, R. C. Bowman, D. P. Broom, C. E. Buckley, F. Chang, P. Chen, Y. W. Cho, J.-C. Crivello, F. Cuevas, W. I. David, P. E. de Jongh, R. V. Denys, M. Dornheim, M. Felderhoff, Y. Filinchuk, G. E. Froudakis, D. M. Grant, E. M. Gray, B. C. Hauback, T. He, T. D. Humphries, T. R. Jensen, S. Kim, Y. Kojima, M. Latroche, H.-W. Li, M. V. Lototskyy, J. W. Makepeace, K. T. Møller, L. Naheed, P. Ngene, D. Noréus, M. M. Nygård, S.-i. Orimo, M. Paskevicius, L. Pasquini, D. B. Ravnsbæk, M. Veronica Sofianos, T. J. Udovic, T. Vegge, G. S. Walker, C. J. Webb, C. Weidenthaler, and C. Zlotea, *Materials for hydrogen-based energy storage – past, recent progress and future outlook,* Journal of Alloys and Compounds **827**, 153548 (2020).

[32] D. Li, K. Yang, J. Lian, J. Yan, and S. F. Liu, *Powering the World with Solar Fuels from Photoelectrochemical CO2 Reduction: Basic Principles and Recent Advances,* Advanced Energy Materials **12**, 2201070 (2022).

[33] A. Mustafa, B. G. Lougou, Y. Shuai, Z. Wang, and H. Tan, *Current technology development for CO2 utilization into solar fuels and chemicals: A review ,* Journal of Energy Chemistry **49**, 96–123 (2020).

[34] J. D. Hunt, B. Zakeri, R. Lopes, P. S. F. Barbosa, A. Nascimento, N. J. d. Castro, R. Brandão, P. S. Schneider, and Y. Wada, *Existing and new arrangements of pumped-hydro storage plants ,* Renewable and Sustainable Energy Reviews **129**, 109914 (2020).

[35] K. M. Tan, T. S. Babu, V. K. Ramachandaramurthy, P. Kasinathan, S. G. Solanki, and S. K. Raveendran, *Empowering smart grid: A comprehensive review of energy storage technology and application with renewable energy integration,* Journal of Energy Storage **39**, 102591 (2021).

[36] M. Y. Worku, *Recent Advances in Energy Storage Systems for Renewable Source Grid Integration: A Comprehensive Review,* Sustainability **14**, 5985 (2022).

[37] *Subcommittee 09, Standard Tables for Reference Solar Spectral Irradiances: Direct Normal and Hemispherical on 37° Tilted Surface, in Book of Standards Volume 14.04 (ASTM International, 2020),* .

[38] Energy Institute - Statistical Review of World Energy (2023), Smil (2017) – with major processing by Our World in Data from https://ourworldindata.org/energy-production-consumption, .

[39] N. M. Haegel, P. Verlinden, M. Victoria, P. Altermatt, H. Atwater, T. Barnes, C. Breyer, C. Case, S. De Wolf, C. Deline, M. Dharmrin, B. Dimmler, M. Gloeckler, J. C. Goldschmidt, B. Hallam, S. Haussener, B. Holder, U. Jaeger, A. Jaeger-Waldau, I. Kaizuka, H. Kikusato, B. Kroposki, S. Kurtz, K. Matsubara, S. Nowak, K. Ogimoto, C. Peter, I. M. Peters, S. Philipps, M. Powalla, U. Rau, T. Reindl, M. Roumpani, K. Sakurai, C. Schorn, P. Schossig, R. Schlatmann, R. Sinton, A. Slaoui, B. L. Smith, P. Schneidewind, B. Stanbery, M. Topic, W. Tumas, J. Vasi, M. Vetter, E. Weber, A. W. Weeber, A. Weidlich, D. Weiss, and A. W. Bett, *Photovoltaics at multi-terawatt scale: Waiting is not an option,* Science **380**, 39–42 (2023).

[40] W. Palz, ed., *Power for the world* (Pan Stanford Publishing, 2010).

[41] E. Becquerel, *La Lumière, ses causes et ses effects: Effets de la lumière* , Vol. 2 (Firmin Didot frères, fils et cie, 1867).

[42] A. C. M. Becquerel, *Traité expérimental de l'électriciteé et du magneétisme, et de leurs rapports avec les pheénomènes naturels* , Vol. 6 (Paris, Firmin Didot frères, 1834).

[43] D. M. Chapin, C. S. Fuller, and G. L. Pearson, *A New Silicon p-n Junction Photocell for Converting Solar Radiation into Electrical Power ,* Journal of Applied Physics **25**, 676 (1954).

[44] G. C. Righini and F. Enrichi, *Solar cells' evolution and perspectives: a short review ,* in *Solar Cells and Light Management* (Elsevier, 2020) p. 1–32.

[45] L. Clapin and T. Longden, *Waiting to generate: An analysis of onshore wind and solar PV project development lead-times in Australia ,* Energy Economics **131**, 107337 (2024).

[46] A. Adenle, *Assessment of solar energy technologies in Africa-opportunities and challenges in meeting the 2030 agenda and sustainable development goals ,* Energy Policy **137**, 111180 (2020).

[47] IRENA, Renewable power generation costs in 2022, International Renewable Energy Agency, Abu Dhabi, (2022).

[48] G. Bilic and S. Scroggins, Lazards, 2023 Levelized Cost Of Energy+ https://www.lazard.com/media/2ozoovyg/lazards-lcoeplus-april-2023.pdf, (2023).

[49] W. Shen, X. Chen, J. Qiu, J. A. Hayward, S. Sayeef, P. Osman, K. Meng, and Z. Y. Dong, *A comprehensive review of variable renewable energy levelized cost of electricity* , Renewable and Sustainable Energy Reviews **133**, 110301 (2020).

[50] A. Romeo and E. Artegiani, *CdTe-Based Thin Film Solar Cells: Past, Present and Future* , Energies **14**, 1684 (2021).

[51] P. M. Mwenda, W. Njoroge, S. Mirenga, and D. M. Kinyua, *Review: Advances in the CIGS Thin Films for Photovoltaic Applications* , Smart Grid and Renewable Energy **13**, 75–87 (2022).

[52] M. F. Islam, N. Md Yatim, and M. A. Hashim@Ismail, *A Review of CZTS Thin Film Solar Cell Technology* , Journal of Advanced Research in Fluid Mechanics and Thermal Sciences **81**, 73–87 (2021).

[53] J. Y. Kim, J.-W. Lee, H. S. Jung, H. Shin, and N.-G. Park, *High-Efficiency Perovskite Solar Cells* , Chemical Reviews **120**, 7867–7918 (2020).

[54] X. feng Zhu, Z. Guo, and Z. Hou, *Solar-powered airplanes: A historical perspective and future challenges* , Progress in Aerospace Sciences **71**, 36 (2014).

[55] E. T. Efaz, M. M. Rhaman, S. A. Imam, K. L. Bashar, F. Kabir, M. E. Mourtaza, S. N. Sakib, and F. A. Mozahid, *A review of primary technologies of thin-film solar cells* , Engineering Research Express **3**, 032001 (2021).

[56] S. Kim, V. Q. Hoang, and C. W. Bark, *Silicon-Based Technologies for Flexible Photovoltaic (PV) Devices: From Basic Mechanism to Manufacturing Technologies,* Nanomaterials **11**, 2944 (2021).

[57] V. Benda and L. Cerna, *A Note on Limits and Trends in PV Cells and Modules* , Applied Sciences **12**, 3363 (2022).

[58] R. Wang, T. Huang, J. Xue, J. Tong, K. Zhu, and Y. Yang, *Prospects for metal halide perovskite-based tandem solar cells* , Nature Photonics **15**, 411 (2021).

[59] S. Mariotti, E. Köhnen, F. Scheler, K. Sveinbjörnsson, L. Zimmermann, M. Piot, F. Yang, B. Li, J. Warby, A. Musiienko, D. Menzel, F. Lang, S. Keßler, I. Levine, D. Mantione, A. Al-Ashouri, M. S. Härtel, K. Xu, A. Cruz, J. Kurpiers, P. Wagner, H. Köbler, J. Li, A. Magomedov, D. Mecerreyes, E. Unger, A. Abate, M. Stolterfoht, B. Stannowski, R. Schlatmann, L. Korte, and S. Albrecht, *Interface engineering for high-performance, triple-halide perovskite–silicon tandem solar cells* , Science **381**, 63–69 (2023).

[60] B. Ehrler and E. M. Hutter, *Routes toward Long-Term Stability of Mixed-Halide Perovskites* , Matter **2**, 800–802 (2020).

[61] L. McGovern, M. H. Futscher, L. A. Muscarella, and B. Ehrler, *Understanding the Stability of $MAPbBr_3$ versus $MAPbI_3$: Suppression of Methylammonium Migration and Reduction of Halide Migration* , The Journal of Physical Chemistry Letters **11**, 7127–7132 (2020).

[62] D. R. Williams, Sun Fact Sheet (website), https://nssdc.gsfc.nasa.gov/planetary/factsheet/sunfact.html, accessed: 2024-02-09, (2018).

[63] H. J. Queisser, *Detailed balance limit for solar cell efficiency* , Materials Science and Engineering: B **159–160**, 322–328 (2009).

[64] W. Shockley and H. J. Queisser, *Detailed Balance Limit of Efficiency of p-n Junction Solar Cells* , Journal of Applied Physics **32**, 510–519 (1961).

[65] J. Nelson, *The Physics of Solar Cells* (Published by Imperial College Press and distributed by World Scientific Publishing CO., 2003).

[66] C. Liu, D. Chen, Y. Chen, Y. Ling, Y. Zou, Y. Wang, J. Gong, Z. Feng, P. P. Altermatt, and P. J. Verlinden, *Industrial TOPCon solar cells on n-type quasi-mono Si wafers with efficiencies above 23%* , Solar Energy Materials and Solar Cells **215**, 110690 (2020).

[67] K. Emery, *Solar simulators and I–V measurement methods* , Solar Cells **18**, 251–260 (1986).

[68] European Chemical Society (EuChemS), published September 2018 under the Creative Commons Attribution NoDerivs CC BY-ND, retrieved on February 6, 2024 from https://www.euchems.eu/element-scarcity-displayed-in-new-euchems-periodic-table-of-elements/, .

[69] Y. Zhang, M. Kim, L. Wang, P. Verlinden, and B. Hallam, *Design considerations for multi-terawatt scale manufacturing of existing and future photovoltaic technologies: challenges and opportunities related to silver, indium and bismuth consumption* , Energy & Environmental Science **14**, 5587–5610 (2021).

[70] J. Li, A. Aierken, Y. Liu, Y. Zhuang, X. Yang, J. H. Mo, R. K. Fan, Q. Y. Chen, S. Y. Zhang, Y. M. Huang, and Q. Zhang, *A Brief Review of High Efficiency III-V Solar Cells for Space Application,* Frontiers in Physics **8**, 631925 (2021).

[71] E. D. Gemechu, C. Helbig, G. Sonnemann, A. Thorenz, and A. Tuma, *Import-based Indicator for the Geopolitical Supply Risk of Raw Materials in Life Cycle Sustainability Assessments,* Journal of Industrial Ecology **20**, 154–165 (2015).

[72] *U.S. Geological Survey, Mineral commodity summaries* (US Geological Survey, 2024).

[73] S. Tepner and A. Lorenz, *Printing technologies for silicon solar cell metallization: A comprehensive review* , Progress in Photovoltaics: Research and Applications **31**, 557 (2023).

[74] N. Vandamme, C. Hung-Ling, A. Gaucher, B. Behaghel, A. Lemaître, A. Cattoni, C. Dupuis, N. Bardou, J. Guillemoles, and S. Collin, *Ultrathin GaAs Solar Cells With a Silver Back Mirror* , IEEE Journal of Photovoltaics **5**, 565 (2015).

[75] V. H. Nguyen, D. T. Papanastasiou, J. Resende, L. Bardet, T. Sannicolo, C. Jiménez, D. Muñoz-Rojas, N. D. Nguyen, and D. Bellet, *Advances in flexible metallic transparent electrodes,* Small **18**, 2106006 (2022).

[76] S. Ye, A. R. Rathmell, Z. Chen, I. E. Stewart, and B. J. Wiley, *Metal Nanowire Networks: The Next Generation of Transparent Conductors* , Advanced Materials **26**, 6670–6687 (2014).

[77] D. S. Hecht, L. Hu, and G. Irvin, *Emerging Transparent Electrodes Based on Thin Films of Carbon Nanotubes, Graphene, and Metallic Nanostructures* , Advanced Materials **23**, 1482–1513 (2011).

[78] G. T. Chavan, Y. Kim, M. Q. Khokhar, S. Q. Hussain, E.-C. Cho, J. Yi, Z. Ahmad, P. Rosaiah, and C.-W. Jeon, *A Brief Review of Transparent Conducting Oxides (TCO): The Influence of Different Deposition Techniques on the Efficiency of*

Solar Cells , Nanomaterials **13**, 1226 (2023).

[79] D. R. Cairns, R. P. Witte, D. K. Sparacin, S. M. Sachsman, D. C. Paine, G. P. Crawford, and R. R. Newton, *Strain-dependent electrical resistance of tin-doped indium oxide on polymer substrates* , Applied Physics Letters **76**, 1425–1427 (2000).

[80] R. Bel Hadj Tahar, T. Ban, Y. Ohya, and Y. Takahashi, *Tin doped indium oxide thin films: Electrical properties* , Journal of Applied Physics **83**, 2631–2645 (1998).

[81] Z. Hu, J. Zhang, Z. Hao, Q. Hao, X. Geng, and Y. Zhao, *Highly efficient organic photovoltaic devices using F-doped SnO2 anodes,* Applied Physics Letters **98**, 123302 (2011).

[82] J. Du, D. Zhang, X. Wang, H. Jin, W. Zhang, B. Tong, Y. Liu, P. L. Burn, H.-M. Cheng, and W. Ren, *Extremely efficient flexible organic solar cells with a graphene transparent anode: Dependence on number of layers and doping of graphene* , Carbon **171**, 350–358 (2021).

[83] A. Díez-Pascual, J. Luceño Sánchez, R. Peña Capilla, and P. García Díaz, *Recent Developments in Graphene/Polymer Nanocomposites for Application in Polymer Solar Cells* , Polymers **10**, 217 (2018).

[84] D. A. Ilatovskii, E. P. Gilshtein, O. E. Glukhova, and A. G. Nasibulin, *Transparent Conducting Films Based on Carbon Nanotubes: Rational Design toward the Theoretical Limit,* Advanced Science **9**, 2201673 (2022).

[85] D. S. Hecht, A. M. Heintz, R. Lee, L. Hu, B. Moore, C. Cucksey, and S. Risser, *High conductivity transparent carbon nanotube films deposited from superacid* , Nanotechnology **22**, 075201 (2011).

[86] T. Tran, M. Shrestha, and Q. H. Fan, *Highly transparent and conductive ITO/ultra-thin silver/ITO/glass sandwich structure for optical coatings and optoelectronic devices* , MRS Communications **13**, 1400–1406 (2023).

[87] L.-H. Qin, Y.-Q. Yan, G. Yu, Z.-Y. Zhang, T. Zhama, and H. Sun, *Research Progress of Transparent Electrode Materials with Sandwich Structure* , Materials **14**, 4097 (2021).

[88] R. F. Hamans, M. Parente, A. Garcia-Etxarri, and A. Baldi, *Optical Properties of Colloidal Silver Nanowires* , The Journal of Physical Chemistry C **126**, 8703–8709 (2022).

[89] J. van de Groep, D. Gupta, M. A. Verschuuren, M. M. Wienk, R. A. J. Janssen, and A. Polman, *Large-area soft-imprinted nanowire networks as light trapping transparent conductors* , Scientific Reports **5**, 11414 (2015).

[90] H. A. Atwater and A. Polman, *Plasmonics for improved photovoltaic devices* , Nature Materials **9**, 205 (2010).

[91] E. C. Garnett, B. Ehrler, A. Polman, and E. Alarcon-Llado, *Photonics for Photovoltaics: Advances and Opportunities* , ACS Photonics **8**, 61 (2021).

[92] P. Mandal and S. Sharma, *Progress in plasmonic solar cell efficiency improvement: A status review* , Renewable and Sustainable Energy Reviews **65**, 537–552 (2016).

[93] A. F. Koenderink, A. Alù, and A. Polman, *Nanophotonics: Shrinking light-based technology* , Science **348**, 516–521 (2015).

[94] J. Gao, K. Kempa, M. Giersig, E. M. Akinoglu, B. Han, and R. Li, *Physics of transparent conductors* , Advances in Physics **65**, 553 (2016).

[95] F. Uleman, V. Neder, A. Cordaro, A. Alù, and A. Polman, *Resonant Metagratings for Spectral and Angular Control of Light for Colored Rooftop Photovoltaics* , ACS Applied Energy Materials **3**, 3150–3156 (2020).

[96] V. Neder, Y. Ra'di, A. Alù, and A. Polman, *Combined Metagratings for Efficient Broad-Angle Scattering Metasurface* , ACS Photonics **6**, 1010–1017 (2019).

[97] M. Sun, D. Huang, P. Golvari, S. M. Kuebler, P. J. Delfyett, and P. G. Kik, *Diffractive light-trapping transparent electrodes using zero-order suppression* , Nanophotonics **12**, 3545–3552 (2023).

[98] Y. Zhang, Z. Lu, X. Zhou, and J. Xiong, *Metallic meshes for advanced flexible optoelectronic devices,* Materials Today **73**, 179–207 (2024).

[99] A. Hubarevich, M. Marus, Y. Mukha, K. Wang, A. Smirnov, and X. W. Sun, *Optoelectronic performance of AgNW transparent conductive films with different width-to-height ratios and a figure of merit embodying an optical haze,* AIP Advances **9**, 045226 (2019).

[100] M. Azani, A. Hassanpour, and T. Torres, *Benefits, Problems, and Solutions of Silver Nanowire Transparent Conductive Electrodes in Indium Tin Oxide (ITO)-Free Flexible Solar Cells,* Advanced Energy Materials **10**, 2002536 (2020).

[101] A. M. Russell and K. L. Lee, *Structure-Property Relations in Nonferrous Metals* (Wiley, 2005).

[102] J. Lindroos and H. Savin, *Review of light-induced degradation in crystalline silicon solar cells* , Solar Energy Materials and Solar Cells **147**, 115–126 (2016).

[103] A. Križan, K. Zimny, A. Guyonnet, E. O. Idowu, E. Duguet, M. Plissonneau, L. d'Alençon, T. Le Mercier, and M. Tréguer-Delapierre, *Bimetallic copper-based nanowires and the means to create next-generation stable transparent electrodes* , Nano Express **4**, 042001 (2023).

[104] S. Huang, Y. Liu, F. Yang, Y. Wang, T. Yu, and D. Ma, *Metal nanowires for transparent conductive electrodes in flexible chromatic devices: a review* , Environmental Chemistry Letters **20**, 3005–3037 (2022).

[105] X. Wu, Z. Zhou, Y. Wang, and J. Li, *Syntheses of silver nanowires ink and printable flexible transparent conductive film: A review* , Coatings **10**, 865 (2020).

[106] L. Hu, H. S. Kim, J.-Y. Lee, P. Peumans, and Y. Cui, *Scalable Coating and Properties of Transparent, Flexible, Silver Nanowire Electrodes* , ACS Nano **4**, 2955–2963 (2010).

[107] X. Zhu, M. Liu, X. Qi, H. Li, Y. Zhang, Z. Li, Z. Peng, J. Yang, L. Qian, Q. Xu, N. Gou, J. He, D. Li, and H. Lan, *Templateless, Plating-Free Fabrication of Flexible Transparent Electrodes with Embedded Silver Mesh by Electric-Field-Driven Microscale 3D Printing and Hybrid Hot Embossing,* Advanced Materials **33**, 2007772 (2021).

[108] B. Sciacca, J. van de Groep, A. Polman, and E. C. Garnett, *Solution-Grown Silver Nanowire Ordered Arrays as Transparent Electrodes* , Advanced Materials **28**, 905 (2016).

[109] S. Lee, J. Jang, T. Park, Y. M. Park, J. S. Park, Y.-K. Kim, H.-K. Lee, E.-C. Jeon, D.-K. Lee, B. Ahn, and C.-H. Chung, *Electrodeposited Silver Nanowire Transparent Conducting Electrodes for Thin-Film Solar Cells* , ACS Applied Materials & Interfaces **12**, 6169–6175 (2020).

[110] T. Li, S. Li, X. Li, Z. Xu, J. Zhao, Y. Shi, Y. Wang, R. Yu, X. Liu, Q. Xu, and W. Guo, *A leaf vein-like hierarchical silver grids transparent electrode towards high-performance flexible electrochromic smart windows* , Science Bulletin **65**, 225–232 (2020).

[111] D. B. Fraser and H. D. Cook, *Highly Conductive, Transparent Films of Sputtered* $In_{2-x}Sn_xO_{3-y}$, Journal of The Electrochemical Society **119**, 1368 (1972).

[112] A. Anand, M. M. Islam, R. Meitzner, U. S. Schubert, and H. Hoppe, *Introduction of a Novel Figure of Merit for the Assessment of Transparent Conductive Electrodes in Photovoltaics: Exact and Approximate Form,* Advanced Energy Materials **11**, 2100875 (2021).

[113] G. Haacke, *New figure of merit for transparent conductors* , Journal of Applied Physics **47**, 4086–4089 (1976).

[114] M. Dressel and G. Grüner, *Electrodynamics of Solids: Optical Properties of Electrons in Matter* (Cambridge University Press, 2002).

[115] S. De, T. M. Higgins, P. E. Lyons, E. M. Doherty, P. N. Nirmalraj, W. J. Blau, J. J. Boland, and J. N. Coleman, *Silver Nanowire Networks as Flexible, Transparent, Conducting Films: Extremely High DC to Optical Conductivity Ratios* , ACS Nano **3**, 1767–1774 (2009).

[116] X. Chen, W. Guo, L. Xie, C. Wei, J. Zhuang, W. Su, and Z. Cui, *Embedded Ag/Ni Metal-Mesh with Low Surface Roughness As Transparent Conductive Electrode for Optoelectronic Applications* , ACS Applied Materials & Interfaces **9**, 37048–37054 (2017).

[117] K. S. Cho, S. Kang, Y.-J. Oh, J. S. Park, S. Lee, J.-S. Wi, J.-H. Park, S. Song, K. Kim, Y.-J. Eo, J. H. Yun, J. Gwak, J.-S. Cho, and C.-H. Chung, *Hierarchical Silver Network Transparent Conducting Electrodes for Thin-Film Solar Cells* , ACS Applied Electronic Materials **4**, 823–830 (2022).

[118] H. Hoppe, M. Seeland, and B. Muhsin, *Optimal geometric design of monolithic thin-film solar modules: Architecture of polymer solar cells* , Solar Energy Materials and Solar Cells **97**, 119–126 (2012).

[119] V. Shanmugam, J. Wong, I. M. Peters, J. Cunnusamy, M. Zahn, A. Zhou, R. Yang, X. Chen, A. G. Aberle, and T. Mueller, *Analysis of Fine-Line Screen and Stencil-Printed Metal Contacts for Silicon Wafer Solar Cells* , IEEE Journal of Photovoltaics **5**, 525–533 (2015).

[120] A. Merlo and G. Léonard, *Magnetron Sputtering vs. Electrodeposition for Hard Chrome Coatings: A Comparison of Environmental and Economic Performances* , Materials **14**, 3823 (2021).

[121] H. Şengül, T. L. Theis, and S. Ghosh, *Toward Sustainable Nanoproducts: An*

Overview of Nanomanufacturing Methods , Journal of Industrial Ecology **12**, 329–359 (2008).

[122] C. P. Muzzillo, *Metal nano-grids for transparent conduction in solar cells* , Solar Energy Materials and Solar Cells **169**, 68–77 (2017).

[123] S. Fahad, H. Yu, L. Wang, Z. ul Abdin, M. Haroon, R. S. Ullah, A. Nazir, K.-u.-R. Naveed, T. Elshaarani, and A. Khan, *Recent progress in the synthesis of silver nanowires and their role as conducting materials* , Journal of Materials Science **54**, 997–1035 (2018).

[124] Y. Zhang, J. Guo, D. Xu, Y. Sun, and F. Yan, *One-Pot Synthesis and Purification of Ultralong Silver Nanowires for Flexible Transparent Conductive Electrodes* , ACS Applied Materials & Interfaces **9**, 25465–25473 (2017).

[125] M. J. Saw, B. Ghosh, M. T. Nguyen, K. Jirasattayaporn, S. Kheawhom, N. Shirahata, and T. Yonezawa, *High Aspect Ratio and Post-Processing Free Silver Nanowires as Top Electrodes for Inverted-Structured Photodiodes* , ACS Omega **4**, 13303–13308 (2019).

[126] V. Scardaci, R. Coull, P. E. Lyons, D. Rickard, and J. N. Coleman, *Spray Deposition of Highly Transparent, Low-Resistance Networks of Silver Nanowires over Large Areas* , Small **7**, 2621–2628 (2011).

[127] T. Akter and W. S. Kim, *Reversibly Stretchable Transparent Conductive Coatings of Spray-Deposited Silver Nanowires* , ACS Applied Materials & Interfaces **4**, 1855–1859 (2012).

[128] A. R. Madaria, A. Kumar, and C. Zhou, *Large scale, highly conductive and patterned transparent films of silver nanowires on arbitrary substrates and their application in touch screens* , Nanotechnology **22**, 245201 (2011).

[129] C. Sachse, L. Müller-Meskamp, L. Bormann, Y. H. Kim, F. Lehnert, A. Philipp, B. Beyer, and K. Leo, *Transparent, dip-coated silver nanowire electrodes for small molecule organic solar cells* , Organic Electronics **14**, 143–148 (2013).

[130] D. Langley, G. Giusti, C. Mayousse, C. Celle, D. Bellet, and J.-P. Simonato, *Flexible transparent conductive materials based on silver nanowire networks: a review* , Nanotechnology **24**, 452001 (2013).

[131] Q. H. Tran, D. T. Chu, V. H. Hoang, Q. T. Do, S. H. Pham, P. Leclère, T. D. Nguyen, and D. C. Nguyen, *Enhancement of electrical and thermal properties of silver nanowire transparent conductive electrode by Ag coating* , Materials Science and Engineering: B **278**, 115640 (2022).

[132] X. Lu, Y. Zhang, and Z. Zheng, *Metal-Based Flexible Transparent Electrodes: Challenges and Recent Advances,* Advanced Electronic Materials **7**, 2001121 (2021).

[133] X. Feng, L. Wang, Y. Y. S. Huang, Y. Luo, J. Ba, H. H. Shi, Y. Pei, S. Zhang, Z. Zhang, X. Jia, and B. Lu, *Cost-Effective Fabrication of Uniformly Aligned Silver Nanowire Microgrid-Based Transparent Electrodes with Higher than 99% Transmittance* , ACS Applied Materials & Interfaces **14**, 39199 (2022).

[134] P. Ren and J. Dong, *Direct electrohydrodynamic printing of aqueous silver nanowires ink on hydrophobic substrates for flexible and stretchable electronics* , Manufacturing Letters **33**, 161–166 (2022).

[135] J. Schneider, P. Rohner, D. Thureja, M. Schmid, P. Galliker, and D. Poulikakos, *Electrohydrodynamic NanoDrip Printing of High Aspect Ratio Metal Grid Transparent Electrodes* , Advanced Functional Materials **26**, 833 (2016).

[136] J. Zhang, M. Ahmadi, G. Fargas, N. Perinka, J. Reguera, S. Lanceros-Méndez, L. Llanes, and E. Jiménez-Piqué, *Silver Nanoparticles for Conductive Inks: From Synthesis and Ink Formulation to Their Use in Printing Technologies* , Metals **12**, 234 (2022).

[137] J. G. Ok, M. K. Kwak, C. M. Huard, H. S. Youn, and L. J. Guo, *Photo–Roll Lithography (PRL) for Continuous and Scalable Patterning with Application in Flexible Electronics* , Advanced Materials **25**, 6554–6561 (2013).

[138] J. Gao, Z. Xian, G. Zhou, J. Liu, and K. Kempa, *Nature-Inspired Metallic Networks for Transparent Electrodes,* Advanced Functional Materials **28**, 1705023 (2017).

[139] A. A. Osipov, A. E. Gagaeva, A. B. Speshilova, E. V. Endiiarova, P. G. Bespalova, A. A. Osipov, I. A. Belyanov, K. S. Tyurikov, I. A. Tyurikova, and S. E. Alexandrov, *Development of controlled nanosphere lithography technology,* Scientific Reports **13**, 3350 (2023).

[140] X. Chen, S. Nie, W. Guo, F. Fei, W. Su, W. Gu, and Z. Cui, *Printable High-Aspect Ratio and High-Resolution Cu Grid Flexible Transparent Conductive Film with Figure of Merit over 80 000* , Advanced Electronic Materials **5**, 1800991 (2019).

[141] C. Pan, K. Kumar, J. Li, E. J. Markvicka, P. R. Herman, and C. Majidi, *Visually Imperceptible Liquid-Metal Circuits for Transparent, Stretchable Electronics with Direct Laser Writing,* Advanced Materials **30**, 1706937 (2018).

[142] Y.-Y. Zhao, M.-L. Zheng, X.-Z. Dong, F. Jin, J. Liu, X.-L. Ren, X.-M. Duan, and Z.-S. Zhao, *Tailored silver grid as transparent electrodes directly written by femtosecond laser,* Applied Physics Letters **108**, 221104 (2016).

[143] M. J. Burek and J. R. Greer, *Fabrication and Microstructure Control of Nanoscale Mechanical Testing Specimens via Electron Beam Lithography and Electroplating* , Nano Letters **10**, 69–76 (2009).

[144] E. J. Menke, M. A. Thompson, C. Xiang, L. C. Yang, and R. M. Penner, *Lithographically patterned nanowire electrodeposition* , Nature Materials **5**, 914–919 (2006).

[145] N. Eliaz and E. Gileadi, *Physical Electrochemistry: Fundamentals, Techniques, and Applications, 2nd Edition* , 2nd ed. (Wiley-VCH, 2019).

[146] B. Grübel, G. Cimiotti, C. Schmiga, S. Schellinger, B. Steinhauser, A. A. Brand, M. Kamp, M. Sieber, D. Brunner, S. Fox, and S. Kluska, *Progress of plated metallization for industrial bifacial TOPCon silicon solar cells* , Progress in Photovoltaics: Research and Applications **30**, 615–621 (2021).

[147] W. Ruythooren, K. Attenborough, S. Beerten, P. Merken, J. Fransaer, E. Beyne, C. V. Hoof, J. D. Boeck, and J. P. Celis, *Electrodeposition for the synthesis of microsystems* , Journal of Micromechanics and Microengineering **10**, 101–107 (2000).

[148] M. A. Verschuuren, M. Megens, Y. Ni, H. Van Sprang, and A. Polman, *Large area nanoimprint by substrate conformal imprint lithography (SCIL)* ,

Advanced Optical Technologies **6**, 243 (2017).

[149] L. J. Guo, *Nanoimprint Lithography: Methods and Material Requirements* , Advanced Materials **19**, 495–513 (2007).

[150] A. J. Bard and L. R. Faulkner, *Electrochemical methods* , 2nd ed. (Wiley Textbooks, 2000).

[151] P. Haynes, W.M. Vanýsek, *"Electrochemical series". In CRC handbook of chemistry and physics* , 97th ed. (CRC Press, 2017).

[152] I. Danaee, *2D-3D nucleation and growth of palladium on graphite electrode* , Journal of Industrial and Engineering Chemistry **19**, 1008 (2013).

[153] D. Grujicic and B. Pesic, *Electrodeposition of copper : the nucleation mechanisms* , Electrochimica Acta **47**, 2901 (2002).

[154] B. Scharifker and G. Hills, *Theoretical and experimental studies of multiple nucleation* , Electrochimica Acta **28**, 879 (1983).

[155] L. Guo, G. Oskam, A. Radisic, P. M. Hoffmann, and P. C. Searson, *Island growth in electrodeposition* , Journal of Physics D: Applied Physics **44**, 443001 (2011).

[156] J. Ustarroz, J. A. Hammons, T. Altantzis, A. Hubin, S. Bals, and H. Terryn, *A generalized electrochemical aggregative growth mechanism* , Journal of the American Chemical Society **135**, 11550 (2013).

[157] F. Nasirpouri, *Electrodeposition of Nanosctructured Materials* (Springer Nature, 2019).

[158] M. Paunovic and M. Schlesinger, *Fundamentals of Electrochemical Deposition* , 2nd ed. (John Wiley & Sons, Inc., Hoboken, New Jersey, 2005).

[159] G. J. Janz and D. J. G. Ives, *Silver, Silver Chloride Electrodes* , Annals of the New York Academy of Sciences **148**, 210 (1968).

[160] S. J. Blair, A. C. Nielander, K. H. Stone, M. E. Kreider, V. A. Niemann, P. Benedek, E. J. McShane, A. Gallo, and T. F. Jaramillo, *Development of a versatile electrochemical cell for in situ grazing-incidence X-ray diffraction during non-aqueous electrochemical nitrogen reduction* , Journal of Synchrotron Radiation **30**, 917–922 (2023).

[161] S. M. Kurtz, *Chemical and Radiation Stability of PEEK* , in *PEEK Biomaterials Handbook* (Elsevier, 2012) p. 75–79.

[162] N. Elgrishi, K. J. Rountree, B. D. McCarthy, E. S. Rountree, T. T. Eisenhart, and J. L. Dempsey, *A Practical Beginner's Guide to Cyclic Voltammetry* , Journal of Chemical Education **95**, 197 (2018).

[163] D. Hamilton, *A theory of dendritic growth in electrolytes* , Electrochimica Acta **8**, 731 (1963).

[164] M. George and V. Vaidyan, *A new electrolytic method to grow silver dendrites and single crystals in gel* , Journal of Crystal Growth **53**, 300 (1981).

[165] J. Fang, H. You, C. Zhu, P. Kong, M. Shi, X. Song, and B. Ding, *Thermodynamic and kinetic competition in silver dendrite growth* , Chemical Physics Letters **439**, 204 (2007).

[166] G. Sandmann, H. Dietz, and W. Plieth, *Preparation of silver nanoparticles on ITO surfaces by a double-pulse method* , Journal of Electroanalytical Chemistry

491, 78 (2000).

[167] M. Ueda, H. Dietz, A. Anders, H. Kneppe, A. Meixner, and W. Plieth, *Double-pulse technique as an electrochemical tool for controlling the preparation of metallic nanoparticles* , Electrochimica Acta **48**, 377 (2002).

[168] H. Osman, G. Castle, and K. Adamiak, *Numerical study of particle deposition in electrostatic painting near a protrusion or indentation on a planar surface* , Journal of Electrostatics **77**, 58 (2015).

[169] T. P. Moffat, J. E. Bonevich, W. H. Huber, A. Stanishevsky, D. R. Kelly, G. R. Stafford, and D. Josell, *Superconformal Electrodeposition of Copper in 500–90 nm Features* , Journal of The Electrochemical Society **147**, 4524 (2000).

[170] S. Hassani, K. Raeissi, and M. A. Golozar, *Effects of saccharin on the electrodeposition of Ni–Co nanocrystalline coatings* , Journal of Applied Electrochemistry **38**, 689–694 (2008).

[171] R. bin Mohd Salleh and L. C. Yung, *Influence of acid copper plating additives on void formation during high temperature storage* , 2015 IEEE 17th Electronics Packaging and Technology Conference (EPTC) , 1 (2015).

[172] G. Wei, H. Ge, L. Huang, Q. Wu, X. Wang, and L. Huang, *Influence of complexing agent on the electrodeposited Co–Pt–W magnetic thin films* , Applied Surface Science **254**, 3425 (2008).

[173] X. C. Jiang, C. Y. Chen, W. M. Chen, and A. B. Yu, *Role of Citric Acid in the Formation of Silver Nanoplates through a Synergistic Reduction Approach,* Langmuir **26**, 4400–4408 (2009).

[174] E. El-Giar, R. Said, G. Bridges, and D. Thomson, *Localized Electrochemical Deposition of Copper Microstructures* , Journal of The Electrochemical Society **147**, 586 (2000).

[175] S. R. Brankovic, N. Vasiljevic, T. J. Klemmer, and E. C. Johns, *Influence of Additive Adsorption on Properties of Pulse Deposited CoFeNi Alloys,* Journal of The Electrochemical Society **152**, C196 (2005).

[176] S.-T. Tsai, P.-C. Chiang, C. Liu, S.-P. Feng, and C.-M. Chen, *Suppression of Void Formation at Sn/Cu Joint Due to Twin Formation in Cu Electrodeposit,* JOM **71**, 3012–3022 (2019).

[177] H. Ueno, S. Takagi, T. Shimizu, S. Miwa, and T. Hayashi, *Characteristics of Iron Electrodeposited from Baths Containing Urea and Ammonium Bifluoride* , Journal of The Surface Finishing Society of Japan **23**, 252 (1972).

[178] S. K. Soni, B. W. Sheldon, and S. J. Hearne, *Origins of saccharin-induced stress reduction based on observed fracture behavior of electrodeposited Ni films* , Journal of Materials Science **49**, 1399–1407 (2013).

[179] J. H. Brown, *Development and Use of a Cyclic Voltammetry Simulator To Introduce Undergraduate Students to Electrochemical Simulations* , Journal of Chemical Education **92**, 1490 (2015).

[180] K. F. Riley, M. P. Hobson, and S. J. Bence, *Mathematical methods for physics and engineering* , 3rd ed. (Cambridge University Press, Cambridge, England, 2006).

[181] P. Haynes, W.M. Vanýsek, *"Electrochemical series". In CRC handbook of chemistry and physics* , 97th ed. (CRC Press, 2017).

[182] D. Lide, *CRC Handbook of Chemistry and Physics : A ready-reference book of chemical and physical data* , 88th ed. (Boca Raton, Florida, CRC Press, 2007).

[183] T. P. Moffat, D. Wheeler, and D. Josell, *Superfilling and the Curvature Enhanced Accelerator Coverage Mechanism* , The Electrochemical Society Interface **13**, 46–52 (2004).

[184] D. Josell, D. Wheeler, and T. P. Moffat, *Modeling Extreme Bottom-Up Filling of Through Silicon Vias* , Journal of The Electrochemical Society **159**, D570–D576 (2012).

[185] https://github.com/ybleiji/CVsim, .

[186] M. Rycenga, C. M. Cobley, J. Zeng, W. Li, C. H. Moran, Q. Zhang, D. Qin, and Y. Xia, *Controlling the synthesis and assembly of silver nanostructures for plasmonic applications* , Chemical Reviews **111**, 3669 (2011).

[187] W. P. Hall, J. Modica, J. Anker, Y. Lin, M. Mrksich, and R. P. Van Duyne, *A Conformation- and Ion-Sensitive Plasmonic Biosensor* , Nano Lett. **11**, 1098 (2011).

[188] W. Plieth, H. Dietz, A. Anders, G. Sandmann, A. Meixner, M. Weber, and H. Kneppe, *Electrochemical preparation of silver and gold nanoparticles: Characterization by confocal and surface enhanced Raman microscopy* , Surface Science **597**, 119 (2005).

[189] J. C. Bian, Z. Li, Z. D. Chen, H. Y. He, X. W. Zhang, X. Li, and G. R. Han, *Electrodeposition of silver nanoparticle arrays on ITO coated glass and their application as reproducible surface-enhanced Raman scattering substrate* , Applied Surface Science **258**, 1831 (2011).

[190] A. Tsuboi, K. Nakamura, and N. Kobayashi, *A Localized Surface Plasmon Resonance-Based Multicolor Electrochromic Device with Electrochemically Size-Controlled Silver Nanoparticles* , Advanced Materials **25**, 3197 (2013).

[191] A. Tsuboi, K. Nakamura, and N. Kobayashi, *Chromatic characterization of novel multicolor reflective display with electrochemically size-controlled silver nanoparticles* , Journal of the Society for Information Display **21**, 361 (2013).

[192] A. Tsuboi, K. Nakamura, and N. Kobayashi, *Chromatic control of multicolor electrochromic device with localized surface plasmon resonance of silver nanoparticles by voltage-step method* , Solar Energy Materials and Solar Cells **145**, 16 (2016).

[193] C. J. Barile, D. J. Slotcavage, J. Hou, M. T. Strand, T. S. Hernandez, and M. D. McGehee, *Dynamic Windows with Neutral Color, High Contrast, and Excellent Durability Using Reversible Metal Electrodeposition* , Joule **1**, 133 (2017).

[194] S. Kimura, T. Sugita, K. Nakamura, and N. Kobayashi, *An improvement in the coloration properties of Ag deposition-based plasmonic EC devices by precise control of shape and density of deposited Ag nanoparticles* , Nanoscale **12**, 23975 (2020).

[195] G. Wang, X. Chen, S. Liu, C. Wong, and S. Chu, *Mechanical Chameleon through Dynamic Real-Time Plasmonic Tuning* , ACS Nano **10**, 1788 (2016).

[196] S. Sarina, E. R. Waclawik, and H. Zhu, *Photocatalysis on supported gold and silver nanoparticles under ultraviolet and visible light irradiation ,* Green Chem. **15**, 1814 (2013).

[197] P. Christopher, H. Xin, and S. Linic, *Visible-light-enhanced catalytic oxidation reactions on plasmonic silver nanostructures ,* Nat. Chem. **3**, 467 (2011).

[198] B. Calderón-Jiménez, M. E. Johnson, A. R. Montoro Bustos, K. E. Murphy, M. R. Winchester, and J. R. Vega Baudrit, *Silver Nanoparticles: Technological Advances, Societal Impacts, and Metrological Challenges ,* Front. Chem. **5**, 6 (2017).

[199] N. Fishelson, A. Inberg, N. Croitoru, and Y. Shacham-Diamand, *Highly corrosion resistant bright silver metallization deposited from a neutral cyanide-free solution ,* Microelectronic Engineering **92**, 126 (2012).

[200] X. Li, Z. Zhang, S. Suo, Y. Qiao, B. Du, H. Deng, Z. Hao, and H. Luo, *Microstructure of silver coating of cyanide-free brush plating based on multicomponent coordination system ,* IOP Conference Series: Materials Science and Engineering **688**, 033047 (2019).

[201] F. Z. Ren, L. T. Yin, S. S. Wang, A. A. Volinsky, and B. H. Tian, *Cyanide-free silver electroplating process in thiosulfate bath and microstructure analysis of Ag coatings ,* Transactions of Nonferrous Metals Society of China **23**, 3822 (2013).

[202] S. C. Kung, W. Xing, K. C. Donavan, F. Yang, and R. M. Penner, *Photolithographically patterned silver nanowire electrodeposition ,* Electrochimica Acta **55**, 8074 (2010).

[203] M. Ijaz, M. Zafar, and T. Iqbal, *Green synthesis of silver nanoparticles by using various extracts: a review ,* Inorganic and Nano-Metal Chemistry **51**, 744 (2020).

[204] D. Zhang and Y. Tang, *Enhancing light reflective properties on ITO glass by plasmonic effect of silver nanoparticles ,* Results in Physics **7**, 2874 (2017).

[205] N. Li, L. Yu, P. Wei, J. Ji, J. Zhao, Q. Zhang, Y. Li, and Y. Yin, *Electrochemical Fabrication and Sensing Application of Multicolored Silver Films ,* Adv. Mater. Interfaces **5**, 1800277 (2018).

[206] L. Guo and P. C. Searson, *On the influence of the nucleation overpotential on island growth in electrodeposition ,* Electrochimica Acta **55**, 4086 (2010).

[207] A. Walsh and C. R. A. Catlow, *Structure, stability and work functions of the low index surfaces of pure indium oxide and Sn-doped indium oxide (ITO) from density functional theory ,* Journal of Materials Chemistry **20**, 10438 (2010).

[208] D. Wan, P. Chen, J. Liang, S. Li, and F. Huang, *(211)-Orientation preference of transparent conducting In_2O_3:Sn films and its formation mechanism ,* ACS Applied Materials and Interfaces **3**, 4751 (2011).

[209] H. Liu and R. M. Penner, *Size-selective electrodeposition of mesoscale metal particles in the uncoupled limit ,* Journal of Physical Chemistry B **104**, 9131 (2000).

[210] M. Nagar, A. Radisic, K. Strubbe, and P. Vereecken, *The effect of cupric ion concentration on the nucleation and growth of copper on RuTa seeded*

substrates , Electrochimica Acta **92**, 474 (2013).

[211] M. Nagar, A. Radisic, K. Strubbe, and P. M. Vereecken, *The Effect of the Substrate Characteristics on the Electrochemical Nucleation and Growth of Copper* , Journal of The Electrochemical Society **163**, D3053 (2016).

[212] E. Budevski, G. Staikov, and W. J. Lorenz, *Electrochemical Phase Formation and Growth: An Introduction to the Initial Stages of Bulk Phase Formation* (Wiley-VCH Verlag GmbH, 1996) pp. 149–199.

[213] A. Radisic, P. Vereecken, P. Searson, and F. Ross, *The morphology and nucleation kinetics of copper islands during electrodeposition* , Surface Science **600**, 1817 (2006).

[214] S. E. Rock, D. E. Simpson, M. C. Turk, J. T. Rijssenbeek, G. D. Zappi, and D. Roy, *Nucleation Controlled Mechanism of Cathode Discharge in a Ni/$NiCl_2$ Molten Salt Half-Cell Battery* , Journal of The Electrochemical Society **163**, A2282 (2016), publisher: IOP Publishing.

[215] B. R. Scharifker, J. Mostany, and A. Serruya, *On the spatial distribution of nuclei on electrode surfaces* , Electrochimica Acta **37**, 2503 (1992).

[216] L. Guo and P. C. Searson, *Simulations of Island growth and Island spatial distribution during electrodeposition* , Electrochemical and Solid-State Letters **10**, D76 (2007).

[217] C. Donley, D. Dunphy, D. Paine, C. Carter, K. Nebesny, P. Lee, D. Alloway, and N. R. Armstrong, *Characterization of Indium-Tin Oxide Interfaces Using X-ray Photoelectron Spectroscopy and Redox Processes of a Chemisorbed Probe Molecule: Effect of Surface Pretreatment Conditions* , Langmuir **18**, 450 (2002).

[218] H. Che and M. El Bouanani, *Effects of argon sputtering and UV-ozone radiation on the physico-chemical surface properties of ITO* , Nuclear Instruments and Methods in Physics Research Section B: Beam Interactions with Materials and Atoms **414**, 170 (2018).

[219] S. Ratanaphan, D. L. Olmsted, V. V. Bulatov, E. A. Holm, A. D. Rollett, and G. S. Rohrer, *Grain boundary energies in body-centered cubic metals* , Acta Materialia **88**, 346 (2015).

[220] D. Y. Kim, M.-J. Kim, G. Sung, and J.-Y. Sun, *Stretchable and reflective displays: materials, technologies and strategies* , Nano Convergence **6**, 21 (2019).

[221] C. G. Granqvist, *Electrochromics for smart windows: Oxide-based thin films and devices* , Thin Solid Films **564**, 1 (2014).

[222] Y. S. Oh, D. Y. Choi, and H. J. Sung, *Direct imprinting of thermally reduced silver nanoparticles via deformation-driven ink injection for high-performance, flexible metal grid embedded transparent conductors* , RSC Advances **5**, 64661 (2015).

[223] A. Salehi, X. Fu, D.-H. Shin, and F. So, *Recent Advances in OLED Optical Design* , Advanced Functional Materials **29**, 1808803 (2019).

[224] C. Han, R. Santbergen, M. van Duffelen, P. Procel, Y. Zhao, G. Yang, X. Zhang, M. Zeman, L. Mazzarella, and O. Isabella, *Towards bifacial silicon heterojunction solar cells with reduced TCO use* , Progress in Photovoltaics: Research and Applications **30**, 750 (2022).

[225] H. Park, Y. J. Lee, J. Park, Y. Kim, J. Yi, Y. Lee, S. Kim, C. K. Park, and K. J. Lim, *Front and Back TCO Research Review of a-Si/c-Si Heterojunction with Intrinsic Thin Layer (HIT) Solar Cell ,* Transactions on Electrical and Electronic Materials **19**, 165 (2018).

[226] Z. Sun, X. Chen, Y. He, J. Li, J. Wang, H. Yan, and Y. Zhang, *Toward Efficiency Limits of Crystalline Silicon Solar Cells: Recent Progress in High-Efficiency Silicon Heterojunction Solar Cells ,* Advanced Energy Materials **12**, 2200015 (2022).

[227] R. Lin, J. Xu, M. Wei, Y. Wang, Z. Qin, Z. Liu, J. Wu, K. Xiao, B. Chen, S. M. Park, G. Chen, H. R. Atapattu, K. R. Graham, J. Xu, J. Zhu, L. Li, C. Zhang, E. H. Sargent, and H. Tan, *All-perovskite tandem solar cells with improved grain surface passivation ,* Nature **603**, 73 (2022).

[228] L. Zhu, M. Zhang, J. Xu, C. Li, J. Yan, G. Zhou, W. Zhong, T. Hao, J. Song, X. Xue, Z. Zhou, R. Zeng, H. Zhu, C.-C. Chen, R. C. I. MacKenzie, Y. Zou, J. Nelson, Y. Zhang, Y. Sun, and F. Liu, *Single-junction organic solar cells with over 19% efficiency enabled by a refined double-fibril network morphology ,* Nature Materials **21**, 656 (2022).

[229] M. A. de Boer and K. Lammertsma, *Scarcity of Rare Earth Elements ,* ChemSusChem **6**, 2045 (2013).

[230] Z. C. Holman, A. Descoeudres, L. Barraud, F. Z. Fernandez, J. P. Seif, S. De Wolf, and C. Ballif, *Current Losses at the Front of Silicon Heterojunction Solar Cells ,* IEEE Journal of Photovoltaics **2**, 7 (2012).

[231] M. W. Knight, J. van de Groep, P. C. Bronsveld, W. C. Sinke, and A. Polman, *Soft imprinted Ag nanowire hybrid electrodes on silicon heterojunction solar cells ,* Nano Energy **30**, 398 (2016).

[232] D. Qiu, W. Duan, A. Lambertz, A. Eberst, K. Bittkau, U. Rau, and K. Ding, *Transparent Conductive Oxide Sputtering Damage on Contact Passivation in Silicon Heterojunction Solar Cells with Hydrogenated Nanocrystalline Silicon ,* Solar RRL **6**, 2200651 (2022).

[233] N. Tavakoli, R. Spalding, A. Lambertz, P. Koppejan, G. Gkantzounis, C. Wan, R. Röhrich, E. Kontoleta, A. F. Koenderink, R. Sapienza, M. Florescu, and E. Alarcon-Llado, *Over 65% Sunlight Absorption in a 1 μm Si Slab with Hyperuniform Texture ,* ACS Photonics **9**, 1206 (2022).

[234] V. Neder, S. W. Tabernig, and A. Polman, *Detailed-balance efficiency limits of two-terminal perovskite/silicon tandem solar cells with planar and Lambertian spectral splitters ,* Journal of Photonics for Energy **12**, 015502 (2022).

[235] H. Guo, N. Lin, Y. Chen, Z. Wang, Q. Xie, T. Zheng, N. Gao, S. Li, J. Kang, D. Cai, and D.-L. Peng, *Copper Nanowires as Fully Transparent Conductive Electrodes,* Scientific Reports **3**, 2323 (2013).

[236] Y. Zhu, Y. Deng, P. Yi, L. Peng, X. Lai, and Z. Lin, *Flexible Transparent Electrodes Based on Silver Nanowires: Material Synthesis, Fabrication, Performance, and Applications ,* Advanced Materials Technologies **4**, 1900413 (2019).

[237] A. Kumar, M. Kumar, M. S. Goyat, and D. K. Avasthi, *A review of the latest developments in the production and applications of Ag-nanowires as*

transparent electrodes , Materials Today Communications **33**, 104433 (2022).

[238] J. Van De Groep, P. Spinelli, and A. Polman, *Transparent conducting silver nanowire networks* , Nano Letters **12**, 3138 (2012).

[239] P. B. Catrysse and S. Fan, *Nanopatterned metallic films for use as transparent conductive electrodes in optoelectronic devices* , Nano Letters **10**, 2944 (2010).

[240] A. Khan, C. Liang, Y. T. Huang, C. Zhang, J. Cai, S. P. Feng, and W. D. Li, *Template-Electrodeposited and Imprint-Transferred Microscale Metal-Mesh Transparent Electrodes for Flexible and Stretchable Electronics* , Advanced Engineering Materials **21**, 1900723 (2019).

[241] H. Zhang, N. Zhang, M. Gilchrist, and F. Fang, *Advances in precision micro/nano-electroforming: A state-of-the-art review* , Journal of Micromechanics and Microengineering **30**, 103002 (2020).

[242] A. Khan, S. Lee, T. Jang, Z. Xiong, C. Zhang, J. Tang, L. J. Guo, and L. Wen-Di, *High-Performance Flexible Transparent Electrode with an Embedded Metal Mesh Fabricated by Cost-Effective Solution Process* , Small **12**, 3021 (2016).

[243] K. Fuchs, *The conductivity of thin metallic films according to the electron theory of metals* , Mathematical Proceedings of the Cambridge Philosophical Society **34**, 100 (1938).

[244] E. Sondheimer, *The mean free path of electrons in metals* , Advances in Physics **1**, 1 (1952).

[245] A. F. Mayadas and M. Shatzkes, *Electrical-Resistivity Model for Polycrystalline Films: the Case of Arbitrary Reflection at External Surfaces* , Physical Review B **1**, 1382 (1970).

[246] W. Steinhögl, G. Schindler, G. Steinlesberger, and M. Engelhardt, *Size-dependent resistivity of metallic wires in the mesoscopic range* , Physical Review B - Condensed Matter and Materials Physics **66**, 1 (2002).

[247] W. Steinhögl, G. Schindler, G. Steinlesberger, M. Traving, and M. Engelhardt, *Comprehensive study of the resistivity of copper wires with lateral dimensions of 100 nm and smaller* , Journal of Applied Physics **97**, 023706 (2005).

[248] H. Kanter, *Slow-Electron Mean Free Paths in Aluminum, Silver, and Gold* , Physical Review B **1**, 522 (1970).

[249] D. Gall, *Electron mean free path in elemental metals* , Journal of Applied Physics **119**, 085101 (2016).

[250] C. Xiang, S. C. Kung, D. K. Taggart, F. Yang, M. A. Thompson, A. G. Güell, Y. Yang, and R. M. Penner, *Lithographically patterned nanowire electrodeposition: A method for patterning electrically continuous metal nanowires on dielectrics* , ACS Nano **2**, 1939 (2008).

[251] A. L. Patterson, *The Scherrer Formula for X-Ray Particle Size Determination* , Physical Review **56**, 978 (1939).

[252] D. Gall, *The search for the most conductive metal for narrow interconnect lines* , Journal of Applied Physics **127**, 050901 (2020).

[253] D.-S. Leem, A. Edwards, M. Faist, J. Nelson, D. D. C. Bradley, and J. C. de Mello, *Efficient Organic Solar Cells with Solution-Processed Silver Nanowire Electrodes*

, Advanced Materials **23**, 4371 (2011).

[254] Y. Luo, T. Ning, Y. Pei, X. Feng, S. Zhang, B. Lu, and L. Wang, *High-performance and tailored honeycombed Ag nanowire networks fabricated by a novel electrospray assisted etching process* , Applied Surface Science **571**, 151081 (2022).

[255] S. De and J. N. Coleman, *Are There Fundamental Limitations on the Sheet Resistance and Transmittance of Thin Graphene Films?* , ACS Nano **4**, 2713–2720 (2010).

[256] D. Caudevilla, E. García-Hemme, E. San Andrés, F. Pérez-Zenteno, I. Torres, R. Barrio, R. García-Hernansanz, S. Algaidy, J. Olea, D. Pastor, and A. del Prado, *Indium tin oxide obtained by high pressure sputtering for emerging selective contacts in photovoltaic cells* , Materials Science in Semiconductor Processing **137**, 106189 (2022).

[257] D. J. Griffiths, *Introduction to electrodynamics* (Pearson education, 2014).

[258] C. F. Bohren and D. R. Huffman, *Absorption and scattering of light by small particles* (John Wiley & Sons“, Nashville, TN”, 1983).

[259] G. Mie, *Beiträge zur Optik trüber Medien, speziell kolloidaler Metallösungen* , Annalen der Physik **330**, 377–445 (1908).

[260] X. Xiong, C. Zou, X. Ren, A. Liu, Y. Ye, F. Sun, and G. Guo, *Silver nanowires for photonics applications* , Laser & Photonics Reviews **7**, 901–919 (2013).

[261] P. L. Stiles, J. A. Dieringer, N. C. Shah, and R. P. Van Duyne, *Surface-enhanced Raman spectroscopy* , Annu. Rev. Anal. Chem. **1**, 601 (2008).

[262] L. Wang, M. Hasanzadeh Kafshgari, and M. Meunier, *Optical Properties and Applications of Plasmonic-Metal Nanoparticles* , Advanced Functional Materials **30**, 2005400 (2020).

[263] N. G. Khlebtsov and L. A. Dykman, *Optical properties and biomedical applications of plasmonic nanoparticles* , Journal of Quantitative Spectroscopy and Radiative Transfer **111**, 1–35 (2010).

[264] V. Amendola, R. Pilot, M. Frasconi, O. M. Maragò, and M. A. Iatì, *Surface plasmon resonance in gold nanoparticles: a review* , Journal of Physics: Condensed Matter **29**, 203002 (2017).

[265] J. P. Kottmann, O. J. F. Martin, D. R. Smith, and S. Schultz, *Plasmon resonances of silver nanowires with a nonregular cross section* , Physical Review B **64**, 235402 (2001).

[266] M. Song, A. Bouhelier, P. Bramant, J. Sharma, E. Dujardin, D. Zhang, and G. Colas-des Francs, *Imaging Symmetry-Selected Corner Plasmon Modes in Penta-Twinned Crystalline Ag Nanowires* , ACS Nano **5**, 5874–5880 (2011).

[267] K. Yee, *Numerical solution of initial boundary value problems involving maxwell's equations in isotropic media* , IEEE Transactions on Antennas and Propagation **14**, 302–307 (1966).

[268] Lumerical Inc., *FDTD: 3D Electromagnetic Simulator* , .

[269] E. D. Palik, *Handbook of Optical Constants of Solids* (Academic Press, 1985).

[270] T. A. F. König, P. A. Ledin, J. Kerszulis, M. A. Mahmoud, M. A. El-Sayed, J. R.

Reynolds, and V. V. Tsukruk, *Electrically Tunable Plasmonic Behavior of Nanocube–Polymer Nanomaterials Induced by a Redox-Active Electrochromic Polymer* , ACS Nano **8**, 6182 (2014).

[271] H. Gao, J. M. McMahon, M. H. Lee, J. Henzie, S. K. Gray, G. C. Schatz, and T. W. Odom, *Rayleigh anomaly-surface plasmon polariton resonances in palladium and gold subwavelength hole arrays* , Optics Express **17**, 2334 (2009).

[272] A. D. Utyushev, V. I. Zakomirnyi, and I. L. Rasskazov, *Collective lattice resonances: Plasmonics and beyond* , Reviews in Physics **6**, 100051 (2021).

[273] Y. Chen, D. Chen, P. P. Altermatt, S. Zhang, L. Wang, X. Zhang, J. Xu, Z. Feng, H. Shen, and P. J. Verlinden, *Technology evolution of the photovoltaic industry: Learning from history and recent progress* , Progress in Photovoltaics: Research and Applications **31**, 1194–1204 (2022).

[274] G. J. Simandl, S. Paradis, and L. Simandl, *Future of photovoltaic materials with emphasis on resource availability, economic geology, criticality, and market size/growth* , CIM Journal **14**, 133–157 (2023).

[275] A. Le Donne, V. Trifiletti, and S. Binetti, *New Earth-Abundant Thin Film Solar Cells Based on Chalcogenides* , Frontiers in Chemistry **7**, 297 (2019).

[276] R. Paul, S. W. Tabernig, J. Reñé Sapera, J. Hurni, A. Tiede, X. Liu, D. A. Damry, V. Conti, M. Zamani, S. Escobar Steinvall, M. Dimitrievska, E. Alarcon-Lladó, V. Piazza, J. Boland, F.-J. Haug, A. Polman, and A. Fontcuberta i Morral, *Carrier generation and collection in Zn_3P_2/InP heterojunction solar cells* , Solar Energy Materials and Solar Cells **256**, 112349 (2023).

[277] R. Chinnam, Éva Ujaczki, and L. O'Donoghue, *Leaching indium from discarded LCD glass: A rapid and environmentally friendly process* , Journal of Cleaner Production **277**, 122868 (2020).

[278] C. Ouyang, D. Liu, K. He, and J. Kang, *Recent Advances in Touch Sensors for Flexible Displays* , IEEE Open Journal of Nanotechnology **4**, 36–46 (2023).

[279] H. Wu, D. Kong, Z. Ruan, P.-C. Hsu, S. Wang, Z. Yu, T. J. Carney, L. Hu, S. Fan, and Y. Cui, *A transparent electrode based on a metal nanotrough network* , Nature Nanotechnology **8**, 421 (2013).

[280] M. Gómez, G. Xu, J. Li, and X. Zeng, *Securing Indium Utilization for High-Tech and Renewable Energy Industries* , Environmental Science & Technology **57**, 2611 (2023).

[281] H. Liu, Y.-F. Liu, P.-P. Xiong, P. Chen, H.-Y. Li, J.-W. Hou, B.-N. Kang, and Y. Duan, *Aluminum-Doped Zinc Oxide Transparent Electrode Prepared by Atomic Layer Deposition for Organic Light Emitting Devices* , IEEE Transactions on Nanotechnology **16**, 634–638 (2017).

[282] A. Way, J. Luke, A. D. Evans, Z. Li, J.-S. Kim, J. R. Durrant, H. K. Hin Lee, and W. C. Tsoi, *Fluorine doped tin oxide as an alternative of indium tin oxide for bottom electrode of semi-transparent organic photovoltaic devices* , AIP Advances **9**, 085220 (2019).

[283] Y. D. Suh, J. Kwon, J. Lee, H. Lee, S. Jeong, D. Kim, H. Cho, J. Yeo, and S. H. Ko, *Maskless Fabrication of Highly Robust, Flexible Transparent Cu Conductor by Random Crack Network Assisted Cu Nanoparticle Patterning and Laser*

Sintering , Advanced Electronic Materials **2**, 1600277 (2016).

[284] A. K. Yadav and S. Chandel, *Tilt angle optimization to maximize incident solar radiation: A review* , Renewable and Sustainable Energy Reviews **23**, 503–513 (2013).

[285] S. W. Glunz, B. Steinhauser, J.-I. Polzin, C. Luderer, B. Grübel, T. Niewelt, A. M. O. M. Okasha, M. Bories, H. Nagel, K. Krieg, F. Feldmann, A. Richter, M. Bivour, and M. Hermle, *Silicon-based passivating contacts: The TOPCon route* , Progress in Photovoltaics: Research and Applications **31**, 341 (2023).

[286] M. A. Verschuuren, M. W. Knight, M. Megens, and A. Polman, *Nanoscale spatial limitations of large-area substrate conformal imprint lithography* , Nanotech. **30**, 345301 (2019).

[287] S. M. Bergin, Y.-H. Chen, A. R. Rathmell, P. Charbonneau, Z.-Y. Li, and B. J. Wiley, *The effect of nanowire length and diameter on the properties of transparent, conducting nanowire films* , Nanoscale **4**, 1996 (2012).

[288] K. R. McIntosh and C. B. Honsberg, *The influence of edge recombination of a solar cell's I–V curve* , Proceedings of the 16th European PVSEC, 1–5 May 2000, Glasgow/UK, pp. 1651 (2000).

[289] B. Veith, T. Ohrdes, F. Werner, R. Brendel, P. P. Altermatt, N.-P. Harder, and J. Schmidt, *Injection dependence of the effective lifetime of n-type Si passivated by Al_2O_3: An edge effect?* , Solar Energy Materials and Solar Cells **120**, 436 (2014).

[290] S. Eiternick, K. Kaufmann, J. Schneider, and M. Turek, *Loss Analysis for Laser Separated Solar Cells* , Energy Procedia **55**, 326–330 (2014).

[291] R. Cariou, J. Benick, F. Feldmann, O. Höhn, H. Hauser, P. Beutel, N. Razek, M. Wimplinger, B. Bläsi, D. Lackner, and et al., *III–V-on-silicon solar cells reaching 33% photoconversion efficiency in two-terminal configuration* , Nature Energy **3**, 326–333 (2018).

[292] *pv-tools gmbh, available from: http://www.pv-tools.de,* .

[293] K. L. Kelly, E. Coronado, L. L. Zhao, and G. C. Schatz, *The Optical Properties of Metal Nanoparticles: The Influence of Size, Shape, and Dielectric Environment* , The Journal of Physical Chemistry B **107**, 668–677 (2002).

[294] B. Tim, P. Błaszkiewicz, and M. Kotkowiak, *Recent Advances in Metallic Nanoparticle Assemblies for Surface-Enhanced Spectroscopy* , International Journal of Molecular Sciences **23**, 291 (2021).

[295] G. Baffou and R. Quidant, *Nanoplasmonics for chemistry* , Chemical Society Reviews **43**, 3898 (2014).

[296] X. Huang, P. K. Jain, I. H. El-Sayed, and M. A. El-Sayed, *Plasmonic photothermal therapy (PPTT) using gold nanoparticles* , Lasers in Medical Science **23**, 217–228 (2007).

[297] Y. Chen, *Nanofabrication by electron beam lithography and its applications: A review* , Microelectronic Engineering **135**, 57–72 (2015).

[298] A. Biswas, I. S. Bayer, A. S. Biris, T. Wang, E. Dervishi, and F. Faupel, *Advances in top–down and bottom–up surface nanofabrication: Techniques, applications*

& future prospects , Advances in Colloid and Interface Science **170**, 2–27 (2012).

[299] B. Satpathy, S. Jena, S. Das, and K. Das, *A comprehensive review of various non-cyanide electroplating baths for the production of silver and gold coatings* , International Materials Reviews **68**, 825–861 (2023).

[300] J. Henzie, J. E. Barton, C. L. Stender, and T. W. Odom, *Large-Area Nanoscale Patterning: Chemistry Meets Fabrication* , Accounts of Chemical Research **39**, 249–257 (2006).

[301] S. H. Ahn and L. J. Guo, *Large-Area Roll-to-Roll and Roll-to-Plate Nanoimprint Lithography: A Step toward High-Throughput Application of Continuous Nanoimprinting* , ACS Nano **3**, 2304–2310 (2009).

[302] D. K. Oh, T. Lee, B. Ko, T. Badloe, J. G. Ok, and J. Rho, *Nanoimprint lithography for high-throughput fabrication of metasurfaces* , Frontiers of Optoelectronics **14**, 229–251 (2021).

[303] L. M. Cox, A. M. Martinez, A. K. Blevins, N. Sowan, Y. Ding, and C. N. Bowman, *Nanoimprint lithography: Emergent materials and methods of actuation* , Nano Today **31**, 100838 (2020).

[304] M. Mayer, M. J. Schnepf, T. A. F. König, and A. Fery, *Colloidal Self-Assembly Concepts for Plasmonic Metasurfaces* , Advanced Optical Materials **7**, 1800564 (2018).

[305] H. Agrawal and E. C. Garnett, *Nanocube Imprint Lithography* , ACS Nano **14**, 11009–11016 (2020).

[306] A. Capitaine, M. Bochet-Modaresialam, P. Poungsripong, C. Badie, V. Heresanu, O. Margeat, L. Santinacci, D. Grosso, E. Garnett, and B. Sciacca, *Nanoparticle Imprint Lithography: From Nanoscale Metrology to Printable Metallic Grids* , ACS Nano **17**, 9361–9373 (2023).

[307] A. Capitaine, M. L. Fajri, and B. Sciacca, *Pushing the Limits of Capillary Assembly for the Arbitrary Positioning of Sub-50nm Nanocubes in Printable Plasmonic Surfaces* , Small Methods , 2300373 (2023).

[308] W. Zhang, Y. Liu, R. Cao, Z. Li, Y. Zhang, Y. Tang, and K. Fan, *Synergy between Crystal Strain and Surface Energy in Morphological Evolution of Five-Fold-Twinned Silver Crystals* , Journal of the American Chemical Society **130**, 15581–15588 (2008).

[309] Q. Zhang, W. Li, C. Moran, J. Zeng, J. Chen, L.-P. Wen, and Y. Xia, *Seed-Mediated Synthesis of Ag Nanocubes with Controllable Edge Lengths in the Range of 30-200 nm and Comparison of Their Optical Properties* , Journal of the American Chemical Society **132**, 11372–11378 (2010).

[310] D. Nečas and P. Klapetek, *Gwyddion: an open-source software for SPM data analysis* , Open Physics **10**, 181 (2012).

List of Publications

Related to this thesis

1. **Y. Bleiji**, M. Dieperink, I. Schuringa, H. Sun, and E. Alarcón-Lladó, *Influence of the crystallographic texture of ITO on the electrodeposition of silver nanoparticles*, RSC Advances **13**, pp. 6490-6497, 2023 (**Chapter 3**)

2. **Y. Bleiji**, A. Cordaro, S.W. Tabernig, and E. Alarcón-Lladó, *High Aspect Ratio Silver Nanogrids by Bottom-Up Electrochemical Growth as Transparent Electrode*, ACS Applied Optical Materials **2**, 3, pp. 508-516, 2024 (**Chapter 4**)

3. **Y. Bleiji**, R. Müller, O. Höhn, B. Bläsi, and E. Alarcón-Lladó, *Electroplated Silver Nanowire Array as Transparent Electrode Without Seed Layer on TOPCon Solar Cells*, in preparation (**Chapter 6**)

4. **Y. Bleiji**, L. Fenzi, A. Capitaine, and B. Sciacca, E. Alarcón-Lladó, *Electrochemical welding of silver nanocubes*, in preparation (**Chapter 7**)

Other publications by the author

5. M. Valenti*, **Y. Bleiji***, J. Blanco Portals, L. A. Muscarella, M. Aarts, F. Peiro, S. Estrade, and E. Alarcón-Lladó, *Grain size control of crystalline III–V semiconductors at ambient conditions using electrochemically mediated growth*, Journal of Materials Chemistry A, **8**, pp. 2752-2759, 2020.

6. M. Valenti, M. D. Wobben, **Y. Bleiji**, A. Cordaro, S. W. Tabernig, M. Aarts, R. D. Buijs, S. R. Rodriguez, A. Polman, E. Alarcón-Lladó, *Optical Characterization of Plasmonic Indium Lattices Fabricated via Electrochemical Deposition*, ACS Applied Optical Materials **1**, pp. 753-758, 2023.

7. M. Krajewski, **Y.Bleiji**, P. Wróbel, E. Alarcón-Lladó, A. Drabínska *Embedded nanomeshes for improved transparent electrode performance for perovskite-silicon and organic solar cells – a numerical study*, in preparation.

* These authors contributed equally.

Acknowledgements

Getting a Ph.D. degree is not just some kind of education. It is a journey that comes with many ups and downs. These include conferences at exotic places, but also dealing with a pandemic, quite some late nights in the lab, and equipment breakdown. In general, I could never have finished this journey without the help and support of some amazing people. Coffee breaks and lunches are always great moments of the day where science is discussed, but most of the time other interesting discussions are held. Thanks to the many international students, I have learnt so much about other cultures and countries without even visiting them. I am very grateful for my time at AMOLF, with its very open atmosphere, where people are always very happy to help and collaborations is highly promoted between the different research groups.

The most important person during my Ph.D. journey has been my amazing supervisor **Esther**. You always made time available to discuss my work and guide me through the Ph.D.. I appreciate all the hard work you have done, especially during the last months of my Ph.D.. You are always very positive and give good and critical feedback without making the person feel bad, which I greatly admire. I feel very honoured for these last 6 years to be part of your group. Thanks a lot Esther!

Albert, thank you for being my second promoter and making it possible to do my Ph.D. in the first place. I really admire the efforts you make to connect all the people within AMOLF, always making a small talk with new students to make them feel very welcome at AMOLF. I think the great academic success of the LMPV team is mainly due to all the collaborations within LMPV, which is the result of a very welcoming working environment. Thank you for making AMOLF a great place.

Furthermore, I would like to express my gratitude to the committee for taking the time to read and evaluate my thesis.

Next, I would like to thank the LMPV group leaders for creating a wonderful environment that stimulates collaborations. **Erik**, thank you for taking the time to read and evaluate my thesis and for the many fruitful discussions. You always asked the right and sharp questions during the LMPV colloquium, which I admire. **Bruno**, you are an extremely open person and I admire you for stimulating all kinds of collaboration between many people within and outside AMOLF with each other. If all scientists were like you, most of the problems would have been solved by now as the result of strong collaborations.

Next, I would like to thank some other group leaders who helped me throughout this journey. **Said**, since I got to know you from the master you are a very enthusiastic and friendly person and are always open to discuss any topic. You always have really interesting critical questions and can explain your arguments in many ways to a very broad audience. **Femius**, I admire you for being always so calm and relaxed while discussing the most difficult problems regarding nanophotonics. You always gave

constructive comments, framing them in such a way that you steer the person in question into the right line of thought. **Wim**, I learnt a lot from you about chemistry and crystal nucleation and growth.

Special and many thanks to the amazing 3DPV group! You guys have been a big part of my life in the last 6 years. A special thanks goes to **Marco** who supervised me throughout the master project and made me feel very welcome in the group. You were always full of ideas, no matter how crazy they sound and whether they were practical or not. **Mark A.**, as the first Ph.D. student in the group, you gave shape to the group and taught me everything about the AFM. I really admire your Dutch "nuchterheid", no matter how many drawbacks you faced, you always kept positive. **Nasim**, your are such a lovely and wonderful person. You were always smiling and very kind to everyone! **Alex**, my man! It was so much fun the last few years! You are always in for a drink and good chat! Keep up the good work! I am very grateful to have you as my paranymph. **Melanie**, we always had so much fun! I really enjoyed working with you and partying with you! Although we never agreed on the temperature in the office, you always allowed me to open the window during the writing of the thesis, even though you needed your winter jacket. I am very grateful to have you as my paranymph. **Daphne**, I really like your enthusiasm and your directness. You are a really lovely person. Many thanks for allowing me to open the window during the writing period of my thesis. **Antony**, you are such an amazing person. You are always very kind and friendly to everyone. You always provided me with all the necessary snacks during the thesis writing. You were my brother in arms during the late night work sessions. **Jaime**, you are such a kind person always smiling and happy. I loved the parties we had together. **Mees**, you were my first student and it feels a bit like you are my academic son. I am very grateful for supervising you during your master project. I am really glad you continued at AMOLF for a Ph.D., and also joining the PV where you even became the chair, a role that suits you very well. **Jelena**, it is incredible how many sports you do. Among many others, cycling was one of them, a passion that we shared. We had quite some nice rides together around Amsterdam exploring the beautiful tulip fields, historic cities, and the dunes. **Dominique**, you are such a lovely person. I really enjoyed your nice stories. **Loriane**, I am still amazed by the story of the floppy disk! From the outside it seems to be that you are a very shy person, but if people get to know you, you are actually a very open and kind person.

Also, a special thanks to all of my students whom I was lucky enough to supervise: **Mees**, **Bram**, **Gaby**, **Nicky**, and **Johanna**. You all have played an important role in completing this thesis! Finally, thanks to all the other people who have been part of this group: **Jose**, **Alexandra**, **Rosa R**, **Jim**, **Merlinde**, **Pepijn**, **Rosa B**, **Blaise**, **Floris B.**, **Jos**, **Paola**, **Juliane**, **Kaj**, **Hallie**, **Anja**, **Jon**, **Marina**, **Chloë**, **Ruerd**, **Margo**, and **Katerina**.

During my time at AMOLF, I have spent almost 2.5 years with the personeelsvereniging (PV). The PV plays an important role in connecting people within AMOLF. Thanks to the events of the PV, I have met so many other people outside my own

research bubble, for which I am very grateful. **Jente**, you always have very nice riddles and you were full of energy. There is no way to stop yourself from running around like a headless chicken. **Timo**, I really love all the small talks we had. Although our research was not related in any way, I always enjoyed talking to you. **Imme**, you always had good and clear ideas for events. You are very effective in organising PV events, which is a great skill to have. **Wessel**, thanks for all the laughter and the nice picture!

Also thanks to all the other members of the PV with whom I had the pleasure to work with: **Alexander**, **Christian**, **Francesca**, **Isabelle**, **Manuel**, **Moritz S.**, **Philip**, and **Yvonne**.

There are many more people at AMOLF who made my Ph.D. journey a pleasure. Thanks **Susan** for the great time together! We go all the way back to the master, where we followed the same track, did both our master projects at AMOLF, and continued both as Ph.D. students. **Stefan**, you are such an amazing person. We had many beers together talking about all kinds of stuff. **Andrea**, the god of imprinting. I have learnt so much from you about nanofabrication. Thanks for teaching me and sharing the knowledge with me! **Kathi**, my (former) office neighbour. We were often one of the few in our corridor that stayed until late and we talked about many things that I always enjoyed. **Francesca**, I enjoyed talking about our shared passion for cycling. Enjoy all the hours to come on the bike! And thank you **Ana**, **Augustin**, **Balazs**, **Benjamin**, **Christiaan**, **Christoph**, **Daan**, **Daphne D**, **Deba**, **Devin**, **Elaina**, **Ethan**, **Evelijn**, **Falco**, **Fiona**, **Floris T.**, **Floris U.**, **George**, **Gianluca Harshal**, **Hongyu**, **Jenny**, **Jeroen**, **Jérôme**, **Jesse**, **Joris**, **Julia**, **Jyoti**, **Linde**, **Loreta**, **Lucie**, **Lukas**, **Nick**, **Nika**, **Nikolai**, **Magda**, **Mareike**, **Marloes**, **Matthias**, **Moritz F.**, **Patrick**, **Rene**, **Robin**, **Roel**, **Rohit**, **Sarah**, **Saskia**, **Sven**, **Tom**, **Thomas**, **Verena**, **Weiyi**, and many others who I might forget!

The experiments performed in this thesis would not have been possible without the help of all of the excellent work of the support departments. A special thanks to our (former) group technicians **Dion** and **Daniel** for always helping me with any kind of technical issue. Also, a thank you **Hinco**, **Niels** and **Marko**, for helping me build the setup and with any small kind of technical issues. Thank you **Marc** for all your chemical support. As a physicist, the world of (organic) chemistry was always magical to me. Thanks for helping me!

In addition to the technical support staff, we have many other excellent support departments, including Mechanical Design, Precision Manufacturing, Finance, Purchase, Facilities, Software, and Electronic Engineering. Thank you **Bas**, **Bob K.**, **Clyde**, **Henk-Jan**, **Ilja**, **Jan**, **Mark W**, **Max**, **Menno**, **Niels**, **Radjin**, **Remco K.**, **Remco R.**, **Ricardo**, **Richard**, **Rutger**, **Sebastiaan**, **Sjoerd W.**, **Wessel**, and **Wiebe**.

Furthermore, the cleanroom has been an important part of this thesis. I am very grateful to have a cleanroom with all the necessary equipment at AMOLF. Thanks **Hans**, **Bob D.**, **Dimitry**, **Andries**, **Igor**, **Dylan**, **Laura** for all the support in the cleanroom!

And to all those other lovely people at AMOLF, thank you!

Last but not least, I want to thank my family and friends. **Mama**, **Papa**, en **Marian**, bedankt voor de onvoorwaardelijke liefde en steun. In het bijzonder wil ik **Alida** bedanken voor alle liefde en steun die ik de afgelopen 10 jaar heb ontvangen. Jij bent een van de belangrijkste personen in mijn leven. Het is mede dankzij jou steun en liefde dat ik mijn Bachelor, Master en Ph.D. zo goed heb kunnen voltooien. Je zult altijd een speciaal plekje in mijn hart hebben.

Besides countless hours in the lab, I spent maybe an equal amount of time on the bike cycling throughout the whole Netherlands and beyond. The student cycling association A.S.S.W.S.V. SKITS has been an important part of my life as a Ph.D. student. No matter how stressed I was or how much I had to do, cycling was a great way to relieve stress. Thank you **Bella**, **Benedikt**, **Finn**, **Floor**, **Geert**, **George**, **Henny**, **Ilse**, **Jeroen**, **Julia**, **Lars**, **Lily**, **Lucas**, **Marcel**, **Marlou**, **Marre**, **Mente**, **Mirabelle**, **Mirthe**, **Marloes**, **Niek**, **Noa**, **Paul**, **Rick**, **Rik**, **Samantha**, **Sep**, **Siranna**, **Stijn M.**, **Stijn R.**, **Theo**, **Volkert**, **Wanja**, and **Zoe** for the great amount of fun!

About the Author

Yorick Bleiji was born in Leiden, the Netherlands, on June 19, 1996, partially growing up in Leiderdorp and Winterswijk. He obtained his high school degree in the direction of Nature & Technology in Winterswijk in 2014. In 2014, he moved back to Leiden to start his bachelor's in Physics at Leiden University. During his bachelor project under the supervision of dr. Nikita Lebedev and prof.dr. Jan Aarts he got inspired by material science and nanofabrication while studying the growth of perovskite thin films using off-axis sputtering. After completing his bachelor's degree in 2017, he moved to Amsterdam to study the master Physics & Astronomy at the University of Amsterdam and the Vrije Universiteit Amsterdam pursuing the Advanced Matter Energy Physics track. In 2018, he carried out his master's research project in the group of prof.dr. Esther Alarcón-Lladó at AMOLF where he studied the inexpensive manufacturing of nanostructured III-V semiconductors using electrochemical mediated growth under the supervision of dr. Marco Valenti and prof.dr. Esther Alarcón-Lladó. Shortly after in 2019, he obtained his master's degree cum laude and joined the group of prof.dr. Esther Alarcón-Lladó as a Ph.D. student focusing on the growth of metal nanowires using electrochemical deposition. During his Ph.D. he attended 22 conferences and symposiums, presenting 8 orals and 12 posters. In 2019, he received the best poster prize award at the ANNIC conference in Paris, France. In 2023, he was nominated for the best poster prize award at the MRS Spring Meeting 2023 in San Francisco, California, United States. The results of his research are shown in this thesis.

In his free time, Yorick has a great passion for road cycling and touring, where he visited all municipalities of the Netherlands by bike, cycled from Amsterdam to Paris within one day, toured from Amsterdam to both Linz, Austria (2021) and the Alpe D'Huez, France (2023). After his defence, he plans to do a 10.000 km bike tour from Amsterdam to the North Cape, Norway and back.